UNIVERSITÀ
DI PAVIA

PhD IN BIOMEDICAL SCIENCES

DEPARTMENT OF MOLECULAR MEDICINE

UNIT OF BIOCHEMISTRY

Zebrafish models of rare skeletal diseases: a tool to investigate bone homeostasis *in vivo* in pathological conditions

PhD Tutor: Prof. Antonella Forlino

PhD dissertation of

Valentina Daponte

XXV cycle a.y. 2022/2023

Declaration

I hereby declare that the contents and organization of this dissertation constitute my own original work and does not compromise in any way the rights of third parties, including those relating to the security of personal data.

Valentina Daponte

2023

Contents

Introduction

Collagen

Collagens are the most abundant protein family in the animal kingdom (Baccetti 1985) and the major component of the extracellular matrix (ECM), in which they play a dominant role in maintaining the structural integrity alongside other important biological functions (Myllyharju and Kivirikko 2001). 28 different types of collagens have been discovered so far (Ricard-Blum 2011). Based on their structure and supramolecular organization, classification includes fibril-forming collagens (I, II, III, V, XI, XXIV, XXVII), Fibril-Associated Collagens with Interrupted Triple helices (FACITs: IX, XII, XIV, XVI, XIX, XX, XXI, XXII, XXVI), network-forming collagens (IV, VI, VIII, X), anchoring fibrils (VII), Membrane-Associated Collagens with Interrupted Triple helices (MACITs: XIII, XVII, XXIII, XXV), and Multiple Triple-helix Domains and Interruptions (MULTIPLEXINs: XV, XVIII) (Shoulders and Raines 2009, Ricard-Blum 2011).

All collagens are characterized by a right-handed triple helix composed of three α-chains. The α-chains can be either identical, generating homotrimers, like collagens type II, III, VII, VIII and X, or different resulting in heterotrimers, like collagens type I, IV, V, VI, IX and XI. Each α-chain is left-handed and supercoils around a central axis in a right-handed manner to form the triple helix (Gelse, Pöschl and Aigner 2003). The repeated sequence $(Gly\text{-}Xaa\text{-}Yaa)_n$ is the characteristic feature of all collagens. The Xaa position is often occupied by a proline, while the Yaa by a hydroxyproline (Gelse et al. 2003). On a molar basis, collagen amino acid composition consists of about 33% glycine, 10% proline, 10% 4-hydroxyproline and 0.1% 3-hydroxyproline residues (Krane 2008). The glycine residue specifically located at every third amino acid allows a close packaging along the central axis because being the smallest amino acid, its side chain is able to fit into the limited triple helix inner space (Myllyharju and Kivirikko 2001). The bulkier side chains of proline and hydroxyproline residues as well as of any Xaa and Yaa positioned amino acids are exposed outward where they are available to interact with adjacent collagen molecules or with non-collagenous proteins (Ishikawa and Bächinger 2013, Viguet-Carrin, Garnero and Delmas 2006).

Collagens have a critical role in maintaining tissue stability and integrity (von der Mark 2006). Defects in collagen structure, biosynthesis and/or assembly lead to a series of severe diseases, such as several chondrodysplasias, certain subtypes of epidermolysis bullosa, arterial aneurysms, osteoarthrosis and osteogenesis imperfecta (Myllyharju and Kivirikko 2001).

Collagen type I structure and biosynthesis

Collagen type I is the most abundant and well-known protein in all vertebrates, constituting more than 90% of bone organic content and being present in several connective tissues such as bone, skin,

tendon and cornea (Gelse et al. 2003). Collagen type I is a heterotrimeric fibril-forming collagen composed by two identical α1 chains, encoded by *COL1A1* and one α2 chain, encoded by *COL1A2* (Ricard-Blum 2011, Gelse et al. 2003) (**Figure 1**).

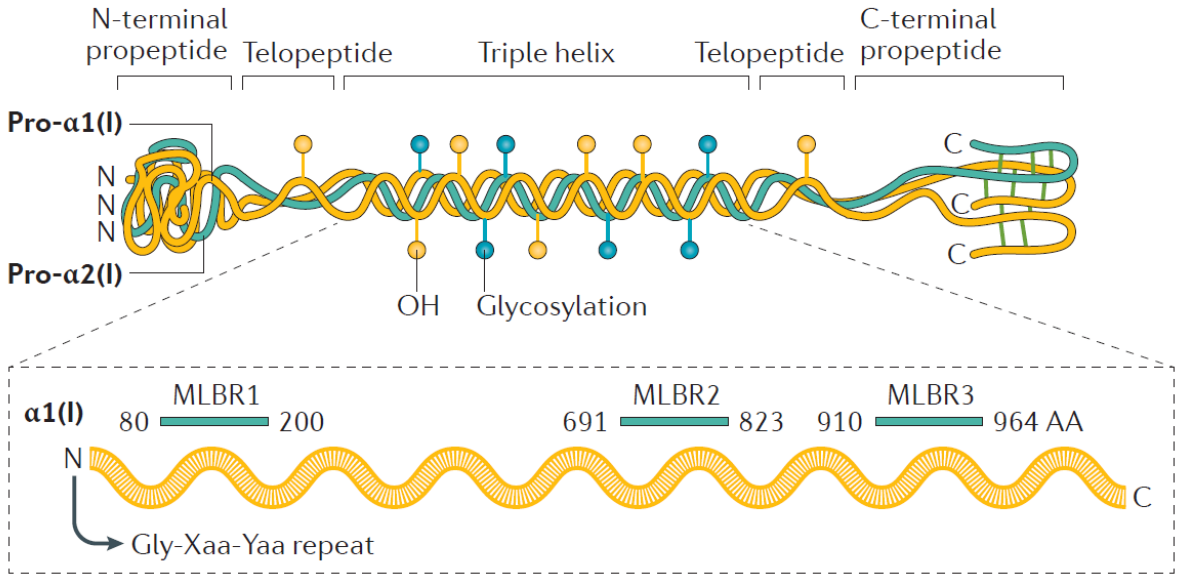

Figure 1. Collagen type I structure. Type I collagen is a heterotrimer composed of two α1 and one α2 left-handed polyproline II-like chains that are assembled into a right-handed triple helix. It is synthesized as a procollagen, containing both amino- and carboxyl-terminal propeptide sequences, which are proteolytically cleaved by specific proteases (a disintegrin and metalloproteinase with thrombospondin motifs 2, ADAMTS2 and bone morphogenetic protein 1, BMP1, respectively). The sequence of each collagen chain is characterized by Gly-Xaa-Yaa repeats (in which Xaa and Yaa can be any amino acid (AA) but are most often proline and hydroxyproline, constituting together ~23% of the amino acid content of collagen (Albaugh, Mukherjee and Barbul 2017)). Along the α1-chain, specific regions that are relevant for the interaction of collagen with other collagen molecules or with extracellular matrix (ECM) proteins were identified, namely, major ligand-binding regions (MLBRs) (from Marini et al. 2017).

As for other types of fibrillar collagens, collagen type I is firstly synthesized as a precursor named procollagen and undergoes an intracellular biosynthesis and an extracellular maturation. First, collagen type I pre-mRNA is capped at the 5' end and polyadenylated at the 3' end. Mature mRNA is transported to the cytoplasm and transferred into the rough endoplasmic reticulum (rER). Here, it is translated into procollagen chains which protrude into the lumen of the rER helped by a signal peptide recognized by corresponding receptors (**Figure 2A**). Proα1 and proα2 chains are composed of three distinct domains: an amino-terminal globular non-collagenous domain (N-telopeptide and N-propeptide), a major collagenous region made of 338 Gly-Xaa-Yaa repeats, and a carboxyl-terminal globular non-collagenous domain (C-telopeptide and C-propeptide) (**Figure 1**). C-propeptides have an essential function in the assembly of the three α chains into trimeric collagen driving the first chain recognition and association (Gelse et al. 2003). Following C-terminal recognition, the three proα chains fold in a zipper like fashion towards the N-terminal end. Before triple helix can be formed, the

procollagen molecules undergo a series of post-translational modifications (PTMs) on specific amino acid residues relevant for procollagen folding, secretion, and ECM assembly. Hydroxylation occurs on unfolded procollagen chains and is mediated by Prolyl 4-hydroxylases (P4Hs), Prolyl 3-hydroxylases (P3Hs) and Lysyl hydroxylases (LHs). All these enzymes use ferrous ions, 2-oxoglutarate, molecular oxygen, and ascorbate as cofactors (von der Mark 2006, Ishikawa and Bächinger 2013). Prolyl 4-hydroxylation occurs on the Yaa position of Gly-Xaa-Yaa repeats. It is the most abundant PTM in vertebrates, fundamental for intramolecular water-mediated hydrogen bonds' formation, that significantly enhance the thermal stability of the triple helix (Shoulders and Raines 2009, Mizuno et al. 2004). P4H is a $\alpha_2\beta_2$ heterotetramer. The β subunit, also known as protein disulphide isomerase (PDI) is fundamental to maintain the solubility of the enzyme but has other important functions (John, Grant and Bulleid 1993). It acts as an oxidoreductase responsible for the formation of both intrachain and interchain disulphide bonds (Bottomley et al. 2001), but also works as a chaperone, binding to nascent collagen polypeptide chains to prevent aggregation (Appenzeller-Herzog and Ellgaard 2008) (**Figure 2B**).

Prolyl 3-hydroxylation is likely to occur after prolyl 4-hydroxylation started (Ishikawa and Bächinger 2013). This PTM is much less frequent, involving only around 1% of the amino acid sequence (Tiainen et al. 2008). Although the role of 3-hydroxyproline residues is not completely understood, it has been proposed that they may generate specific regions of lower stability within the triple helix that may be necessary for the interaction with other ECM molecules such as small leucine-rich proteoglycans and FACITs. LHs catalyze the formation of hydroxylysine in both helical domains and telopeptides. LHs exist in three isoforms: LH1, LH2 and LH3. LH1 primarily hydroxylates lysine residues in the helical domain. LH2 has two spliced variants, LH2a and the longer LH2b, which is the major form and acts on telopeptides (Uzawa et al. 1999). The hydroxylation activity of the multifunctional enzyme LH3 is not significant in collagen type I (Ruotsalainen et al. 2006), but its galactosyltransferase (GT) and glucosyltransferase (GGT) activities are fundamental for O-linked glycosylation of hydroxylysine residues in the α(I) chains (Myllylä et al. 2007). Hydroxylation and subsequential glycosylation of lysine residues are essential to modulate fibrillogenesis (Hennet 2019).

The post translational modifications stop upon triple helical folding whose kinetic is determined by *cis–trans* isomerization of prolyl peptide bonds (Bächinger et al. 1978). Two main peptidyl prolyl *cis-trans* isomerases (PPIs) catalyze this conversion: the FK506 binding protein FKBP65 and cyclophilin B (CyPB). FKBP65 prevents premature association between procollagen chains (Ishikawa et al. 2008). CyPB is a major triple helical catalyst and is able to associate in complexes with other ER collagen-related proteins. Among these, the P3H1/CRTAP/CyPB complex works as a

molecular chaperone by stabilizing the junction between folded and unfolded procollagen chains during triple helix formation (Ishikawa and Bächinger 2013) (**Figure 2C**).

HSP47, a collagen specific chaperone belonging to the serine protease inhibitor (SERPIN) superfamily, is able to recognize and interact with the triple helical in a pH-dependent manner. HSP47 transiently binds procollagen in the ER (neutral pH) and releases it after reaching *cis*-Golgi or ER-Golgi intermediate compartment (ERGIC) (more acidic pH). Then, the triple helical molecules are packed inside large coat protein complex II (COPII)-coated vesicles, conveyed to Golgi and secreted into the extracellular space (Yuan et al. 2018). Since folded procollagen is too large to enter inside conventional COPII-coated vesicles, this trafficking is mediated by the transport and Golgi organization protein TANGO1, located at ER exit sites (ERES). TANGO1 interacts with HSP47 bound to procollagen through its luminal Src Homology 3 (SH3) domain and to COPII-coated vesicles through its cytoplasmic proline rich domain (PRD), delaying the completion of the vesicles which grow to the point that they can contain the large procollagen molecules (Saito et al. 2009). After the release, HSP47 is recycled back to the ER via a KDEL receptor (Ito and Nagata 2017). In the extracellular space, N- and C-propeptides of procollagen are then cleaved by the two metalloproteinases A Disintegrin And Metalloproteinase with Thrombospondin motifs 2 (ADAMTS2) and Bone Morphogenetic Protein 1 (BMP1), respectively (Yamauchi and Sricholpech 2012) (**Figure 2D**).

The new-formed mature collagen type I molecule assembles spontaneously to form collagen fibrils thanks to hydrophobic and electrostatic interactions, additionally stabilized by intramolecular and intermolecular covalent bonds involving lysine or hydroxylysine residues. Such bonds, known as cross-links, are catalyzed by the enzyme lysyl oxidase (LOX), which oxidizes lysine or hydroxylysine ε-amino group to aldehyde groups. Lysine-derived telopeptide aldehydes interact with lysine residues from adjacent molecules, forming covalent interchain cross-links that considerably increase the tensile strength of the fibrils (von der Mark 2006) (**Figure 2D**). The packing arrangement of collagen molecules creates polar and non-polar regions within the fibril with a periodicity of 64 nm, forming a characteristic banding called D-period. This unique pattern is crucial for the physical and mechanical properties of collagen and varies through different species (Gelse et al. 2003).

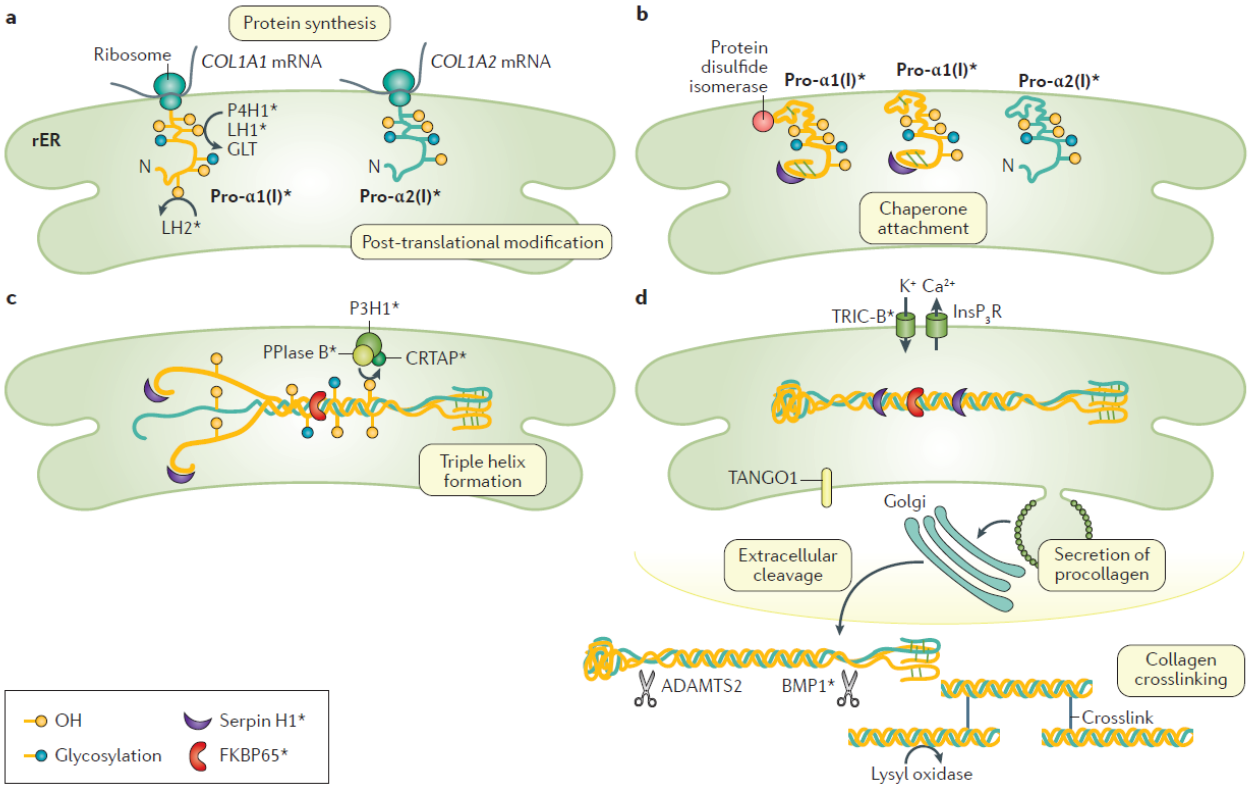

Figure 2. Type I collagen synthesis and processing. a) Translation and post-translational modifications of pro-α1(I) and pro-α2(I). **b)** Interactions with molecular chaperones to prevent premature triple helix formation. **c)** Triple helix formation that comprises two pro-α1-chains and one pro-α2-chain. **d)** Secretion of procollagen, extracellular cleavage to collagen and crosslinking. ADAMTS2, a disintegrin and metalloproteinase with thrombospondin motifs 2; BMP1, bone morphogenetic protein 1; CRTAP, cartilage-associated protein; GLT, galactosyltransferase 1; InsP3R, inositol-1,4,5-triphosphate receptor; LH, lysyl hydroxylase; P3H1, prolyl 3-hydroxylase 1; P4H1, prolyl 4-hydroxylase 1; PPIase B, peptidyl-prolyl *cis–trans* isomerase B; rER, rough endoplasmic reticulum; TANGO1, transport and Golgi organization protein 1; TRIC-B, trimeric intracellular cation channel type B. *Mutations in the genes encoding these proteins are associated with osteogenesis imperfecta (from Marini et al. 2017).

Bone

Bone is a specialized, mineralized connective tissue that exerts several fundamental functions such as locomotion, protection and support of internal tissues, accommodation of the bone marrow, calcium and phosphate storage and homeostasis (Robling, Castillo and Turner 2006).

The structural components of bone consist of an inorganic and an organic phase. The inorganic phase if for the most part constituted by the mineral hydroxyapatite [$Ca_{10}(PO_4)_6(OH)_2$], while the organic phase consists of a cellular part including bone forming, bone resorbing and mechanosensor cells and a large extracellular component, consisting mainly of two collagen types, about 95% type I and about 5% type V and several non-collagenous proteins (NCPs) (von der Mark 2006). Despite its inert appearance, bone is a highly dynamic organ that is continuously remodeled due to the coordinated action of osteoclasts, osteoblasts, osteocytes, and bone lining cells which together form the basic multicellular unit (BMU). Bone remodeling requires a balance between the resorbing activity of osteoclasts and the anabolic activity of osteoblasts. Disruption of this delicate equilibrium leads to several bone diseases, among which osteogenesis imperfecta (OI).

Bone cells

Bone includes four cell types: osteoblasts, bone lining cells, osteocytes and osteoclasts, characterized by different localization and origin. Osteoblasts, bone lining cells and osteoclasts localize along the bone surface, whereas osteocytes are located in the interior part of bone. Also, osteoblasts, osteocytes, and bone lining cells originate from mesenchymal stem cells known as osteoprogenitor cells, whereas osteoclasts originate from hematopoietic stem cells (Buckwalter et al. 1996) (**Figure 3**).

Mesenchymal stem cells

Mesenchymal stem cells (MSCs) are a multipotent stem cell population first discovered in the bone marrow, but also located in the bone canals, endosteum, and periosteum. They can also migrate in the bone from adjacent tissues or from the blood (Buckwalter et al. 1996). MSCs are irregularly shaped cells, characterized by a small cytoplasm and few organelles. Their ability to differentiate into osteoblasts, cartilage cells, but also skeletal muscle cells and adipose cells is at the basis of their fundamental role in bone repair (Buckwalter et al. 1996). For example, after a fracture, a sequence of events stimulates migration, proliferation, and differentiation of these undifferentiated cells into osteoblasts responsible for fracture-healing. Specifically, *RUNX2* and *OSX* are the main transcription factors that enable the initiation and promotion of MSC differentiation towards an osteogenic fate (Salhotra et al. 2020).

Osteoblasts

Osteoblasts account for 4-6% of the total resident cells in bone (Capulli, Paone and Rucci 2014). They are cuboidal cells displaying abundant ER and Golgi as a consequence of their high translational and secretory activity. Their main function is the production of bone matrix by secretion of collagen type I and proteoglycans and its subsequent mineralization. Osteoblasts derive from MSCs, which commit towards the osteoprogenitor lineage. Initially, expression of SRY-box transcription factor 9 (SOX9) induces mesenchymal condensation and the commitment to osteoprogenitor cell (Maes et al. 2012). The following expression of Runt-related transcription factor 2 (RUNX2), the master regulator of osteoblast differentiation, marks the commitment to preosteoblast (Salhotra et al. 2020). RUNX2 upregulates osteoblast-related genes encoding collagen type I (*COL1A1*), osteopontin (*SPP1*), bone sialoprotein (*IBSP*), alkaline phosphatase (*ALP*), osterix (*SP7*), and bone γ-carboxyglutamic acid-containing protein (*BGLAP*), which define cell differentiation into osteoblast (Fakhry et al. 2013). Mature osteoblasts can either undergo to apoptosis (Jilka et al. 1998) or become embedded in the matrix, forming osteocytes (Compton and Lee 2014). Another possible fate is osteoblasts inactivation into bone lining cells (Florencio-Silva et al. 2015).

Bone lining cells

Bone lining cells are flat, elongated cells that cover the bone surfaces of the mature skeleton (Miller et al. 1989). The function of these cells is not completely understood; however, there is evidence that they may prevent the direct interaction between osteoclasts and bone matrix when bone resorption should not occur (Andersen et al. 2009). Also, although bone lining cells are generally metabolically inactive, they can acquire a secretory activity in specific bone physiological conditions and participate to osteoclast differentiation producing osteoprotegerin (OPG) and the receptor activator of nuclear factor kappa-B ligand (RANKL) (Mosley 2000).

Osteocytes

Osteocytes are the most abundant cell type in bone, making up 90-95% of total bone cells. Osteocytes derive from osteoblasts, which are firstly surrounded by bone matrix and eventually become mature and smaller as they get deeper within the bone tissue (Downey and Siegel 2006, Florencio-Silva et al. 2015). Osteocytes have a dendritic morphology. Their cell body localizes inside the lacuna, while long cytoplasmatic processes extend within the matrix through tiny tunnels named *canaliculi* to connect with adjacent osteocytes, but also bone lining cells and osteoblasts on the bone surface. These connections are extremely important in facilitating cellular communication and intercellular transport of small signaling molecules within the mineralized matrix.

Due to their localization within the bone matrix, osteocytes exercise a mechanosensitive function to keep bone maintenance. During mechanical loading, osteocytes decrease the expression of Dickkopf-related protein 1 (DKK1) and sclerostin, leading to increased bone formation through activation of WNT–β-catenin signaling in osteoblasts (Robling et al. 2008). Vice versa, in response to mechanical unloading, osteocytes express RANKL, promoting bone resorption by osteoclast activation (Tatsumi et al. 2007). Furthermore, osteocyte apoptosis has been showed to act as chemotactic signal to bone resorption mediated by osteoclasts (Bellido 2014). Indeed, during bone resorption, apoptotic osteocytes are engulfed by osteoclasts (Boabaid, Cerri and Katchburian 2001, Cerri, Boabaid and Katchburian 2003).

Osteoclasts

Osteoclasts are large, multinucleated cells responsible for bone resorption. Differently from the other bone cells, osteoclasts originate from mononuclear cells of the hematopoietic cell lineage under the stimulation of macrophage colony-stimulating factor (M-CSF), secreted by osteoprogenitor mesenchymal cells and osteoblasts (Boyce et al. 1999), and RANKL, secreted by osteoblasts, osteocytes, and stromal cells (Crockett et al. 2011). Osteoclasts are characterized by a very high mobility; when active, they polarize and their plasma membrane in contact with bone surface assumes an infolded appearance known as the ruffled border. In the ruffled border, vacuolar-type H+-ATPase (V-ATPase) and chloride channels help to acidify the extracellular environment, enabling dissolution of hydroxyapatite crystals (Stenbeck 2002). Bone degradation is further enhanced by the activity of enzymes such as tartrate-resistant acid phosphatase (TRAP), cathepsin K, and matrix metalloproteinase-9 (MMP-9), that are released into the Howship lacuna (Ljusberg et al. 2005, Mulari, Vääräniemi and Väänänen 2003). Degradation products are finally endocytosed across the ruffled border and transcytosed to the functional exit site at the opposite side of the cell, where they are secreted (Arana-Chavez and Bradaschia-Correa 2009).

It has been shown that osteoclasts display several functions other than bone resorption. For instance, they can produce factors called clastokines that can control osteoblast bone formation activity (Drissi and Sanjay 2016). Also, recent evidence shows that osteoclasts may directly regulate the hematopoietic stem cell niche (Mansour et al. 2012).

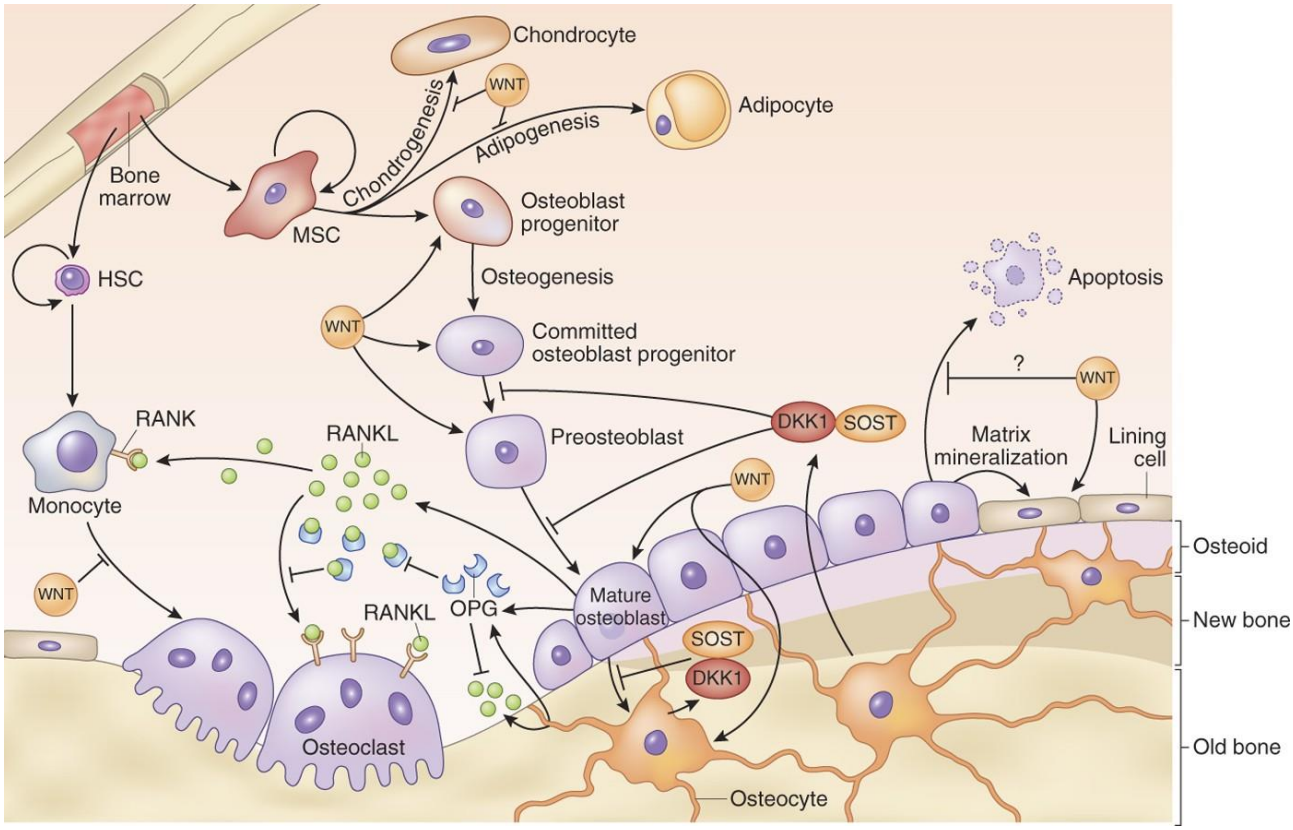

Figure 3. Bone cell types. Bone-forming osteoblasts derive from pluripotent MSCs. MSCs can differentiate into chondrocytes, adipocytes, and osteoblast progenitors. Once osteoblast progenitors are committed, they proliferate and differentiate until becoming mature osteoblasts. Osteoclasts derive from HSCs, which first differentiate into monocytes and then, under RANKL stimulation, become bone resorbing osteoclasts DKK1: Dickkopf-related protein 1; HSC: hematopoietic stem cell; MSC: mesenchymal stem cell; OPG: osteoprotegerin; RANK: receptor activator of nuclear factor kappa-B; RANKL: receptor activator of nuclear factor kappa-B ligand; SOST: sclerostin (from Baron and Kneissel 2013).

Structural organization of bone

Based on the shape, bones can be short, flat or long/tubular. Examples of short bones are the vertebral bodies, the carpals, and the tarsals, characterized by thin cortices. Flat bones provide broad extension for muscular attachment and include the skull, the scapula, the sternum, the hip. Finally, long bones, such as the tibia and the femur, are characterized by a thick-walled tubular diaphysis sided at both ends by a large metaphysis and epiphysis (Buckwalter et al. 1996).

Structurally, bone can be classified into cortical (compact) versus cancellous (trabecular). Cortical bone, which surrounds the bone marrow cavity and the cancellous bone plates, is dense and solid and forms around 80% of the mature skeleton (Buckwalter et al. 1996). Cortical osteons are formed by concentric rings of lamellae, also known as Haversian systems, which are cylindrically shaped and run longitudinally along the cortex (Downey and Siegel 2006, Clarke 2008). The central canals (Haversian canals) contain blood vessels, lymph vessels, and occasionally, nerves. Haversian canals are interconnected by transverse and obliquely oriented vascular anastomoses, known as Volkmann's

canals (Clarke 2008). Haversian and Volkmann's canals are fundamental to bring oxygen and nutrients to osteocytes that are surrounded by hard, mineralized matrix.

Cortical bone is composed of an outer layer, called periosteum, and an inner part, the endosteum. The periosteum is a fibrous connective tissue sheath tightly attached to the outer cortical surface of bone (except for joints, where bone is lined by articular cartilage) helped by thick collagenous fibers called Sharpey's fibers. Periosteum contains blood vessels, nerve fibers, osteoblasts and osteoclasts and is highly active in bone formation, as periosteal cells continue to form new bone throughout life, increasing diameter of the diaphysis of long bones over age (Buckwalter et al. 1996). The endosteum is a membranous structure in contact with the bone marrow space covering the inner surface of cortical bone, trabecular bone, and Volkmann's canals and containing osteoblasts and osteoclasts (Clarke 2008).

Trabecular bone accounts for 20% of the skeleton and is a highly porous form of bone tissue that is organized into a network of interconnected plates and rods called trabeculae. It localizes at the epiphyses of long bones and in the vertebral bodies. Trabecular bone is metabolically more active than cortical bone and, as a consequence, less mineralized, with lower calcium content and tissue density (Dyson and Whitehouse 1968).

Cortical and trabecular bone can be formed by either woven or lamellar bone. Woven bone forms as primary bone during embryogenesis and is later resorbed and replaced by lamellar, or secondary, bone. Woven bone, however, appears also during the initial stages of fracture healing, within cranial sutures, ear ossicles, and epiphyseal plates and can be found in high bone turnover conditions such as osteitis fibrosa cystica and Paget's disease (Clarke 2008). Woven bone has a high rate of metabolic activity and has a scattered, irregular appearance, with disorganized collagen fibrils. Lamellar bone is significantly stronger due to an orderly arrangement in which collagen fibrils are laid down in alternating orientations and osteocytes are uniform and aligned with the other bone structures (Eriksen, Axelrod and Melsen 1994).

Bone extracellular matrix

Bone ECM is composed of an organic matrix and inorganic salts. Bone organic content is constituted by 85-90% collagenous proteins, for the most part collagen type I, with small amounts of collagen type III and V and FACIT collagens, that help determining collagen fibril diameter during fibrillogenesis (Clarke 2008). The other 10-15% is composed by non-collagenous proteins (NCPs), that have a regulatory role and influence matrix organization, bone mineralization and bone cells' behavior. Bone NCPs include proteoglycans, glycosylated proteins, and γ-carboxylated (gla) proteins.

The most abundant NCP of bone ECM is bone γ-carboxyglutamic acid-containing protein (BGLAP), also known as osteocalcin, synthesized exclusively by osteoblasts (Komori 2020). Osteocalcin has a fundamental role in regulating the alignment of hydroxyapatite crystal parallel to collagen fibrils and is required for optimal bone strength in the longitudinal direction of long bones (Moriishi et al. 2020). Osteocalcin function in regulating bone quantity is debated, as previous studies using an osteocalcin-deficient ($Ocn^{-/-}$) mouse indicating osteocalcin as a bone formation inhibitor (Ducy et al. 1996) were not recapitulated by two more recent mouse models (Moriishi et al. 2020, Diegel et al. 2020, Moriishi and Komori 2020).

The inorganic matrix of bone provides tensile yield strength and is involved in mineral metabolism as an ion reservoir. Mineral salts of bone consist predominantly of calcium and phosphorus, but significant amounts of sodium, magnesium, bicarbonate, potassium, citrate, carbonate, fluorite, zinc, barium, and strontium are also present (Buckwalter et al. 1996).

Matrix mineralization associates with increased expression of alkaline phosphatase (ALP) and several NCPs, including osteocalcin, osteopontin, and bone sialoprotein. This process occurs in an organized fashion. Bone mineral is first deposited in specific hole zone regions between collagen fibrils (Buckwalter et al. 1996). Here, matrix extracellular vesicles synthesized by chondrocytes and osteoblasts act as protected microenvironments in which calcium- and phosphate-binding proteins form a nucleation core sufficient to precipitate hydroxyapatite crystals in an ordered manner (Anderson 2003). Calcium and phosphate ions nucleate to form the hydroxyapatite crystals, while collagen and NCPs form a scaffold for hydroxyapatite deposition (Datta et al. 2008). As bone matures, hydroxyapatite crystals enlarge, both by crystal growth and by aggregation (Clarke 2008), increasing bone stiffness (Torzilli et al. 1982). In this expansion phase of mineralization, ALP is fundamental to hydrolyze inorganic pyrophosphate (PPi) into adequate levels of inorganic phosphate (Pi) in order to allow the continuous production of new hydroxyapatite crystals (Vimalraj 2020) (**Figure 4**).

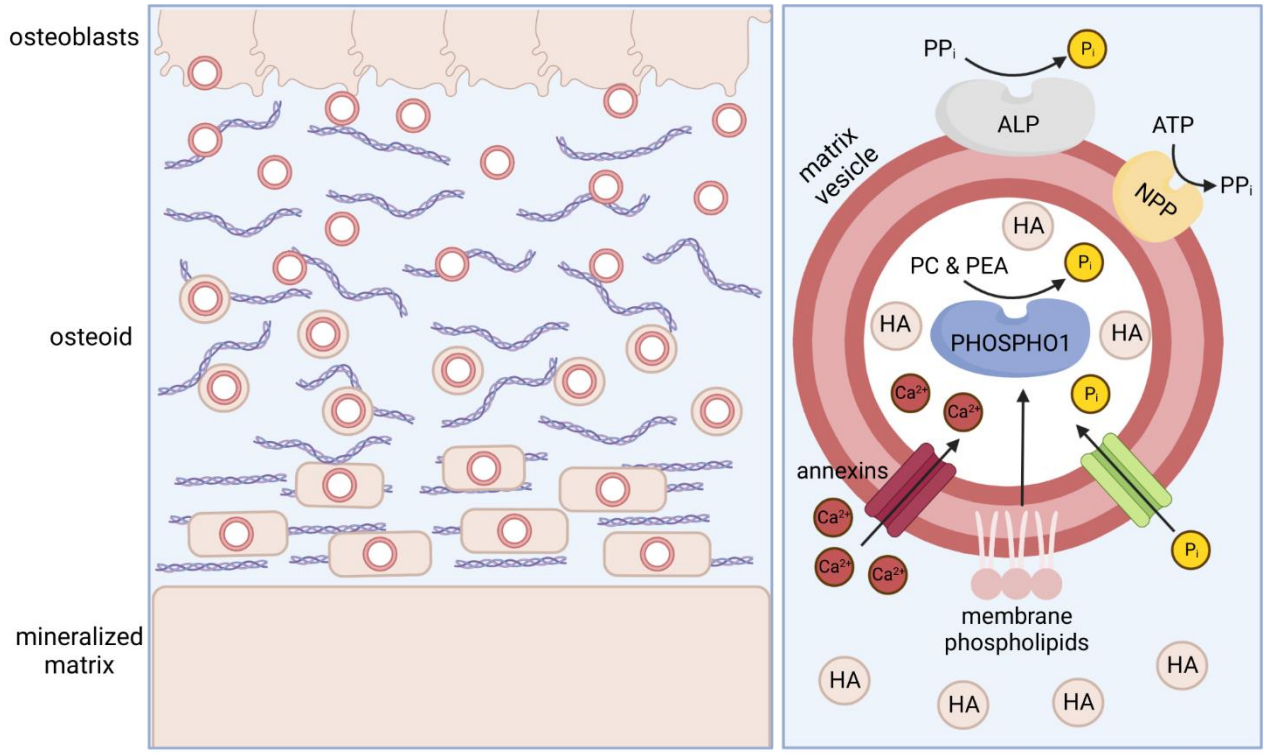

Figure 4. Bone mineralization. Osteoblasts secrete collagen type I, several glycoproteins, and proteoglycans into the matrix. Some of these factors, notably osteocalcin, bind Ca^{2+} with high affinity, raising the local concentration of these ions. Osteoblasts also release small membrane-enclosed matrix vesicles associated to several enzymes, such as alkaline phosphatase (ALP) that hydrolyze phosphate ions from various macromolecules, creating a high concentration of these ions locally. The high ion concentrations induce the formation of calcified nanocrystals in and around the matrix vesicles. The crystals grow and mineralize further with formation of small growing masses of calcium hydroxyapatite (HA) which surround the collagen fibers and all other macromolecules, eventually converging as a solid bony mineralized matrix. On the right: detailed structure of a matrix vesicle. Inside the matrix vesicle, HA forms due to inorganic phosphate provided by hydrolysis of phospholipids, such as phosphocoline (PC) and phosphoethanolamine (PEA), and by the sodium–phosphate cotransporter, together with calcium provided by annexin channels. HA exits through the matrix vesicle membrane and elongates using extracellular P_i and Ca^{2+}. Nucleotide pyrophosphate phosphodiesterase (NPP) provides inorganic pyrophosphate (PPi), that inhibits HA formation, balancing ALP activity. Created with BioRender.com.

Bone ossification

Bone ossification, or skeletogenesis, is the process by which osteoblasts first lay down the osteoid matrix, and then deposit the hydroxyapatite crystals (**Figure 4**). The starting point of bone formation is the migration of mesenchymal cells derived from these embryonic lineages to the sites of ossification. Here cells condensate, creating areas of high cellular density that outline shape and size of the future bones (Berendsen and Olsen 2015, Hall and Miyake 1992).

Intramembranous ossification accounts for the formation of skull, mandible, and clavicle. This type of ossification occurs when condensed mesenchymal cells differentiate and become osteoblasts to

directly form bone. They first produce an organic matrix which later calcifies in a radial way starting from an ossification center located in the middle of each future bone (Lefebvre and Bhattaram 2010) (**Figure 5A**).

In endochondral ossification, characterizing long bones, cells differentiate first in chondrocytes, producing a cartilage template (anlagen) that will then be replaced by bone (Berendsen and Olsen 2015). Endochondral ossification is a complex process, which starts when proliferating chondrocytes in the center of cartilage anlagen differentiate towards a non-proliferative hypertrophic state. Subsequently, the hypertrophic cartilage is invaded by osteoblast progenitors, osteoclasts, blood vessel endothelial cells and hematopoietic cells from the perichondrium. The hypertrophic cartilage is then resorbed, osteoblast progenitors differentiate into trabecular bone-forming osteoblasts, and hematopoietic and endothelial cells form the bone marrow. In this region, the primary ossification center is established (Maes et al. 2010). Along the circumference of the developing endochondral bone, the perichondrium develops osteogenic potential and start depositing a thin layer of cortical bone, the periosteum, around the cartilage anlage. During growth, primary ossification center expands longitudinally, forming the diaphysis, and secondary ossification centers form the epiphyses, which retain a thin layer of hyaline cartilage along the articular surface. The border between the diaphysis and epiphysis of developing long bones is called epiphyseal growth plate, responsible for continued longitudinal bone growth until physical maturity (Kronenberg 2003, Karsenty and Wagner 2002) (**Figure 5B**).

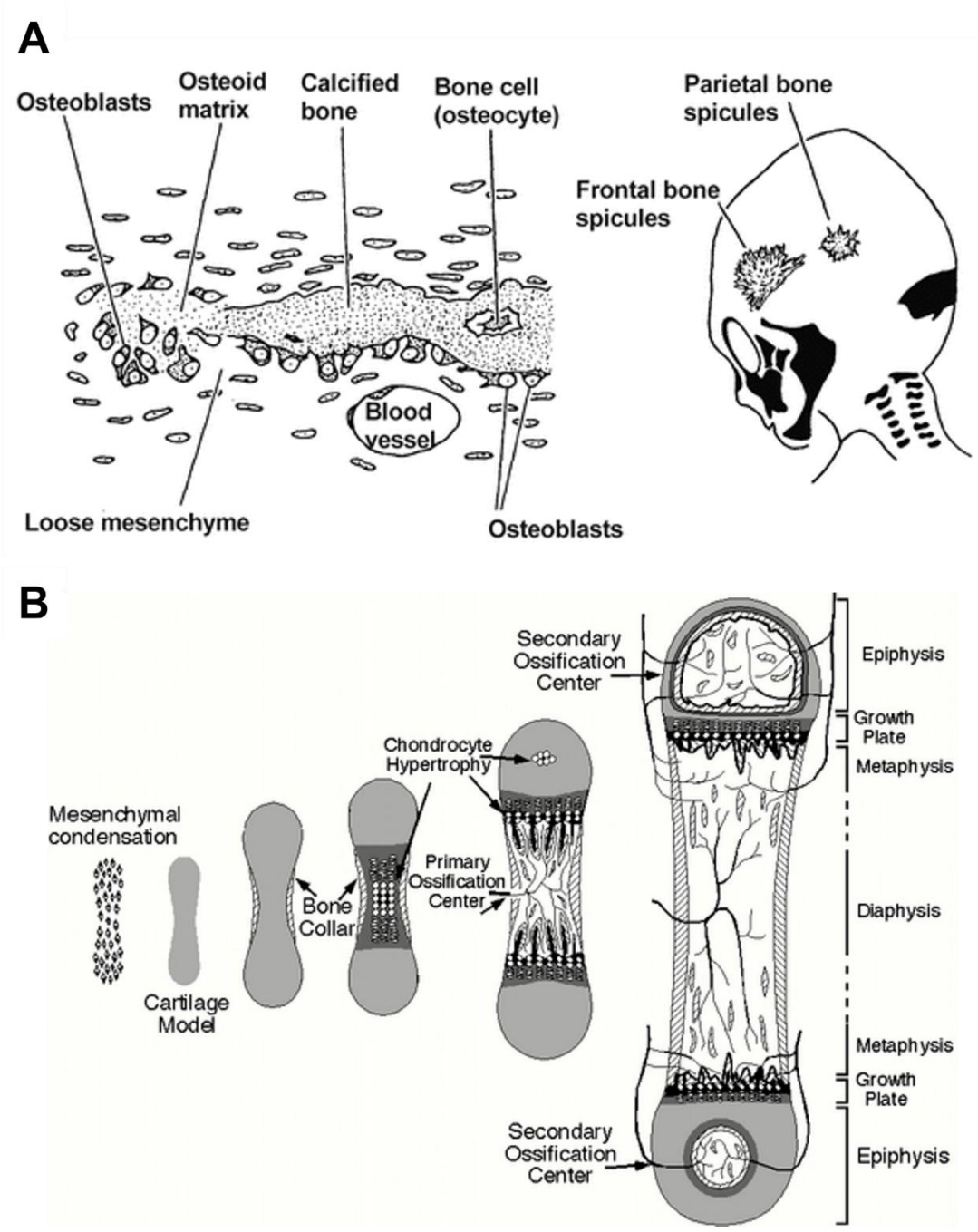

Figure 5. Bone ossification. (A) Intramembranous ossification, typical of cranial bones. Loose mesenchymal cells aggregate and directly differentiate into osteoblasts, which start laying down calcified matrix in a radial way. **(B)** Endochondral ossification, typical of long bones. Mesenchymal cells condense to form a cartilage model with the shape of the bone that will be formed. Chondrocytes undergo hypertrophy and apoptosis while cartilage matrix mineralizes. This allows blood vessel invasion, which bring in osteoblasts that bind the degenerating cartilage matrix and deposit bone matrix, forming the primary, and then the secondary ossification centers. In mature adult bones, the growth plate is fully resorbed, so that one marrow cavity extends the full length of the bone (from Moreira et al. 2000 and from the website https://pocketdentistry.com/biological-mineralization/).

Osteogenesis imperfecta (OI)

Osteogenesis imperfecta (OI), also known as brittle bone disease, is a group of common rare heritable connective tissue disorders primarily affecting bone and causing bone deformity and skeletal fragility (Forlino and Marini 2016). Other possible manifestations can occur in different organs, such as blue sclerae, dentinogenesis imperfecta, abnormalities in cardiovascular and pulmonary systems, hearing loss and muscle weakness (Forlino and Marini 2016, Marini et al. 2017). OI has long been known as an autosomal dominant disorder caused by mutations in *COL1A1* and *COL1A2* genes encoding collagen type I α1 and α2 chains. In 1979, Sillence classified OI into four types, from mild to lethal, based on clinical and radiographic features: OI type I, the mildest form, relates to quantitative deficiency of structurally normal collagen. OI type II, perinatal lethal, OI type III, progressively deforming, and OI type IV, moderate, are due to mutations altering collagen structure (Sillence, Senn and Danks 1979).

In 2006, the first gene for recessive OI, *CRTAP*, was discovered (Barnes et al. 2006). From then on, especially thanks to the next generation sequencing approach (NGS), new mutations with a recessive inheritance pattern were identified in genes involved in collagen biosynthesis, maturation and folding, as well as in osteoblast differentiation and activity. The new findings imposed a revision of the original classification and a new functional one in 5 groups based on the compromised pathway (defects in collagen structure or processing, collagen modification defects, collagen folding and cross-linking defects, ossification or mineralization defects, osteoblast development defects) was proposed by Forlino and Marini (Marini et al. 2017). This classification has been adopted by the Osteogenesis Imperfecta Foundation (OIF) (Marini et al. 2017). Recently new OI forms were added requiring further studies for a proper classification and including OI type XVIII, caused by mutation in *FAM46A* gene (Doyard et al. 2018), OI type XX due to mutated *MESD* (Moosa et al. 2019), OI type XXI due to mutation in *KDELR2* (van Dijk et al. 2020), OI type XXII caused by mutation in *CCDC134* (Dubail et al. 2020) and a still not yet classified X-linked form caused by mutation in *PLS3* (Hu et al. 2020) (**Figure 6, Table 1**).

OI classification

Defects in collagen synthesis and structure

This group includes the four classical dominant OI forms (I-IV) from the original Sillence's classification, caused by mutations in *COL1A1* or *COL1A2*.

OI type I is the mildest form of the disorder, mainly caused by null mutations in *COL1A1*, leading to the production of approximately half of structurally normal collagen type I (Marini et al. 2007). Patients display blue sclerae, low occurrence of fractures and occasionally develop hearing loss during adulthood. OI type I can be divided into A and B subtypes based on the presence or absence of dentinogenesis imperfecta (Levin, Salinas and Jorgenson 1978).

Collagen type I structural defects cause OI type II, III and IV. The most common mutations are glycine substitutions with another bulkier or charged residue within the Gly-Xaa-Yaa repetition. These substitutions disrupt triple helical folding, leading to intracellular retention of the misfolded collagen which undergoes overmodification by enzymes such as P4H1, LHs, GTs and GGTs (Jovanovic, Guterman-Ram and Marini 2022). The polar amino acid serine (Ser) is the most frequent substitute in both α(I) chains, accounting for 44.5% of glycine substitutions in α1(I) and 42.6% in α2(I). The polar serine and the charged aspartate account for around half of lethality frequency in both chains (Garibaldi et al. 2022). Mutations in 3' or 5' splice sites result in both *COL1A1* and *COL1A2* exon skipping. In this case, the Gly-Xaa-Yaa sequence is not altered, but chain alignment can be shifted, thus again affecting collagen folding and processing (Marini et al. 2017). Duplication or deletion of one or two Gly-Xaa-Yaa repetitions cause a shift of collagen chains in the heterotrimer (Marini et al. 2017). A small portion of mutations (around 5%) can occur in the C-propeptide, impairing chain association and leading to paradoxical high bone mass OI (Marini et al. 2017). The localization of mutations along the chain strongly affects the outcome of the disease. Due to the C-terminal to N-terminal direction of collagen folding, mutations close to N-terminal minimally disturb helical formation, while mutations in the C-terminal are usually associated with severe OI phenotype (Marini et al. 2017). Also, due to collagen type I stoichiometry, mutations in *COL1A1* are more likely to result in lethal OI than *COL1A2* ones (Marini et al. 2017). Recently, discrete amino acid residues variants leading to lethal OI were identified in the major ligand-binding regions 2 and 3 (MLBR2 and MLBR3), both important for interactions with non-collagenous ECM proteins (Marini et al. 2007, Garibaldi et al. 2022).

Among classical OI types caused by collagen type I structural defects, OI type II is the most severe, characterized by high perinatal lethality due to cardiac and respiratory complications. Radiological features include absent or limited calvarial mineralization, flat vertebral bodies, short and broad femurs and ribs, bowing of long bones (Marini et al. 2017). Children with OI type III who survive the neonatal period present frequent fractures of the long bones, scoliosis, and chest deformities (Sinikumpu et al. 2015). OI type IV is a moderate form, ranging from mild symptoms similar to OI

type I, to more severe manifestations resembling OI type III. Clinical features and fracture occurrence are variable (Fratzl-Zelman et al. 2015a).

Defects in bone mineralization

Mutations in *IFITM5* and *SERPINF1* are responsible for OI type V and VI, respectively. OI types belonging to this group are not due to altered collagen synthesis or processing, but to impaired bone mineralization and ossification.

Interferon-induced transmembrane protein 5 (IFITM5), also known as BRIL, is a bone-specific protein that localizes on the osteoblast plasma membrane, where it acts as a positive modulator of mineralization (Moffatt et al. 2008). To date, a single recurrent autosomal domination mutation in this gene has been identified: a c.-14C>T point mutation in the 5'-UTR region, that creates a new start codon upstream of the normal translation start, resulting in the addition of 5 residues (MALEP) to the cytoplasmic N-terminus of the protein (Semler et al. 2012). Patients have a remarkable predisposition to develop hyperplastic calli after fractures or surgical interventions and show an irregular pattern of bone lamellation under polarized light microscopy (Semler et al. 2012).

SERPINF1 encodes for the pigment epithelium-derived factor (PEDF), an anti-angiogenic factor expressed in osteoblasts, chondrocytes, and, to a lesser extent, osteoclasts (Becker et al. 2011). PEDF contributes to the maintenance of bone homeostasis, being able to regulate osteoclast activity via osteoprotegerin (OPG) and RANKL (Akiyama et al. 2010). Null mutations in *SERPINF1* lead to delayed mineralization. Bone from patients with OI type VI undergoes progressive degeneration, with reduced bone mineral density and vertebral compressions (Trejo et al. 2017). Bone histomorphometry is characteristic, with broad osteoid (unmineralized bone matrix) and a fish-scale pattern under polarized light (Fratzl-Zelman et al. 2015b).

BRIL and PEDF roles during osteoblast development, osteoid formation and mineralization are connected. Patients with p.S40L substitution in *IFITM5*, which interferes with the modification of BRIL palmitoylation sites (Farber et al. 2014, Tsukamoto et al. 2013), show normal *IFITM5* expression and BRIL protein level, but have decreased *SERPINF1* expression and minimal secreted PEDF (Farber et al. 2014). These patients show atypical OI type VI, characterized by clinical features and bone histology compatible with OI type VI, but not with OI type V (Jovanovic et al. 2022).

Defects in collagen modification

Inside the ER, procollagen undergoes a series of PTMs. One of the main players of this process is the Prolyl 3-hydroxylation complex, constituted by three proteins associated in a 1:1:1 ratio: prolyl 3-hydroxylase 1 (P3H1), cartilage-associated protein (CRTAP), and cyclophilin B (CyPB). P3H1 is the enzyme catalyzing the hydroxylation of α1(I)-Pro986 and α2(I)-Pro707 residues (Vranka, Sakai and Bächinger 2004), while CRTAP is a helper protein which takes P3H1 closer to the substrate and stabilizes the complex (Morello et al. 1999). CyPB is a *cis-trans* isomerase which assists proline residues to acquire *trans* conformation, required for proper folding into the triple helix (Marini et al. 2017).

Null mutations in *CRTAP* and *P3H1* genes cause OI type VII and OI type VIII, respectively (Morello et al. 2006, Barnes et al. 2006, Cabral et al. 2007). Both result in reduced to absent α1(I)-Pro986 hydroxylation associated to collagen type I overmodification (Cabral et al. 2007). OI type VII and VIII patients have lethal or extremely severe phenotype overlapping with the clinical features of dominant types II and III (Chang et al. 2010). Both types share severe osteochondrodysplasia, rhizomelia, undertubulated long bones and fragile ribs (Marini et al. 2017).

Missense and nonsense mutations in *PPIB*, encoding for CyPB, are responsible for OI type IX, which has distinct biochemical and phenotypical features only partially overlapping with P3H1 and CRTAP defects. Patients with lethal phenotype show around 30% reduced α1(I)-Pro986 hydroxylation (although never absent), while some patients with moderate form and normal levels of hydroxylation have been reported (Barnes et al. 2010). Clinical manifestations include white sclerae and undertubulated long bones as OI type VII and VIII patients, but not rhizomelia (Barnes et al. 2010).

Defects in collagen folding and cross-linking

After collagen type I folding is completed, several molecular chaperones intervene to stabilize the triple helix. Heat shock protein 47 (HSP47) is an ER resident collagen-specific chaperone encoded by *SERPINH1*. HSP47 is able to bind triple helical collagen, to stabilize it, and to mediate its shuttling towards *cis*-Golgi thanks to an RDEL recognition site (Satoh et al. 1996). Various homozygous mutations in the *SERPINH1* gene have been described, all leading to the moderate-severe OI type X. These mutations are located in the serine-type endopeptidase inhibitor domain and reduce the chaperone activity of the protein (Drögemüller et al. 2009), leading to the secretion of incompletely folded and more protease-sensitive collagen type I. OI type X features include multiple bone deformities and fractures, generalized osteopenia, presence of dentinogenesis imperfecta, and blue sclerae (Christiansen et al. 2010, Duran et al. 2015).

FKBP10 encodes for the ER-resident immunophilin FKBP65, which through direct and indirect interactions mediated by modifying enzymes is also crucial for normal collagen synthesis (Forlino and Marini 2016). Defects in FKBP65 are clinically and genetically heterogeneous and cause a range of overlapping phenotypes, classified into three distinct pathologies. The first one is the recessive OI type XI, progressively deforming characterized by severe osteopenia, fractures, long bone deformities and a distinctive kyphoscoliosis with platyspondyly and wedging of the thoracic vertebrae (Alanay et al. 2010). Secondly, mutations in *FKBP10* can also cause Bruck syndrome 1, characterized by congenital contractures of joints, short stature, and scoliosis (Schwarze et al. 2013). The last outcome is Kuskokwim syndrome, a congenital contracture disorder in which residual activity of FKBP65 (around 5%) is sufficient to prevent skeletal dysplasia (Barnes et al. 2013).

Collagen type I maturation is reached through hydroxylation of lysine residues at the carboxyl-terminal of telopeptides, which allow cross-linking between collagen molecules, fundamental to provide stability and tensile strength to the fibrils (Uzawa et al. 1999). Procollagen-lysine, 2-oxoglutarate 5-dioxygenase 2 (*PLOD2*) encodes for lysyl hydroxylase 2 (LH2), which is the enzyme responsible for this process. Several biallelic *PLOD* variants have been demonstrated to cause Bruck syndrome 2 (Bank et al. 1999), a rare form of autosomal recessive OI without classification number. Almost all patients share congenital joint contractures, presence of pterygia in the bone prohibiting ambulation, recurrence of fractures, and severe bone pain (Leal et al. 2018). Different mutations have been reported to cause various degrees of loss of hydroxylation of lysine in procollagen telopeptides *in vitro* (Hyry, Lantto and Myllyharju 2009), and patients within the same family may manifest a high phenotypic variability (Leal et al. 2018).

Mutations affecting bone morphogenic protein 1 (BMP1) are responsible for autosomal recessive OI type XIII. BMP1 is a tolloid-like proteinase acting on procollagen type I to cleave the C-propeptide during procollagen processing. Cleavage defects cause secretion and incorporation of pC-collagen (collagen still including C-propeptide) in the extracellular matrix, which affect fibril structure and acts as a mineral nucleator. The consequence is a paradoxical OI with high bone mass, characterized by abnormal high mineralization associated with bone fragility (Lindahl et al. 2011). *BMP1* mutations result in more severe OI respect to α1(I) and α2(I) C-terminal cleavage site mutations because this enzyme family also processes other procollagens (Kessler et al. 1996), small leucine-rich proteoglycans, such as prodecorin and probiglycan (Syx et al. 2015, Scott et al. 2000), and activates LOX enzyme (Uzel et al. 2001). OI type XIII patients due to missense and frameshift mutations are characterized by short stature, frequent fractures, normal sclerae, umbilical hernia and high bone mass (Forlino and Marini 2016). An exception is the homozygous substitution (Phe249Leu) in the BMP1

protease domain which results in residual enzyme activity and has an osteoporotic outcome (Martínez-Glez et al. 2012).

Defects in osteoblast development with collagen insufficiency

Several genes are involved in osteoblast development and differentiation. Defects of these genes cause quantitative defects in collagen, resulting in osteopenia and other clinical manifestations of impaired osteoblast differentiation (Forlino and Marini 2016).

OI type XII is caused by loss of function mutations in *SP7*, encoding the zinc finger osteoblast-specific transcription factor SP7 (also known as Osterix), essential for bone formation and homeostasis by promoting osteoblast differentiation and maturation (Hojo and Ohba 2022). So far, three variants in *SP7* have been associated with recessive OI, leading to a phenotype characterized by recurrent fractures, mild bone deformities and short stature (Lapunzina et al. 2010, Fiscaletti et al. 2018, Hayat et al. 2020). In addition to recessive mutations, an heterozygous *SP7* variant (p.Glu340Ala) has recently been shown to be causative of a dominant form of OI (Ludwig et al. 2022). The predominant characteristic of this form is low cortical density, present also in patients affected by recessive *SP7* mutations. However, bone turnover is low, in contrast with the high bone turnover observed in recessive OI XIII. Furthermore, it was observed that dominant mutations decrease SP7 transactivation activity, suggesting a specific effect on osteoblasts and osteocytes (Ludwig et al. 2022).

TMEM38B encodes the ubiquitous voltage-dependent Trimeric Cation Channel B (TRIC-B), a potassium ER-membrane channel responsible for the transport of potassium ions across the ER membrane. The activity of TRIC-B synchronizes with inositol trisphosphate receptors (IP_3Rs), mediating calcium release from the ER to the cytosol (Zhou et al. 2014). Large deletions and single point mutations in *TMEM38B* were identified as causative of recessive OI XIV. These mutations disrupt ER calcium homeostasis, fundamental to regulate the activity of several ER proteins and enzymes involved in collagen type I biosynthesis (Cabral et al. 2016). Patients display low bone turnover with consequently low bone mass, mild bone deformities and frequent fractures (Cabral et al. 2016).

OI type XV is characterized by mutations in *WNT1*. WNT1, belonging to a family of secreted glycoproteins, binds to transmembrane receptors LRP5/6 and Frizzled, leading to β-catenin nuclear translocation to promote the expression of several genes implicated in bone formation (Forlino and Marini 2016). Heterozygous WNT1 mutations are associated to early onset osteoporosis (Baron and Kneissel 2013). Patients with homozygous nonsense, frameshift, missense or splicing mutations are

characterized by short stature, frequent fractures and vertebral compressions (Liu et al. 2016, Faqeih, Shaheen and Alkuraya 2013).

OI type XVI is caused by mutations in *CREB3L1*, encoding the ER-stress transducer old astrocyte specifically induced substance (OASIS) (Lindahl et al. 2018). OASIS is a transcription factor, mainly expressed in osteoblasts, that is processed in response to ER stress and is involved in collagen type I transcription, bone matrix proteins secretion and osteoblasts maturation (Murakami et al. 2009, Kondo et al. 2005). Interestingly, it was demonstrated that OASIS regulates the expression of SEC24D, involved in COPII vesicles organization and in conferring directionality from ER to Golgi (Guillemyn et al. 2019). Various *CREB3L1* homozygous variants have been reported, resulting in a severe OI phenotype (Keller et al. 2018). In 2018, the first case of recessive OASIS-deficiency associated to OI, who survived during infancy, was described. The patient presented a homozygous *CREB3L1* stop codon mutation in exon 11 (c.1284C>A) and showed hypermineralized bone matrix, generalized connective tissue symptoms, reduced trabecular and osteoid thickness and low mineral apposition rate (Lindahl et al. 2018).

OI type XVII is due to defects in Secreted protein acidic and rich in cysteine (SPARC), also known as Osteonectin. It is one of the most abundant non-collagenous proteins in mineralized tissues. In the osteoid, SPARC binds collagen type I and hydroxyapatite crystals to release calcium ions, increasing mineralization of the collagen matrix in bones (Rosset and Bradshaw 2016). SPARC binds to collagen thanks to an intramolecular salt bridge formed by conserved Arg166 and Glu263 residues. Homozygous missense mutations in these amino acids significantly reduce SPARC affinity for collagen type I, leading to OI (Rosset and Bradshaw 2016, Mendoza-Londono et al. 2015). Patients affected by mutations in SPARC develop severe bone fragility with mild joint hyperlaxity (Mendoza-Londono et al. 2015).

X-linked OI type XIX is caused by mutation in *MBTPS2* (Lindert et al. 2016) that encodes for the membrane bound zinc site-2 metalloprotease (S2P), involved in the regulated intramembrane proteolysis (RIP) pathway and cholesterol metabolism (Kang, Aryal A C and Marini 2017). *MBTPS2* mutations interfere with S2P ability to process the RIP substrates OASIS, Activating Transcription Factor 6 (ATF6) and Sterol Regulatory Element-Binding Protein (SREBP), dysregulating bone homeostasis and bone formation (Lindert et al. 2016). Clinical features of patients include fractures of ribs and long bones, *pectus carinatum*, blue sclerae and generalized osteopenia. Collagen extracted from patients shows significantly reduced hydroxylation of helical lysine residue 87, critical for collagen crosslinking in bone, due to decreased LH1 protein expression (Lindert et al. 2016).

Recently classified OI forms

FAM46A belongs to the nucleotidyl-transferases (NTase) fold superfamily and encodes for a soluble protein with little information about its biological role (Kuchta et al. 2016). In humans, FAM46A (also known as TENT5A) has been hypothesized to be a SMAD signaling pathway related protein (Colland et al. 2004, Etokebe et al. 2009). It has also been demonstrated that FAM46A polyadenylates mRNAs encoding α(I) chains and other secreted proteins involved in osteogenesis, enhancing their expression (Gewartowska et al. 2021).

A loss-of-function mutation in *FAM46A*, originally diagnosed as causative of Stüve-Wiedemann syndrome, resulted in a severe skeletal phenotype overlapping with OI characterized by bowing of the lower limbs and spontaneous fractures in the first years of life (Doyard et al. 2018). Homozygous duplications and missense mutations in *FAM46A* lead to OI type XVIII. Clinical features of patients include congenital bowing of the lower limbs and wormian bones (Doyard et al. 2018).

Homozygous mutations in Mesoderm Development LRP Chaperone (MESD) were reported as causative of a new autosomal recessive form of OI, OI type XX (Moosa et al. 2019). *MESD* is a mesoderm development gene encoding an ER chaperone protein binding the canonical Wingless-related integration site (WNT) signalling receptors LRP5 and LRP6. Four different mutations in MESD were reported, localizing downstream of the chaperone domain and upstream of the ER-retention domain. All these mutations were identified as hypomorphic rather than complete loss-of-function mutations and they resulted in a reduced chaperone activity of MESD (Moosa et al. 2019). Patients are characterized by progressive skeletal deformity, osteopenia, and bone fractures. Patients do not present dentinogenesis imperfecta but are characterized by disorganized dentition and/or oligodontia, which seems to be a unique feature of this type of OI (Moosa et al. 2019).

KDELR2 is a member of the KDEL receptor family consisting of seven transmembrane (TM) domains organized into two triple helix bundles separated by a linking domain (TM4). The KDEL receptors are mostly localized on the *cis*-Golgi, the ER, and the intermediate ER-Golgi compartment (ERGIC), where they regulate protein trafficking between Golgi and ER (Lewis and Pelham 1992). Soluble ER-resident proteins harboring a C-terminal Lys-Asp-Glu-Leu (KDEL)-like motif are recognized by KDEL receptors and are returned back to the ER via *cis*-Golgi. Homozygous frameshift and missense variants in *KDELR2* have been identified as causative of recessive OI type XXI (van Dijk et al. 2020, Efthymiou et al. 2021). In presence of the mutation, KDELR2 ability to bind peptides is compromised, with negative effects on HSP47 and collagen type I trafficking and metabolism. A recent study on fibroblast cultures from patients revealed the inability of HSP47 to bind mutant

KDELR2 and thus to dissociate from collagen type I, remaining bound to collagen molecules extracellularly and disrupting fiber formation (van Dijk et al. 2020). Features observed in affected patients include short stature, wormian bones, bowed limbs, chest deformity and joint hyperlaxity (Efthymiou et al. 2021).

Coiled-coil domain-containing protein 134 (*CCDC134*) encodes a secreted protein that work as a transcriptional regulator by inhibiting the extracellular signal-regulated kinase (ERK) or c-JUN N-terminal kinase (JNK) phosphorylation of mitogen-activated protein kinase (MAPKs) (Huang et al. 2008). Erk1/2 and JNK play a major role in bone homeostasis; in particular, Erk1/2 modulates collagen type I and osteopontin (OPN) deposition in the ECM of osteoblasts (Katz, Boland and Santillán 2006), whereas JNK is involved in osteocyte apoptosis in response to oxidative stress (Fontani et al. 2015). A recurrent c.2T-C homozygous mutation has been identified as causative of OI type XXII (Dubail et al. 2020, Holick, Shirvani and Charoenngam 2021, Ali et al. 2022). Fibroblasts and osteoblasts from patients are characterized by the absence of CCDC134 protein, with consequently increased Erk1/2 phosphorylation, decreased osteopontin and *COL1A1* mRNA expression and reduced mineralization compared to controls (Dubail et al. 2020). Clinical features are gracile and bowed long bone, pseudarthroses, and growth retardation (Dubail et al. 2020, Holick et al. 2021, Ali et al. 2022).

Unclassified OI forms

Plastins are a family of actin-binding proteins. In particular, Plastin 3 (PLS3) works in the formation of F-actin bundles and, being expressed in osteoblasts, osteocytes and osteoclasts, is involved in bone homeostasis (Fahiminiya et al. 2014). PLS3 interacts with the NF-kB repressing factor (NKRF) in the cytosol, allowing its translocation into the nucleus. Here, NKRF in osteoclasts inhibits the transcription of Nuclear Factor of Activated T-cells Cytoplasmic 1 (NFATC1), a key regulator of osteoclastogenesis, favouring osteoclast activity (Neugebauer et al. 2018, Takayanagi et al. 2002). A study from 2013 identified 5 families with X-linked mutations in *PLS3* characterized by osteoporosis and osteoporotic fractures, with clinical outcome ranging from normal bone density and absence of fractures to early-onset osteoporosis and vertebral compression fractures (van Dijk et al. 2013). A rare variant in *PLS3*, c.321T-A in exon 4, was identified in patients referred for possible OI type I as significantly associated with decreased BMD and doubled risk of fractures (van Dijk et al. 2013).

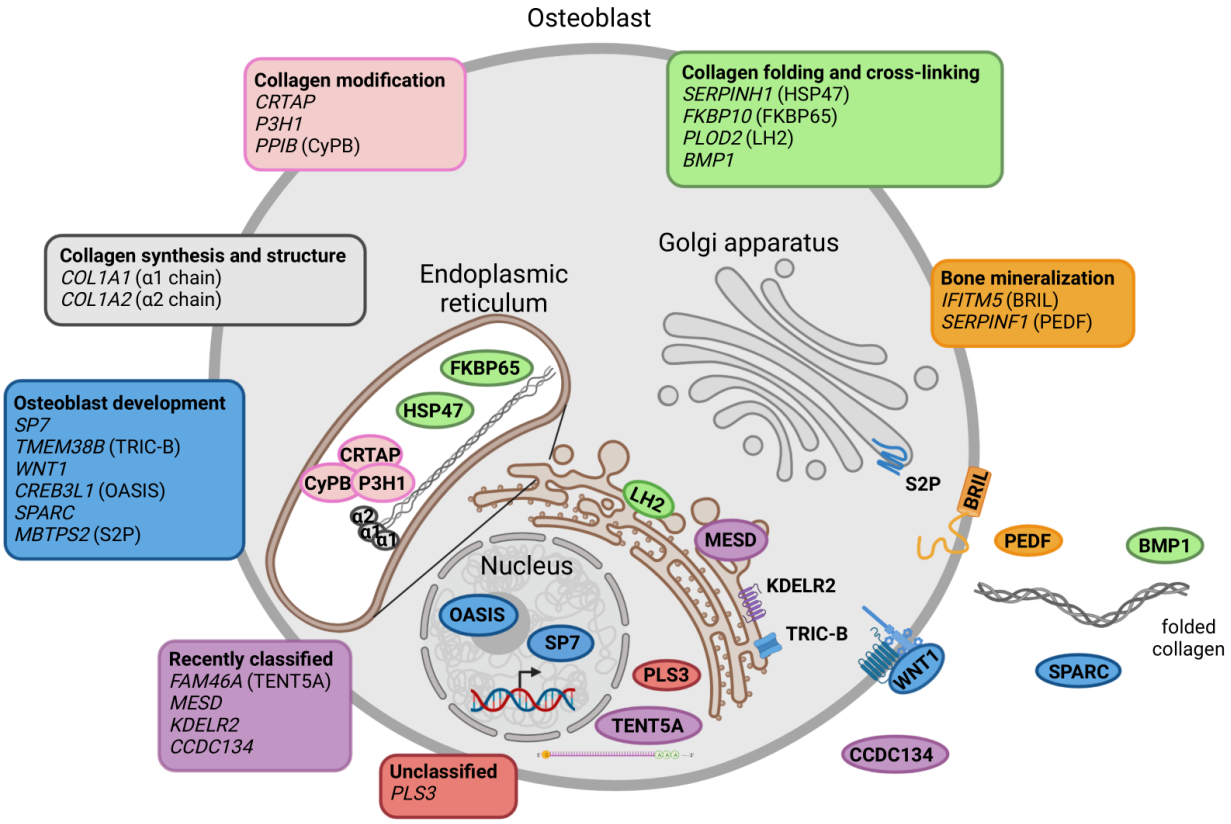

Figure 6. Schematic classification of OI-related genes and protein localization within the osteoblast. Created with BioRender.com.

Table 1. Osteogenesis imperfecta classification. BMD = bone mineral density; DI = dentinogenesis imperfecta; HBM = high bone mass.

Inheritance	Gene	OMIM number	OI type	Protein	Typical features
Defects in collagen synthesis and structure					
AD	*COL1A1*	166200	I	Collagen type I, α1	Mild to very severe bone deformity; normal or grey to dark blue sclerae; absent to common hearing loss and DI
		166210	II		
		259420	III		
		166220	IV		
AD	*COL1A2*	166200	I	Collagen type I, α2	Mild to very severe bone deformity; normal or grey to dark blue sclerae; absent to common hearing loss and DI
		166210	II		
		259420	III		
		166220	IV		
Defects in bone mineralization					
AD	*IFITM5*	610967	V	Interferon- induced transmembrane protein 5/BRIL	Variable bone deformity; normal to blue sclerae; infrequent hearing loss; ossification of the interosseous membrane; radial head dislocation
			Atypical VI		Moderate to severe bone deformity; normal sclerae; unmineralized osteoid; fish scale appearance of lamellar bone pattern
AR	*SERPINF1*	613982	VI	Pigment epithelium-derived factor (PEDF)	
Defects in collagen modification					
AR	*CRTAP*	610682	VII	Cartilage-associated protein	Severe rhizomelia; bone fractures; reduced BMD; popcorn calcification at epiphyses; growth retardation; normal sclerae
AR	*P3H1*	610915	VIII	Leucine proline-enriched proteoglycan 1/Prolyl 3-hydroxylase 1	
AR	*PPIB*	259440	IX	Peptidylprolyl *cis-trans* isomerase B/Cyclophilin B	Severe bone deformity; grey sclerae
Defects in collagen folding and cross-linking					
AR	*SERPINH1*	613848	X	Serpin peptidase inhibitor, clade H, member 1/heat shock protein 47 (HSP47)	Severe bone deformity; blue sclerae; presence of DI; skin blisters and bullae at birth; inguinal hernia
AR	*FKBP10*	610968	XI	FK506 binding protein 10	Mild to severe bone deformity; normal to grey sclerae; variable congenital contractures
AR	*PLOD2*	609220	-	Lysyl hydroxylase 2 (LH2)	Moderate to severe bone deformity; progressive joint contractures
AR	*BMP1*	614856	XIII	Bone morphogenetic protein 1	Mild to severe bone deformity; normal sclerae; umbilical hernia and HBM
Defects in osteoblast development with collagen insufficiency					
AR	*SP7*	613849	XII	Transcription factor 7/Osterix	Severe bone deformity; normal sclerae; delayed tooth eruption; midface hypoplasia
AR	*TMEM38B*	615066	XIV	Trimeric intracellular cation channel B (TRIC-B)	Severe bone deformity; normal to blue sclerae
AR	*WNT1*	615220	XV	Wingless-type MMTV integration site family, member 1	Severe bone deformity; white sclerae; possible neurological defects
AD		Unknown			
AR	*CREB3L1*	616229	XVI	cAMP responsive element binding protein 3 like 1	Severe bone deformity
AR	*SPARC*	616507	XVII	Secreted acid cysteine-rich protease/osteonectin	White sclerae; occurrence of bone fractures after the first year; mild joint hyperlaxity
XR	*MBTPS2*	301014	XIX	Membrane- bound transcription factor site-2 metalloprotease	Prenatal fractures of ribs and long bones; moderate short stature; blue sclerae; *pectus carinatum*; bowing of lower extremity long bone; generalized osteopenia
Recently classified OI forms					
AR	*FAM46A*	617952	XVIII	Terminal nucleotidyltransferase 46 member A (TENT5A)	Frequent fractures; bowing of long bones; wormian bones; blue sclerae; joint hyperlaxity

AR	*MESD*	618644	XX	ER-retention domain of Mesoderm Development LRP Chaperone	Osteopenia; skeletal deformity; disorganized dentition and/or oligodontia
AR	*KDELR2*	619131	XXI	Endoplasmic reticulum protein retention receptor 2	Short stature; wormian bones; bowed limbs; joint hyperlaxity; blue sclerae; DI
AR	*CCDC134*	619795	XXII	Coiled-coil domain containing 134	Gracile and bowed long bones; pseudarthroses; pre- and postnatal growth retardation
Unclassified OI forms					
XR	*PLS3*	-	-	Plastin 3	Reduced BMD; vertebral compression; long bone fractures

Zebrafish in biomedical research

Zebrafish (*Danio rerio*) is a small freshwater fish belonging to the Cyprinidae family. It was originally described in 1822, when the Scottish physician Francis Hamilton found several specimens in Kosi River, in Bengal (Hamilton 1822). Due to several advantages such as the transparency of embryos, the external fertilization, the possibility to obtain hundreds of embryos from one breeding and the complete knowledge of its genome, zebrafish has quickly become one of the most widely used animal model in biomedical research.

Zebrafish collagen type I

In tetrapods, collagen type I is composed of two identical α1 chains and one α2 chain, encoded by *COL1A1* and *COL1A2* genes, respectively. In many teleosts, including zebrafish, collagen type I α chains are encoded by three genes, *col1a1a*, *col1a1b* and *col1a2*, and named α1, α3 and α2, respectively. Interesting, zebrafish α3(I) and α1(I) chains share 78% of homology (Gistelinck et al. 2016a). This similarity is likely the consequence of the duplication occurred during the whole genome duplication event at the basis of teleost evolution, ~340 million years ago, involving the ancestor α(I) coding gene (Christoffels et al. 2004). Expression of zebrafish collagen type I has been mainly observed in the ectoderm, on developing bony elements, ligaments, and tendons. Zebrafish collagen type I genes are expressed in the same tissue as in humans, including bone and skin (Gistelinck et al. 2016a). Also, they are particularly conserved, with zebrafish *col1a1a* and *col1a1b* sequences being 76% and *col1a2* sequence being 71% identical to the human ones (Gistelinck et al. 2016a).

Zebrafish bone biology

Basic skeletal components and essential developmental genes are conserved between teleost and mammals. Zebrafish skeleton consists of a dermal skeleton (exoskeleton) and an endoskeleton. Scales, teeth, and fin rays belong to the dermal skeleton and are all characterized by the ability to regenerate (Witten, Huysseune and Hall 2010). Zebrafish endoskeleton is inherited from the common bony fish (osteichthyan) ancestor, shared with mammals. For this reason, it is remarkably similar to the skeleton of other vertebrates and consists of cranial, axial, and appendicular skeletal elements (Bird and Mabee 2003).

The skeletal system of teleost contains cartilage, bone, and the main skeletal cells: chondroblasts, chondrocytes, osteoblasts, osteocytes and osteoclasts (Tonelli et al. 2020a) (**Figure 7A**). Similarly to mammals, skeletogenesis involves the differentiation of chondroblasts and osteoblasts from MSCs (Eames et al. 2012, Schlombs, Wagner and Scheel 2003). Osteocytes, which are the predominant

bone type in mice and humans, are present in mature zebrafish skeleton, but characterized by a smaller volume and reduced number of canaliculi (Weigele and Franz-Odendaal 2016). Acellular bone, devoid of trapped osteocytes, can be found in the early zebrafish skeleton and in many zebrafish cranial bones and fin rays (Witten and Huysseune 2009, Horton and Summers 2009, Watson and Kwon 2015). Osteon-like structures in zebrafish, despite being uncommon, have been reported in the lateral ethmoid bone (Weigele and Franz-Odendaal 2016).

As in mammals, the development and growth of zebrafish skeleton requires bone resorption and remodeling to guarantee mineral homeostasis, for fin regeneration and fracture healing. Osteoclasts activity is well conserved and essential for these processes. However, although multinucleated osteoclasts can be found, several studies have shown that in teleosts, cells involved in bone resorption can differ from ‘‘standard’’ multinucleated mammalian osteoclasts. These cells are smaller, mononucleated osteoclasts characterized by a marked flat shape, that work in bone resorption without generating any typical resorption lacunae (Witten, Bendahmane and Abou-Haila 1997). Mononucleated osteoclasts are predominant at the juvenile stage (around 20 dpf), but can be found also in adults, mainly in the nasal, in the neural arches and in sites of cartilage degradation (Witten, Hansen and Hall 2001). Nevertheless, they retain the molecular regulators of mammalian osteoclast function, such as Tartare-resistant acid phosphatase (Trap) and Cathepsin K (Ctsk), which are both required for matrix components degradation (Witten and Huysseune 2009).

Zebrafish bone starts to form around 4-5 days post fertilization (dpf). Bone ossification can be intramembranous or endochondral, as in mammals, or perichondral (**Figure 7B**). Intramembranous ossification, which does not require a cartilage template, occurs in the cranial roof, in the operculum, in the vertebral column, in the scales and in the fin rays (Hall 2014). Endochondral ossification is uncommon in teleosts and can occur by two different mechanisms. Type I endochondral ossification resembles the mammalian process and takes place at the level of epiphysis in few bones such as the ceratohyal and the radials of the pectoral fin. It is characterized by the deposition of a calcifying cartilaginous matrix, that is finally degraded by chondroclasts and substituted by bone matrix. Type II endochondral ossification occurs in branchial arches, ethmoid and hypuralia. In these bones, the cartilage template is replaced by adipose cells, leading to tubular concave bones filled with adipose tissue (Tonelli et al. 2020a, Weigele and Franz-Odendaal 2016). Perichondral ossification, unique to teleosts, occurs in the hyomandibular bones and in Meckel’s cartilage, where osteoblasts aggregate on the surface of a cartilaginous template and deposit bone matrix into the perichondrium (Tonelli et al. 2020a).

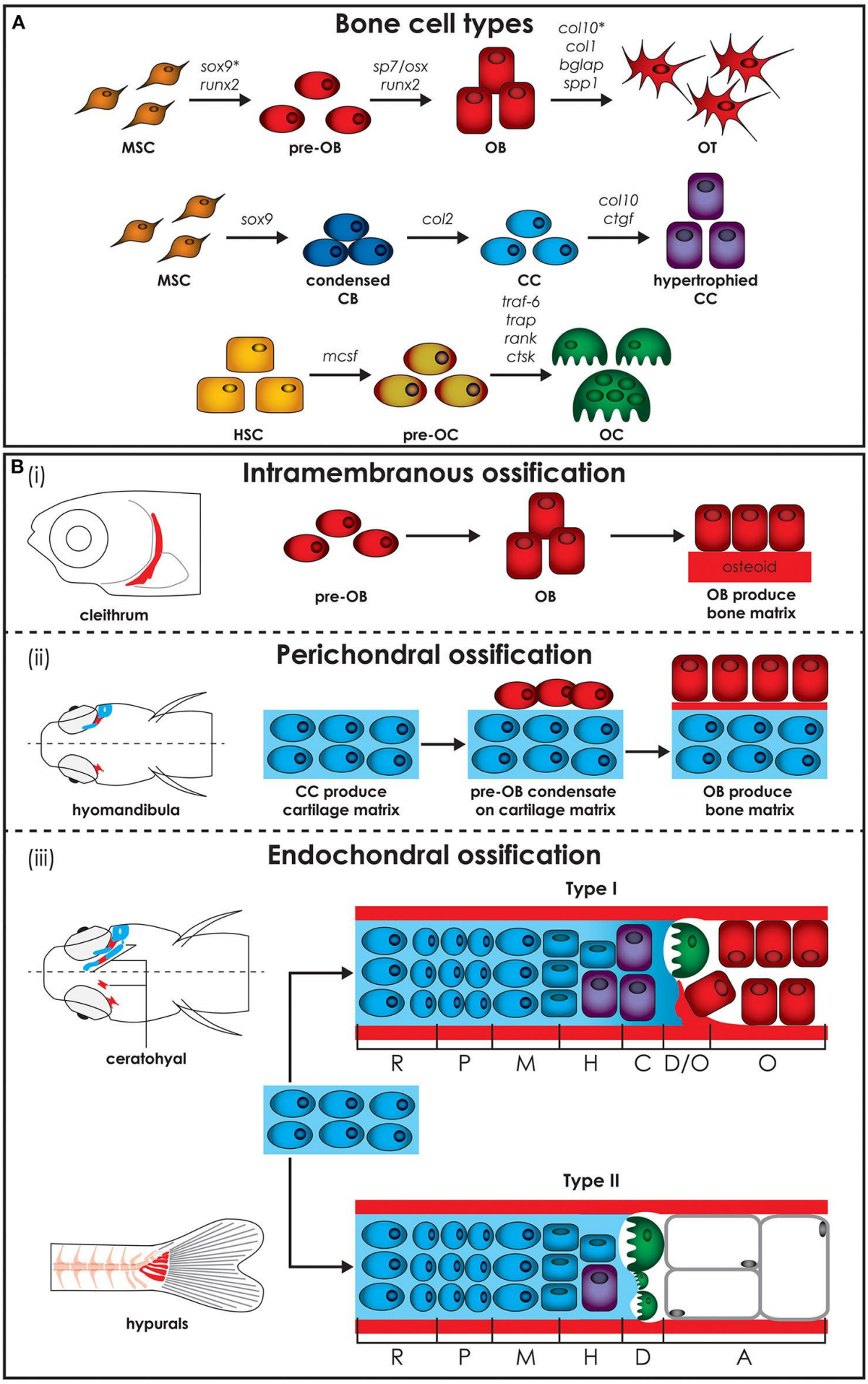
A
Bone cell types
sox9*
runx2
sp7/osx
runx2
col10*
col1
bglap
spp1
MSC
pre-OB
OB
OT
sox9
col2
col10
ctgf
MSC
condensed CB
CC
hypertrophied CC
traf-6
trap
rank
ctsk
mcsf
HSC
pre-OC
OC
B (i)
Intramembranous ossification
cleithrum
pre-OB
OB
osteoid
OB produce bone matrix
(ii)
Perichondral ossification
hyomandibula
CC produce cartilage matrix
pre-OB condensate on cartilage matrix
OB produce bone matrix
(iii)
Endochondral ossification
Type I
ceratohyal
R P M H C D/O O
Type II
hypurals
R P M H D A

Figure 7. Zebrafish bone cells and ossification types. (A) Bone is formed by osteoblasts and osteocytes, while cartilage is formed by chondroblasts and chondrocytes, and both bone and cartilage are degraded by osteoclasts. All bone cell types develop from progenitors similar to the mammalian counterpart and share similar gene expression profiles (genes are indicated above arrows). Note however that hematopoietic stem cells (HSCs) in zebrafish are not present in the bone marrow but in the head kidney. In addition, the genes for collagen X, encoded by col10, and SRY-box transcription factor 9 (indicated by*), encoded by sox9, are expressed during osteoblasts differentiation in zebrafish, but not in humans. **(B)** Three types of ossification are present in zebrafish: **(i)** intramembranous ossification, **(ii)** perichondral ossification, present in teleosts but not in humans, and **(iii)** endochondral ossification. **(i)** During intramembranous ossification mesenchymal stem cells condensate and differentiate into pre-osteoblasts and finally into mature osteoblasts that deposit bone matrix (osteoid) that subsequently mineralizes. **(ii)** Perichondral ossification starts at the surface of a cartilaginous template where osteoblasts deposit bone matrix without replacing the cartilage. **(iii)** Endochondral ossification is the process by which growing cartilage is replaced by bone to allow the skeleton to grow. For ossification to start, matrix surrounding the chondrocytes must calcify so that osteoclasts can break down the cartilage. In teleost two types of endochondral ossification exist. Type I endochondral ossification, typical in the ceratohyal, resembles the mammalian endochondral ossification process. This is characterized by a hypertrophic zone, where the cartilage matrix calcifies, followed by a degradation zone where osteoclasts (also referred to as chondroclasts) degrade the cartilaginous matrix, and a bone formation zone. Type II ossification, in the hypurals, is characterized by a lack of the calcification and ossification zones, leading to tubular concave bones filled with adipose tissue. A, adipose zone; C, calcification zone; CB, chondroblasts; CC, chondrocytes; D, degradation zone; H, hypertrophic zone; HSC, hematopoietic stem cell; M, maturation zone; MSC, mesenchymal stem cell; O, ossification zone; OB, osteoblasts; OC, osteoclasts; OT, osteocytes; P, proliferation zone; R, rest zone (from Tonelli et al. 2020a).

Zebrafish as a model for human diseases

In the recent years, zebrafish are increasingly used for studying human diseases due to the high conservation of osteogenic developmental programs with mammals. Zebrafish genome has been almost entirely sequenced and annotated, with most human genes having orthologs in zebrafish. It is estimated that approximately 70% of human disease genes have functional homologs in zebrafish (Howe et al. 2013). Thus, gene functionality and pathway analysis in zebrafish can produce relevant insights into human diseases.

One of the most widely used techniques applied in the past years to generate mutant zebrafish models is *N*-Ethyl-*N*-nitrosourea (ENU) mutagenesis. ENU is an alkylating agent which ethylates oxygen or nitrogen atoms in DNA bases, causing full mutations over the course of two rounds of replication. Usually, ENU mutagenesis is repeatedly performed on adult male zebrafish which then are mated with WT females in order to generate a progeny characterized by specific heterozygous point mutations (de Bruijn, Cuppen and Feitsma 2009). Over the years. several limitations, like cost and complexity to identify mutations causative of the observed phenotype, have limited the use of this technique (Lawson and Wolfe 2011).

In the early 2000s, antisense morpholino oligonucleotides (MOs) were rapidly adopted by zebrafish researchers to temporarily abolish the function of genes that had not been yet uncovered by forward genetic screens. MOs are short, chemically synthesized oligomers that bind a complementary target

mRNA, preventing its translation or splicing (Stainier et al. 2017). MOs are typically injected into 1-cell stage zebrafish embryos and are able to knock-down gene expression until 5 dpf, when the majority of tissues and organs is completely formed, representing a quick strategy to investigate gene function *in vivo* (Nasevicius and Ekker 2000). However, a recent study on about 20 zebrafish mutants showed that approximately 80% of phenotypes observed in MO-injected fish were not successfully recapitulated in actual genetic mutants (Kok et al. 2015). This discrepancy could be related to the short time of action because of degradation and dilution, to the uncertain off-target effects, such as non-specific p53 activation (Robu et al. 2007). Although, it cannot be excluded that in full knock out model the activation if compensatory genes may alleviate the outcome.

In the last decade the use of reverse genome editing techniques such as zinc finger nucleases (ZFNs), transcription activator-like effector nucleases (TALENs) and clustered regularly interspaced short palindromic repeats (CRISPR) became available. The CRISPR/Cas9 system is currently the most employed technology for the creation of both knock-out and knock-in disease models. The system works by introducing a Cas9 protein and a single-guide RNA (sgRNA) into the cell. The two molecules form a complex together with the target DNA site, a sequence of around 20 nucleotides neighboring a protospacer adjacent motif (PAM). Cas9 nuclease induces double-stranded breaks (DSBs) in the targeted genomic sites, which are subsequently repaired through error-prone non-homologous end-joining (NHEJ). NHEJ tends to produce insertions or deletions (indels) mutations, resulting in gene knock-out. Sequence templates can also be introduced in the process of homology-directed repair (HDR) into defined genomic sites to produce knock-in models (Cornet, Di Donato and Terriente 2018). The use of these gene-editing tools has been revolutionary in zebrafish research, making it an alternative model to efficiently get insights in genetics, developmental biology, drug discovery, toxicology. Many disease models for various genetic disorders and pathological processes have been rapidly and successfully generated using zebrafish transgenic lines (Tonelli et al. 2020a). This, in combination with the availability of transgenic zebrafish lines expressing fluorescent proteins under cell- or pathway- specific promoters, enables the study of cell differentiation and signaling *in vivo* in health and disease (Tonelli et al. 2020a) (**Table 2**).

Table 2. Available transgenic fluorescent reporter lines to study bone phenotype.

Cell type	Gene	Transgenic line	ZFIN Genomic Feature ID	Reference
Neural crest-derived skeletal cells	*sox10*	*Tg(-1252sox10:GFP)^{ba5}*	ZDB-ALT-090819-3	(Dutton et al. 2008)
		Tg(sox10:Kaede)^{zf393}	ZDB-ALT-130911-8	(Chen and Galloway 2014)
		Tg(sox10:mRFP)^{vu234}	ZDB-ALT-080321-3	(Sarmah et al. 2010)
		Tg(-4.7sox10:Cre)^{ba74}	ZDB-ALT-121128-2	(Brunt et al. 2017)
		Tg(−4.9sox10:EGFP)^{ba2}	ZDB-ALT-050913-4	(McDonald et al. 2021)
Cartilage cells	*col2a1a*	*TgBAC(col2a1a:mCherry)^{hu5910}*	ZDB-ALT-120726-4	(Brunt et al. 2017)
		Tg(-1.7col2a1a:EGFP-CAAX)^{nu12}	ZDB-ALT-111205-1	(Dale and Topczewski 2011)
	col18a1	*Tg(16Hsa.COL18A1-Mmu.Fos:EGFP)^{zf215}*	ZDB-ALT-110322-6	(Kague et al. 2010)
	foxp2	*Tg(foxP2- enhancerA:EGFP)^{zc42}*	ZDB-ALT-100412-5	(Bonkowsky et al. 2008)
Preosteoblasts	*cyp26b1*	*TgBAC(cyp26b1:YFP)^{hu7426}*	ZDB-ALT-180919-1	(Pogoda et al. 2018)
Notochord and intervertebral disc cells	*cyp26a1*	*Tg(cyp26a1:eYFP)^{nju1}*	ZDB-ALT-091007-1	(Hu et al. 2008)
	shhb	*Tg(-5.2shhb:GFP)^{mb1}*	ZDB-ALT-101026-2	(Haga, Dominique and Du 2009)
	twist	*Tg(Ola.Twist1:EGFP)^{ca104}*	ZDB-ALT-190319-4	(Ma et al. 2018)
Early osteoblasts	*col10a1*	*TgBAC(col10a1:Citrine)^{hu7050}*	ZDB-ALT-130306-2	(Mitchell et al. 2013)
		Tg(-2.2col10a1a:GFP)^{ck3}	ZDB-ALT-150714-1	(Kim et al. 2013)
	runx2	*Tg(Hsa.RUNX2:EGFP)^{zf259}*	ZDB-ALT-120209-60	(Geurtzen et al. 2017)
	sp7/osterix	*Tg(sp7:EGFP)^{b1212}*	ZDB-ALT-100402-1	(Huycke, Eames and Kimmel 2012)
		Tg(OlSp7:nlsGFP)^{zf132}	ZDB-ALT-090415-2	(Spoorendonk et al. 2008)
		Tg(OlSp7:mCherry)^{zf131}	ZDB-ALT-090415-1	(Spoorendonk et al. 2008)
		Tg(Ola.Sp7:mCherry-Eco.NfsB)^{pd46}	ZDB-ALT-120503-4	(Singh, Holdway and Poss 2012)
		Tg(Ola.Sp7:Kaede)^{pd64}	ZDB-ALT-190516-2	(Bek et al. 2021)
Mature osteoblasts	*bglap/osteocalcin*	*Tg1(Ola.Bglap:EGFP)^{hu4008}*	ZDB-ALT-110713-1	(Vanoevelen et al. 2011)
	col1a1	*Tg(col1a1a:EGFP)^{zf195}*	ZDB-ALT-100712-1	(Hutson et al. 2017)
	entpd5a	*TgBAC(entpd5a:YFP)^{hu5939}*	ZDB-ALT-130412-1	(Huitema et al. 2012)
		TgBAC(entpd5a:Kaede)^{hu6867}	ZDB-ALT-150223-1	(Geurtzen et al. 2014)
Osteoclasts	*ctsk*	*Tg(Ola.Ctsk:EGFP)^{zf305}*	ZDB-ALT-120611-4	(Chatani, Takano and Kudo 2011)
		TgBAC(ctsk:Citrine)^{zf336}	ZDB-ALT-120801-3	(Apschner et al. 2014)
		Tg(Ola.ctsk:FRT-DsRed-FRT-Cre,myl7:EGFP)^{mh201}	ZDB-ALT-200429-9	(Caetano-Lopes et al. 2020)
	trap	*Tg(en.acp5a:GFP-CAAX)^{ou2038}*	ZDB-ALT-210415-1	(Kobayashi-Sun et al. 2020)

Zebrafish models for OI

In the last decade, the use of mutant and transgenic fish lines strongly contributed to facilitate the study of many skeletal pathologies that affect millions of people worldwide and which incidence is growing due to the increase in human life span (Laizé, Gavaia and Cancela 2014). Osteoporosis, craniosynostosis, osteoarthritis, spinal curvature disorders are just some examples of pathologies whose zebrafish corresponding models are available and being studied for the discovery of new molecular mechanisms and identification of novel therapeutic targets (Laizé et al. 2014). Various zebrafish mutants, mutated directly in collagen type I or in genes involved in collagen type I maturation and osteoblast differentiation are currently established as representative models for the brittle bone disorder OI (**Figure 8, Table 3**).

OI zebrafish models with defects in collagen type I

Zebrafish knock-out mutants successfully recapitulate quantitative defects in collagen type I. *col1a1a* and *col1a1b* zebrafish knock-out mutants present a premature stop-codon mutation (p.Gly1179X and p.Cys68X, respectively), resulting in truncated and not functional collagen type I. Heterozygous mutations do not generate skeletal abnormalities, likely due to the functional redundancy between the paralogs (Gistelinck et al. 2018). The double heterozygous mutant, *col1a1a*$^{+/-}$*; col1a1b*$^{+/-}$ shows a mild skeletal phenotype, with a low frequency of spontaneous fractures, scoliosis and compression, fusions, and mild malformation of the vertebral bodies in some of the mutant fish, reminiscent of OI type I (Gistelinck et al. 2018).

Chihuahua (*Chi/+*) was discovered after a large ENU-mutagenesis screening and identified by an X-Ray-based screening focusing on abnormal skeletal patterning (Fisher, Jagadeeswaran and Halpern 2003). *Chi/+* carries in heterozygosis the same mutation that was identified in a human patient with severe and heavily deforming OI type III: a glycine substitution (p.Gly736Asp) in *col1a1a*, the homologue of human *COL1A1*. This results in Gly-Xaa-Yaa motif disruption, the most common cause of classical OI. *Chi/+* shows skeletal deformities, reduced body size, altered mineralization, and fracture calli in the ribs (Fiedler et al. 2018, Gioia et al. 2017). *Chi/+* also presents distorted bones with irregular radiodensity starting from early developmental stages and defective bone growth, features observed also in patients (Fiedler et al. 2018). Furthermore, collagen type I from *Chi/+* is over-modified and retained in the ER, causing cellular stress (Gioia et al. 2017).

Another set of zebrafish mutants presenting qualitative collagen type I defects due to glycine substitution was generated in a large ENU mutagenesis screening and characterized. *Dmh13/+* and *dmh14/+* zebrafish carry mutations resulting in substitutions of a conserved glycine residue in α1

chain (p.Gly1093Arg and p.Gly1144Glu, respectively), *dmh15/+* in α2 chain (p.Gly882Asp) and *dmh29/+* in α3 chain (p.Gly1123Asp) of collagen type I (Henke et al. 2017, Gistelinck et al. 2018). *Dmh13, dmh14, dmh15*, and *dmh29* are shorter respect to WT, with strong deformations of the vertebrae, especially of the haemal and neural arches, and excessive bone formation in the centrum of the vertebrae (Henke et al. 2017). *Dmh15* and *dmh29* mutants exhibit the most severe outcome, with *dmh15* heterozygous mutants showing the greatest reduction in body length and *dmh29* presenting kyphoscoliosis together with shorter, thicker, hypermineralized vertebral bodies and frequent rib fractures (Henke et al. 2017, Gistelinck et al. 2018). Furthermore, *dmh13, dmh14*, and *dmh29* mutations cluster in the region that in human has been identified as major ligand binding region 3 (MLBR3) of collagen type I representing a hotspot for ligand interactions (Gistelinck et al. 2018). Mutations in this location are associated with variable phenotypic outcomes, ranging from moderate OI type IV to perinatal lethal OI type II (Gistelinck et al. 2018).

Microwaved (*med$^{-/-}$)* zebrafish was characterized in 1996 as having curtain-like waves in its fin epithelium (van Eeden et al. 1996). *Med$^{-/-}$* zebrafish carry a substitution of a highly conserved glutamic acid for a lysine (p.Glu888Lys) in *col1a1a* gene. They show delayed bone ossification, undulation of the larval fin, and severe reduction of bone density. *Med$^{-/-}$* zebrafish were validated as a model for dominant OI type II–IV, even if no comparable mutations have been so far identified in human patients (Asharani et al. 2012, Gistelinck et al. 2018).

OI zebrafish models with defects in genes related to collagen type I maturation and osteoblasts differentiation

The *crtap$^{-/-}$* and *p3h1$^{-/-}$* are models for recessive OI type VII and VIII, respectively generated by CRISPR/Cas9 gene editing. *Crtap$^{-/-}$* carries a c.199_202delTTTCinsAG mutation in *crtap,* predicted to insert a premature stop codon at amino acid 80 of Crtap, while *p3h1$^{-/-}$* carries a c.645delCinsGGAGAA mutation in *p3h1*, predicted to insert a premature stop codon at amino acid 266 of P3h1. *crtap$^{-/-}$* and *p3h1$^{-/-}$* display a moderately severe OI phenotype and are characterized by reduced size, body disproportion and impaired mineralization. They also show the presence of vertebral fusions, deformities and fractures, together with reduced bone thickness and bone volume. Collagen type I from these mutants is overmodified and partially retained in the ER (Tonelli et al. 2020b).

Plod2 zebrafish mutant was generated by ENU mutagenesis by the zebrafish mutation project (ZMP) (Kettleborough et al. 2013). This model was then characterized to further elucidate the function of LH2 in vertebrate skeletal development. LH2 defects cause human Bruck syndrome, clinically

overlapping with OI associated to contractures. *Plod2* zebrafish model harbors a homozygous nonsense mutation (p.Tyr679X), resulting in reduced telopeptide hydroxylation and cross-linking of type I collagen in bone (Gistelinck et al. 2016b). Adult *Plod2*$^{-/-}$ body axis appears shortened, with severe skeletal abnormalities characterized by bone fragility and fractures. The vertebral column is short and scoliotic with compressed vertebrae due to excessive bone formation at the vertebral end plates, and increased tissue mineral density in the vertebral centrum (Gistelinck et al. 2016b). These molecular and phenotypical features are in agreement with clinical findings in Bruck syndrome patients, making *Plod2* zebrafish mutants a valid model for the study of the pathology.

Zebrafish mutant *frilly fin (frf)* carries a mutation in *bmp1a* gene, resembling OI type XIII. Sequencing of five different *frf* alleles, generated by ENU mutagenesis, identified two missense mutations (p.Ile124Asn and p.Val223Asp); a nonsense mutation (p.Tyr306*); and two splice site mutations (Asharani et al. 2012). All affected the protease domain of the protein. Homozygous mutants show a remarkable reduction in bone density and vertebrae ossification, shortened body axis and malformed bones. *Frf*$^{-/-}$ osteoblasts exhibit a more cuboidal structure than in WT fish (Asharani et al. 2012). The osteoids contain a disruption in the periodic fibrillar–collagen structure, coherent with the impairment in collagen processing (Mackay, Apschner and Schulte-Merker 2013).

Zebrafish with a mutation in *sp7* were generated via target-selected ENU mutagenesis, which introduced a stop codon at position 145 (p.Leu145*), truncating the protein before the three zinc finger domains (Wienholds et al. 2003). *Sp7* mutants show scoliosis and fractures of the ribs. While most of their skeleton is normally patterned, specific defects can be seen at the level of the craniofacial skeleton, with domed skull, midface hypoplasia, protruding mandible, and delayed cranial sutures closure. These mutants also display impaired bone growth and mineralization, as their osteoblasts fail to differentiate (Kague et al. 2016).

One of the main uses of OI zebrafish models of is as fast and high-throughput platforms for drug screening. Beyond that, the availability of transgenic lines offers the possibility for basic and applied research. Indeed, several zebrafish OI models have already contributed to elucidate the role of proteins and pathways in the pathology *in vivo*, confirming zebrafish as a low-cost alternative to murine models.

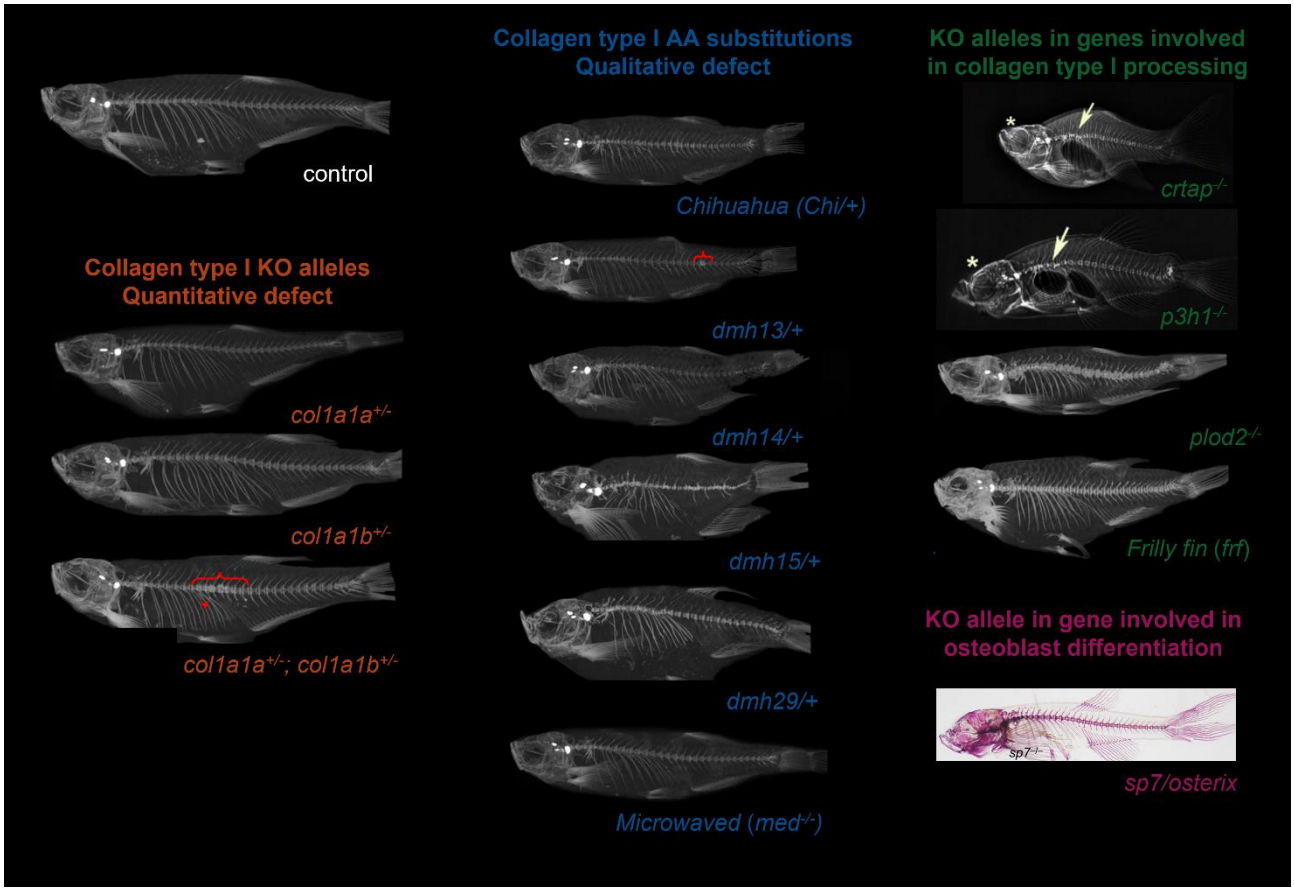

Figure 8. Representative image of available OI zebrafish models. WT fish is represented as a control. The first group, indicated as "Collagen type I knockout (KO) alleles — quantitative defect" (shown in orange) includes *col1a1a*$^{+/-}$, *col1a1b*$^{+/-}$, and the double heterozygous *col1a1a*$^{+/-}$; *col1a1b*$^{+/-}$. The second group is indicated as "Collagen type I amino acid (AA) substitutions — qualitative defect" (shown in blue). This includes *Chi*/+, *dmh13*/+, *dmh14*/+ (all carrying a Gly substitution in α1(I)), *dmh15*/+ (Gly substitution in α2(I)), and *dmh29*/+ (Gly substitution in α3(I)). Finally, *med*$^{-/-}$ mutant carries a homozygous Glu substitution in α1(I). Another group, indicated as "KO alleles in genes involved in collagen type I processing" (shown in green) includes four mutant models with a knockout mutation in *crtap*, *p3h1*, *plod2* and *bmp1a* (*frilly fin*) genes, respectively. Finally, the *sp7/osterix* knockout fish is indicated in "KO allele in gene involved in osteoblast differentiation" (shown in purple). Representative X-rays of fish from each mutant genotype are shown. *Sp7/osterix* model is represented with Alizarin Red staining. Callus formation in ribs (arrows), local compressions of the vertebral column (brackets) or the cranium (asterisks) are indicated (modified from Gistelinck et al. 2018).

Table 3. Zebrafish models for OI.

Zebrafish model	Inheritance	Gene	Encoded protein	Protein defect(s)	OI type	Features	Reference
Collagen type I quantitative defects							
col1a1a$^{+/-}$	AD	*col1a1a*	Type I collagen, α1	p.Gly1179X	I	Increased fracture risk, no skeletal abnormalities	(Gistelinck et al. 2018)
col1a1b$^{+/-}$	AD	*col1a1b*	Type I collagen, α3	p.Cys68X	I		(Gistelinck et al. 2018)
col1a1a$^{+/-}$***; col1a1b***$^{+/-}$	AD	*col1a1a; col1a1b*	Type I collagen, α1 and α3	p.Gly1179X; Cys68X	I	Mild skeletal phenotype with spontaneous fractures	(Gistelinck et al. 2018)
Collagen type I qualitative defects							
Chihuahua (Chi/+)	AD	*col1a1a*	Type I collagen, α1	p.Gly736Asp	III	Skeletal deformities, altered mineralization, reduced body size	(Fisher et al. 2003)
dmh29/+	AD	*col1a1b*	Type I collagen, α3	p.Gly1123Asp	III	Kyphoscoliosis, shorter and overmineralized vertebral bodies	(Gistelinck et al. 2018)
dmh15/+	AD	*col1a2*	Type I collagen, α2	p.Gly882Asp	III	Distorted and overmineralized axial and cranial skeletons	(Gistelinck et al. 2018)
dmh13/+	AD	*col1a1a*	Type I collagen, α1	p.Gly1093Arg	IV	Vertebral deformities, excessive bone formation	(Gistelinck et al. 2018)
dmh14/+	AD	*col1a1a*	Type I collagen, α1	p.Gly1144Glu	IV		(Gistelinck et al. 2018)
Microwaved (med$^{-/-}$***)***	AR	*col1a1a*	Type I collagen, α1	p.Glu888Lys	II-IV	Impaired mineralization, reduced bone density	(Asharani et al. 2012)
Defects in genes involved in collagen type I folding and cross-linking							
crtap$^{-/-}$	AR	*crtap*	Cartilage associated protein	p.Phe63Serfs*80	VII	Reduced size, body disproportion, vertebral body fusions, deformities and fractures	(Tonelli et al. 2020b)
p3h1$^{-/-}$	AR	*p3h1*	Prolyl-3-hydoxylase 1	p.Asp196Glufs*266	VIII		
plod2$^{-/-}$	AR	*plod2*	Lysyl hydroxylase 2	p.Tyr679X	-	Shortened body axis, severe skeletal abnormalities, fractures	(Gistelinck et al. 2016b)
frilly fin (frf)	AR	*bmp1*	Bone morphogenetic protein 1	Two missense mutations, one nonsense mutation and two splice-site mutations	XIII	Ruffled larval fin, shortened body axis, malformed craniofacial structures and fin shape	(Asharani et al. 2012)
Defects in genes involved in osteoblasts differentiation							
sp7/osterix	AR	*sp7*	Sp7/Osterix	p.Leu145*	XII	Uneven mineralization, severe fractures and misshapen bones	(Kague et al. 2016)

Introduction - References

Akiyama, T., C. R. Dass, Y. Shinoda, H. Kawano, S. Tanaka & P. F. Choong (2010) PEDF regulates osteoclasts via osteoprotegerin and RANKL. *Biochem Biophys Res Commun,* 391**,** 789-94.

Alanay, Y., H. Avaygan, N. Camacho, G. E. Utine, K. Boduroglu, D. Aktas, M. Alikasifoglu, E. Tuncbilek, D. Orhan, F. T. Bakar, B. Zabel, A. Superti-Furga, L. Bruckner-Tuderman, C. J. Curry, S. Pyott, P. H. Byers, D. R. Eyre, D. Baldridge, B. Lee, A. E. Merrill, E. C. Davis, D. H. Cohn, N. Akarsu & D. Krakow (2010) Mutations in the gene encoding the RER protein FKBP65 cause autosomal-recessive osteogenesis imperfecta. *Am J Hum Genet,* 86**,** 551-9.

Albaugh, V. L., K. Mukherjee & A. Barbul (2017) Proline Precursors and Collagen Synthesis: Biochemical Challenges of Nutrient Supplementation and Wound Healing. *J Nutr,* 147**,** 2011-2017.

Ali, T. M., B. D. W. Linnenkamp, G. L. Yamamoto, R. S. Honjo, H. Cabral de Menezes Filho, C. A. Kim & D. R. Bertola (2022) The recurrent homozygous translation start site variant in CCDC134 in an individual with severe osteogenesis imperfecta of non-Morrocan ancestry. *Am J Med Genet A,* 188**,** 1545-1549.

Andersen, T. L., T. E. Sondergaard, K. E. Skorzynska, F. Dagnaes-Hansen, T. L. Plesner, E. M. Hauge, T. Plesner & J. M. Delaisse (2009) A physical mechanism for coupling bone resorption and formation in adult human bone. *Am J Pathol,* 174**,** 239-47.

Anderson, H. C. (2003) Matrix vesicles and calcification. *Curr Rheumatol Rep,* 5**,** 222-6.

Appenzeller-Herzog, C. & L. Ellgaard (2008) The human PDI family: versatility packed into a single fold. *Biochim Biophys Acta,* 1783**,** 535-48.

Apschner, A., L. F. Huitema, B. Ponsioen, J. Peterson-Maduro & S. Schulte-Merker (2014) Zebrafish enpp1 mutants exhibit pathological mineralization, mimicking features of generalized arterial calcification of infancy (GACI) and pseudoxanthoma elasticum (PXE). *Dis Model Mech,* 7**,** 811-22.

Arana-Chavez, V. E. & V. Bradaschia-Correa (2009) Clastic cells: mineralized tissue resorption in health and disease. *Int J Biochem Cell Biol,* 41**,** 446-50.

Asharani, P. V., K. Keupp, O. Semler, W. Wang, Y. Li, H. Thiele, G. Yigit, E. Pohl, J. Becker, P. Frommolt, C. Sonntag, J. Altmüller, K. Zimmermann, D. S. Greenspan, N. A. Akarsu, C. Netzer, E. Schönau, R. Wirth, M. Hammerschmidt, P. Nürnberg, B. Wollnik & T. J. Carney (2012) Attenuated BMP1 function compromises osteogenesis, leading to bone fragility in humans and zebrafish. *Am J Hum Genet,* 90**,** 661-74.

Baccetti, B. (1985) Collagen and Animal Phylogeny.

Bank, R. A., S. P. Robins, C. Wijmenga, L. J. Breslau-Siderius, A. F. Bardoel, H. A. van der Sluijs, H. E. Pruijs & J. M. TeKoppele (1999) Defective collagen crosslinking in bone, but not in ligament or cartilage, in Bruck syndrome: indications for a bone-specific telopeptide lysyl hydroxylase on chromosome 17. *Proc Natl Acad Sci U S A,* 96**,** 1054-8.

Barnes, A. M., E. M. Carter, W. A. Cabral, M. Weis, W. Chang, E. Makareeva, S. Leikin, C. N. Rotimi, D. R. Eyre, C. L. Raggio & J. C. Marini (2010) Lack of cyclophilin B in osteogenesis imperfecta with normal collagen folding. *N Engl J Med,* 362**,** 521-8.

Barnes, A. M., W. Chang, R. Morello, W. A. Cabral, M. Weis, D. R. Eyre, S. Leikin, E. Makareeva, N. Kuznetsova, T. E. Uveges, A. Ashok, A. W. Flor, J. J. Mulvihill, P. L. Wilson, U. T. Sundaram, B. Lee & J. C. Marini (2006) Deficiency of cartilage-associated protein in recessive lethal osteogenesis imperfecta. *N Engl J Med,* 355**,** 2757-64.

Barnes, A. M., G. Duncan, M. Weis, W. Paton, W. A. Cabral, E. L. Mertz, E. Makareeva, M. J. Gambello, F. L. Lacbawan, S. Leikin, A. Fertala, D. R. Eyre, S. J. Bale & J. C. Marini (2013) Kuskokwim syndrome, a recessive congenital contracture disorder, extends the phenotype of FKBP10 mutations. *Hum Mutat,* 34**,** 1279-88.

Baron, R. & M. Kneissel (2013) WNT signaling in bone homeostasis and disease: from human mutations to treatments. *Nat Med,* 19**,** 179-92.

Becker, J., O. Semler, C. Gilissen, Y. Li, H. J. Bolz, C. Giunta, C. Bergmann, M. Rohrbach, F. Koerber, K. Zimmermann, P. de Vries, B. Wirth, E. Schoenau, B. Wollnik, J. A. Veltman, A. Hoischen & C. Netzer (2011) Exome sequencing identifies truncating mutations in human SERPINF1 in autosomal-recessive osteogenesis imperfecta. *Am J Hum Genet,* 88**,** 362-71.

Bek, J. W., C. Shochat, A. De Clercq, H. De Saffel, A. Boel, J. Metz, F. Rodenburg, D. Karasik, A. Willaert & P. J. Coucke (2021) Lrp5 Mutant and Crispant Zebrafish Faithfully Model Human Osteoporosis, Establishing the Zebrafish as a Platform for CRISPR-Based Functional Screening of Osteoporosis Candidate Genes. *J Bone Miner Res,* 36**,** 1749-1764.

Bellido, T. (2014) Osteocyte-driven bone remodeling. *Calcif Tissue Int,* 94**,** 25-34.

Berendsen, A. D. & B. R. Olsen (2015) Bone development. *Bone,* 80**,** 14-18.

Bird, N. C. & P. M. Mabee (2003) Developmental morphology of the axial skeleton of the zebrafish, Danio rerio (Ostariophysi: Cyprinidae). *Dev Dyn,* 228**,** 337-57.

Boabaid, F., P. S. Cerri & E. Katchburian (2001) Apoptotic bone cells may be engulfed by osteoclasts during alveolar bone resorption in young rats. *Tissue Cell,* 33**,** 318-25.

Bonkowsky, J. L., X. Wang, E. Fujimoto, J. E. Lee, C. B. Chien & R. I. Dorsky (2008) Domain-specific regulation of foxP2 CNS expression by lef1. *BMC Dev Biol,* 8**,** 103.

Bottomley, M. J., M. R. Batten, R. A. Lumb & N. J. Bulleid (2001) Quality control in the endoplasmic reticulum: PDI mediates the ER retention of unassembled procollagen C-propeptides. *Curr Biol,* 11**,** 1114-8.

Boyce, B. F., K. R. Hughes De Fau - Wright, L. Wright Kr Fau - Xing, A. Xing L Fau - Dai & A. Dai (1999) Recent advances in bone biology provide insight into the pathogenesis of bone diseases. *Laboratory Investigation,* 79**,** 83-94.

Brunt, L. H., K. Begg, E. Kague, S. Cross & C. L. Hammond (2017) Wnt signalling controls the response to mechanical loading during zebrafish joint development. *Development,* 144**,** 2798-2809.

Buckwalter, J. A., M. J. Glimcher, R. R. Cooper & R. Recker (1996) Bone biology. I: Structure, blood supply, cells, matrix, and mineralization. *Instr Course Lect,* 45**,** 371-86.

Bächinger, H. P., P. Bruckner, R. Timpl & J. Engel (1978) The role of cis-trans isomerization of peptide bonds in the coil leads to and comes from triple helix conversion of collagen. *Eur J Biochem,* 90**,** 605-13.

Cabral, W. A., W. Chang, A. M. Barnes, M. Weis, M. A. Scott, S. Leikin, E. Makareeva, N. V. Kuznetsova, K. N. Rosenbaum, C. J. Tifft, D. I. Bulas, C. Kozma, P. A. Smith, D. R. Eyre & J. C. Marini (2007) Prolyl 3-hydroxylase 1 deficiency causes a recessive metabolic bone disorder resembling lethal/severe osteogenesis imperfecta. *Nat Genet,* 39**,** 359-65.

Cabral, W. A., M. Ishikawa, M. Garten, E. N. Makareeva, B. M. Sargent, M. Weis, A. M. Barnes, E. A. Webb, N. J. Shaw, L. Ala-Kokko, F. L. Lacbawan, W. Högler, S. Leikin, P. S. Blank, J. Zimmerberg, D. R. Eyre, Y. Yamada & J. C. Marini (2016) Absence of the ER Cation Channel TMEM38B/TRIC-B Disrupts Intracellular Calcium Homeostasis and Dysregulates Collagen Synthesis in Recessive Osteogenesis Imperfecta. *PLoS Genet,* 12**,** e1006156.

Caetano-Lopes, J., K. Henke, K. Urso, J. Duryea, J. F. Charles, M. L. Warman & M. P. Harris (2020) Unique and non-redundant function of *csf1r* paralogues in regulation and evolution of post-embryonic development of the zebrafish. *Development,* 147.

Capulli, M., R. Paone & N. Rucci (2014) Osteoblast and osteocyte: games without frontiers. *Arch Biochem Biophys,* 561**,** 3-12.

Cerri, P. S., F. Boabaid & E. Katchburian (2003) Combined TUNEL and TRAP methods suggest that apoptotic bone cells are inside vacuoles of alveolar bone osteoclasts in young rats. *J Periodontal Res,* 38**,** 223-6.

Chang, W., A. M. Barnes, W. A. Cabral, J. N. Bodurtha & J. C. Marini (2010) Prolyl 3-hydroxylase 1 and CRTAP are mutually stabilizing in the endoplasmic reticulum collagen prolyl 3-hydroxylation complex. *Hum Mol Genet,* 19**,** 223-34.

Chatani, M., Y. Takano & A. Kudo (2011) Osteoclasts in bone modeling, as revealed by in vivo imaging, are essential for organogenesis in fish. *Dev Biol,* 360**,** 96-109.

Chen, J. W. & J. L. Galloway (2014) The development of zebrafish tendon and ligament progenitors. *Development,* 141**,** 2035-45.

Christiansen, H. E., U. Schwarze, S. M. Pyott, A. AlSwaid, M. Al Balwi, S. Alrasheed, M. G. Pepin, M. A. Weis, D. R. Eyre & P. H. Byers (2010) Homozygosity for a missense mutation in SERPINH1, which encodes the collagen chaperone protein HSP47, results in severe recessive osteogenesis imperfecta. *Am J Hum Genet,* 86**,** 389-98.

Christoffels, A., E. G. Koh, J. M. Chia, S. Brenner, S. Aparicio & B. Venkatesh (2004) Fugu genome analysis provides evidence for a whole-genome duplication early during the evolution of ray-finned fishes. *Mol Biol Evol,* 21**,** 1146-51.

Clarke, B. (2008) Normal bone anatomy and physiology. *Clin J Am Soc Nephrol,* 3 Suppl 3**,** S131-9.

Colland, F., X. Jacq, V. Trouplin, C. Mougin, C. Groizeleau, A. Hamburger, A. Meil, J. Wojcik, P. Legrain & J. M. Gauthier (2004) Functional proteomics mapping of a human signaling pathway. *Genome Res,* 14**,** 1324-32.

Compton, J. T. & F. Y. Lee (2014) A review of osteocyte function and the emerging importance of sclerostin. *J Bone Joint Surg Am,* 96**,** 1659-68.

Cornet, C., V. Di Donato & J. Terriente (2018) Combining Zebrafish and CRISPR/Cas9: Toward a More Efficient Drug Discovery Pipeline. *Front Pharmacol,* 9**,** 703.

Crockett, J. C., D. J. Mellis, D. I. Scott & M. H. Helfrich (2011) New knowledge on critical osteoclast formation and activation pathways from study of rare genetic diseases of osteoclasts: focus on the RANK/RANKL axis. *Osteoporos Int,* 22**,** 1-20.

Dale, R. M. & J. Topczewski (2011) Identification of an evolutionarily conserved regulatory element of the zebrafish col2a1a gene. *Dev Biol,* 357**,** 518-31.

Datta, H. K., W. F. Ng, J. A. Walker, S. P. Tuck & S. S. Varanasi (2008) The cell biology of bone metabolism. *J Clin Pathol,* 61**,** 577-87.

de Bruijn, E., E. Cuppen & H. Feitsma (2009) Highly Efficient ENU Mutagenesis in Zebrafish. *Methods Mol Biol,* 546**,** 3-12.

Diegel, C. R., S. Hann, U. M. Ayturk, J. C. W. Hu, K. E. Lim, C. J. Droscha, Z. B. Madaj, G. E. Foxa, I. Izaguirre, V. V. A. Transgenics Core, N. Paracha, B. Pidhaynyy, T. L. Dowd, A. G. Robling, M. L. Warman & B. O. Williams (2020) An osteocalcin-deficient mouse strain without endocrine abnormalities. *PLoS Genet,* 16**,** e1008361.

Downey, P. A. & M. I. Siegel (2006) Bone biology and the clinical implications for osteoporosis. *Phys Ther,* 86**,** 77-91.

Doyard, M., S. Bacrot, C. Huber, M. Di Rocco, A. Goldenberg, M. S. Aglan, P. Brunelle, S. Temtamy, C. Michot, G. A. Otaify, C. Haudry, M. Castanet, J. Leroux, J. P. Bonnefont, A. Munnich, G. Baujat, P. Lapunzina, S. Monnot, V. L. Ruiz-Perez & V. Cormier-Daire (2018) *FAM46A* mutations are responsible for autosomal recessive osteogenesis imperfecta. *J Med Genet,* 55**,** 278-284.

Drissi, H. & A. Sanjay (2016) The Multifaceted Osteoclast; Far and Beyond Bone Resorption. *J Cell Biochem,* 117**,** 1753-6.

Drögemüller, C., D. Becker, A. Brunner, B. Haase, P. Kircher, F. Seeliger, M. Fehr, U. Baumann, K. Lindblad-Toh & T. Leeb (2009) A missense mutation in the SERPINH1 gene in Dachshunds with osteogenesis imperfecta. *PLoS Genet,* 5**,** e1000579.

Dubail, J., P. Brunelle, G. Baujat, C. Huber, M. Doyard, C. Michot, P. Chavassieux, A. Khairouni, V. Topouchian, S. Monnot, E. Koumakis & V. Cormier-Daire (2020) Homozygous Loss-of-Function Mutations in CCDC134 Are Responsible for a Severe Form of Osteogenesis Imperfecta. *J Bone Miner Res,* 35**,** 1470-1480.

Ducy, P., C. Desbois, B. Boyce, G. Pinero, B. Story, C. Dunstan, E. Smith, J. Bonadio, S. Goldstein, C. Gundberg, A. Bradley & G. Karsenty (1996) Increased bone formation in osteocalcin-deficient mice. *Nature,* 382**,** 448-52.

Duran, I., L. Nevarez, A. Sarukhanov, S. Wu, K. Lee, P. Krejci, M. Weis, D. Eyre, D. Krakow & D. H. Cohn (2015) HSP47 and FKBP65 cooperate in the synthesis of type I procollagen. *Hum Mol Genet,* 24**,** 1918-28.

Dutton, J. R., A. Antonellis, T. J. Carney, F. S. Rodrigues, W. J. Pavan, A. Ward & R. N. Kelsh (2008) An evolutionarily conserved intronic region controls the spatiotemporal expression of the transcription factor Sox10. *BMC Dev Biol,* 8**,** 105.

Dyson, E. D. & W. J. Whitehouse (1968) Composition of trabecular bone in children and its relation to radiation dosimetry. *Nature,* 217**,** 576-8.

Eames, B. F., A. Amores, Y. L. Yan & J. H. Postlethwait (2012) Evolution of the osteoblast: skeletogenesis in gar and zebrafish. *BMC Evol Biol,* 12**,** 27.

Efthymiou, S., I. Herman, F. Rahman, N. Anwar, R. Maroofian, J. Yip, T. Mitani, D. G. Calame, J. V. Hunter, V. R. Sutton, E. Yilmaz Gulec, R. Duan, J. M. Fatih, D. Marafi, D. Pehlivan, S. N. Jhangiani, R. A. Gibbs, J. E. Posey, S. Maqbool, J. R. Lupski, H. Houlden & S. S. Group (2021) Two novel bi-allelic KDELR2 missense variants cause osteogenesis imperfecta with neurodevelopmental features. *Am J Med Genet A,* 185**,** 2241-2249.

Eriksen, E. F., D. W. Axelrod & F. Melsen. 1994. *Bone histomorphometry*. New York, NY: Raven Press.

Etokebe, G. E., A. M. Küchler, G. Haraldsen, M. Landin, H. Osmundsen & Z. Dembic (2009) Family-with-sequence-similarity-46, member A (Fam46a) gene is expressed in developing tooth buds. *Arch Oral Biol,* 54**,** 1002-7.

Fahiminiya, S., J. Majewski, H. Al-Jallad, P. Moffatt, J. Mort, F. H. Glorieux, P. Roschger, K. Klaushofer & F. Rauch (2014) Osteoporosis caused by mutations in PLS3: clinical and bone tissue characteristics. *J Bone Miner Res,* 29**,** 1805-14.

Fakhry, M., E. Hamade, B. Badran, R. Buchet & D. Magne (2013) Molecular mechanisms of mesenchymal stem cell differentiation towards osteoblasts. *World J Stem Cells,* 5**,** 136-48.

Faqeih, E., R. Shaheen & F. S. Alkuraya (2013) WNT1 mutation with recessive osteogenesis imperfecta and profound neurological phenotype. *J Med Genet,* 50**,** 491-2.

Farber, C. R., A. Reich, A. M. Barnes, P. Becerra, F. Rauch, W. A. Cabral, A. Bae, A. Quinlan, F. H. Glorieux, T. L. Clemens & J. C. Marini (2014) A novel IFITM5 mutation in severe atypical osteogenesis imperfecta type VI impairs osteoblast production of pigment epithelium-derived factor. *J Bone Miner Res,* 29**,** 1402-11.

Fiedler, I. A. K., F. N. Schmidt, E. M. Wölfel, C. Plumeyer, P. Milovanovic, R. Gioia, F. Tonelli, H. A. Bale, K. Jähn, R. Besio, A. Forlino & B. Busse (2018) Severely Impaired Bone Material Quality in Chihuahua Zebrafish Resembles Classical Dominant Human Osteogenesis Imperfecta. *J Bone Miner Res,* 33**,** 1489-1499.

Fiscaletti, M., A. Biggin, B. Bennetts, K. Wong, J. Briody, V. Pacey, C. Birman & C. F. Munns (2018) Novel variant in Sp7/Osx associated with recessive osteogenesis imperfecta with bone fragility and hearing impairment. *Bone,* 110**,** 66-75.

Fisher, S., P. Jagadeeswaran & M. E. Halpern (2003) Radiographic analysis of zebrafish skeletal defects. *Developmental Biology,* 264**,** 64-76.

Florencio-Silva, R., G. R. Sasso, E. Sasso-Cerri, M. J. Simões & P. S. Cerri (2015) Biology of Bone Tissue: Structure, Function, and Factors That Influence Bone Cells. *Biomed Res Int,* 2015**,** 421746.

Fontani, F., G. Marcucci, T. Iantomasi, M. L. Brandi & M. T. Vincenzini (2015) Glutathione, N-acetylcysteine and lipoic acid down-regulate starvation-induced apoptosis, RANKL/OPG ratio and sclerostin in osteocytes: involvement of JNK and ERK1/2 signalling. *Calcif Tissue Int,* 96**,** 335-46.

Forlino, A. & J. C. Marini (2016) Osteogenesis imperfecta. *Lancet,* 387**,** 1657-71.

Fratzl-Zelman, N., B. M. Misof, P. Roschger & K. Klaushofer (2015a) Classification of osteogenesis imperfecta. *Wien Med Wochenschr,* 165**,** 264-70.

Fratzl-Zelman, N., I. Schmidt, P. Roschger, A. Roschger, F. H. Glorieux, K. Klaushofer, W. Wagermaier, F. Rauch & P. Fratzl (2015b) Unique micro- and nano-scale mineralization pattern of human osteogenesis imperfecta type VI bone. *Bone,* 73**,** 233-41.

Garibaldi, N., R. Besio, R. Dalgleish, S. Villani, A. M. Barnes, J. C. Marini & A. Forlino (2022) Dissecting the phenotypic variability of osteogenesis imperfecta. *Dis Model Mech,* 15.

Gelse, K., E. Pöschl & T. Aigner (2003) Collagens--structure, function, and biosynthesis. *Adv Drug Deliv Rev,* 55**,** 1531-46.

Geurtzen, K., F. Knopf, D. Wehner, L. F. Huitema, S. Schulte-Merker & G. Weidinger (2014) Mature osteoblasts dedifferentiate in response to traumatic bone injury in the zebrafish fin and skull. *Development,* 141**,** 2225-34.

Geurtzen, K., A. Vernet, A. Freidin, M. Rauner, L. C. Hofbauer, J. E. Schneider, M. Brand & F. Knopf (2017) Immune Suppressive and Bone Inhibitory Effects of Prednisolone in Growing and Regenerating Zebrafish Tissues. *J Bone Miner Res,* 32**,** 2476-2488.

Gewartowska, O., G. Aranaz-Novaliches, P. S. Krawczyk, S. Mroczek, M. Kusio-Kobiałka, B. Tarkowski, F. Spoutil, O. Benada, O. Kofroňová, P. Szwedziak, D. Cysewski, J. Gruchota, M. Szpila, A. Chlebowski, R. Sedlacek, J. Prochazka & A. Dziembowski (2021) Cytoplasmic polyadenylation by TENT5A is required for proper bone formation. *Cell Rep,* 35**,** 109015.

Gioia, R., F. Tonelli, I. Ceppi, M. Biggiogera, S. Leikin, S. Fisher, E. Tenedini, T. A. Yorgan, T. Schinke, K. Tian, J. M. Schwartz, F. Forte, R. Wagener, S. Villani, A. Rossi & A. Forlino (2017) The chaperone activity of 4PBA ameliorates the skeletal phenotype of Chihuahua, a zebrafish model for dominant osteogenesis imperfecta. *Hum Mol Genet,* 26**,** 2897-2911.

Gistelinck, C., R. Gioia, A. Gagliardi, F. Tonelli, L. Marchese, L. Bianchi, C. Landi, L. Bini, A. Huysseune, P. E. Witten, A. Staes, K. Gevaert, N. De Rocker, B. Menten, F. Malfait, S. Leikin, S. Carra, R. Tenni, A. Rossi, A. De Paepe, P. Coucke, A. Willaert & A. Forlino (2016a) Zebrafish Collagen Type I: Molecular and Biochemical Characterization of the Major Structural Protein in Bone and Skin. *Sci Rep,* 6**,** 21540.

Gistelinck, C., R. Y. Kwon, F. Malfait, S. Symoens, M. P. Harris, K. Henke, M. B. Hawkins, S. Fisher, P. Sips, B. Guillemyn, J. W. Bek, P. Vermassen, H. De Saffel, P. E. Witten, M. Weis, A. De Paepe, D. R. Eyre, A. Willaert & P. J. Coucke (2018) Zebrafish type I collagen mutants faithfully recapitulate human type I collagenopathies. *Proc Natl Acad Sci U S A,* 115**,** E8037-E8046.

Gistelinck, C., P. E. Witten, A. Huysseune, S. Symoens, F. Malfait, D. Larionova, P. Simoens, M. Dierick, L. Van Hoorebeke, A. De Paepe, R. Y. Kwon, M. Weis, D. R. Eyre, A. Willaert & P. J. Coucke (2016b) Loss of Type I Collagen Telopeptide Lysyl Hydroxylation Causes

Musculoskeletal Abnormalities in a Zebrafish Model of Bruck Syndrome. *Journal of bone and mineral research : the official journal of the American Society for Bone and Mineral Research,* 31**,** 1930-1942.

Guillemyn, B., H. Kayserili, L. Demuynck, P. Sips, A. De Paepe, D. Syx, P. J. Coucke, F. Malfait & S. Symoens (2019) A homozygous pathogenic missense variant broadens the phenotypic and mutational spectrum of CREB3L1-related osteogenesis imperfecta. *Hum Mol Genet,* 28**,** 1801-1809.

Haga, Y., V. J. Dominique & S. J. Du (2009) Analyzing notochord segmentation and intervertebral disc formation using the twhh:gfp transgenic zebrafish model. *Transgenic Res,* 18**,** 669-83.

Hall , B. K. 2014. *Bones and Cartilage*. Academic Press.

Hall, B. K. & T. Miyake (1992) The membranous skeleton: the role of cell condensations in vertebrate skeletogenesis. *Anat Embryol (Berl),* 186**,** 107-24.

Hamilton, F. 1822. *An account of the fishes found in the river Ganges and its branches*. Edimburgh: Archibald Constable.

Hayat, A., S. Hussain, M. Bilal, M. Kausar, B. Almuzzaini, S. Abbas, A. Tanveer, A. Khan, S. Siddiqi, J. N. Foo, F. Ahmad, F. Khan, B. Khan, M. Anees, O. Mäkitie, M. Alfadhel, W. Ahmad & M. Umair (2020) Biallelic variants in four genes underlying recessive osteogenesis imperfecta. *Eur J Med Genet,* 63**,** 103954.

Henke, K., J. M. Daane, M. B. Hawkins, C. M. Dooley, E. M. Busch-Nentwich, D. L. Stemple & M. P. Harris (2017) Genetic Screen for Postembryonic Development in the Zebrafish (*Danio rerio*): Dominant Mutations Affecting Adult Form. *Genetics,* 207**,** 609-623.

Hennet, T. (2019) Collagen glycosylation. *Curr Opin Struct Biol,* 56**,** 131-138.

Hojo, H. & S. Ohba (2022) Sp7 Action in the Skeleton: Its Mode of Action, Functions, and Relevance to Skeletal Diseases. *Int J Mol Sci,* 23.

Holick, M. F., A. Shirvani & N. Charoenngam (2021) Fetal Fractures in an Infant with Maternal Ehlers-Danlos Syndrome, CCDC134 Pathogenic Mutation and a Negative Genetic Test for Osteogenesis Imperfecta. *Children (Basel),* 8.

Horton, J. M. & A. P. Summers (2009) The material properties of acellular bone in a teleost fish. *J Exp Biol,* 212**,** 1413-20.

Howe, K., M. D. Clark, C. F. Torroja, J. Torrance, C. Berthelot, M. Muffato, J. E. Collins, S. Humphray, K. McLaren, L. Matthews, S. McLaren, I. Sealy, M. Caccamo, C. Churcher, C. Scott, J. C. Barrett, R. Koch, G. J. Rauch, S. White, W. Chow, B. Kilian, L. T. Quintais, J. A. Guerra-Assunção, Y. Zhou, Y. Gu, J. Yen, J. H. Vogel, T. Eyre, S. Redmond, R. Banerjee, J. Chi, B. Fu, E. Langley, S. F. Maguire, G. K. Laird, D. Lloyd, E. Kenyon, S. Donaldson, H.

Sehra, J. Almeida-King, J. Loveland, S. Trevanion, M. Jones, M. Quail, D. Willey, A. Hunt, J. Burton, S. Sims, K. McLay, B. Plumb, J. Davis, C. Clee, K. Oliver, R. Clark, C. Riddle, D. Elliot, G. Threadgold, G. Harden, D. Ware, S. Begum, B. Mortimore, G. Kerry, P. Heath, B. Phillimore, A. Tracey, N. Corby, M. Dunn, C. Johnson, J. Wood, S. Clark, S. Pelan, G. Griffiths, M. Smith, R. Glithero, P. Howden, N. Barker, C. Lloyd, C. Stevens, J. Harley, K. Holt, G. Panagiotidis, J. Lovell, H. Beasley, C. Henderson, D. Gordon, K. Auger, D. Wright, J. Collins, C. Raisen, L. Dyer, K. Leung, L. Robertson, K. Ambridge, D. Leongamornlert, S. McGuire, R. Gilderthorp, C. Griffiths, D. Manthravadi, S. Nichol, G. Barker, et al. (2013) The zebrafish reference genome sequence and its relationship to the human genome. *Nature,* 496**,** 498-503.

Hu, P., M. Tian, J. Bao, G. Xing, X. Gu, X. Gao, E. Linney & Q. Zhao (2008) Retinoid regulation of the zebrafish cyp26a1 promoter. *Dev Dyn,* 237**,** 3798-808.

Hu, J., L. J. Li, W. B. Zheng, D. C. Zhao, O. Wang, Y. Jiang, X. P. Xing, M. Li & W. Xia (2020) A novel mutation in PLS3 causes extremely rare X-linked osteogenesis imperfecta. *Mol Genet Genomic Med,* 8**,** e1525.

Huang, J., T. Shi, T. Ma, Y. Zhang, X. Ma, Y. Lu, Q. Song, W. Liu, D. Ma & X. Qiu (2008) CCDC134, a novel secretory protein, inhibits activation of ERK and JNK, but not p38 MAPK. *Cell Mol Life Sci,* 65**,** 338-49.

Huitema, L. F., A. Apschner, I. Logister, K. M. Spoorendonk, J. Bussmann, C. L. Hammond & S. Schulte-Merker (2012) Entpd5 is essential for skeletal mineralization and regulates phosphate homeostasis in zebrafish. *Proc Natl Acad Sci U S A,* 109**,** 21372-7.

Hutson, M. R., A. L. Keyte, M. Hernández-Morales, E. Gibbs, Z. A. Kupchinsky, I. Argyridis, K. N. Erwin, K. Pegram, M. Kneifel, P. B. Rosenberg, P. Matak, L. Xie, J. Grandl, E. E. Davis, N. Katsanis, C. Liu & E. J. Benner (2017) Temperature-activated ion channels in neural crest cells confer maternal fever-associated birth defects. *Sci Signal,* 10.

Huycke, T. R., B. F. Eames & C. B. Kimmel (2012) Hedgehog-dependent proliferation drives modular growth during morphogenesis of a dermal bone. *Development,* 139**,** 2371-80.

Hyry, M., J. Lantto & J. Myllyharju (2009) Missense mutations that cause Bruck syndrome affect enzymatic activity, folding, and oligomerization of lysyl hydroxylase 2. *J Biol Chem,* 284**,** 30917-24.

Ishikawa, Y. & H. P. Bächinger (2013) A molecular ensemble in the rER for procollagen maturation. *Biochim Biophys Acta,* 1833**,** 2479-91.

Ishikawa, Y., J. Vranka, J. Wirz, K. Nagata & H. P. Bächinger (2008) The rough endoplasmic reticulum-resident FK506-binding protein FKBP65 is a molecular chaperone that interacts with collagens. *J Biol Chem,* 283**,** 31584-90.

Ito, S. & K. Nagata (2017) Biology of Hsp47 (Serpin H1), a collagen-specific molecular chaperone. *Semin Cell Dev Biol,* 62**,** 142-151.

Jilka, R. L., R. S. Weinstein, T. Bellido, A. M. Parfitt & S. C. Manolagas (1998) Osteoblast programmed cell death (apoptosis): modulation by growth factors and cytokines. *J Bone Miner Res,* 13**,** 793-802.

John, D. C., M. E. Grant & N. J. Bulleid (1993) Cell-free synthesis and assembly of prolyl 4-hydroxylase: the role of the beta-subunit (PDI) in preventing misfolding and aggregation of the alpha-subunit. *EMBO J,* 12**,** 1587-95.

Jovanovic, M., G. Guterman-Ram & J. C. Marini (2022) Osteogenesis Imperfecta: Mechanisms and Signaling Pathways Connecting Classical and Rare OI Types. *Endocr Rev,* 43**,** 61-90.

Kague, E., S. L. Bessling, J. Lee, G. Hu, M. R. Passos-Bueno & S. Fisher (2010) Functionally conserved cis-regulatory elements of COL18A1 identified through zebrafish transgenesis. *Dev Biol,* 337**,** 496-505.

Kague, E., P. Roy, G. Asselin, G. Hu, J. Simonet, A. Stanley, C. Albertson & S. Fisher (2016) Osterix/Sp7 limits cranial bone initiation sites and is required for formation of sutures. *Dev Biol,* 413**,** 160-72.

Kang, H., S. Aryal A C & J. C. Marini (2017) Osteogenesis imperfecta: new genes reveal novel mechanisms in bone dysplasia. *Transl Res,* 181**,** 27-48.

Karsenty, G. & E. F. Wagner (2002) Reaching a genetic and molecular understanding of skeletal development. *Dev Cell,* 2**,** 389-406.

Katz, S., R. Boland & G. Santillán (2006) Modulation of ERK 1/2 and p38 MAPK signaling pathways by ATP in osteoblasts: involvement of mechanical stress-activated calcium influx, PKC and Src activation. *Int J Biochem Cell Biol,* 38**,** 2082-91.

Keller, R. B., T. T. Tran, S. M. Pyott, M. G. Pepin, R. Savarirayan, G. McGillivray, D. A. Nickerson, M. J. Bamshad & P. H. Byers (2018) Monoallelic and biallelic CREB3L1 variant causes mild and severe osteogenesis imperfecta, respectively. *Genet Med,* 20**,** 411-419.

Kessler, E., K. Takahara, L. Biniaminov, M. Brusel & D. S. Greenspan (1996) Bone morphogenetic protein-1: the type I procollagen C-proteinase. *Science,* 271**,** 360-2.

Kettleborough, R. N., E. M. Busch-Nentwich, S. A. Harvey, C. M. Dooley, E. de Bruijn, F. van Eeden, I. Sealy, R. J. White, C. Herd, I. J. Nijman, F. Fényes, S. Mehroke, C. Scahill, R. Gibbons, N. Wali, S. Carruthers, A. Hall, J. Yen, E. Cuppen & D. L. Stemple (2013) A

systematic genome-wide analysis of zebrafish protein-coding gene function. *Nature,* 496**,** 494-7.

Kok, F. O., M. Shin, C. W. Ni, A. Gupta, A. S. Grosse, A. van Impel, B. C. Kirchmaier, J. Peterson-Maduro, G. Kourkoulis, I. Male, D. F. DeSantis, S. Sheppard-Tindell, L. Ebarasi, C. Betsholtz, S. Schulte-Merker, S. A. Wolfe & N. D. Lawson (2015) Reverse genetic screening reveals poor correlation between morpholino-induced and mutant phenotypes in zebrafish. *Dev Cell,* 32**,** 97-108.

Kim, Y. I., S. Lee, S. H. Jung, H. T. Kim, J. H. Choi, M. S. Lee, K. H. You, S. Y. Yeo, K. W. Yoo, S. Kwak, J. N. Lee, R. Park, S. K. Choe & C. H. Kim (2013) Establishment of a bone-specific col10a1:GFP transgenic zebrafish. *Mol Cells,* 36**,** 145-50.

Kobayashi-Sun, J., S. Yamamori, M. Kondo, J. Kuroda, M. Ikegame, N. Suzuki, K. I. Kitamura, A. Hattori, M. Yamaguchi & I. Kobayashi (2020) Uptake of osteoblast-derived extracellular vesicles promotes the differentiation of osteoclasts in the zebrafish scale. *Commun Biol,* 3**,** 190.

Komori, T. (2020) Functions of Osteocalcin in Bone, Pancreas, Testis, and Muscle. *Int J Mol Sci,* 21.

Kondo, S., T. Murakami, K. Tatsumi, M. Ogata, S. Kanemoto, K. Otori, K. Iseki, A. Wanaka & K. Imaizumi (2005) OASIS, a CREB/ATF-family member, modulates UPR signalling in astrocytes. *Nat Cell Biol,* 7**,** 186-94.

Krane, S. M. (2008) The importance of proline residues in the structure, stability and susceptibility to proteolytic degradation of collagens. *Amino Acids,* 35**,** 703-10.

Kronenberg, H. M. (2003) Developmental regulation of the growth plate. *Nature,* 423**,** 332-6.

Kuchta, K., A. Muszewska, L. Knizewski, K. Steczkiewicz, L. S. Wyrwicz, K. Pawlowski, L. Rychlewski & K. Ginalski (2016) FAM46 proteins are novel eukaryotic non-canonical poly(A) polymerases. *Nucleic Acids Res,* 44**,** 3534-48.

Laizé, V., P. J. Gavaia & M. L. Cancela (2014) Fish: a suitable system to model human bone disorders and discover drugs with osteogenic or osteotoxic activities. *Drug Discovery Today: Disease Models,* 13**,** 29-37.

Lapunzina, P., M. Aglan, S. Temtamy, J. A. Caparrós-Martín, M. Valencia, R. Letón, V. Martínez-Glez, R. Elhossini, K. Amr, N. Vilaboa & V. L. Ruiz-Perez (2010) Identification of a frameshift mutation in Osterix in a patient with recessive osteogenesis imperfecta. *Am J Hum Genet,* 87**,** 110-4.

Lawson, N. D. & S. A. Wolfe (2011) Forward and reverse genetic approaches for the analysis of vertebrate development in the zebrafish. *Dev Cell,* 21**,** 48-64.

Leal, G. F., G. Nishimura, U. Voss, D. R. Bertola, E. Åström, J. Svensson, G. L. Yamamoto, A. Hammarsjö, E. Horemuzova, N. Papadiogannakis, E. Iwarsson, G. Grigelioniene & E. Tham (2018) Expanding the Clinical Spectrum of Phenotypes Caused by Pathogenic Variants in PLOD2. *J Bone Miner Res,* 33**,** 753-760.

Lefebvre, V. & P. Bhattaram (2010) Vertebrate skeletogenesis. *Curr Top Dev Biol,* 90**,** 291-317.

Levin, L. S., C. F. Salinas & R. J. Jorgenson (1978) Classification of osteogenesis imperfecta by dental characteristics. *Lancet,* 1**,** 332-3.

Lewis, M. J. & H. R. Pelham (1992) Ligand-induced redistribution of a human KDEL receptor from the Golgi complex to the endoplasmic reticulum. *Cell,* 68**,** 353-64.

Lindahl, K., A. M. Barnes, N. Fratzl-Zelman, M. P. Whyte, T. E. Hefferan, E. Makareeva, M. Brusel, M. J. Yaszemski, C. J. Rubin, A. Kindmark, P. Roschger, K. Klaushofer, W. H. McAlister, S. Mumm, S. Leikin, E. Kessler, A. L. Boskey, O. Ljunggren & J. C. Marini (2011) COL1 C-propeptide cleavage site mutations cause high bone mass osteogenesis imperfecta. *Hum Mutat,* 32**,** 598-609.

Lindahl, K., E. Åström, A. Dragomir, S. Symoens, P. Coucke, S. Larsson, E. Paschalis, P. Roschger, S. Gamsjaeger, K. Klaushofer, N. Fratzl-Zelman & A. Kindmark (2018) Homozygosity for CREB3L1 premature stop codon in first case of recessive osteogenesis imperfecta associated with OASIS-deficiency to survive infancy. *Bone,* 114**,** 268-277.

Lindert, U., W. A. Cabral, S. Ausavarat, S. Tongkobpetch, K. Ludin, A. M. Barnes, P. Yeetong, M. Weis, B. Krabichler, C. Srichomthong, E. N. Makareeva, A. R. Janecke, S. Leikin, B. Röthlisberger, M. Rohrbach, I. Kennerknecht, D. R. Eyre, K. Suphapeetiporn, C. Giunta, J. C. Marini & V. Shotelersuk (2016) MBTPS2 mutations cause defective regulated intramembrane proteolysis in X-linked osteogenesis imperfecta. *Nat Commun,* 7**,** 11920.

Liu, Y., L. Song, D. Ma, F. Lv, X. Xu, J. Wang, W. Xia, Y. Jiang, O. Wang, Y. Song, X. Xing, Asan & M. Li (2016) Genotype-phenotype analysis of a rare type of osteogenesis imperfecta in four Chinese families with WNT1 mutations. *Clin Chim Acta,* 461**,** 172-80.

Ljusberg, J., Y. Wang, P. Lång, M. Norgård, R. Dodds, K. Hultenby, B. Ek-Rylander & G. Andersson (2005) Proteolytic excision of a repressive loop domain in tartrate-resistant acid phosphatase by cathepsin K in osteoclasts. *J Biol Chem,* 280**,** 28370-81.

Ludwig, K., L. M. Ward, N. Khan, M. E. Robinson, V. Miranda, G. Bardai, P. Moffatt & F. Rauch (2022) Dominant osteogenesis imperfecta with low bone turnover caused by a heterozygous SP7 variant. *Bone,* 160**,** 116400.

Ma, R. C., C. T. Jacobs, P. Sharma, K. M. Kocha & P. Huang (2018) Stereotypic generation of axial tenocytes from bipartite sclerotome domains in zebrafish. *PLoS Genet,* 14**,** e1007775.

Mackay, E. W., A. Apschner & S. Schulte-Merker (2013) A bone to pick with zebrafish. *Bonekey Rep,* 2**,** 445.

Maes, C., T. Kobayashi, M. K. Selig, S. Torrekens, S. I. Roth, S. Mackem, G. Carmeliet & H. M. Kronenberg (2010) Osteoblast precursors, but not mature osteoblasts, move into developing and fractured bones along with invading blood vessels. *Dev Cell,* 19**,** 329-44.

Maes, C., H. M. Kronenberg, F. H. Glorieux, J. M. Pettifor & H. Jüppner. 2012. Chapter 4 - Postnatal Bone Growth: Growth Plate Biology, Bone Formation, and Remodeling. In *Pediatric Bone (Second Edition)*, 55-82. San Diego: Academic Press.

Mansour, A., G. Abou-Ezzi, E. Sitnicka, S. E. Jacobsen, A. Wakkach & C. Blin-Wakkach (2012) Osteoclasts promote the formation of hematopoietic stem cell niches in the bone marrow. *J Exp Med,* 209**,** 537-49.

Marini, J. C., A. Forlino, H. P. Bächinger, N. J. Bishop, P. H. Byers, A. Paepe, F. Fassier, N. Fratzl-Zelman, K. M. Kozloff, D. Krakow, K. Montpetit & O. Semler (2017) Osteogenesis imperfecta. *Nat Rev Dis Primers,* 3**,** 17052.

Marini, J. C., A. Forlino, W. A. Cabral, A. M. Barnes, J. D. San Antonio, S. Milgrom, J. C. Hyland, J. Körkkö, D. J. Prockop, A. De Paepe, P. Coucke, S. Symoens, F. H. Glorieux, P. J. Roughley, A. M. Lund, K. Kuurila-Svahn, H. Hartikka, D. H. Cohn, D. Krakow, M. Mottes, U. Schwarze, D. Chen, K. Yang, C. Kuslich, J. Troendle, R. Dalgleish & P. H. Byers (2007) Consortium for osteogenesis imperfecta mutations in the helical domain of type I collagen: regions rich in lethal mutations align with collagen binding sites for integrins and proteoglycans. *Hum Mutat,* 28**,** 209-21.

Martínez-Glez, V., M. Valencia, J. A. Caparrós-Martín, M. Aglan, S. Temtamy, J. Tenorio, V. Pulido, U. Lindert, M. Rohrbach, D. Eyre, C. Giunta, P. Lapunzina & V. L. Ruiz-Perez (2012) Identification of a mutation causing deficient BMP1/mTLD proteolytic activity in autosomal recessive osteogenesis imperfecta. *Hum Mutat,* 33**,** 343-50.

McDonald, G. L. K., M. Wang, C. L. Hammond & D. J. M. Bergen (2021) Pharmacological Manipulation of Early Zebrafish Skeletal Development Shows an Important Role for Smad9 in Control of Skeletal Progenitor Populations. *Biomolecules,* 11.

Mendoza-Londono, R., S. Fahiminiya, J. Majewski, M. Tétreault, J. Nadaf, P. Kannu, E. Sochett, A. Howard, J. Stimec, L. Dupuis, P. Roschger, K. Klaushofer, T. Palomo, J. Ouellet, H. Al-Jallad, J. S. Mort, P. Moffatt, S. Boudko, H. P. Bächinger, F. Rauch & C. R. C. Consortium (2015) Recessive osteogenesis imperfecta caused by missense mutations in SPARC. *Am J Hum Genet,* 96**,** 979-85.

Miller, S. C., L. de Saint-Georges, B. M. Bowman & W. S. Jee (1989) Bone lining cells: structure and function. *Scanning Microsc,* 3**,** 953-60; discussion 960-1.

Mitchell, R. E., L. F. Huitema, R. E. Skinner, L. H. Brunt, C. Severn, S. Schulte-Merker & C. L. Hammond (2013) New tools for studying osteoarthritis genetics in zebrafish. *Osteoarthritis Cartilage,* 21**,** 269-78.

Mizuno, K., T. Hayashi, D. H. Peyton & H. P. Bächinger (2004) Hydroxylation-induced stabilization of the collagen triple helix. Acetyl-(glycyl-4(R)-hydroxyprolyl-4(R)-hydroxyprolyl)(10)-NH(2) forms a highly stable triple helix. *J Biol Chem,* 279**,** 38072-8.

Moffatt, P., M. H. Gaumond, P. Salois, K. Sellin, M. C. Bessette, E. Godin, P. T. de Oliveira, G. J. Atkins, A. Nanci & G. Thomas (2008) Bril: a novel bone-specific modulator of mineralization. *J Bone Miner Res,* 23**,** 1497-508.

Moosa, S., G. L. Yamamoto, L. Garbes, K. Keupp, A. Beleza-Meireles, C. A. Moreno, E. R. Valadares, S. B. de Sousa, S. Maia, J. Saraiva, R. S. Honjo, C. A. Kim, H. Cabral de Menezes, E. Lausch, P. V. Lorini, A. Lamounier, T. C. B. Carniero, C. Giunta, M. Rohrbach, M. Janner, O. Semler, F. Beleggia, Y. Li, G. Yigit, N. Reintjes, J. Altmüller, P. Nürnberg, D. P. Cavalcanti, B. Zabel, M. L. Warman, D. R. Bertola, B. Wollnik & C. Netzer (2019) Autosomal-Recessive Mutations in MESD Cause Osteogenesis Imperfecta. *Am J Hum Genet,* 105**,** 836-843.

Moreira, C. A., D. W. Dempster, R. Baron, K. R. Feingold, B. Anawalt, A. Boyce, G. Chrousos, W. W. de Herder, K. Dhatariya, K. Dungan, J. M. Hershman, J. Hofland, S. Kalra, G. Kaltsas, C. Koch, P. Kopp, M. Korbonits, C. S. Kovacs, W. Kuohung, B. Laferrère, M. Levy, E. A. McGee, R. McLachlan, J. E. Morley, M. New, J. Purnell, R. Sahay, F. Singer, M. A. Sperling, C. A. Stratakis, D. L. Trence & D. P. Wilson. 2000. Anatomy and Ultrastructure of Bone – Histogenesis, Growth and Remodeling.

Morello, R., T. K. Bertin, Y. Chen, J. Hicks, L. Tonachini, M. Monticone, P. Castagnola, F. Rauch, F. H. Glorieux, J. Vranka, H. P. Bächinger, J. M. Pace, U. Schwarze, P. H. Byers, M. Weis, R. J. Fernandes, D. R. Eyre, Z. Yao, B. F. Boyce & B. Lee (2006) CRTAP is required for prolyl 3- hydroxylation and mutations cause recessive osteogenesis imperfecta. *Cell,* 127**,** 291-304.

Morello, R., L. Tonachini, M. Monticone, L. Viggiano, M. Rocchi, R. Cancedda & P. Castagnola (1999) cDNA cloning, characterization and chromosome mapping of Crtap encoding the mouse cartilage associated protein. *Matrix Biol,* 18**,** 319-24.

Moriishi, T. & T. Komori (2020) Lack of reproducibility in osteocalcin-deficient mice. *PLoS Genet,* 16**,** e1008939.

Moriishi, T., R. Ozasa, T. Ishimoto, T. Nakano, T. Hasegawa, T. Miyazaki, W. Liu, R. Fukuyama, Y. Wang, H. Komori, X. Qin, N. Amizuka & T. Komori (2020) Osteocalcin is necessary for the alignment of apatite crystallites, but not glucose metabolism, testosterone synthesis, or muscle mass. *PLoS Genet,* 16**,** e1008586.

Mosley, J. (2000) Osteoporosis and bone functional adaptation: Mechanobiological regulation of bone architecture in growing and adult bone, a review. *The Journal of Rehabilitation Research and Development,* 37**,** 189-199.

Mulari, M., J. Vääräniemi & H. K. Väänänen (2003) Intracellular membrane trafficking in bone resorbing osteoclasts. *Microsc Res Tech,* 61**,** 496-503.

Murakami, T., A. Saito, S. Hino, S. Kondo, S. Kanemoto, K. Chihara, H. Sekiya, K. Tsumagari, K. Ochiai, K. Yoshinaga, M. Saitoh, R. Nishimura, T. Yoneda, I. Kou, T. Furuichi, S. Ikegawa, M. Ikawa, M. Okabe, A. Wanaka & K. Imaizumi (2009) Signalling mediated by the endoplasmic reticulum stress transducer OASIS is involved in bone formation. *Nat Cell Biol,* 11**,** 1205-11.

Myllyharju, J. & K. I. Kivirikko (2001) Collagens and collagen-related diseases. *Ann Med,* 33**,** 7-21.

Myllylä, R., C. Wang, J. Heikkinen, A. Juffer, O. Lampela, M. Risteli, H. Ruotsalainen, A. Salo & L. Sipilä (2007) Expanding the lysyl hydroxylase toolbox: new insights into the localization and activities of lysyl hydroxylase 3 (LH3). *J Cell Physiol,* 212**,** 323-9.

Nasevicius, A. & S. C. Ekker (2000) Effective targeted gene 'knockdown' in zebrafish. *Nat Genet,* 26**,** 216-20.

Neugebauer, J., J. Heilig, S. Hosseinibarkooie, B. C. Ross, N. Mendoza-Ferreira, F. Nolte, M. Peters, I. Hölker, K. Hupperich, T. Tschanz, V. Grysko, F. Zaucke, A. Niehoff & B. Wirth (2018) Plastin 3 influences bone homeostasis through regulation of osteoclast activity. *Hum Mol Genet,* 27**,** 4249-4262.

Pogoda, H. M., I. Riedl-Quinkertz, H. Löhr, J. S. Waxman, R. M. Dale, J. Topczewski, S. Schulte-Merker & M. Hammerschmidt (2018) Direct activation of chordoblasts by retinoic acid is required for segmented centra mineralization during zebrafish spine development. *Development,* 145.

Ricard-Blum, S. (2011) The collagen family. *Cold Spring Harb Perspect Biol,* 3**,** a004978.

Robling, A. G., A. B. Castillo & C. H. Turner (2006) Biomechanical and molecular regulation of bone remodeling. *Annu Rev Biomed Eng,* 8**,** 455-98.

Robling, A. G., P. J. Niziolek, L. A. Baldridge, K. W. Condon, M. R. Allen, I. Alam, S. M. Mantila, J. Gluhak-Heinrich, T. M. Bellido, S. E. Harris & C. H. Turner (2008) Mechanical stimulation of bone in vivo reduces osteocyte expression of Sost/sclerostin. *J Biol Chem,* 283**,** 5866-75.

Robu, M. E., J. D. Larson, A. Nasevicius, S. Beiraghi, C. Brenner, S. A. Farber & S. C. Ekker (2007) p53 activation by knockdown technologies. *PLoS Genet,* 3**,** e78.

Rosset, E. M. & A. D. Bradshaw (2016) SPARC/osteonectin in mineralized tissue. *Matrix Biol,* 52-54**,** 78-87.

Ruotsalainen, H., L. Sipilä, M. Vapola, R. Sormunen, A. M. Salo, L. Uitto, D. K. Mercer, S. P. Robins, M. Risteli, A. Aszodi, R. Fässler & R. Myllylä (2006) Glycosylation catalyzed by lysyl hydroxylase 3 is essential for basement membranes. *J Cell Sci,* 119**,** 625-35.

Saito, K., M. Chen, F. Bard, S. Chen, H. Zhou, D. Woodley, R. Polischuk, R. Schekman & V. Malhotra (2009) TANGO1 facilitates cargo loading at endoplasmic reticulum exit sites. *Cell,* 136**,** 891-902.

Salhotra, A., H. N. Shah, B. Levi & M. T. Longaker (2020) Mechanisms of bone development and repair. *Nat Rev Mol Cell Biol,* 21**,** 696-711.

Sarmah, S., A. Barrallo-Gimeno, D. B. Melville, J. Topczewski, L. Solnica-Krezel & E. W. Knapik (2010) Sec24D-dependent transport of extracellular matrix proteins is required for zebrafish skeletal morphogenesis. *PLoS One,* 5**,** e10367.

Satoh, M., K. Hirayoshi, S. Yokota, N. Hosokawa & K. Nagata (1996) Intracellular interaction of collagen-specific stress protein HSP47 with newly synthesized procollagen. *J Cell Biol,* 133**,** 469-83.

Schlombs, K., T. Wagner & J. Scheel (2003) Site-1 protease is required for cartilage development in zebrafish. *Proc Natl Acad Sci U S A,* 100**,** 14024-9.

Schwarze, U., T. Cundy, S. M. Pyott, H. E. Christiansen, M. R. Hegde, R. A. Bank, G. Pals, A. Ankala, K. Conneely, L. Seaver, S. M. Yandow, E. Raney, D. Babovic-Vuksanovic, J. Stoler, Z. Ben-Neriah, R. Segel, S. Lieberman, L. Siderius, A. Al-Aqeel, M. Hannibal, L. Hudgins, E. McPherson, M. Clemens, M. D. Sussman, R. D. Steiner, J. Mahan, R. Smith, K. Anyane-Yeboa, J. Wynn, K. Chong, T. Uster, S. Aftimos, V. R. Sutton, E. C. Davis, L. S. Kim, M. A. Weis, D. Eyre & P. H. Byers (2013) Mutations in FKBP10, which result in Bruck syndrome and recessive forms of osteogenesis imperfecta, inhibit the hydroxylation of telopeptide lysines in bone collagen. *Hum Mol Genet,* 22**,** 1-17.

Scott, I. C., Y. Imamura, W. N. Pappano, J. M. Troedel, A. D. Recklies, P. J. Roughley & D. S. Greenspan (2000) Bone morphogenetic protein-1 processes probiglycan. *J Biol Chem,* 275**,** 30504-11.

Semler, O., L. Garbes, K. Keupp, D. Swan, K. Zimmermann, J. Becker, S. Iden, B. Wirth, P. Eysel, F. Koerber, E. Schoenau, S. K. Bohlander, B. Wollnik & C. Netzer (2012) A mutation in the

5'-UTR of IFITM5 creates an in-frame start codon and causes autosomal-dominant osteogenesis imperfecta type V with hyperplastic callus. *Am J Hum Genet,* 91**,** 349-57.

Shoulders, M. D. & R. T. Raines (2009) Collagen structure and stability. *Annu Rev Biochem,* 78**,** 929-58.

Sillence, D. O., A. Senn & D. M. Danks (1979) Genetic heterogeneity in osteogenesis imperfecta. *J Med Genet,* 16**,** 101-16.

Singh, S. P., J. E. Holdway & K. D. Poss (2012) Regeneration of amputated zebrafish fin rays from de novo osteoblasts. *Dev Cell,* 22**,** 879-86.

Sinikumpu, J. J., M. Ojaniemi, P. Lehenkari & W. Serlo (2015) Severe osteogenesis imperfecta Type-III and its challenging treatment in newborn and preschool children. A systematic review. *Injury,* 46**,** 1440-6.

Spoorendonk, K. M., J. Peterson-Maduro, J. Renn, T. Trowe, S. Kranenbarg, C. Winkler & S. Schulte-Merker (2008) Retinoic acid and Cyp26b1 are critical regulators of osteogenesis in the axial skeleton. *Development,* 135**,** 3765-74.

Stainier, D. Y. R., E. Raz, N. D. Lawson, S. C. Ekker, R. D. Burdine, J. S. Eisen, P. W. Ingham, S. Schulte-Merker, D. Yelon, B. M. Weinstein, M. C. Mullins, S. W. Wilson, L. Ramakrishnan, S. L. Amacher, S. C. F. Neuhauss, A. Meng, N. Mochizuki, P. Panula & C. B. Moens (2017) Guidelines for morpholino use in zebrafish. *PLoS Genet,* 13**,** e1007000.

Stenbeck, G. (2002) Formation and function of the ruffled border in osteoclasts. *Semin Cell Dev Biol,* 13**,** 285-92.

Syx, D., B. Guillemyn, S. Symoens, A. B. Sousa, A. Medeira, M. Whiteford, T. Hermanns-Lê, P. J. Coucke, A. De Paepe & F. Malfait (2015) Defective Proteolytic Processing of Fibrillar Procollagens and Prodecorin Due to Biallelic BMP1 Mutations Results in a Severe, Progressive Form of Osteogenesis Imperfecta. *J Bone Miner Res,* 30**,** 1445-56.

Takayanagi, H., S. Kim, T. Koga, H. Nishina, M. Isshiki, H. Yoshida, A. Saiura, M. Isobe, T. Yokochi, J. Inoue, E. F. Wagner, T. W. Mak, T. Kodama & T. Taniguchi (2002) Induction and activation of the transcription factor NFATc1 (NFAT2) integrate RANKL signaling in terminal differentiation of osteoclasts. *Dev Cell,* 3**,** 889-901.

Tatsumi, S., K. Ishii, N. Amizuka, M. Li, T. Kobayashi, K. Kohno, M. Ito, S. Takeshita & K. Ikeda (2007) Targeted ablation of osteocytes induces osteoporosis with defective mechanotransduction. *Cell Metab,* 5**,** 464-75.

Tiainen, P., A. Pasanen, R. Sormunen & J. Myllyharju (2008) Characterization of recombinant human prolyl 3-hydroxylase isoenzyme 2, an enzyme modifying the basement membrane collagen IV. *J Biol Chem,* 283**,** 19432-9.

Tonelli, F., J. W. Bek, R. Besio, A. De Clercq, L. Leoni, P. Salmon, P. J. Coucke, A. Willaert & A. Forlino (2020a) Zebrafish: A Resourceful Vertebrate Model to Investigate Skeletal Disorders. *Front Endocrinol (Lausanne),* 11**,** 489.

Tonelli, F., S. Cotti, L. Leoni, R. Besio, R. Gioia, L. Marchese, S. Giorgetti, S. Villani, C. Gistelinck, R. Wagener, B. Kobbe, I. A. K. Fiedler, D. Larionova, B. Busse, D. Eyre, A. Rossi, P. E. Witten & A. Forlino (2020b) Crtap and p3h1 knock out zebrafish support defective collagen chaperoning as the cause of their osteogenesis imperfecta phenotype. *Matrix Biol,* 90**,** 40-60.

Torzilli, P. A., K. Takebe, A. H. Burstein, J. M. Zika & K. G. Heiple (1982) The material properties of immature bone. *J Biomech Eng,* 104**,** 12-20.

Trejo, P., T. Palomo, K. Montpetit, F. Fassier, A. Sato, F. H. Glorieux & F. Rauch (2017) Long-term follow-up in osteogenesis imperfecta type VI. *Osteoporos Int,* 28**,** 2975-2983.

Tsukamoto, T., X. Li, H. Morita, T. Minowa, T. Aizawa, N. Hanagata & M. Demura (2013) Role of S-palmitoylation on IFITM5 for the interaction with FKBP11 in osteoblast cells. *PLoS One,* 8**,** e75831.

Uzawa, K., W. J. Grzesik, T. Nishiura, S. A. Kuznetsov, P. G. Robey, D. A. Brenner & M. Yamauchi (1999) Differential expression of human lysyl hydroxylase genes, lysine hydroxylation, and cross-linking of type I collagen during osteoblastic differentiation in vitro. *J Bone Miner Res,* 14**,** 1272-80.

Uzel, M. I., I. C. Scott, H. Babakhanlou-Chase, A. H. Palamakumbura, W. N. Pappano, H. H. Hong, D. S. Greenspan & P. C. Trackman (2001) Multiple bone morphogenetic protein 1-related mammalian metalloproteinases process pro-lysyl oxidase at the correct physiological site and control lysyl oxidase activation in mouse embryo fibroblast cultures. *J Biol Chem,* 276**,** 22537-43.

van Dijk, F. S., O. Semler, J. Etich, A. Köhler, J. A. Jimenez-Estrada, N. Bravenboer, L. Claeys, E. Riesebos, S. Gegic, S. R. Piersma, C. R. Jimenez, Q. Waisfisz, C. L. Flores, J. Nevado, A. J. Harsevoort, G. J. M. Janus, A. A. M. Franken, A. M. van der Sar, H. Meijers-Heijboer, K. E. Heath, P. Lapunzina, P. G. J. Nikkels, G. W. E. Santen, J. Nüchel, M. Plomann, R. Wagener, M. Rehberg, H. Hoyer-Kuhn, E. M. W. Eekhoff, G. Pals, M. Mörgelin, S. Newstead, B. T. Wilson, V. L. Ruiz-Perez, A. Maugeri, C. Netzer, F. Zaucke & D. Micha (2020) Interaction between KDELR2 and HSP47 as a Key Determinant in Osteogenesis Imperfecta Caused by Bi-allelic Variants in KDELR2. *Am J Hum Genet,* 107**,** 989-999.

van Dijk, F. S., M. C. Zillikens, D. Micha, M. Riessland, C. L. Marcelis, C. E. de Die-Smulders, J. Milbradt, A. A. Franken, A. J. Harsevoort, K. D. Lichtenbelt, H. E. Pruijs, M. E. Rubio-Gozalbo, R. Zwertbroek, Y. Moutaouakil, J. Egthuijsen, M. Hammerschmidt, R. Bijman, C.

M. Semeins, A. D. Bakker, V. Everts, J. Klein-Nulend, N. Campos-Obando, A. Hofman, G. J. te Meerman, A. J. Verkerk, A. G. Uitterlinden, A. Maugeri, E. A. Sistermans, Q. Waisfisz, H. Meijers-Heijboer, B. Wirth, M. E. Simon & G. Pals (2013) PLS3 mutations in X-linked osteoporosis with fractures. *N Engl J Med,* 369**,** 1529-36.

van Eeden, F. J., M. Granato, U. Schach, M. Brand, M. Furutani-Seiki, P. Haffter, M. Hammerschmidt, C. P. Heisenberg, Y. J. Jiang, D. A. Kane, R. N. Kelsh, M. C. Mullins, J. Odenthal, R. M. Warga & C. Nüsslein-Volhard (1996) Genetic analysis of fin formation in the zebrafish, Danio rerio. *Development,* 123**,** 255-62.

Vanoevelen, J., A. Janssens, L. F. Huitema, C. L. Hammond, J. R. Metz, G. Flik, T. Voets & S. Schulte-Merker (2011) Trpv5/6 is vital for epithelial calcium uptake and bone formation. *FASEB J,* 25**,** 3197-207.

Viguet-Carrin, S., P. Garnero & P. D. Delmas (2006) The role of collagen in bone strength. *Osteoporos Int,* 17**,** 319-36.

Vimalraj, S. (2020) Alkaline phosphatase: Structure, expression and its function in bone mineralization. *Gene,* 754**,** 144855.

von der Mark, K. 2006. Structure, Biosynthesis and Gene Regulation of Collagens in Cartilage and Bone.

Vranka, J. A., L. Y. Sakai & H. P. Bächinger (2004) Prolyl 3-hydroxylase 1, enzyme characterization and identification of a novel family of enzymes. *J Biol Chem,* 279**,** 23615-21.

Watson, C. J. & R. Y. Kwon (2015) Osteogenic programs during zebrafish fin regeneration. *Bonekey Rep,* 4**,** 745.

Weigele, J. & T. A. Franz-Odendaal (2016) Functional bone histology of zebrafish reveals two types of endochondral ossification, different types of osteoblast clusters and a new bone type. *J Anat,* 229**,** 92-103.

Wienholds, E., F. van Eeden, M. Kosters, J. Mudde, R. H. Plasterk & E. Cuppen (2003) Efficient target-selected mutagenesis in zebrafish. *Genome Res,* 13**,** 2700-7.

Witten, P. E., M. Bendahmane & A. Abou-Haila (1997) Enzyme histochemical characteristics of osteoblasts and mononucleated osteoclasts in a teleost fish with acellular bone (Oreochromis niloticus, Cichlidae). *Cell Tissue Res,* 287**,** 591-9.

Witten, P. E., A. Hansen & B. K. Hall (2001) Features of mono- and multinucleated bone resorbing cells of the zebrafish Danio rerio and their contribution to skeletal development, remodeling, and growth. *J Morphol,* 250**,** 197-207.

Witten, P. E. & A. Huysseune (2009) A comparative view on mechanisms and functions of skeletal remodelling in teleost fish, with special emphasis on osteoclasts and their function. *Biol Rev Camb Philos Soc,* 84**,** 315-46.

Witten, P. E., A. Huysseune & B. K. Hall (2010) A practical approach for the identification of the many cartilaginous tissues in teleost fish. *Journal of Applied Ichthyology,* 26**,** 257-262.

Yamauchi, M. & M. Sricholpech (2012) Lysine post-translational modifications of collagen. *Essays Biochem,* 52**,** 113-33.

Yuan, L., S. J. Kenny, J. Hemmati, K. Xu & R. Schekman (2018) TANGO1 and SEC12 are copackaged with procollagen I to facilitate the generation of large COPII carriers. *Proc Natl Acad Sci U S A,* 115**,** E12255-E12264.

Zhou, X., P. Lin, D. Yamazaki, K. H. Park, S. Komazaki, S. R. Chen, H. Takeshima & J. Ma (2014) Trimeric intracellular cation channels and sarcoplasmic/endoplasmic reticulum calcium homeostasis. *Circ Res,* 114**,** 706-16.

Rationale and research objectives

Aims and rationale

Altogether, rare monogenic heritable skeletal diseases, such as osteogenesis imperfecta (OI), affect thousands of people worldwide and are still without a cure. Dominant OI caused by mutations in collagen type I genes, *COL1A1* and *COL1A2*, are the most common forms of the disease. However, recessive OI due to defects in genes involved in collagen type I processing or affecting bone cell differentiation and activity have been described and continuously updated thanks to the advance in the Next Generation Sequencing technology. Given such genetic variety, shedding light on the molecular basis of each form of the pathology becomes fundamental to advance the understanding of the disease and to develop personalized therapeutic approaches.

To this purpose, the zebrafish (*Danio rerio*) stands out as a unique animal model due to several advantages impossible to replicate in the more largely used murine models. Zebrafish has a small size and a high proliferative rate, allowing large scale studies also in combination with drug testing. Thanks to the transparency of embryos, larvae, and also of some skeletal appendages, such as the caudal fin, *in vivo* studies can be performed. This distinguishes zebrafish from mice, in which intravital imaging can be challenging. Finally, zebrafish generally display a less severe phenotype respect to their murine counterparts and can therefore provide a useful complementation when murine models are poorly viable.

Zebrafish is a proven valid model for investigating skeletal diseases. It shares 71% of its genome with humans, and bone development and skeletal components are highly conserved among the two species. Furthermore, zebrafish ability to regenerate bony structures in a process that reproduces bone formation allows to easily investigate the skeleton in health and disease. In the past years, thanks to the feasibility of approaches such as CRISPR/Cas9, the number of zebrafish models for skeletal disorders, including OI, has enormously increased, strongly contributing to the understanding of the pathology.

My doctoral research activity was based on the use of zebrafish as an animal model to study skeletal disorders. The first specific objective was to contribute to the generation and characterization of a zebrafish model, the *rpl13* mutant, to better elucidate the role of the ribosomal protein eL13 on the onset of a rare skeletal dysplasia (Manuscript 1). During the pandemic lockdown, I mostly focused on studying the molecular bases of regeneration, writing a review in which I compare the regeneration processes of three vertebrates, including zebrafish (Manuscript 2). The third objective was to generate and characterize two new zebrafish models with mutations in *tmem38b*, causing the recessive OI type XIV, aiming to better dissect the role of TRIC-B during skeletal development (Manuscript 3). Finally,

I investigated in deep in the two zebrafish OI *Chi/+* and *p3h1*$^{-/-}$, models for dominant and recessive OI, respectively, the effect of altered homeostasis on bone cell differentiation *in vivo* during caudal fin regeneration (Manuscript 4).

Specific research objectives

Objective 1

Generating and characterizing a zebrafish model to elucidate the role of rpl13 on the onset of a rare skeletal dysplasia

Spondyloepimetaphyseal dysplasias (SEMDs) are a class of rare skeletal dysplasias caused by multiple genetic defects. This study was carried out in collaboration with Dr. Outi Mäkitie and her group from the Department of Molecular Medicine and Surgery and Center for Molecular Medicine of the Karolinska Institut (Stockholm, Sweden). The global aim of the study was to identify the genetic cause underlying a SEMD phenotype observed in four unrelated families.

First, whole genome sequencing (WGS), whole exome (WES), and Sanger sequencing approaches allowed to identify two monoallelic missense variants and one monoallelic splice site variant in *RPL13* gene, encoding for the ribosomal protein eL13, in four families with SEMD. Genetic and pedigree analysis of patients revealed autosomal dominant inheritance with incomplete penetrance and variable clinical expressivity. Clinical and radiological data highlighted severe skeletal impairments with vertebral abnormalities and delayed ossification at the metaphyseal and epiphyseal sites. In the second part of the study, in which I was directly involved during my PhD, we aimed to further elucidate the role of eL13 *in vivo* by establishing a *rpl13* zebrafish model. The *rpl13* mutant, generated by CRISPR/Cas9, harbored a frameshift deletion predicted to alter the amino acid sequence of the protein. Alcian blue staining was performed at different developmental stages to evaluate cranial cartilage structure. The analysis revealed the presence of cartilage deformities and craniofacial defects, partially recapitulating the patients' phenotype. These findings supported the conserved, relevant role for eL13 in skeletogenesis and skeletal disease.

Objective 2

Providing a detailed overview of molecular and cellular mechanisms driving appendage regeneration in vertebrates, including zebrafish caudal fin regeneration

Zebrafish has a remarkable ability to regenerate bony structures like fins, jaw, but also several organs such as heart, brain, pancreas, kidney, and liver. This feature is shared with few other vertebrates,

such as salamanders, that can regenerate limbs, and lizards, able to regenerate the tail after amputation or autotomy.

Few months after the start of my PhD, COVID-19 pandemic breakout forced all of us to lockdown. Together with my Supervisor we decided to make the most of that time by writing a review on appendage regeneration in vertebrates with the help of our collaborator Przemko Tylzanowski (University of Leuven, Belgium), expert in limb development. The aim of this study was to compare regeneration mechanisms of three vertebrates capable of regeneration (zebrafish, salamander and lizard). First, we described in deep the experimental tools that can be applied to each model for regenerative studies. We then proceeded in providing a detailed comparison of morphological, cellular and epigenetic changes during regeneration in the three models. We commented common topics in regeneration, such as patterning and positional memory, the role of inflammation and immune system, and the influence of aging. Molecular pathways implicated in regeneration were discussed, showing strong similarities between the three vertebrates. Finally, we focused on the power of zebrafish caudal fin regeneration to be used as a tool for biomedical research, a feature still not possible in salamander and lizard. This review provides a strong addiction to the literature in the field of the regeneration and gave me the necessary knowledge to successfully complete the Objectives 3 and 4 of my PhD.

Objective 3

Generating and characterizing two zebrafish models with different mutations in *tmem38b*

Mutations in *TMEM38B*, encoding for the ER channel TRIC-B, cause recessive OI type XIV. The murine *Tric-b* KO model, perinatal lethal, allowed characterization of the pathology only immediately after birth. In this study, we generated two *tmem38b* zebrafish mutants with the aim of investigating the role of TRIC-B channel during skeletal development. We first demonstrated the expression and, thus likely the relevance of *tmem38b* in zebrafish during early developmental stages. Then, using CRISPR/Cas9 technology we generated two t*mem38b* mutants, one carrying an out-of-frame mutation introducing a premature stop codon (*tmem38b*$^{-/-}$) and one with an in-frame deletion removing the highly conserved KEV domain, fundamental for channel activity (*tmem38b*$^{\Delta 120\text{-}7/\Delta 120\text{-}7}$). SDS-PAGE and TEM analyses revealed collagen type I under-modification and ER retention in both models, as described in OI type XIV patients. Alizarin Red, performed at different developmental stages, showed a mild skeletal phenotype in *tmem38b*$^{-/-}$ during the larval-juvenile transition stage of development; *tmem38b*$^{\Delta 120\text{-}7/\Delta 120\text{-}7}$ presented a milder bone phenotype, limited to reduced vertebral dimension at 21 days post fertilization (dpf). Caudal fin regeneration studies were performed to

evaluate bone formation and allowed to point out an impaired osteoblast and osteoclast activity. Taken together, these results supported the relevance of TRIC-B in skeletal development and bone cells' differentiation.

Objective 4

Investigating the effect of altered homeostasis on bone cells' differentiation *in vivo* in two zebrafish models of dominant and recessive OI using caudal fin regeneration as a tool

In the last decade, OI phenotype has been linked to impaired osteoblasts homeostasis due to mutant collagen retention in the ER, in dominant as well as in several recessive forms. The aim of my main PhD project was to investigate osteoblast and osteoclast differentiation *in vivo* in dominant and recessive OI characterized by collagen type I with altered structure, using the two zebrafish models *Chi/+* and *p3h1*$^{-/-}$. To do that, I took advantage of regeneration of the caudal fin, mainly composed by bone, in mutant fish crossed with the transgenic lines *sp7:GFP* and *bglap:GFP*. First, the global caudal fin regeneration ability was assessed in the two models, demonstrating a delay in bone formation. Indeed, morphometric analysis revealed defects in caudal fin morphology before and during regeneration in both models. To deeply understand the mechanisms behind the delay in bone formation, we proceeded to study bone cellular components. qPCR analysis of *runx2* and *sox9* expression revealed no changes in early differentiation in mutants respect to WT. Further investigation of osteoblast differentiation, carried out by qPCR and confocal imaging analyses, demonstrated a significant impairment in osteoblastogenesis in *Chi/+*, but not in *p3h1*$^{-/-}$. Surprisingly, during fin regeneration osteoclast activity was found to be impaired in both models. The swimming behavior was explored in the dominant model *Chi/+*, since we notice that the fish stay longer time on the bottom of the tanks. We proved a defect in the caudal fin movement likely due to the impairment of the caudal fin joints ECM organization as revealed by TEM and immunofluorescence. The analyses showed, together with increase inter-joint space, collagen type I disorganization and increased amount of collagen XIV, one of the FACIT collagen type present in collagen type I fibrils. Overall, this study highlights, for the first time *in vivo*, how specific gene mutations leading to OI have a different impact on bone cells' differentiation and ECM organization during bone formation.

Results

MANUSCRIPT 1

Novel RPL13 Variants and Variable Clinical Expressivity in a Human Ribosomopathy With Spondyloepimetaphyseal Dysplasia

A. Costantini, J. Alm, F. Tonelli, H. Valta, C. Huber, A. Tran, **V. Daponte**, N. Kirova, Y. Kwon, J. Bae, W. Chung, S. Tan, Y. Sznajer, G. Nishimura, T. Nareoja, A. Warren, V. Cormier-Daire, O. Kim, A. Forlino, T. Cho, O. Makitie. *Journal of Bone and Mineral Research*, 2020. https://doi.org/10.1002/jbmr.4177

Ribosomal protein eL13 (RPL13) and spondyloepimetaphyseal dysplasias (SEMDs)

Ribosomes are the molecular machines involved in mRNA translation and consequently responsible for the quality and quantity of all cellular proteins. In eukaryotes, ribosomes (80S) consist of a small 40S subunit and a large 60S subunit. The 40S subunit consists of 18S ribosomal RNAs (rRNAs) and 33 different ribosomal proteins. The 60S subunit is formed by 25S, 5.8S, and 5S rRNAs and 47 ribosomal proteins, among which eL13 (encoded by *RPL13*) (Baßler and Hurt 2019). Despite being ubiquitously expressed, variants in genes encoding ribosomal proteins have been linked to a class of genetic conditions called ribosomopathies that cause tissue-specific phenotypes and are responsible for several skeletal diseases (Trainor and Merrill 2014).

Spondyloepimetaphyseal dysplasias (SEMDs) are a heterogeneous group of disorders with variable growth failure and skeletal impairments affecting the spine and long bone epiphyses and metaphyses. Several genes encoding proteins with different functions have been identified as causative of SEMDs. Some of them are extracellular structural proteins, such as collagen type 2 (*COL2A1*), cartilage oligomeric matrix protein (*COMP*), matrillin 3 (*MATN3*) and perlecan; others encode proteins involved in post-translational processing and transport, such as eukaryotic translation initiation factor 2-alpha kinase 3 (*EIF2AK3*), galactosamine-6-sulphatase (*GALNS*), beta-galactosidase (*GLBI*), 3′-phosphoadenosine 5′-phosphosulfate synthase (*ATPSK2*), and dymeclin (Cormier-Daire 2008).

In 2019, Le Caignec and colleagues first reported an association between *RPL13* variants and SEMD with short stature. Since loss of function of ribosomal proteins were already demonstrated to cause specific developmental defects in mouse models without global translation changes (Kondrashov et al. 2011, Anderson et al. 2007), eL13 was hypothesized to play a specific role in the translation of mRNAs from chondrocytes and/or osteoblasts present at the level of the growth plate, resulting in severe skeletal defects (Le Caignec et al. 2019).

It is therefore fundamental to better investigate the specific impact of *RPL13* variants on skeletal development, also taking advantage of zebrafish as an animal model.

In our study, new variants in *RPL13* gene were identified in four unrelated families as causative of SEMD with short stature and skeletal dysplasia. *In vitro* studies on patients dermal fibroblasts revealed impaired ribosomal assembly and function, resulting in reduced global translation. To validate the data obtained *in vitro*, during my first year of PhD I contributed to the generation and characterization of a *rpl13* mutant zebrafish. The mutant showed cartilage defects in line with the human phenotype, validating *in vivo* the role of the protein in skeletogenesis.

Personal contribution to Manuscript 1

- Genotyping of the *rpl13* mutant zebrafish line.
- Morphometric evaluation of 5, 7 dpf and 1 mpf *rpl13* mutant zebrafish: experiments and data analysis.
- Evaluation of swim bladder insufflation in WT and *rpl13* mutant zebrafish: experiments and data analysis.
- Alcian Blue cartilage staining: experiments and data analysis.
- Figure making.
- Manuscript revision.

References

Anderson, S. J., J. P. Lauritsen, M. G. Hartman, A. M. Foushee, J. M. Lefebvre, S. A. Shinton, B. Gerhardt, R. R. Hardy, T. Oravecz & D. L. Wiest (2007) Ablation of ribosomal protein L22 selectively impairs alphabeta T cell development by activation of a p53-dependent checkpoint. *Immunity,* 26**,** 759-72.

Baßler, J. & E. Hurt (2019) Eukaryotic Ribosome Assembly. *Annu Rev Biochem,* 88**,** 281-306.

Cormier-Daire, V. (2008) Spondylo-epi-metaphyseal dysplasia. *Best Pract Res Clin Rheumatol,* 22**,** 33-44.

Kondrashov, N., A. Pusic, C. R. Stumpf, K. Shimizu, A. C. Hsieh, J. Ishijima, T. Shiroishi & M. Barna (2011) Ribosome-mediated specificity in Hox mRNA translation and vertebrate tissue patterning. *Cell,* 145**,** 383-397.

Le Caignec, C., B. Ory, F. Lamoureux, M. F. O'Donohue, E. Orgebin, P. Lindenbaum, S. Téletchéa, M. Saby, A. Hurst, K. Nelson, S. R. Gilbert, Y. Wilnai, L. Zeitlin, E. Segev, R. Tesfaye, M. Nizon, B. Cogne, S. Bezieau, L. Geoffroy, A. Hamel, E. Mayrargue, B. de Courtivron, A. Decock-Giraudaud, C. Charrier, O. Pichon, C. Retière, R. Redon, A. Pepler, K. McWalter, L. Da Costa, A. Toutain, P. E. Gleizes, M. Baud'huin & B. Isidor (2019) RPL13 Variants Cause Spondyloepimetaphyseal Dysplasia with Severe Short Stature. *Am J Hum Genet,* 105**,** 1040-1047.

Trainor, P. A. & A. E. Merrill (2014) Ribosome biogenesis in skeletal development and the pathogenesis of skeletal disorders. *Biochim Biophys Acta,* 1842**,** 769-78.

Abstract

Spondyloepimetaphyseal dysplasias (SEMDs) are a heterogeneous group of disorders with variable growth failure and skeletal impairments affecting the spine and long bone epiphyses and metaphyses. Here we report on four unrelated families with SEMD in which we identified two monoallelic missense variants and one monoallelic splice site variant in *RPL13*, encoding the ribosomal protein eL13. In two out of four families, we observed autosomal dominant inheritance with incomplete penetrance and variable clinical expressivity; the phenotypes of the mutation-positive subjects ranged from normal height with or without hip dysplasia to severe SEMD with severe short stature and marked skeletal dysplasia. *In vitro* studies on patient-derived dermal fibroblasts harboring *RPL13* missense mutations demonstrated normal eL13 expression, with proper subcellular localization but reduced colocalization with eL28 ($p < 0.001$). Cellular functional defects in fibroblasts from mutation-positive subjects indicated a significant increase in the ratio of 60S subunits to 80S ribosomes ($p = 0.007$) and attenuated global translation ($p = 0.017$). In line with the human phenotype, our *rpl13* mutant zebrafish model, generated by CRISPR-Cas9 editing, showed cartilage deformities at embryonic and juvenile stages. These findings extend the genetic spectrum of *RPL13* mutations causing this novel human ribosomopathy with variable skeletal features. Our study underscores for the first time incomplete penetrance and broad phenotypic variability in SEMD-RPL13 type and confirms impaired ribosomal function. Furthermore, the newly generated *rpl13* mutant zebrafish model corroborates the role of eL13 in skeletogenesis. © 2020 The Authors. *Journal of Bone and Mineral Research* published by Wiley Periodicals LLC on behalf of American Society for Bone and Mineral Research (ASBMR).

Introduction

Osteochondrodysplasias, also known as skeletal dysplasias, are a heterogeneous group of genetic diseases affecting development of bone and cartilage. More than 450 different forms have so far been recognized and classified based on radiological or molecular features.[1] Spondyloepimetaphyseal dysplasias (SEMDs) are characterized by severe short stature and major skeletal abnormalities in the spine, epiphyses, and metaphyses. Nowadays SEMDs are classified in 19 different subtypes.[1] Despite phenotypic similarities, the underlying molecular defects cover diverse biological processes ranging from extracellular matrix composition[2-4] to cell signaling.[5, 6]

Recently, Le Caignec and colleagues reported monoallelic *de novo* mutations in the gene encoding the ribosomal protein eL13 (*RPL13*) in four patients with SEMD.[7] This finding expands the number of ribosomopathies, a group of congenital diseases defined by mutations in genes encoding ribosomal proteins (RPs), transcribing ribosomal RNAs (rRNAs), or factors involved in ribosome biogenesis.[8, 9] Ribosomopathies, which often feature a broad phenotypic variability, include for instance Diamond-Blackfan anemia (MIM #105650), Shwachman-Diamond syndrome (MIM #260400), Treacher Collins syndrome (MIM #154500), and cartilage-hair hypoplasia (MIM #250250).[10-15] These diseases are most commonly characterized by defects in the hematopoietic system and the skeleton, but the phenotypic presentation varies between disorders, among individuals with the same disorder and even among family members sharing identical gene defects.[8, 9, 16]

eL13 is an integral component of the large (60S) ribosomal subunit that is required for pre-ribosomal RNA processing.[7] Despite the fact that eukaryotic ribosomes (80S) are essential for cell growth and proliferation, it is still largely unclear why mutations in *RPL13* and other genes partaking in ribosome biogenesis lead to tissue-specific consequences. Furthermore, molecular mechanisms underlying ribosome dysfunction remain inadequately explored.

As part of our research program on genetic causes of osteochondrodysplasia, we recruited four unrelated families in which the index patients featured SEMD with a severe growth disorder and uniform radiological features. In each of these families, we identified an *RPL13* mutation and studied the disease pathogenesis by performing both *in vitro* and *in vivo* studies. Zebrafish was chosen as our disease model not only because 71% of the genome is conserved between humans and this teleost fish, but also because zebrafish is a proven model for investigating skeletal diseases during development,[17-19] as bone development and some skeletal components are highly conserved between these two species.[20]

Materials and Methods

Subjects

Our study included one Finnish index patient (patient 1), two Korean index patients (patients 2 and 3), and one French/Congolese patient (patient 4), all affected by an unusual form of SEMD. Their parents and other family members, some of whom were possibly affected, were also enrolled in the study. Clinical data and radiographs were collected from medical records and reviewed for disease features and skeletal characteristics. All subjects were also clinically examined as part of this research. Unrelated healthy controls were included for functional validations on dermal fibroblasts.

Whole-genome and exome sequencing

To identify the genetic defect underlying severe skeletal dysplasia in families 1 to 4, we adopted different strategies. The genetic cause of disease was first characterized in families 1 and 4 by performing massively parallel sequencing (MPS).

In family 1, we performed trio whole-genome sequencing (WGS) as previously described.[21, 22] For data analysis, we applied the following filtering criteria: (i) homozygous/compound heterozygous variant or *de novo* variant; (ii) MAF <0.001 the gnomAD[23] and SweGen[24] databases; and (iii) impact severity other than LOW in GEMINI.[25]

In family 4, the index patient underwent whole-exome sequencing analysis (WES), which was carried out using our previously described in-house pipeline.[26]

Further information about these two methods are included in Supplemental Materials and Methods.

Sanger sequencing

To identify the genetic cause of the skeletal disease in families 2 and 3, we screened for mutations the candidate gene identified in families 1 and 4 using Sanger sequencing, as previously described.[21] This method was also chosen to validate the MPS findings in families 1 and 4. Primer sequences are available from the authors upon request.

Molecular modeling

The PyMOL Molecular Graphics System, Version 2.0.7 (Schrödinger, LLC, New York, NY, USA) was used to generate atomic models based on human ribosome structures derived by cryo-electron microscopy (pdb codes: 6EK0 and 4V6X)[27, 28] and to simulate *in silico* the effects of the identified mutations on protein folding.

Dermal fibroblast cultures

Skin biopsies were harvested from four mutation-positive subjects (patients 1, 2, and 3 and the affected mother of patient 2) and five controls (both parents of patient 1 and three unrelated controls). Fibroblasts were isolated as previously described,[29] and cultures expanded in high-glucose DMEM (Thermo Fisher Scientific, Waltham, MA, USA; cat. #11960044) supplemented with 1% GlutaMAX (Thermo Fisher Scientific; cat. #35050038), antibiotics (penicillin and streptomycin at a final concentration of 100 U/mL), and 15% fetal bovine serum. Media were changed every 3 to 4 days, and cells were split upon 80% confluence. Cells of passage 3 to 6 were used for characterization assays. See Supplemental Materials and Methods for details.

Total protein extraction and Western immunoblotting

For characterization of the fibroblasts at the protein level, cells were grown to 90% confluence in 100 mm dishes and lysed in ice-cold RIPA-buffer containing protease inhibitors. Cell lysate was collected by centrifugation followed by total protein quantification (BCA kit according to manufacturer's protocol). Expression of eL13 was evaluated in 10 µg of denatured protein samples by Western immunoblotting (WB) using a primary antibody against RPL13 (mouse monoclonal, Santa Cruz Biotechnology, Dallas, TX, USA; #sc-100829; 1:1,000 dilution) and a HRP-conjugated anti-mouse secondary antibody (Thermo Fisher Scientific; #31430, 1:20,000 dilution) according to standard procedures. Acetylated-tubulin (Sigma-Aldrich, St. Louis, MO, USA; #T7451, 1:10,000 dilution) was used as a loading control. Further information is available in the Supplemental Materials and Methods.

Immunocytochemistry

To investigate possible effects of the mutations on the colocalization of eL13 with other RPs, fibroblasts were cultured on glass cover slips supplemented with 100 µM ascorbic acid 2-phosphate to stimulate extracellular matrix (ECM) production. This culture condition was chosen to put cells under higher protein synthesis demands, which could emphasize possible alterations in patient-derived cells. Immunocytochemistry was performed using standard procedures (detailed information in Supplemental Materials and Methods and in Supplemental Table **S1**). For colocalization analysis, eL13 was co-stained with eL7, eL28, eS19, and calnexin, respectively. Cover slips (3/donor/staining) were imaged with a NikonA1+ confocal laser microscope system. Z-stacks were captured using 60× objective fulfilling Nyquist sampling theorem. Laser power and detector gain were adjusted to cover the widest possible range of intensity values for colocalization analysis. From the entire Z-stacks, 3D colocalization was measured per cell as Pearson's correlation coefficient using the Colocalization Test

plugin in ImageJ Fiji.[30] Pictures shown are z-stacks processed to maximum intensity projections. See Supplemental Materials and Methods for further details.

Sucrose density gradients

Sucrose density gradient fractionation of cell extracts was performed, with minor modifications, as previously described.[31-33] Refer to the Supplemental Materials and Methods for a detailed description of the method.

Measurement of protein synthesis

Protein synthesis was measured as described by Tan and colleagues[33] and in the Supplemental Materials and Methods.

Zebrafish husbandry

Wild-type (AB) zebrafish (*Danio rerio*), obtained from the European Zebrafish Resource Center (EZRC; Eggenstein-Leopoldshafen, Germany), were housed in the animal facility of the University of Pavia in a ZebTEC semi-closed recirculation housing system (Tecniplast, Buguggiate, Italy) at 28°C, pH 7.5, and conductivity 500 μS on a 14/10 light/dark cycle. Fish were fed three times a day alternating dry food and brine shrimps (Zebrafish Management Ltd., Twyford, UK). Embryos were kept in petri dishes in fish water ($NaHCO_3$ 1.2 mM, instant ocean 0.1 g/L, $CaSO_4$ 1.4 mM, methylene blue 0.00002% w/v) at 28°C. For experiments, embryos and juveniles were anesthetized using 0.016% w/v tricaine (3-amino benzoic acidethylester, Sigma-Aldrich, Darmstadt, Germany) in zebrafish water and euthanized by tricaine overdose (0.03% w/v).

The mutant rpl13 CRISPR-Cas9 zebrafish line

To investigate the role of eL13 in skeletal development *in vivo*, a zebrafish model harboring a homozygous mutation in *rpl13*, hereafter called "*rpl13* mutant", was generated. *rpl13* (transcript ID: ENSDART000001168460.2), the ortholog of the human *RPL13*, was targeted by CRISPR-Cas9 gene editing. The guide RNA (gRNA) was designed using the free online software CHOPCHOP (**https://chopchop.rc.fas.harvard.edu**)[34, 35] to target exon 6 (5′-GGCACGGATGCCGAAAAGACGGG-3′). Details on cloning, transcription of gRNA and Cas9, embryo-injection, and mutation screening are described in Supplemental Materials and Methods.

Transcript and protein analysis in the rpl13 mutant zebrafish

To evaluate the expression of *rpl13* at the RNA and protein levels in zebrafish, quantitative PCR (qPCR) and WB were performed. Detailed information about these methods can be found in Supplemental Materials and Methods.

Morphometric analysis of the rpl13 mutant zebrafish

For studying fish morphology, zebrafish embryos at 5 days post fertilization (dpf) (wild-type, WT n = 23, *rpl13* mutant n = 10), at 7 dpf (WT n = 34, *rpl13* mutant n = 47), and juvenile fish at 1 month post fertilization (mpf) (WT n = 37, *rpl13* mutant n = 22) were anesthetized with tricaine and images were acquired with a Leica (Buffalo Grove, IL, USA) M165 FC stereomicroscope connected to a Leica DFC425 C digital camera. The Leica LAS v4.5 software was used to evaluate the standard length (SL), the height at the anterior margin of the anal fin (HAA), the snout-operculum length (SOL), and the height at eye (HE) as previously described.[36, 37] In addition, the level of inflation of the swim bladder was evaluated by counting the numbers of no (0), partially (0.5), or fully (1 or 2) inflated lobes on lateral transmission images at 5 (WT n = 23, *rpl13* mutant n = 10), 7 dpf (WT n = 34, *rpl13* mutant n = 47), and 1 mpf (WT n = 38, *rpl13* mutant n = 22).

Cartilage staining of the rpl13 mutant zebrafish

To investigate cartilage development, after euthanasia, 5 dpf (WT n = 21, *rpl13* mutant n = 9), 7 dpf (WT n = 32, *rpl13* mutant n = 33), and 1 mpf (WT n = 34, *rpl13* mutant n = 20) zebrafish were fixed overnight in 4% (w/v) paraformaldehyde (PFA, Merck KGaA, Darmstadt, Germany) at 4°C and stained in 0.02% (w/v) Alcian blue (Sigma-Aldrich) as previously described.[17] Images were acquired on ventral orientation using M165 FC stereomicroscope (Leica) connected to DFC425C digital camera (Leica). The presence of cartilage deformities was investigated by measuring the following parameters: the angle of the ceratohyal (CH) cartilage, the width of Meckel's cartilage (MK), which is the distance between the two opposite sites of MK, and the distance between the tip of CH and the tip of MK.[38] To investigate body disproportions in the head and body of the fish at 1 mpf, the SL/HAA and SOL/HE ratios were analyzed. Measurements were performed using the LAS v4.5 (Leica) software.

Statistics

Data analyses were performed using two-tailed statistical tests. Results from qPCR and densitometries of WBs are presented as mean ± SD and analyzed using Student's t test. Colocalization analyses in fibroblasts were quantified as Pearson's correlation coefficient from z-stacks of three

samples/donor/staining and analyzed using non-parametric Mann–Whitney *U* test in SPSS (IBM Inc., Armonk, NY, USA) because the data did not fulfill criteria of normal distribution or equal variances. Mann–Whitney *U* test was also used to analyze the data from the protein synthesis assay because the data were not normally distributed. Because of the limited sample size of the control group ($n = 2$) from sucrose profiling, data from mutation-positive cells were compared against the median (0.5205) of the control group using one-sample *t* test. Zebrafish data are presented as following. SL, distance between the tip of CH and the tip of MK, width of MK and CH angle in the fish larvae at 5 and 7 dpf were analyzed by Student's *t* test. Statistics for swim bladder inflation was performed as frequency analysis of number of inflated lobes (0, 0.5, 1, or 2 lobes) using crosstabs with chi-square test. Data concerning SL, distance between the tip of CH and the tip of MK, and width of MK in fish at 1 mpf were divided in categories based on global quartiles and analyzed using chi-square test. The same strategy was applied for analyzing SL/HAA and SOL/HE ratios, where frequencies were analyzed using chi-square test after categorizing based on global quartiles. All data are presented as means/medians with interquartile ranges. A p value <0.05 was considered significant.

Study approval

All studies were conducted in accordance with the Declaration of Helsinki.[39] Research protocols were approved by the Institutional Ethics Committees of the Helsinki University Hospital, the Necker Enfants Malades Hospital in Paris, and the Seoul National University Children's Hospital. A written informed consent was signed by all participants and/or their caregivers before inclusion and sample collection. The zebrafish experiments were performed in agreement with EU Directive 2010/63/EU for animals, and the animal protocol was approved by the Italian Ministry of Health (approval no. 1191-2016-PR).

Results

Similar skeletal features but variable severity in the four index patients

The major skeletal findings in the four index patients with SEMD were very similar, although severity varied significantly. The most striking features included disproportionate short stature and severe delayed ossification at the metaphyseal and epiphyseal sites. All clinical features are summarized in the clinical reports (Supplemental Materials and Methods), in Table **1**, and shown in Fig. **1** and Supplemental Fig. **S1**.

Table 1. Clinical Features of the Four Index Patients With SEMD

	Patient 1	**Patient 2**	**Patient 3**	**Patient 4**
Ethnicity	Finnish	Korean	Korean	French/Congolese
Sex	Male	Female	Male	Male
Age (years)	4.5	4.6	3.4	Deceased at 3
Duration of pregnancy	38 + 1 weeks	40 weeks	37 + 1 weeks	37 weeks
Birth weight	2445 g (−2.3 SD)	NA	NA	NA
Birth length	42 cm (−4.5 SD)	NA	NA	NA
Head circumference at birth	34.8 cm (0 SD)	NA	NA	NA
Height	69.2 cm (−9.4 SD)	84.9 cm (−4.4 SD)	90.5 cm (−7.9 SD)	53 cm (−4 SD)
Facial dysmorphism	Mild	Mild	None	NA

	Patient 1	Patient 2	Patient 3	Patient 4
Chest anomalies	Narrow thorax	Narrow thorax	Pectus excavatum	Narrow thorax
Scoliosis/lordosis	Both	Scoliosis	Scoliosis	Lordosis
Coxa vara/genu valgum	Coxa vara	NA	NA	NA
Hematological/ immunological impairments	No	No	No	No
Cognitive impairment	No	No	No	No
Hearing	Normal	Normal	Normal	Normal
Vision	Normal	Normal	Normal	NA
Dental anomalies	Prenatal hypoplasia and hypomineralization of the enamel; one extra tooth	NA	None	NA
Surgeries	None	None	Yes	None
Main complaints/other features	NA	None	Airway narrowing after general anesthesia	Abnormal sleep

- SEMD = spondyloepimetaphyseal dysplasia; SD = standard deviation; NA = not available.

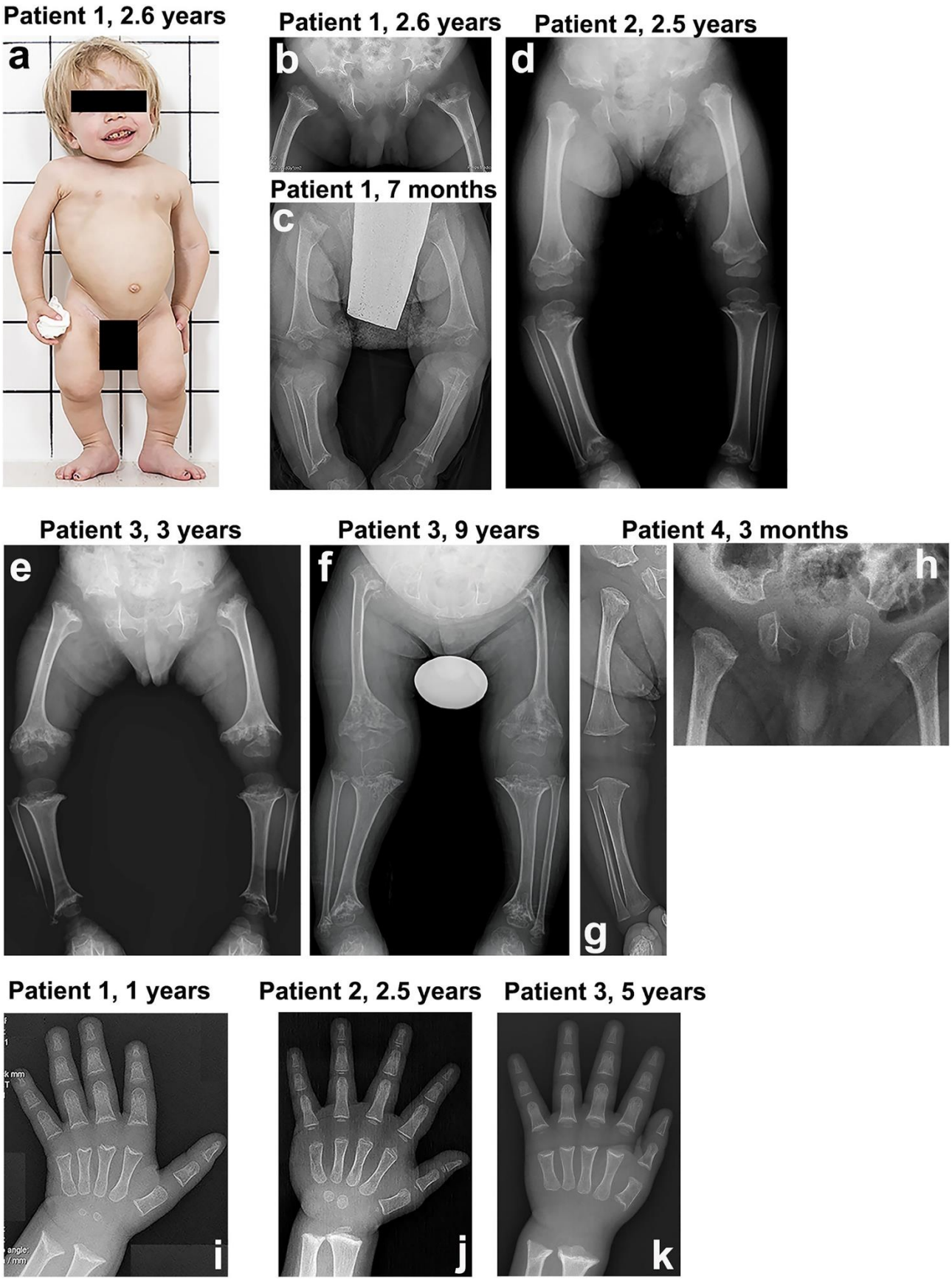

Fig 1. Clinical and radiological features of the four index patients with spondyloepimetaphyseal dysplasia. (*A*) Patient 1 at 2.6 years. The clinical features include mild coarseness of facial features with short nose, depressed

nasal bridge and hypomineralization of the teeth, severe short stature with short neck, trunk, and limbs, narrow thorax, protruding abdomen, and flexion contractures of the hip and knee joints. Pelvis and lower limbs in patient 1 (*B*, *C*), patient 2 (*D*), patient 3 (*E*, *F*), and patient 4 (*G*, *H*). The iliac bones are short and broad with serrated iliac crests. The acetabulae are flat and wide with spur-like projections at the medial and lateral margins. The ischia and pubes are thick with serration at the lateral margin of the ischia. The femora are mildly bowed. The metaphyses of the long bones are wide, cupped, and severely irregular (arrows). The capital femoral epiphyses display significantly delayed ossification, while the other epiphyses of the long bones show normal maturation. The epimetaphyseal changes in patient 3 progressively worsened with age (*E*, *F*). Megaepiphyses are found at the knee and ankle. Wrist and hand in patient 1 (*I*), patient 2 (*J*), and patient 3 (*K*). Metaphyseal cupping and irregularity of the radius and ulna are apparent in patients 1 and 3, while those are mild in patient 2. Metaphyseal cupping and irregularity of the metacarpals and proximal phalanges are also found in patients 1 and 3. Delayed carpal bone age is detected in all three patients, but it is more severe in patients 1 and 3. No carpal ossifications are visible in patient 3 at 5 years. Brachydactyly is not apparent in all.

RPL13 variants underlying SEMD with severe short stature

No variant in any gene listed in the OMIM database and linked to SEMD or other osteochondrodysplasia was identified in patient 1 at the time of analysis. However, two *de novo* candidate variants were identified by WGS: (i) a heterozygous missense mutation in the *UBC* gene, NM_021009.6: c.2045G>A (p.R682K), which is also reported in one subject in the gnomAD database[40] and (ii) a novel heterozygous missense mutation in the *RPL13* gene, NM_000977.3: c.533C>A (p.A178D) (Fig. **2A**). Both mutations lie within the last exon of the respective gene. The first variant affected the gene encoding ubiquitin C, a polyubiquitin precursor. Both SIFT and Polyphen-2 classified this SNV as likely benign. The second variant affected the gene encoding the ribosomal protein eL13. *RPL13* mutations were not linked to any disease at the time of the analysis. However, mutations in genes encoding other RPs or partaking in ribosome biogenesis had been identified in patients with hematological and skeletal impairments.[8, 9, 16] This SNV is absent from the gnomAD database, but another missense variant in the same codon, p.A178V, has been described once. The variant was predicted to be deleterious by most *in silico* programs (Table **2**).

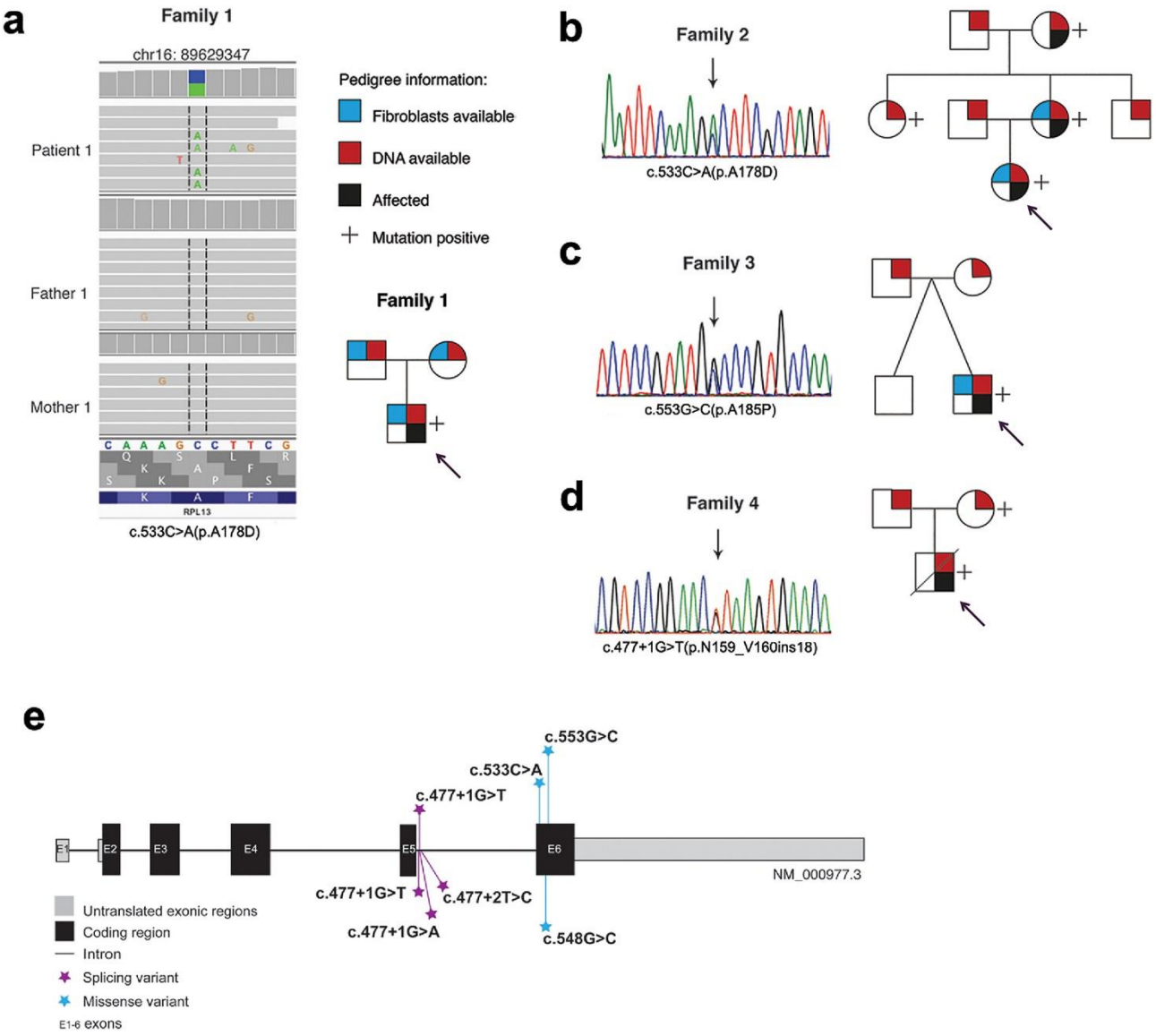

Fig 2. Genetic findings in the *RPL13* gene. Genetic variants and pedigrees of the four families. *RPL13* mutations were identified by WGS in family 1 (*A*), by Sanger sequencing in families 2 and 3 (*B*, *C*), and by WES followed by Sanger sequencing in family 4 (*D*). Schematic illustration of the *RPL13* gene showing all the variants identified in this report (marked above the gene) and previously reported (below the gene) (*E*).

Table 2. Description of the *RPL13* Mutations and Predictions for Their Pathogenicity

	Patient 1	**Patient 2**	**Patient 3**	**Patient 4**
Mutation at the DNA level	c.533C>A[a]	c.533C>A[a]	c.553G>C[a]	c.477 + 1G>T[a]
Mutation at the protein level	p.A178D; missense	p.A178D; missense	p.A185P; missense	p.N159_V160ins18; splice site
Inherited or *de novo*	*De novo*	Inherited from mother; aunt and grandmother share the same mutation	*De novo*	Inherited from mother
GERP score	4.52	4.52	3.56	4.47
CADD score (phred)	23.6	23.6	25.9	23.4
SIFT prediction	Deleterious	Deleterious	Deleterious	NA
Polyphen-2 prediction	Benign	Benign	Probably damaging	NA
PROVEAN	Deleterious	Deleterious	Deleterious	NA
M-CAP	Possibly pathogenic	Possibly pathogenic	Possibly pathogenic	NA

- NA = not available.
- [a] Reference sequence: NM_000977.3.

WES in patient 4 led to the identification of a heterozygous genetic variant located in intron 5 of *RPL13*, c.477+1G>T (Fig. **2D**; Table **2**). This variant, recently reported also by Le Caignec and colleagues, affects the splicing mechanism leading to a longer transcript and a larger protein (p.N159_V160ins18).[7] Patient 4 inherited this variant from his mother.

Considering the *RPL13* variant as the likely candidate for the disease in patients 1 and 4, we sequenced *RPL13* in patients 2 and 3 displaying the same skeletal phenotype. Sanger sequencing revealed a heterozygous *RPL13* mutation in each patient.

Patient 2 had inherited the same missense mutation c.533C>A (p.A178D) as detected in patient 1 from her mother (Fig. **2B**; Table **2**).

Patient 3 had a *de novo* heterozygous missense mutation c.553G>C (p.A185P) located 20 nucleotides downstream of the one identified in patients 1 and 2 (Fig. **2C**; Table **2**). This mutation is absent in gnomAD, but a mutation affecting the same codon, c.554C>T (p.A185V), has been reported five times in this database. All applied prediction programs predicted the p.A185P change to be deleterious (Table **2**).

All the reported variants affect either the splicing donor site of intron 5 or exon 6 of *RPL13* (Fig. **2E**).

Incomplete penetrance and variable clinical expressivity in families 2 and 4

Our genetic analyses showed that patient 2 had inherited the missense mutation c.533C>A (p.A178D) from her mother. Interestingly, in addition to the mother, also the grandmother was found to harbor the same *RPL13* variant (Fig. **2B**). Review of their clinical and radiological data revealed skeletal abnormalities, although remarkably milder than in the index (Supplemental Fig. **S2**). The mother is short (144.5 cm, −3.46 SD), has mild scoliosis, and has undergone surgery to correct pectus excavatum. She has had pain in ankles and hips since childhood and had recently sustained both spine and hip fractures. The grandmother is also short (135.8 cm, −5.6 SD), has had joint pain, especially at the knees, since adolescence, and genua valga. Radiography detected coxa vara in both the mother and grandmother (Supplemental Fig. **S2**), being more severe in the latter. Further, the same *RPL13* variant was also identified in the patient's aunt (157.9 cm, −0.6 SD), who does not show any radiological skeletal abnormalities (Supplemental Fig. **S2**).

In family 4, the clinically unaffected mother of patient 4 was found to harbor the same *RPL13* splice site variant as her child (Fig. **2D**), who had severe SEMD and died during early childhood. The mother's height is 168 cm; no skeletal radiographs were available.

These findings in families 2 and 4 suggest variable disease expressivity in individuals harboring an *RPL13* mutation.

Predicted effects of *RPL13* variants on the protein structure

We set out to interpret the potential consequences of the identified mutations by examining the structure of the eL13 protein in the context of the human ribosome (pdb codes 6EK0 and 4V6X). The eL13 protein binds to the large ribosomal subunit, straddling between 28S rRNA expansion segments ES7L, ES9L, and ES43L and interacting with several ribosomal proteins including eL27, the eL36 N-terminus, and the eL33 C-terminus (Fig. **3A**). The disease-associated missense mutations A178D and A185P map to two highly conserved residues within the C-terminal α-helix of eL13 (high GERP score, Table **2**). Introduction of a charged aspartate residue (p.A178D) is likely to destabilize the eL13 C-terminal α-helix and disrupt the interaction with eL27. Introduction of a proline residue (p.A185P) likely breaks the C-terminal α-helix, disrupting the interactions with the 28S rRNA ES9L. The third intronic mutation (p.N159_V160ins18) is predicted to result in the incorporation of 18 additional residues within an extended loop of eL13 that interacts with ES7L. We concur with Le Caignec and colleagues[7] that this mutation may disrupt the specific interaction between eL13 residue Y161 and ES7L nucleotide A509. All the identified disease mutations are likely to impair the function of eL13 in the ribosome.

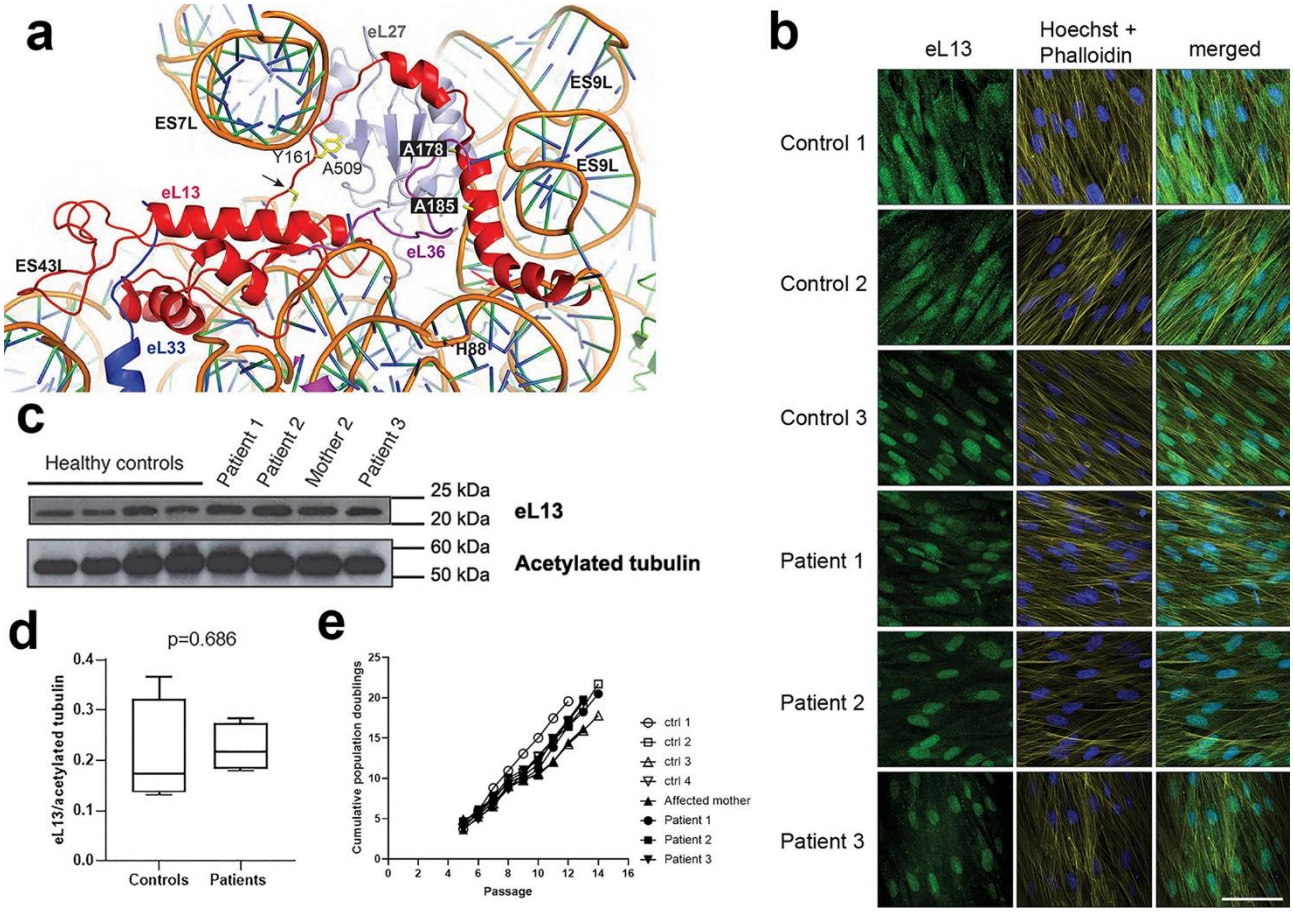

Fig 3. Expression of the eL13 protein in dermal fibroblasts from mutation-positive and control subjects. (*A*) Ribbon representation of eL13 bound to the human 60S subunit (based on pdb code 4V6X). Residues in eL13 targeted by the two missense mutations are highlighted in black boxes. The starting position of the affected region caused by the intronic mutation at N159 (p.N159_V160ins18) (black arrow) and the potentially disrupted interaction between Y161 and nucleotide A509 are highlighted. The start of the frameshift deletion harbored by our zebrafish model, p.L191Afs*32, which occurs at the point where the C-terminal α-helix of eL13 binds to the rRNA, is also marked (red arrow). Ribosomal proteins that interact with eL13 (red) include eL33 (blue), eL36 (purple), or eL27 (gray) are shown. Figure was generated using the PyMOL molecular graphics system, version 2.0.7 (Schrödinger, LLC). (*B*) Representative immunofluorescence images of dermal fibroblasts from patients and healthy controls showing staining for eL13 (column 1), structural dyes Hoechst and Phalloidin (column 2), and merged (column 3). Scale bar = 30 μm. (*C*) Western immunoblotting (WB) demonstrated expression of the eL13 protein in dermal fibroblasts from mutation-positive subjects at similar levels as in fibroblasts from control subjects. Acetylated tubulin was used as a loading control. (*D*) Densitometry analysis of the immunoblot confirmed the lack of significant differences in eL13 expression (mean ± SD, Student's *t* test). (*E*) Dermal fibroblasts from patients and controls showed similar growth kinetics over time in culture. Control 1 = male, age 29 years; control 2 = female age 30 years; control 3 = male age 17 years; control 4 = female age 31 years.

Mutated eL13 is expressed in patient-derived fibroblasts

Since our structural analysis indicated that the *RPL13* mutations are likely to affect eL13, we studied patient-derived fibroblasts to investigate the expression and the subcellular localization of the mutated protein. Immunofluorescence staining demonstrated presence of eL13 in patient-derived cells (Fig. **3B**), with distribution in both the nucleus and the perinuclear area, the latter representing the location of the endoplasmic reticulum (ER). In most samples, eL13 located predominantly to the nucleus. WB revealed no significant differences in protein expression between the control group and the patient group (Fig. **3C, D**). These analyses suggest that the mutated protein is not degraded. Patient-derived fibroblasts displayed similar growth kinetics over time as fibroblasts from controls (Fig. **3E**).

eL13 subcellular localization and colocalization with other RPs

Co-stainings of eL13 with ribosomal protein eL7 and eL28 were conducted to examine assembly of eL13 to large ribosomal subunit (60S); both suggested a similar subcellular location in control and patient cells (Fig. **4A, C**). Colocalization analysis showed a medium agreement in localization between eL13 and eL7 in control (0.48, 0.33–0.54) and patient cells (0.38, 0.30–0.48) with no significant difference ($p = 0.060$) (Fig. **4B**). However, eL28 demonstrated low colocalization with eL13, being significantly lower in patient (0.1, 0.01–0.33) than control cells (0.44, 0.20–0.51, $p < 0.001$) (Fig. **4D**). Co-staining with ribosomal protein S19 was done to investigate if the 60S' harboring mutated eL13 could colocalize with the smaller ribosomal subunit (40S) (Fig. **4E**). A median level colocalization was observed in both control (0.54, 0.33–0.65) and patient cells (0.37, 0.26–0.65) without significant difference ($p = 0.059$) (Fig. **4F**). Calnexin staining was performed to measure ribosomes' localization to ER; co-staining with eL13 showed similar localization in patient (0.56, 0.47–0.66) and control cells (0.54, 0.33–0.70, $p = 0.975$) (Fig. **4G, H**).

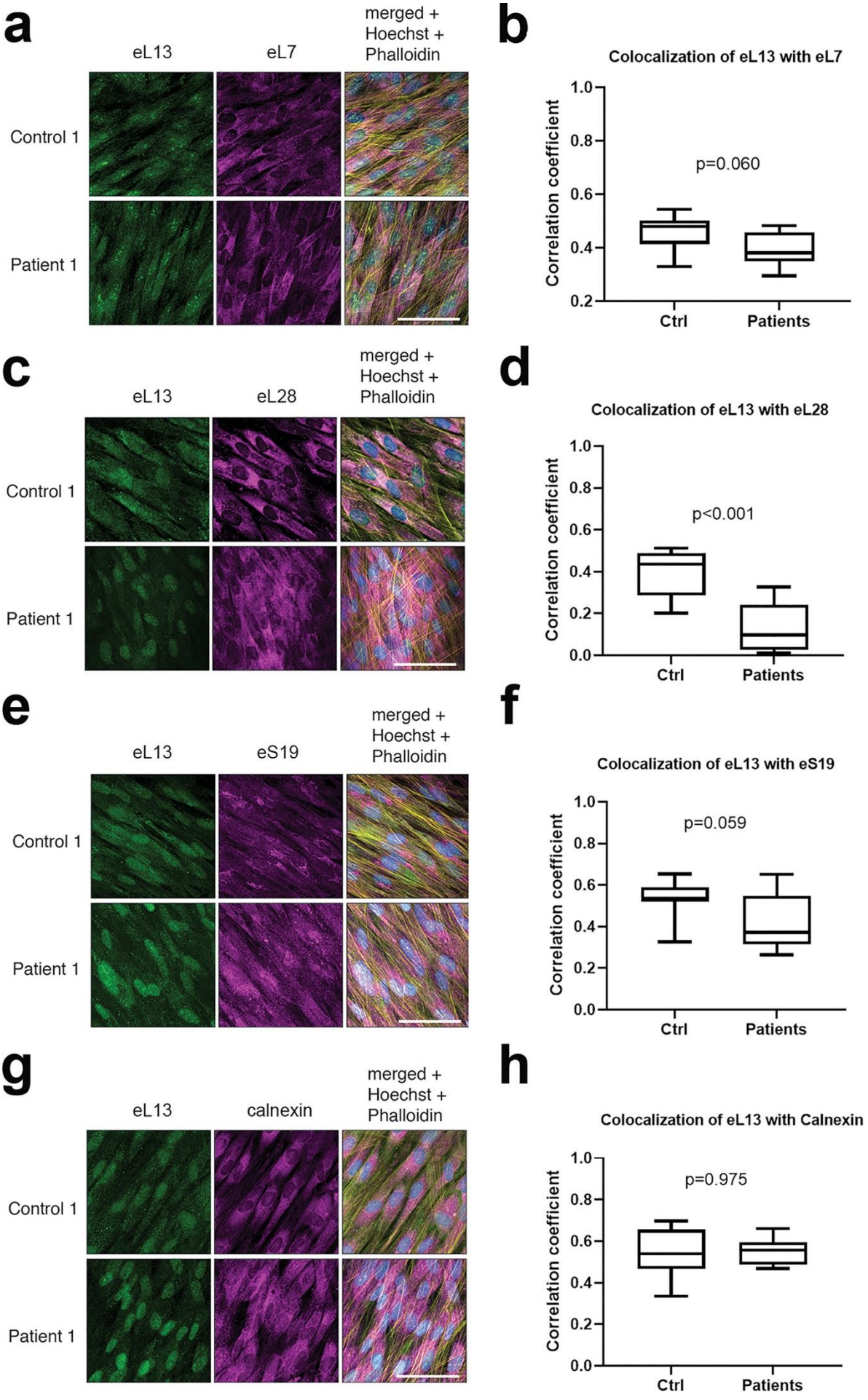
a
eL13
eL7
merged + Hoechst + Phalloidin
Control 1
Patient 1
b
Colocalization of eL13 with eL7
Correlation coefficient
1.0
0.8
0.6
0.4
0.2
p=0.060
Ctrl
Patients
c
eL13
eL28
merged + Hoechst + Phalloidin
Control 1
Patient 1
d
Colocalization of eL13 with eL28
Correlation coefficient
1.0
0.8
0.6
0.4
0.2
0.0
p<0.001
Ctrl
Patients
e
eL13
eS19
merged + Hoechst + Phalloidin
Control 1
Patient 1
f
Colocalization of eL13 with eS19
Correlation coefficient
1.0
0.8
0.6
0.4
0.2
0.0
p=0.059
Ctrl
Patients
g
eL13
calnexin
merged + Hoechst + Phalloidin
Control 1
Patient 1
h
Colocalization of eL13 with Calnexin
Correlation coefficient
1.0
0.8
0.6
0.4
0.2
0.0
p=0.975
Ctrl
Patients

Fig 4. Comparison of colocalization of eL13 with other ribosomal proteins and with ER. Representative immunofluorescence images of dermal fibroblasts from patient 1 and one healthy control showing co-staining of eL13 with eL7 (*A*), eL28 (*C*), eS19 (*E*), and with calnexin as a marker of ER (*G*). Scale bars = 30 μm. 3D colocalization of mutant and WT eL13 with the selected ribosomal markers was analyzed from entire z-stacks of three samples from patients 1 to 3 ($n = 3$) and each healthy control ($n = 3$) using the colocalization test plugin of ImageJ Fiji and is expressed as correlation coefficient (*B*, *D*, *F*, *H*). Box plots with median and range; *p* values from Mann–Whitney *U* test.

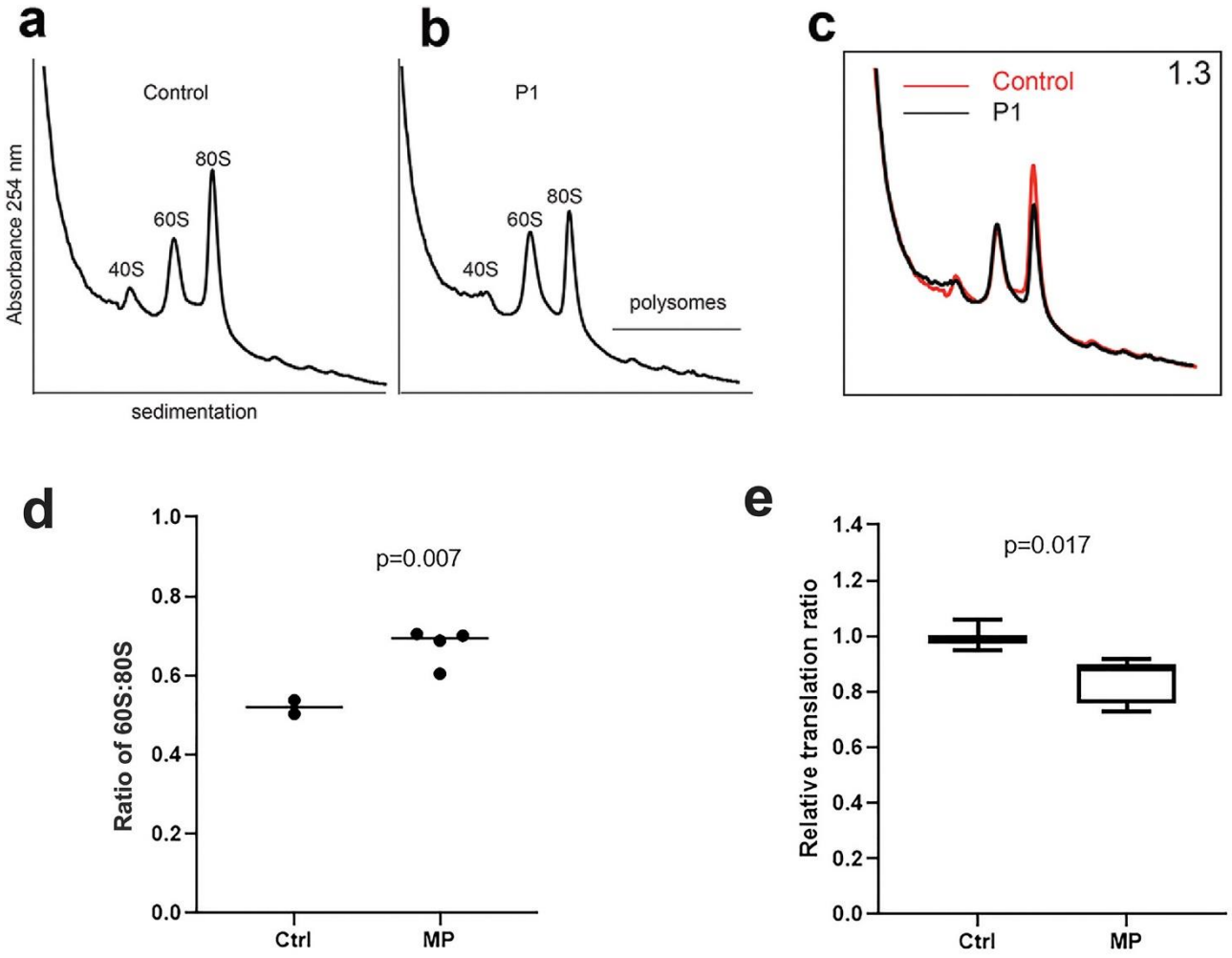

Fig 5. Sucrose profiles and global translation in patients 1, 2, and 3. Comparison of ribosomal fractions from fibroblasts of healthy control parent (*A*) and affected patient 1 (P1) heterozygous for the p.A178D *RPL13* mutation (*B*). (*C*) Overlay of sucrose gradient profiles derived from healthy control parent (red line) and affected individual P1 (black line). Ribosomal subunit ratio (60S:80S) is indicated in the top right corner. (*D*) Box plot showing the results of the 60S:80S from fibroblasts of healthy controls (parents of patient 1) and mutation-positive (MP) subjects (patients 1 to 3 and mother of patient 2), each of whom is heterozygous for an *RPL13* mutation. An increase median value for the 60S:80S ratio is observed in the MP group. The *p* value from one-sample *t* test comparing mutation-positive group against the median of the control samples. (*E*) Relative translation ratio from OP-puro translation assay. Global protein rate is reduced

in the MP subjects (patients 1 to 3 and mother of patient 2) compared with controls ($n = 2$). Data are presented as mean and interquartile range. Experiments were performed twice, in duplicate or triplicate/donor/experiment, and analyzed using Mann–Whitney *U* test.

rpl13$^{L191Afs/L191Afs}$ zebrafish features skeletal abnormalities

Homozygous *rpl13* mutant fish harbored a seven-nucleotide deletion, c.571_577delCTTTTCG, responsible for a frameshift predicted to alter the amino acid sequence and to elongate the C-terminal end of the protein by 11 amino acids, L191Afs*32 (Fig. **6A**). The mutation occurs at the site where the C-terminal α-helix of eL13 binds to the rRNA (Fig. **3A**). The terms "*rpl13* mutant fish" and "*rpl13*$^{L191Afs/L191Afs}$" are used for the fish harboring the homozygous p.L191Afs*32 change.

qPCR analysis revealed a partial activation of nonsense-mediated mRNA decay, with 62% reduction of *rpl13* expression in mutant compared with WT ($p = 0.02$) (Fig. **6B**). The mutant eL13 protein is translated in *rpl13*$^{L191Afs/L191Afs}$ fish but with a 14% reduced level compared with WT ($p = 0.006$) (Fig. **6C**).

Mendelian ratios at 5 dpf, 7 dpf, and 1 mpf indicate that there is no significantly reduced viability of homozygous *rpl13* mutant zebrafish at these stages. Homozygous *rpl13* mutant fish presented with cranial cartilage deformities. At 5 dpf, the CH was significantly wider in mutant embryos (Fig. **6D-E**) and at 7 dpf the distance between the tip of CH and the tip of MK was reduced (Fig. **6D, F**). At 1 mpf, homozygous *rpl13* mutants showed both a reduced distance between the tip of CH and the tip of MK (Fig. **6G**) and a narrower MK compared with WT (Fig. **6H**), indicating craniofacial developmental defects. Compared with WT fish, a significant difference in standard length distribution (Fig. **6I**), a significant increase in the SL/HAA ratio (Fig. **6J**), and a normal SOL/HE ratio were detected in *rpl13*$^{L191Afs/L191Afs}$ at 1 mpf, thus supporting the presence of body disproportions.

Finally, *rpl13*$^{L191Afs/L191Afs}$ embryos showed a significant delay in swim bladder inflation at both 5 and 7 dpf compared with WT (Fig. **6K**). This feature was rescued at 1 mpf.

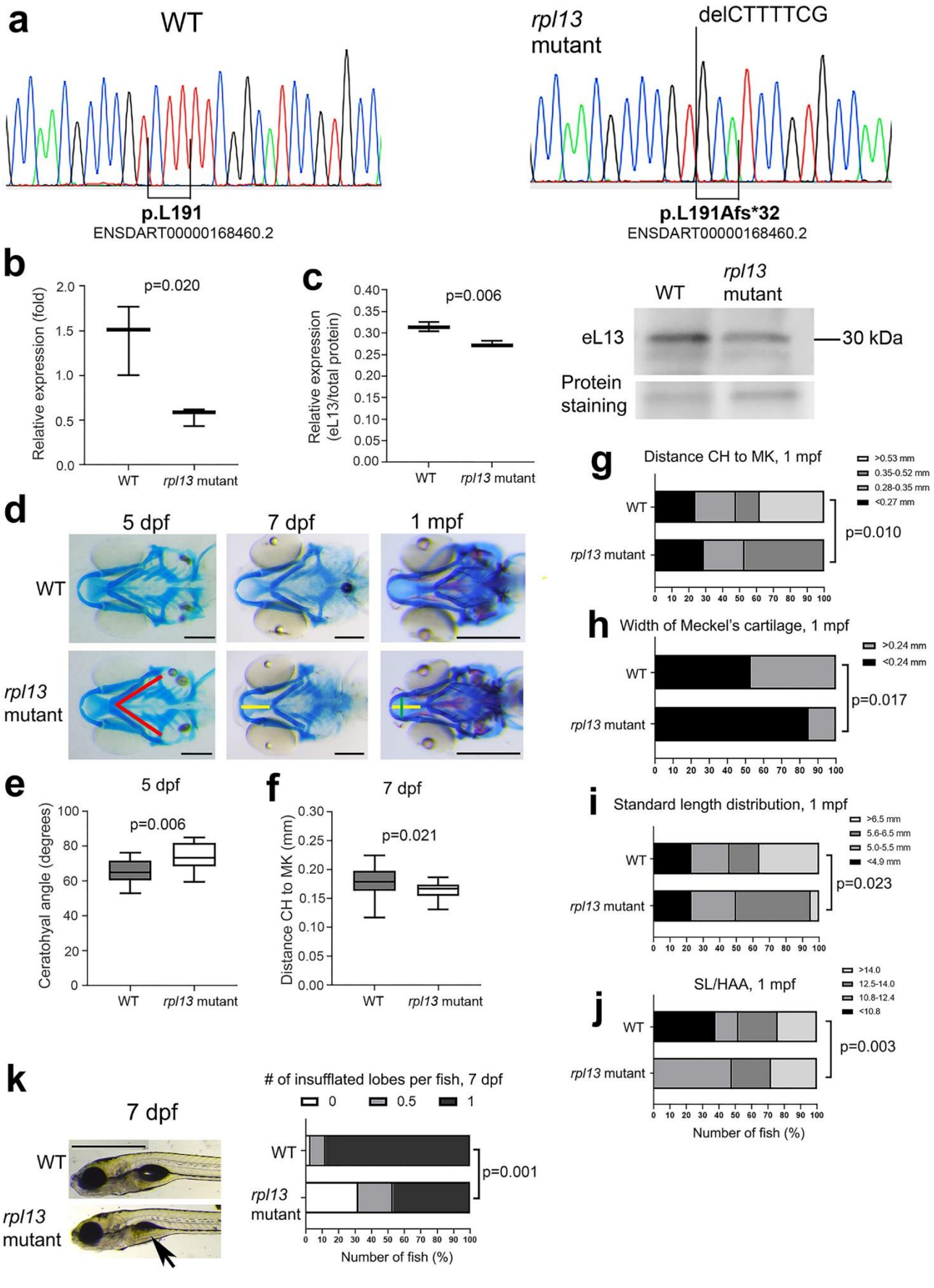
a
WT
rpl13 mutant
delCTTTTCG
p.L191
ENSDART00000168460.2
p.L191Afs*32
ENSDART00000168460.2
b
p=0.020
Relative expression (fold)
WT
rpl13 mutant
c
p=0.006
Relative expression (eL13/total protein)
WT
rpl13 mutant
WT
rpl13 mutant
eL13
30 kDa
Protein staining
d
5 dpf
7 dpf
1 mpf
WT
rpl13 mutant
e
5 dpf
p=0.006
Ceratohyal angle (degrees)
WT
rpl13 mutant
f
7 dpf
p=0.021
Distance CH to MK (mm)
WT
rpl13 mutant
g
Distance CH to MK, 1 mpf
>0.53 mm
0.35-0.52 mm
0.28-0.35 mm
<0.27 mm
WT
rpl13 mutant
p=0.010
h
Width of Meckel's cartilage, 1 mpf
>0.24 mm
<0.24 mm
WT
rpl13 mutant
p=0.017
i
Standard length distribution, 1 mpf
>6.5 mm
5.6-6.5 mm
5.0-5.5 mm
<4.9 mm
WT
rpl13 mutant
p=0.023
j
SL/HAA, 1 mpf
>14.0
12.5-14.0
10.8-12.4
<10.8
WT
rpl13 mutant
p=0.003
Number of fish (%)
k
7 dpf
WT
rpl13 mutant
# of insufflated lobes per fish, 7 dpf
0
0.5
1
WT
rpl13 mutant
p=0.001
Number of fish (%)

Fig 6. Evaluation of the *rpl13*$^{L191Afs/L191Afs}$ zebrafish. (*A*) Sanger sequencing confirmed the genotype of the homozygous *rpl13*$^{L191Afs/L191Afs}$ (*rpl13* mutant) fish. (*B*) qPCR performed on RNA extracted from three WT and three *rpl13*$^{L191Afs/L191Afs}$ reveals a partial activation of nonsense-mediated mRNA decay in mutant zebrafish compared with WT. The *p* value from Student's *t* test. (*C*) WB performed on protein extracts from three WT and three *rpl13*$^{L191Afs/L191Afs}$ fish reveals reduced expression of eL13 in mutant fish compared with WT. The *p* value from Student's *t* test. (*D*) Alcian blue staining of control (WT) and *rpl13*$^{L191Af/L191Afs}$ zebrafish at 5 dpf, 7 dpf, and 1 mpf. Compared with WT, cartilage deformities in the head of the *rpl13*$^{L191Afs/L191Afs}$ are evident. Red lines indicate the ceratohyal (CH) angle, yellow line indicates the distance between the tip of CH and the tip of Meckel's (MK) cartilages, and green line indicates the MK width. Scale bar at 5 and 7 dpf = 200 μm; scale bar at 1 mpf = 500 μm. (*E*) At 5 dpf, *rpl13*$^{L191Af/L191Afs}$ show a significant increase of the CH angle compared with WT and (*F*) at 7 dpf a significant reduction in the distance between the CH and MK cartilages is evident in mutants compared with WT. The *p* values from Student's *t* test. (*G*) At 1 mpf, the frequency of fish with short distance (<0.53 mm) between the CH and MK cartilages and (*H*) the frequency of fish with narrower MK cartilage were significantly higher in mutants compared with WT. The *p* values from chi-square test. (*I*) Standard length (SL) distribution is significantly different in WT compared with *rpl13* mutants at 1 mpf, with a higher number of long fish (>6.5 mm) in the WT population compared with mutants. The *p* value from chi-square test. (*J*) A higher frequency of fish with high SL/HAA (height at anterior margin of anal fin) ratio is found in the mutant group compared with WT group. Morphometric parameters (panels G-J) were categorized by global quartiles, presented as number of fish (%) in each category, and frequencies analyzed by chi-square test. (*K*) Swim bladder inflation in control (WT) and *rpl13*$^{L191Af/L191Afs}$ zebrafish at 7 dpf. Arrows indicate a partially inflated lobe in mutants compared with WT. Scale bar = 1 mm. Quantitative analysis shows a significant delay in the swim bladder inflation of the first lobe in *rpl13*$^{L191Af/L191Afs}$ compared with WT. The *p* values from crosstabs with chi-square test for frequencies.

Discussion

In the present study, we provide significant new data on a novel ribosomopathy with major skeletal involvement and absent extraskeletal manifestations. Our study confirms an association between monoallelic variants in *RPL13* and SEMD in four unrelated families. Moreover, we also describe novel features in SEMD-RPL13 type, including incomplete penetrance and variable clinical expressivity within families harboring the same mutation. Cellular defects in these individuals include a reduction in 80S ribosomes and attenuated global translation. Furthermore, we modeled the human condition in zebrafish.

Only one study has previously reported on *RPL13* mutations in four patients with skeletal dysplasia and negative family history.[7] We here report on four additional families with altogether eight mutation-positive subjects. We identified two novel missense *RPL13* mutations and one previously reported splicing variant. The two missense mutations, p.A178D and p.A185P, affect two residues that map to the C-terminal α-helix of eL13. At the DNA level, both variants affect exon 6. The third mutation, altering the splice donor site in intron 5, leads to partial intron retention, thus generating an elongated protein (p.N159_V160ins18).[7] This mutation has now been reported twice and a different mutation affecting the same nucleotide has been reported once before.[7] Interestingly, all the currently known *RPL13* mutations associated with SEMD cluster within the same region, suggesting that this region is critical for eL13 function, especially in skeletal tissues. According to our *in silico* predictions, the identified mutations are likely to disrupt the interaction of eL13 with either eL27 or the 28S rRNA, thus leading to ribosomal dysfunction. Previous studies have shown that haploinsufficiency of genes encoding other RPs or some ribosomal components lead to ribosomopathies with skeletal involvement.[8, 9] For instance, monoallelic mutations in 19 different RP genes are responsible for Diamond-Blackfan anemia,[41] characterized by congenital erythroid aplasia but also skeletal defects in 40% to 62% of cases.[42, 43]

Our four index patients, all feature a similar phenotype, characterized by short stature and severe skeletal impairments with vertebral abnormalities and delayed ossification at the metaphyseal and epiphyseal sites. Although patient 2 has a milder phenotype, comparable to the recently reported SEMD patients with *RPL13* mutations,[7] patients 1, 3, and 4 feature more severe skeletal changes and are likely to represent the severest end of the disease spectrum. In contrast to other patients with ribosomopathies, our patients did not present any remarkable extraskeletal defects such as hematological or immunological manifestations, which is in line with the recent report by Le Caignec and colleagues. Based on the clinical phenotypes with bone and cartilage tissue specificity, it can be speculated that functional eL13 is of special importance in the growth plate and sites of endochondral

ossification. Production of the unique ECM vital for normal growth plate development poses high translational demands to the chondrocytes of the growth plate,[9, 44] possibly making them more sensitive to changes in protein synthesis than other cell types. This hypothesis is supported by the skeletal phenotypes in ribosomopathies,[8, 9] and recent findings indicating that genes involved in ribosome biogenesis are upregulated in human articular chondrocytes.[45] Moreover, some RPs are also likely to have tissue-specific functions, thus leading to a unique spectrum of manifestations in each ribosomopathy.[46]

This is the first report describing extreme variability in phenotypic expression in individuals with disease-causing *RPL13* variants. In family 2, the index patient is the most severely affected, followed by her grandmother and mother, respectively. On the other hand, the aunt does not present any skeletal impairments despite harboring the same heterozygous *RPL13* mutation. Similarly, the mutation-positive mother in family 4 has no clinical manifestations. Increased expression from the wild-type allele or even monoallelic expression or presence of protective genetic modifiers might impede the disease development in healthy or mildly affected subjects harboring *RPL13* mutations. Since RPs have multiple pseudogenes dispersed throughout the genome,[47] a partially functional *RPL13* pseudogene could also compensate for the activity of the impaired "parental gene". Further, lifestyle factors or even chance could impact disease expression in subjects harboring the mutation. Moreover, it is possible that epimetaphyseal changes ameliorate with increasing age and skeletal maturation. Such observation has been reported in patients with some other osteochondrodysplasias, including spondylometaphyseal dysplasia with "corner fractures" caused by mutations in the fibronectin gene and metaphyseal anadysplasia caused by mutations in metalloproteinases.[48-51] Interestingly, incomplete penetrance and variable expression among patients with identical mutations is a common feature in ribosomopathies,[8] but the underlying mechanisms still remain largely unknown.

When investigating consequences of the *RPL13* mutations in dermal fibroblasts, we identified a significant decrease in colocalization of eL13 with eL28 in patient-derived cells. This might indicate altered assembly and/or function of the 80S, supported by increased 60S:80S ratio and attenuated global translation rates detected in subjects harboring *RPL13* mutations. Because an increased 60S:80S ratio was also detected in a patient with an *RPL13* splice site mutation,[7] we can speculate that both missense and splicing mutations lead to similar outcome. Nevertheless, further studies are needed to confirm this hypothesis. The similar growth kinetic of patient- and control-derived fibroblasts despite the patients being younger (4 to 12 years) than controls (17 to 31 years) could be an indirect indicator of decreased proliferative capacity due to *RPL13* mutations, based on the well-

established age-related decline in cell proliferation[52-54] and the well-known importance of ribosome biogenesis in general cell growth and cell-cycle regulation.[9]

As a further approach to elucidate disease mechanisms, we established an *rpl13* mutant zebrafish model harboring a frameshift deletion. The *rpl13*$^{L191Afs/L191Afs}$ fish partly recapitulated the phenotype of patients with *RPL13* mutations by featuring cartilage deformities both at embryonic and juvenile stage of development. *rpl13* mutants at 1 mpf also show a prevalence of short standard length and an increased SL/HAA ratio compared with WT fish, thus indicating some degree of body disproportion, which is a common feature in SEMD-RPL13 type. In addition, the delay in swim bladder inflation in 5 and 7 dpf homozygous *rpl13*$^{L191Afs/L191Afs}$ larvae suggests possible general developmental delay. Although our zebrafish mutant does not fully reproduce the patients' molecular defects and mutated *rpl13* is expressed at both transcript and protein levels, it is likely that the introduced mutation impairs the structure and function of eL13 by disrupting the binding of the C-terminal α-helix to rRNA. Therefore, our zebrafish model represents a proof-of-principle for the relevant role of eL13 in skeletal development and a valuable tool for further studies at later stages.

Collectively, our findings delineate and expand the SEMD-RPL13 type by reporting novel *RPL13* mutations in subjects with severe skeletal manifestations and by describing large variability in disease severity even within families. Moreover, our *in vitro* experiments provide direct evidence for impaired 60S:80S ratio and attenuated global translation in cells from mutation-positive subjects. Finally, we have established an *rpl13*$^{L191Afs/L191Afs}$ zebrafish model displaying cartilage deformities partly recapitulating the human disease, which provides a model for further studies and deeper understanding of the molecular basis of the disease that could eventually be used for drug testing as well.

Despite a clear association between *RPL13* variants and SEMD, our findings from colocalization studies need to be validated by other methods that allow investigation of protein–protein interactions. Moreover, additional samples and replicates should be analyzed to confirm our results from sucrose profiling. Future studies should explore the molecular mechanisms leading to ribosome dysfunction and the consequent severe, early manifesting skeletal features in our patients and elucidate factors partially or totally preventing disease manifestation in some subjects. Additionally, a characterization of our zebrafish model at an adult stage will potentially further highlight the features common to patients with SEMD-RPL13 type, such as reduced growth.

Our novel findings will be important for genetic counseling in families with *RPL13* mutations and for screening undiagnosed SEMD patients.

Disclosures

All authors state that they have no conflicts of interest.

Acknowledgments

We are grateful to Lindsay Davies for her help with the cell analysis. We also thank the SciLifeLab infrastructure for providing bioinformatics support.

This study was financially supported by the Academy of Finland (277843), the Sigrid Jusélius Foundation, the Folkhälsan Research Foundation, the Novo Nordisk Foundation (21322), the Swedish Research Council (2603, 2013), and the Stockholm County Council to OM. This research was also supported by a grant of the Italian Ministry of Education, University and Research (MIUR) under the initiative “Dipartimenti di Eccellenza (2018–2022)” to AF. The work was also supported by a Specialist Programme from Bloodwise (12048) and the UK Medical Research Council (MC_U105161083) to AJW, a Wellcome Trust strategic award to the Cambridge Institute for Medical Research (100140), a core support grant from the Wellcome Trust and MRC to the Wellcome Trust-Medical Research Council Cambridge Stem Cell Institute and the Cambridge National Institute for Health Research Biomedical Research Centre. JJA is supported by grants from The Finnish Cultural Foundation, HKH Princess Lovisa's foundation for child health care and Sällskapet Barnavård in Stockholm.

Authors’ roles: Study design: AC, JJA, FT, AF, T-JC, and OM. Collection and interpretation of the clinical data of the patients: HV, CH, YS, GN, VC-D, O-HK, T-JC, and OM. Study conduct and data analysis: AC, JJA, FT, CH, ANT, VD, NK, Y-UK, JYB, WYC, CH, ST, YS, TN, AJW, VC-D, AF, T-JC, and OM. Statistical analysis: JJA. Data interpretation: AC, JJA, FT, TN, AF, T-JC, and OM. Drafting manuscript: AC, JJA, FT, AF, and OM. Data collection and manuscript revising: all authors.

Manuscript 1 - References

1. Mortier GR, Cohn DH, Cormier-Daire V, et al. Nosology and classification of genetic skeletal disorders: 2019 revision. *Am J Med Genet A.* 2019; **179**: 2393– 419.

2. Tiller GE, Polumbo PA, Weis MA, et al. Dominant mutations in the type II collagen gene, COL2A1, produce spondyloepimetaphyseal dysplasia. *Strudwick type. Nat Genet.* 1995; **11**: 87– 9.

3. Kennedy AM, Inada M, Krane SM, et al. MMP13 mutation causes spondyloepimetaphyseal dysplasia, Missouri type (SEMDMO). *J Clin Investig.* 2005; **115**: 2832– 42.

4. Nakajima M, Mizumoto S, Miyake N, et al. Mutations in B3GALT6, which encodes a glycosaminoglycan linker region enzyme, cause a spectrum of skeletal and connective tissue disorders. *Am J Hum Genet.* 2013; **92**: 927– 34.

5. Faiyaz ul Haque M, King LM, Krakow D, et al. Mutations in orthologous genes in human spondyloepimetaphyseal dysplasia and the brachymorphic mouse. *Nat Genet.* 1998; **20**: 157– 62.

6. Min BJ, Kim N, Chung T, et al. Whole-exome sequencing identifies mutations of KIF22 in spondyloepimetaphyseal dysplasia with joint laxity, leptodactylic type. *Am J Hum Genet.* 2011; **89**: 760– 6.

7. Le Caignec C, Ory B, Lamoureux F, et al. RPL13 variants cause spondyloepimetaphyseal dysplasia with severe short stature. *Am J Hum Genet.* 2019; **105**: 1040– 7.

8. Mills EW, Green R. Ribosomopathies: there's strength in numbers. *Science.* 2017; 358.

9. Trainor PA, Merrill AE. Ribosome biogenesis in skeletal development and the pathogenesis of skeletal disorders. *Biochim Biophys Acta.* 2014; **1842**: 769– 78.

10. Draptchinskaia N, Gustavsson P, Andersson B, et al. The gene encoding ribosomal protein S19 is mutated in diamond-Blackfan anaemia. *Nat Genet.* 1999. 1999; **21**: 169– 75.

11. Boocock GR, Morrison JA, Popovic M, et al. Mutations in SBDS are associated with Shwachman-diamond syndrome. *Nat Genet.* 2003; **33**: 97– 101.

12. Warren AJ. Molecular basis of the human ribosomopathy Shwachman-diamond syndrome. *Adv Biol Regul.* 2018; **67**: 109– 27.

13. Wise CA, Chiang LC, Paznekas WA, et al. TCOF1 gene encodes a putative nucleolar phosphoprotein that exhibits mutations in Treacher Collins syndrome throughout its coding region. *Proc Natl Acad Sci U S A.* 1997; **94**: 3110– 5.

14. Makitie O, Marttinen E, Kaitila I. Skeletal growth in cartilage-hair hypoplasia. A radiological study of 82 patients. *Pediatr Radiol.* 1992; **22**: 434– 9.

15. Ridanpaa M, van Eenennaam H, Pelin K, et al. Mutations in the RNA component of RNase MRP cause a pleiotropic human disease, cartilage-hair hypoplasia. *Cell.* 2001; **104**: 195– 203.

16. Wang R, Yoshida K, Toki T, et al. Loss of function mutations in RPL27 and RPS27 identified by whole-exome sequencing in diamond-Blackfan anaemia. *Br J Haematol.* 2015; **168**: 854– 64.

17. Gioia R, Tonelli F, Ceppi I, et al. The chaperone activity of 4PBA ameliorates the skeletal phenotype of Chihuahua, a zebrafish model for dominant osteogenesis imperfecta. *Hum Mol Genet.* 2017; **26**: 2897– 911.

18. Fiedler IAK, Schmidt FN, Wolfel EM, et al. Severely impaired bone material quality in Chihuahua zebrafish resembles classical dominant human osteogenesis imperfecta. *J Bone Miner Res.* 2018; **33**: 1489– 99.

19. Gistelinck C, Kwon RY, Malfait F, et al. Zebrafish type I collagen mutants faithfully recapitulate human type I collagenopathies. *Proc Natl Acad Sci U S A.* 2018; **115**: E8037– 46.

20.Witten PE, Harris MP, Huysseune A, Winkler C. Small teleost fish provide new insights into human skeletal diseases. *Methods Cell Biol.* 2017; **138**: 321– 46.

21. Costantini A, Skarp S, Kampe A, et al. Rare copy number variants in Array-based comparative genomic hybridization in early-onset skeletal fragility. *Front Endocrinol (Lausanne).* 2018; **9**: 380.

22. Costantini A, Valta H, Baratang NV, et al. Novel fibronectin mutations and expansion of the phenotype in spondylometaphyseal dysplasia with "corner fractures". *Bone*. 2019; **121**: 163– 71.

23. Lek M, Karczewski KJ, Minikel EV, et al. Analysis of protein-coding genetic variation in 60,706 humans. *Nature.* 2016; **536**: 285– 91.

24. Ameur A, Dahlberg J, Olason P, et al. SweGen: a whole-genome data resource of genetic variability in a cross-section of the Swedish population. *Eur J Hum Genet.* 2017; **25**: 1253– 60.

25. Paila U, Chapman BA, Kirchner R, Quinlan AR. GEMINI: integrative exploration of genetic variation and genome annotations. *PLoS Comput Biol.* 2013; **9**:e1003153.

26. Doyard M, Bacrot S, Huber C, et al. FAM46A mutations are responsible for autosomal recessive osteogenesis imperfecta. *J Med Genet.* 2018; **55**: 278– 84.

27. Natchiar SK, Myasnikov AG, Kratzat H, Hazemann I, Klaholz BP. Visualization of chemical modifications in the human 80S ribosome structure. *Nature.* 2017; **551**: 472– 7.

28. Anger AM, Armache JP, Berninghausen O, et al. Structures of the human and drosophila 80S ribosome. *Nature.* 2013; **497**: 80– 5.

29. Pekkinen M, Terhal PA, Botto LD, et al. Osteoporosis and skeletal dysplasia caused by pathogenic variants in SGMS2. *JCI Insight*. 2019; **4**:e126180.

30. Dunn KW, Kamocka MM, McDonald JH. A practical guide to evaluating colocalization in biological microscopy. *Am J Physiol Cell Physiol.* 2011; **300**: C723– 42.

31. Finch AJ, Hilcenko C, Basse N, et al. Uncoupling of GTP hydrolysis from eIF6 release on the ribosome causes Shwachman-diamond syndrome. *Genes Dev.* 2011; **25**: 917– 29.

32. Wong CC, Traynor D, Basse N, Kay RR, Warren AJ. Defective ribosome assembly in Shwachman-diamond syndrome. *Blood.* 2011; **118**: 4305– 12.

33. Tan S, Kermasson L, Hoslin A, et al. EFL1 mutations impair eIF6 release to cause Shwachman-diamond syndrome. *Blood.* 2019; **134**: 277– 90.

34. Montague TG, Cruz JM, Gagnon JA, Church GM, Valen E. CHOPCHOP: a CRISPR/Cas9 and TALEN web tool for genome editing. *Nucleic Acids Res.* 2014; **42**: W401– 7.

35. Labun K, Montague TG, Gagnon JA, Thyme SB, Valen E. CHOPCHOP v2: a web tool for the next generation of CRISPR genome engineering. *Nucleic Acids Res.* 2016; **44**: W272– 6.

36. Tonelli F, Cotti S, Leoni L, et al. Crtap and p3h1 knock out zebrafish support defective collagen chaperoning as the cause of their osteogenesis imperfecta phenotype. *Matrix Biol.* 2020; **90**: 40– 60.

37. Parichy DM, Elizondo MR, Mills MG, Gordon TN, Engeszer RE. Normal table of postembryonic zebrafish development: staging by externally visible anatomy of the living fish. *Dev Dynam.* 2009; **238**: 2975– 3015.

38. Kimmel CB, Miller CT, Moens CB. Specification and morphogenesis of the zebrafish larval head skeleton. *Dev Biol.* 2001; **233**: 239– 57.

39. World Medical A. World Medical Association Declaration of Helsinki: ethical principles for medical research involving human subjects. *JAMA.* 2013; **310**: 2191– 4.

40. Karczewski KJ, Francioli LC, Tiao G, et al. The mutational constraint spectrum quantified from variation in 141,456 humans. 2020; **581**: 434– 43.

41. Ulirsch JC, Verboon JM, Kazerounian S, et al. The genetic landscape of Diamond-Blackfan anemia. *Am J Hum Genet.* 2018; **103**: 930– 47.

42. Lipton JM, Ellis SR. Diamond-Blackfan anemia: diagnosis, treatment, and molecular pathogenesis. *Hematol Oncol Clin North Am.* 2009; **23**: 261– 82.

43. Boria I, Garelli E, Gazda HT, et al. The ribosomal basis of Diamond-Blackfan anemia: mutation and database update. *Hum Mutat.* 2010; **31**: 1269– 79.

44. Baron J, Savendahl L, De Luca F, et al. Short and tall stature: a new paradigm emerges. *Nat Rev Endocrinol.* 2015; **11**: 735– 46.

45. Ferguson GB, Van Handel B, Bay M, et al. Mapping molecular landmarks of human skeletal ontogeny and pluripotent stem cell-derived articular chondrocytes. *Nat Commun.* 2018; **9**:3634.

46. Kondrashov N, Pusic A, Stumpf CR, et al. Ribosome-mediated specificity in Hox mRNA translation and vertebrate tissue patterning. *Cell.* 2011; **145**: 383– 97.

47. Zhang Z, Harrison P, Gerstein M. Identification and analysis of over 2000 ribosomal protein pseudogenes in the human genome. *Genome Res.* 2002; **12**: 1466– 82.

48. Cadoff EB, Sheffer R, Wientroub S, Ovadia D, Meiner V, Schwarzbauer JE. Mechanistic insights into the cellular effects of a novel FN1 variant associated with a spondylometaphyseal dysplasia. *Clin Genet.* 2018; **94**: 429– 37.

49. Costantini A, Valta H, Baratang NV, et al. Novel fibronectin mutations and expansion of the phenotype in spondylometaphyseal dysplasia with "corner fractures". *Bone.* 2019; **121**: 163– 71.

50. Lausch E, Keppler R, Hilbert K, et al. Mutations in MMP9 and MMP13 determine the mode of inheritance and the clinical spectrum of metaphyseal anadysplasia. *Am J Hum Genet.* 2009; **85**: 168– 78.

51. Sharony R, Borochowitz Z, Cohen L, et al. Prenatal course of metaphyseal anadysplasia associated with homozygous mutation in MMP9 identified by exome sequencing. *Clin Genet.* 2017; **92**: 645– 8.

52. Schneider EL. Aging and cultured human skin fibroblasts. *J Invest Dermatol.* 1979; **73**: 15– 8.

53. Lago JC, Puzzi MB. The effect of aging in primary human dermal fibroblasts. *PloS One.* 2019; **14**:e0219165.

54. Glowacki J, Alm JJ, Zhou S. Clinical variables that influence properties of human mesenchymal stromal cells. *Regenerat Eng Transl Med.* Epub 2019 Sep 12. https://doi.org/10.1007/s40883-019-00123-4.

Supplemental Materials and Methods

Novel *RPL13* variants and variable clinical expressivity in a human ribosomopathy with spondyloepimetaphyseal dysplasia

1. Clinical reports

In Family 1, the index patient (patient 1), presently a 4.5-year-old boy, was evaluated for disproportionate short stature and severe skeletal impairments (Figs. 1 and 2). He is the only child of healthy unrelated Finnish parents. His growth retardation was noted already during pregnancy (Supplemental Table S1). Karyotype, plasma amino acids, urine organic acids, glycosaminoglycans and oligosaccharides, as well as heart and abdominal ultrasounds were all normal. At 6 months, radiographs of the spine and long bones indicated skeletal dysplasia: he had abnormal pelvis, bilateral coxa vara, short long bones with broad and flared metaphyseal areas and abnormal epiphyses. He walked independently by 2.1 years and at 3 years bracing treatment was initiated for early-onset scoliosis. At 4.5 years the patient has severe disproportionate short stature (height -9.4 SD) with large head relative to his small and slim body (Fig. 1). He has mild facial coarseness, low nasal bridge, and hypoplastic primary teeth with hypomineralization. Hearing, vision and mental development are normal. Total blood count, immunoglobulins, infection rate, and kidney and liver functions are also

normal. In Family 2, the presently 4.6-year-old girl (patient 2), was clinically investigated for short stature and spinal deformity. She is the only child of healthy unrelated Korean parents. She started walking independently at 16 months. At 2.6 years she was hospitalized due to pneumonia. A skeletal dysplasia was suspected, and she was referred to a tertiary pediatric center where scoliosis and coxa vara were detected (Fig. 1; Supplemental Figure S1) but no laboratory abnormalities were noted. Her height was -4.4 SD. Radiographs showed abnormal skeletal changes in the pelvis and tubular bones; hand radiographs showed delayed carpal ossification. She also had a short and abnormal thorax, scoliosis and spinal irregularities. Her liver, spleen and kidneys were of normal size and heart function was normal. The total blood count, renal function, liver enzymes, thyroid hormones and serum IGF-1 and IGFBP-3 were normal. Family 3 is of Korean origin and the index patient (patient 3) was investigated at age 3.4 years because of short stature, protruded abdomen, and spine curvature. He was one of dizygotic twins, the twin sister being healthy, conceived by *in vitro* fertilization between the healthy parents; there was no parental consanguinity. At age 4 months he had severe bronchiolitis requiring ventilator care. Motor development was delayed with independent walking at 20 months.

He showed marked bilateral genu varum, lumbar lordosis, protruded abdomen, and pectus excavatum. Ligamentous laxity (Beighton score 9) was noted. Skeletal survey further showed scoliosis, spinal changes, and abnormalities in his chest and lower limbs, with most striking abnormalities at the metaphyses (Fig. 1; Supplemental Figure S1); scoliosis necessitated spinal fusion at 6.4 years. At 9.5 years his height was 90.5 cm (-7.9 SD). He underwent femoral osteotomy to correct progressive coxa vara. Postoperatively he developed progressive dyspnea and was found to have grade III subglottic stenosis, which persisted despite several trials of dilatation. In Family 4, the index patient (patient 4) is the third child of healthy unrelated parents. The mother originates from France and Belgium and the father from Congo. Polyhydramnios was noted at 30 weeks of gestation. He was first investigated for respiratory distress related to narrow thorax. Sleep study was abnormal with numerous obstructive episodes together with bradycardia. By 2 months he developed disproportionate short stature (-4.0 SD). Karyotype, plasma amino acids, urine organic acids, as well as heart and abdominal ultrasounds were all normal. Radiographs of long bones (Fig. 1) and spine (Supplemental Figure S1) showed metaphyseal flaring and epiphyseal delay, short ribs and severe spinal anomalies with major platyspondyly. At 14 months of age, severe growth retardation persisted (-6.0 SD). He started walking independently at 22 months of age. Narrow thorax, lumbar lordosis, and protruding abdomen were observed. Audiometry and cognitive development were normal. He died at 3 years of age due to respiratory insufficiency.

2. Supplemental figures

Supplemental Figure S1. Patients' radiographs of the thorax and spine. Thorax and spine radiographs of patient 1 (a, b), patient 2 (c, d), patient 3 (e, f) and patient 4 (g, h). The thorax appears short and broad with cupped and flared anterior ends of the ribs. The vertebral bodies show ventral biconvexity and dorsal constriction. Thoracolumbar scoliosis is evident in patients 2 and 3.

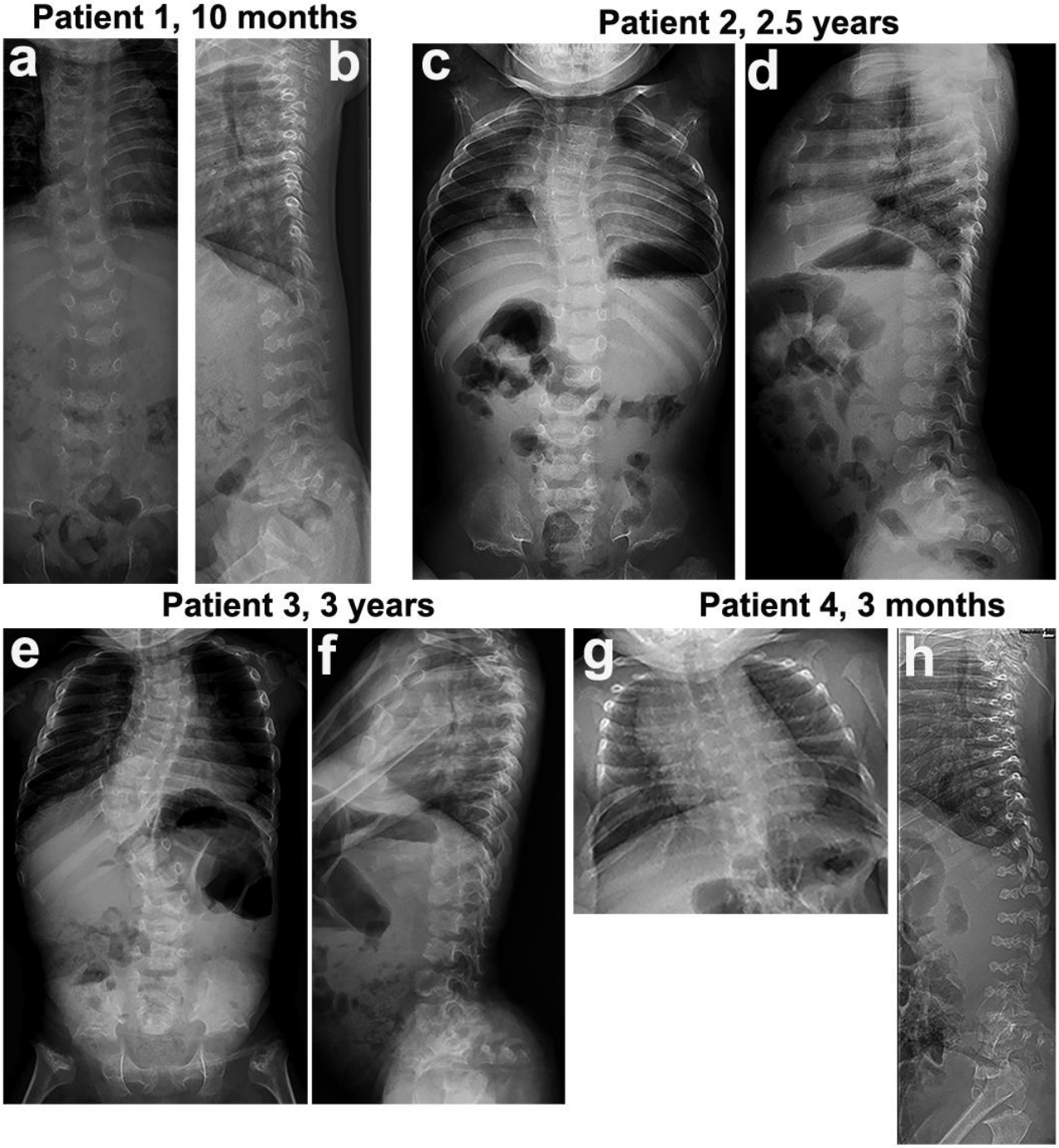

Supplemental Figure S2. Radiographs of the mutation positive members in Family 2. In Family 2 only the index patient (Fig. 1d) showed severe skeletal dysplasia while the other mutation-positive family members show mild to normal radiological findings. Radiographs of the mother at 23 years (Left panel), the maternal grandmother at 49 years (Central panel) and the aunt at 25 years (Right panel). The mother has mild scoliosis (a-c), significant endplate irregularity in the thoracic spine and short ribs. The grandmother has reduced vertebral height and abnormal vertebral shape with depressed middle parts (g-i). Both the mother (e, f) and the grandmother (k, l) have coxa vara deformity and significant degenerative changes at the proximal hip and to lesser degree in the knees. The hand radiographs (d, j) do not show major abnormalities apart from degenerative changes in the wrist in the grandmother (j). No abnormal skeletal features are detected in the aunt (m-r).

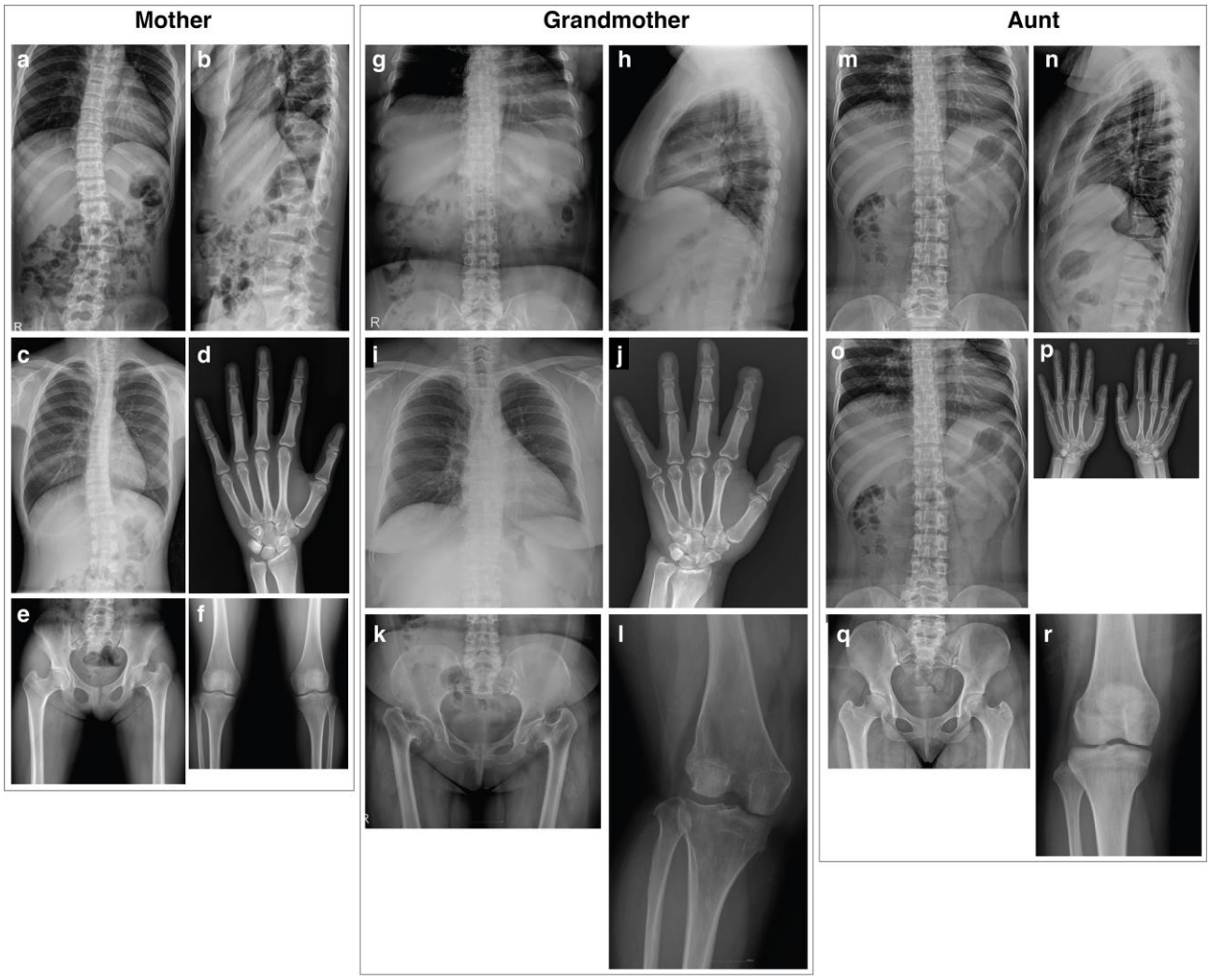

3. Supplemental notes on the methods

Whole-genome and whole-exome sequencing

For whole-genome sequencing, genomic DNA was extracted from blood according to standard procedures. Library preparation was carried out at the Science for Life Laboratory (SciLifeLab) using the Illumina TruSeq PCR-Free method. Pair-end sequencing (2 x 150 base-pair) was performed on the Illumina HiSeq X instrument at an average autosomal coverage of 30X at the same facility. Read alignment, quality control, variant calling and variant annotation were performed using our previously described in-house pipeline (1,2). Exome capture was carried out at the genomic platform of the IMAGINE Institute (Paris, France) with the SureSelect Human All Exon kit (Agilent Technologies). Agilent SureSelect Human All Exon (V4) libraries were prepared from 3 μg of genomic DNA sheared with Ultrasonicator (Covaris) as recommended by the manufacturer. Barcoded exome libraries were pooled and sequenced using HiSep2500 (Illumina) generating paired-end reads. Read alignment, quality control, variant calling and variant annotation were performed as previously described (3).

Dermal fibroblasts culture

For isolation of patient- and control-derived dermal fibroblasts, skin biopsies were collected and transported in sterile complete culture medium (DMEM supplemented with 20% fetal bovine serum (FBS) and antibiotics (50 IU/ml penicillin, 50 μg/ml streptomycin). The biopsies were minced into smaller fragments in sterile phosphate buffered saline (PBS), samples were treated with 1000 U/ml Collagenase Type II (Clostridium histolyticum, Gibco) in Mg- and Ca-free PBS for 2h at 37 °C. Following inactivation of collagenase with ice-cold culture media and vigorous vortexing, tissue lysates were centrifuged at 150 x g for 10 min at 4 °C. Cell pellets were re-suspended in complete media, seeded in tissue culture flasks and incubated at 37 °C in a 5% CO2 humidified incubator. Non-adherent cells were discarded after 2-3 days, and after 1-2 weeks cells were trypsinized for further expansion. Cells were expanded by seeding at 7 000-10 000 cells/cm2 in high glucose DMEM (Thermo Scientific Cat. #11960044) supplemented with 1% GlutaMAX™ (Thermo Scientific Cat. #35050038) and antibiotics. For the first 3-4 passages, 20% FBS was used, thereafter 15%. Media was changed every 3-4 days, and cells were splitted upon 80% confluence. Cells of passage 3-6 were used for characterization assays. For monitoring the *in vitro* proliferative capacity, fibroblasts were expanded under same conditions up to passage 15 and population doublings (PDs) at each passage was calculated as *log N/log 2*, where *N* is the number of cells yielded at trypsinization divided by the number of cells seeded. Growth kinetics through several passages was expressed by calculating cumulative PDs.

Western immunoblotting

Briefly, denatured protein samples were separated on 10% SDS-Page gel followed by wet transfer to a PVDF membrane. After blocking (5% non-fat milk in 1xTBST at room temperature (RT) for 1-2 hours), membrane was incubated with primary antibody in 5% nonfat milk-TBST at 4°C overnight (o/n). Membrane was washed 3 x 15 minutes in 1xTBST before incubation with secondary antibody in blocking solution for 1h at RT. After washing 3 x 15 minutes in 1xTBST, membrane was incubated for 3-5 minutes in Bio-Rad's Clarity ECL developing mixture, wrapped in plastic film and developed on photo paper. Protein expression was analyzed semi-quantitatively by densitometry of captured gel images using Fiji.

Immunocytochemistry

Dermal fibroblasts were cultured on glass coverslips, fixed in 4% paraformaldehyde for 15 minutes and washed in PBS. Following permeabilization in 0.1% triton-X in PBS for 15 minutes at RT and washing in PBS, samples were blocked in 0.1% BSA in PBS at RT for 2 hours. The primary antibodies were diluted in 0.1% BSA and added to the samples for overnight incubation at 4°C. After washing in PBS five times, samples were incubated with secondary antibodies (in 0.1% BSA) at 4°C overnight in the dark, followed by three washes in PBS and one in distilled water. Coverslips were mounted onto glass microscope slides using ProLong Diamond mounting medium (Thermofisher Scientific, #P36961) and left to set overnight at RT in the dark. Hoechst and pahlloidin staining were used as structural dyes. A list of primary and secondary antibodies used is found in Supplemental Table 1.

Sucrose density gradients

Briefly, fibroblasts (60% - 80% confluence) were treated with cyclohexamide (CHX) at final concentration of 100 μg/ml for 15 min at 37 °C before harvesting. After washing in cold PBS (with CHX, 100 µg/ml) cells were lysed in lysis buffer (20 mM HEPES at pH 7.4, 50 mM KCl, 5 mM Mg(OAC)2, 0.5 % [v/v] IGEPAL® CA-630 (Sigma), 0.5 % [w/v] deoxycholate (Sigma), 100 μg/mL cycloheximide (Sigma) with complete EDTA-free protease inhibitors (Roche) and 500 U/mL RNase inhibitor (RNaseOUTTM, Invitrogen). After incubating 15 min on ice, cell lysates were cleared in a microfuge at 20,000 g for 10 min at 4 °C. Equal amounts (typically 1.0 A254 nm unit) of sample were loaded onto 5 % – 45 % (w/v) sucrose gradients in 14 mL of gradient buffer (20 mM HEPES pH 7.4, 50 mM KCl, 5 mM Mg(OAC)2, 100 µg/ml CHX) with complete EDTA-free protease inhibitors (Roche) and centrifuged (Beckmann SW40 rotor at 284,600 g for 2.5 hr at 4°C). Sucrose gradients were prepared using a Biocomp Gradient Master according to the manufacture's manual. Samples

were unloaded using a Brandel gradient fractionator and the polysome profiles detected using an ÄKTAprime Plus system (GE Healthcare).

Measurement of protein synthesis

OP-Puro (Invitrogen; final concentration 50 μM) was added to the culture medium (Dulbecco's Modified Eagle Medium (DMEM, GibcoTM GlutaMAXTM), 10 % fetal bovine serum (Sigma) and 1 % Penicillin- Streptomycin (Pen-Strep, Sigma)) for 60 min. Cells were removed from wells and washed twice in ice-cold PBS with 100 μg/ml cycloheximide. Cells were fixed and permeabilized using the Cytofix/Cytoperm Fixation Permeabilization Kit (BD Biosciences). Azide-alkyne cycloaddition was performed using the Click-iT Cell Reaction Buffer Kit (Invitrogen) with azide conjugated to Alexa Fluor 488 at 5 μM final concentration. Following the 30 min reaction, cells were washed twice in PBS and then resuspended in PBS supplemented with 2% fetal bovine serum and analyzed by flow cytometry (Becton Dickinson LSR Fortessa analyzer). Flow cytometry data analysis was performed using FlowJo v10.1 (FlowJo, Ashland, OR). Relative rate of protein synthesis was calculated by normalizing OP-Puro signals to control cells after subtracting background fluorescence (cells without OP-Puro incorporation).

Generation of the *rpl13* mutant CRISPR-Cas9 zebrafish model

The synthesis of the specific oligonucleotides (Eurofins Genomics, Vimodrone, Italy) and the preparation of gRNA were carried out as previously described (4). The gRNA template, upon subcloning in the pT7-gRNA plasmid (Addgene), was in vitro transcribed using MEGAshortscript T7 kit (Invitrogen) and purified with mirVana miRNA Isolation Kit (Invitrogen). The size and quality of the resulting gRNA were confirmed by electrophoresis on a 10% (v/v) polyacrylamide-urea-SDS gel. For the Cas9 mRNA *in vitro* transcription, the pT3TS-nCas9n vector (Addgene, #46757) was linearized by XbaI (New England BioLabs, Ipswich, Massachusetts, USA) digestion and purified using the Nucleospin Gel and PCR Clean-up Kit (Macherey-Nagel, Düren, Germany). DNA was transcribed using mMESSAGE mMACHINE T3 Kit (Invitrogen, Carlsbad, California, USA). mRNA polyadenylation was performed using the Poly(A) Tailing Kit (Ambion, Waltham, Massachusetts, USA) and the Cas9 transcript was purified by RNeasy Mini Kit (Qiagen, Hilden, Germany)(4). The mRNA quality was checked by electrophoresis on 1% (w/v) formaldehyde agarose gel. The gRNA (12.5 ng/μL) and Cas9 mRNA (300 ng/μL) were mixed in Danieau solution (58 mM NaCl, 0.7 mM KCl, 0.4 mM MgSO4, 0.6 mM Ca(NO3)2, 5 mM Hepes, pH 7.6) with a tracer dye (0.5 mg/mL, dextran conjugated with tetramethylrhodamine, Molecular Probes, Carlsbad, California, USA) in a final volume of 5 μL and pre-heated at 60°C for 10 min. Microinjection was carried out using an

InjectMan micromanipulator (Eppendorf, Hamburg, Germany) assembled on a Leica M165 FC stereomicroscope. Injection pressure and time were modulated to calibrate the injected volume, ranging from 2 to 4 nL per embryo. Mosaic fish were screened by T7 endonuclease assay, briefly after 24 hours the DNA from single injected embryos was extracted by proteinase K digestion (2.5 mg/mL, Sigma Aldrich, Darmstadt, Germany) in lysis buffer (100 mM Tris HCl, pH 8.5, 5 mM EDTA, 0.2% (w/v) SDS, 200 mM NaCl) o/n at 55°C, followed by isopropanol precipitation and resuspension in 20 mM Tris-HCl, 1 mM EDTA, pH 8.0. DNA was PCR amplified using the following primers: *rpl13* sense 5'-GTGTACATGCATTGTCGTTGACT-3' and reverse 5'-GATTCCAGGAAAGCAGAATTTTT-3' spanning the target sequence. The PCR amplicon (10 μL) underwent a denaturing/annealing cycle consisting of 5 min at 94°C, followed by cooling to 85°C, at −2°C per sec and further to 25°C, at −0.1°C per sec, and was finally digested with 0.2 U/μL T7 endonuclease I (New England BioLabs) at 37°C for 1 h. The sample was run on 8% (v/v) polyacrylamide gel. The targeting was then confirmed by Sanger Sequencing. The mutation allele in heterozygous (*rpl13+/ L191Lfs*) and homozygous (*rpl13L191Lfs/L191Lfs*) zebrafish was determined by DNA extraction from tail clip of adult zebrafish, followed by Sanger sequencing.

Quantitative PCR (qPCR) and Western immunoblotting (WB) in zebrafish

RNA was extracted from adult WT and *rpl13L191Lfs/ L191Lfs* skin (n=3 per genotype) using Qiazol (Qiagen) following manufacturer's instructions. RNA quantity was determined by NanoDrop spectrophotometer and RNA quality by agarose gel electrophoresis. cDNA was synthesized using the High Capacity cDNA Transcription kit (Applied Biosystems) according to manufacturer's protocol in a final volume of 20 μL. qPCR for *rpl13* and *dna15ta1* was performed in 25 μL reaction mixtures with 12.5 μL SYBR Green Master mix (Applied Biosystems) using the QuantStudio 3 thermocycler and the QuantStudio Design & analysis software (Applied Biosystems). The following primers were used: for *rpl13* forward, 5'-GGACCAGTCATGCCCATCAA-3' (nt 466-485) and reverse, 5'-TTCTTCTCGACGTCCTGCTC-3' and for *dna15ta1* forward, 5'-TACTGTGCTCAAATTGCTTCA-3' and reverse, 5'-AATGAGTACTGTGAACTTAATCCAT-3'. The annealing temperature was 60 °C and samples were run in triplicate. ΔΔCt was used for quantitation. Protein extract was obtained from adult WT and *rpl13L191Lfs/ L191Lfs* soft tissue (n=3 per genotype) as described in the paper by Tonelli et al.(36). For each sample 30 μg were run on 4-20% Mini-PROTEAN TGX Gel (Bio-Rad). Expression of eL13 was evaluated by WB using a primary antibody against eL13 (RPL13 Polyclonal Antibody, Invitrogen, #PA5-41715, 1:500 dilution) and a HRP-conjugated anti-rabbit secondary antibody (Anti-rabbit IgG, Cell Signaling, #7074S 1:10000 dilution) according to standard procedures. The signal was detected by Westar

Supernova ECL western reagent (Cyanagen) and images were acquired and analysed with ImageQuant LAS 4000 (GE Healthcare), using the ImageQuant LAS 4000 1.2 software.

Supplemental Table S1. Antibodies and immunocytochemistry reagents

Ab/probe name	Company, code	Type	Host species	Reactivity	ICC concentration/dilution
RPL13	Santa Cruz, #sc-100829	primary, monoclonal	mouse	mouse, rat and human	2 µg/ml
RPL7	Sigma, #HPA058373	primary, polyclonal	rabbit	mouse, human	1 µg/ml
RPL28	Sigma, #HPA050459	primary, polyclonal	rabbit	human	2.5 µg/ml
RPS19	Abcam, #ab40833	primary, polyclonal	goat	human	10 µg/ml
Calnexin	Abcam, #ab192439	primary, polyclonal	goat	mouse, rat, dog, human, african green monkey	4 µg/ml
Goat antiMouse IgG	Thermofisher Scientific, #A32723	secondary, conjugated Alexa Fluor™ 488	goat	mouse	1:250
Donkey anti-Mouse IgG	Thermofisher Scientific, #A10037	secondary, conjugated Alexa Fluor™ 568	donkey	mouse	1:250
Donkey anti-Goat IgG	Thermofisher Scientific, #A11055	secondary, conjugated Alexa Fluor™ 488	donkey	goat	1:300
Phalloidin	Thermofisher Scientific, #A22287	conjugated Alexa Fluor™ 647	X	X	1:40
Hoechst	Thermofisher Scientific, #H3570	Hoechst 33342	X	X	1:3000

ICC= immunocytochemistry

Supplemental references

1. Costantini A, Skarp S, Kampe A, Makitie RE, Pettersson M, Mannikko M, et al. Rare Copy Number Variants in Array-Based Comparative Genomic Hybridization in Early-Onset Skeletal Fragility. Front Endocrinol (Lausanne). 2018;9:380.

2. Costantini A, Valta H, Baratang NV, Yap P, Bertola DR, Yamamoto GL, et al. Novel fibronectin mutations and expansion of the phenotype in spondylometaphyseal dysplasia with "corner fractures". Bone. Apr 2019;121:163-71.

3. Doyard M, Bacrot S, Huber C, Di Rocco M, Goldenberg A, Aglan MS, et al. FAM46A mutations are responsible for autosomal recessive osteogenesis imperfecta. J Med Genet. Apr 2018;55(4):278-84.

4. Jao L-E, Wente SR, Chen W. Efficient multiplex biallelic zebrafish genome editing using a CRISPR nuclease system. Proceedings of the National Academy of Sciences of the United States of America. 2013;110(34):13904-9.

MANUSCRIPT 2

Appendage Regeneration in Vertebrates: What Makes This Possible?

V. Daponte, P. Tylzanowski, A. Forlino. *Cells*, 2021.
https://doi.org/10.3390/cells10020242

Regenerative ability in vertebrates

Zebrafish has the fascinating ability to regenerate several organs and tissues, such as the heart, the brain, the liver, the kidney, and also bony appendages such as the caudal fin (Gemberling et al. 2013). This capability is, at least in part, recapitulated by other two vertebrates: the salamander, able to regenerate tail and limbs (Joven, Elewa and Simon 2019), and the lizard, that after amputation or autotomy is capable to restore its tail (Jacyniak, McDonald and Vickaryous 2017). Why at some point during evolution this ability was lost is still not understood. For this reason, the investigation of shared mechanisms among regenerating vertebrates could be useful to identify the pathways and the cellular cues with the potential to, at least partially, re-induce regeneration in mammals.

The field of regeneration is intriguing and being my main project focused on zebrafish caudal fin regeneration I quickly became interested in its biochemical and molecular bases. In this review, to which I worked right after the start of my PhD, I provide a comparison between appendage regeneration of zebrafish, salamander and lizard with the aim to identify not only shared mechanisms, but also fundamental differences. This review focuses on a wide range of topics, starting from morphological aspects to deeper cellular, epigenetic and molecular changes during regeneration. Popular themes in the field of regeneration are explored in depth, such as inflammation, the role of the immune system and the nerves, and aging. Finally, a brief paragraph is dedicated to the use of zebrafish regenerating caudal fin for biomedical research purposes.

Personal contribution to Manuscript 2

- Literature research.
- Manuscript writing and editing.
- Figure making.

References

Gemberling, M., T. J. Bailey, D. R. Hyde & K. D. Poss (2013) The zebrafish as a model for complex tissue regeneration. *Trends Genet,* 29**,** 611-20.

Jacyniak, K., R. P. McDonald & M. K. Vickaryous (2017) Tail regeneration and other phenomena of wound healing and tissue restoration in lizards. *J Exp Biol,* 220**,** 2858-2869.

Joven, A., A. Elewa & A. Simon (2019) Model systems for regeneration: salamanders. *Development,* 146.

Abstract

The ability to regenerate amputated or injured tissues and organs is a fascinating property shared by several invertebrates and, interestingly, some vertebrates. The mechanism of evolutionary loss of regeneration in mammals is not understood, yet from the biomedical and clinical point of view, it would be very beneficial to be able, at least partially, to restore that capability. The current availability of new experimental tools, facilitating the comparative study of models with high regenerative ability, provides a powerful instrument to unveil what is needed for a successful regeneration. The present review provides an updated overview of multiple aspects of appendage regeneration in three vertebrates: lizard, salamander, and zebrafish. The deep investigation of this process points to common mechanisms, including the relevance of Wnt/β-catenin and FGF signaling for the restoration of a functional appendage. We discuss the formation and cellular origin of the blastema and the identification of epigenetic and cellular changes and molecular pathways shared by vertebrates capable of regeneration. Understanding the similarities, being aware of the differences of the processes, during lizard, salamander, and zebrafish regeneration can provide a useful guide for supporting effective regenerative strategies in mammals.

Introduction

Regeneration is the capacity of an organism to regrow a part of the body after injury. Many species of anamniote vertebrates are capable of spectacular accomplishment of regeneration. Among them, the best known is salamander, which is able to restore limb, tail, eye, jaw, and heart [1]. Regeneration is also present in various members of the class of actinopterygians [2]. The adult zebrafish (Danio rerio), a small teleost, exhibits remarkable regeneration of fins, central nervous system structures, or entire organs including heart, pancreas, liver, and kidney [3]. The ability to activate the regeneration morphogenetic program is almost completely lost mainly in terrestrial animals, such as amniotes, in which nearly all structures are unable to regenerate, with some exceptions such as the regeneration of digit tips in children [4] and young mice [5], ear pinna in the spiny mouse [6], or the antler regeneration in deer [7]. Lizards are the only terrestrial amniotes that can regenerate a structure long and complex as the tail [8]. The distribution of the regenerative capacity along the phylogenetic tree is haphazard and a common pattern is difficult to identify (**Figure 1**). Regeneration appeared very early during evolution, likely coinciding with the origin of multicellularity [9]. The similarities between regeneration and development may suggest that the former originated as an epiphenomenon of an ontogenetic program that an organism accesses and employs when a structure is lost. Based on these observations, regeneration could be an ancestral property, lost due to higher energetic maintenance costs (for a detailed review, see [10]). In salamanders, several genes are associated with the regeneration ability, one of them is the one coding for the glycerophosphatidyl (GPI)-anchored cell surface Prod1, which mediates positional memory through a proximal-distal gradient of cell adhesion [11]. Despite a protein with similar functions being recently identified in the regenerating tail of the lizard *Gekko japonicus* [12], the Prod1 gene has not been found in any other species [13]. The ability to regenerate paired and unpaired fins was documented in many ray-finned fish (Actinopterygii). Teleosts possess a wide range of regenerative abilities, from complete absence of regeneration in some members of the family Blennidae [14] to a high regenerative ability of zebrafish. However, this trait is limited to the bony fin rays and does not include the proximal structures such as musculature and endoskeleton. The only exception are Polypteriformes, one of the basal lineages of Actinopterygii [15,16]. The strong regenerative potential found in this taxon suggests that regeneration in this case has emerged early during evolution, long before the appearance of Teleostei. In terrestrial amniotes, the evolution of a strong adaptive immune system could have favored a more defensive role of macrophages during the early phases of regeneration to the expenses of their ability of tissue remodeling [17]. The extreme “non-lethal predation” of lizards’ tails in the wild could instead explain the presence of a regenerative program in these amniotes [18]. Many factors have

contributed to the loss of regeneration in the evolution, and further phylogenetic and comparative studies are necessary to unravel the mechanisms regulating the process. The investigation of the regeneration of different organs, from the simple tail to the more complex limb in different organisms, represents a powerful tool to shed light on the process. This review will examine appendage regeneration in vertebrates, with a specific focus on tail regeneration in lizards, limb regeneration in salamanders, and fin regeneration in zebrafish. We will describe common cellular mechanisms across the regenerative process in these animals and investigate differences that could have led to the loss of regenerative capacity in mammals.

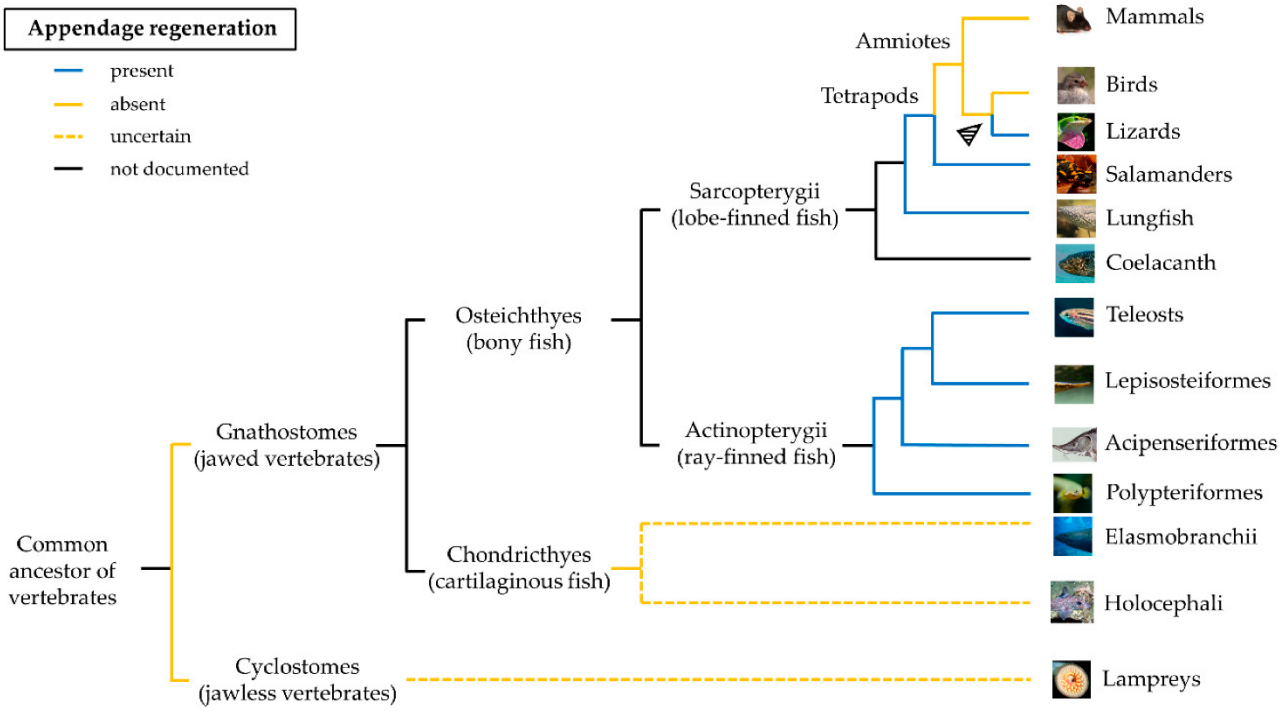

Figure 1. Phylogenetic distribution of appendage regeneration among vertebrates according to the current literature. The blue line indicates lineages containing one or more species capable of appendage regeneration, the orange line those incapables of regeneration, and the black line those in which appendage regeneration has not yet been documented. The dashed yellow line indicates the uncertain presence of appendage regeneration in chondrichthyes and cyclostomes. The arrow indicates the reactivation of the regenerative process in amniotes.

Experimental Approaches

The study of the regenerative process in lizard, salamander, and zebrafish, expanded in the last years by the development of new experimental tools, provided a better understanding of the regeneration mechanisms in these species pointing out similarities and differences. The ability of lizards to spontaneously lose their tail and then regrow it as an antipredation strategy (known as “autotomy”) made lizards one of the animal models used to study healing and regeneration. Autotomy is often exploited in laboratories to induce less invasive traumas and avoid surgery, so that simply pinching

the tail causes the tail to drop [8]. After tail loss, tissues are easily accessible, allowing manipulation and study in vivo. In recent years, several lizard genomes have been characterized, including that of the green lizard Anolis carolinensis, the primary candidate for regeneration studies [19]. This allowed to carry out genomic and transcriptomic analysis of genes involved in wound healing, cell proliferation and inflammatory-immune response to injury [20–24]. Nonetheless, transgenic or knockout/knockdown lizard models are still difficult to generate due to the complexity of accessing zygotes for genetic manipulation. With the advent of CRISPRCas9-mediated gene editing, this will likely change and recently, the first gene-edited Anolis, deficient for tyrosinase gene, has been created [25]. Given their close relation to mammals, as the only amniote model system for regeneration, the establishment of transgenic and mutant lizard models may help to clarify the loss of regenerative capacities in mammals during evolution.

Salamanders are another example of vertebrates with remarkable regeneration capabilities, being able not only to regenerate tail, but also limbs, neural cells [26], and heart [27]. Various salamander species captured the interest of regenerative research. Among them, the paedomorphic axolotl (*Ambystoma mexicanum*) has been investigated since the 1860s [28], emerging as the first salamander model for regenerative studies. Recently, a newt model (*Pleurodeles waltl*), sharing the same regeneration abilities and the short life cycle of the axolotl, has been established [29]. Given the feasibility for functional genetic approaches provided by both models, a large number of tools, including transgenesis and gene silencing, has begun to accumulate [30–32]. Axolotl and Pleurodeles genomes are large and rich in long terminal repeat (LTR) retrotransposons [33]. Their genomes are now sequenced and annotated [29,34,35], paving the ways for deeper genetic approaches, such as mutagenesis [36], transcriptomics [37], and genetic lineage tracking [38].

Zebrafish (*Danio rerio*), a freshwater teleost, has become one of the most widely used vertebrates for the study of regeneration. It has several experimental advantages, such as ease of manipulation and short developmental cycle. Its genome was sequenced and revealed about 70% coding sequence conservation to humans [39]. Importantly, zebrafish can regenerate several organs such as fin, heart, kidney, liver or brain [3]. The rapid regeneration of zebrafish caudal fin has made them one of the most powerful tools for regenerative studies, especially since the transcriptomics approaches are possible [40–42], and transgenesis and morpholinos techniques are readily available [43–46]. The recently established CRISPR-Cas9 gene editing additionally increased the value of this model. Zebrafish are also particularly suitable for small-molecule drug application, which, in skeletal field, takes enormous advantage of tail regeneration [47].

To summarize, lizard, salamander, and zebrafish offer a variety of experimental approaches for the investigation of the regeneration processes (**Table 1**), which will represent a huge opportunity to expand the understanding of appendage regeneration in vertebrates.

Table 4. Experimental accessibility and tools for vertebrate species used in regeneration research.

	Lizard			**Salamander**		**Zebrafish**
	A. carolinensis	***E. macularius***	***G. japonicus***	***P. muralis***	***A. mexicanum***	***P. waltl***	***D. rerio***
Experimental Accessibility							
Genome Size	1.78 Gb	2.23 Gb	2.55 Gb	1.51 Gb	~32 Gb	~20 Gb	1.67 Gb
Fertilization	internal	internal	internal	internal	external	external	external
Egg Size	~6 mm	~12 mm [48]	~13 mm [49]	~11 mm [50]	~2 mm	~2 mm	<1 mm [51]
Egg Transparency	no	no	no	no	yes	yes	yes
Experimental Tools							
Genome Annotation	Ensembl NCBI	NCBI	NCBI	Ensembl NCBI	NCBI	NCBI	Ensembl NCBI
Transcriptome Annotation	NCBI	NCBI	NCBI	NCBI	NCBI	NCBI	NCBI
Knock-down *	no	no	no	no	yes [31]	no	yes [46]
Transgenesis	no	no	no	no	yes [30,38]	yes [52]	yes [43,53]
Knock-out/Knock-in	no	no	no	no	yes [54] **	yes [55] **	yes [42,56] ** #

* = morpholino ** = CRISPR/Cas9 # = ENU mutagenesis.

Common Morphological Aspects of Early Regenerative Response

Lizard tail, salamander limb, and zebrafish fin regeneration are examples of epimorphosis. The term epimorphic regeneration, coined by Thomas H. Morgan in 1901 [57], describes the restoration of a part of the organism without remodeling, characterized by the formation of the blastema. This mass of undifferentiated cells at the wound site mediates tissue differentiation [58,59]. Epimorphosis is characterized by a high degree of cellular differentiation and stands in contrast with morphallaxis, usually observed in hydras, in which blastema is not formed and the majority of regeneration is taking place by reorganization of the remaining parts of the body [58,59].

Lizard, salamander, and zebrafish share several common morphological aspects of epimorphic regeneration that distinguish this process from the limited regeneration in mammals. Some differences were however identified. For example, lizards, unlike salamanders, are unable to regenerate amputated limbs. Also, after autotomy or amputation, lizard tail undergoes an "imperfect regeneration" in which the bony vertebral column is replaced with a hollow cone of cartilage and the fracture planes, that are structures evolved to allow autotomy at precise locations, are not regenerated [60]. On the contrary, salamanders and zebrafish can restore the original appendage. Lastly, while lizard and salamander appendage regeneration occur following cartilage formation, zebrafish caudal fin rays are directly generated as bone.

The regenerative process begins immediately after an appendage loss and consists of three phases: wound healing, blastema formation and regenerative outgrowth (**Figure 2**).

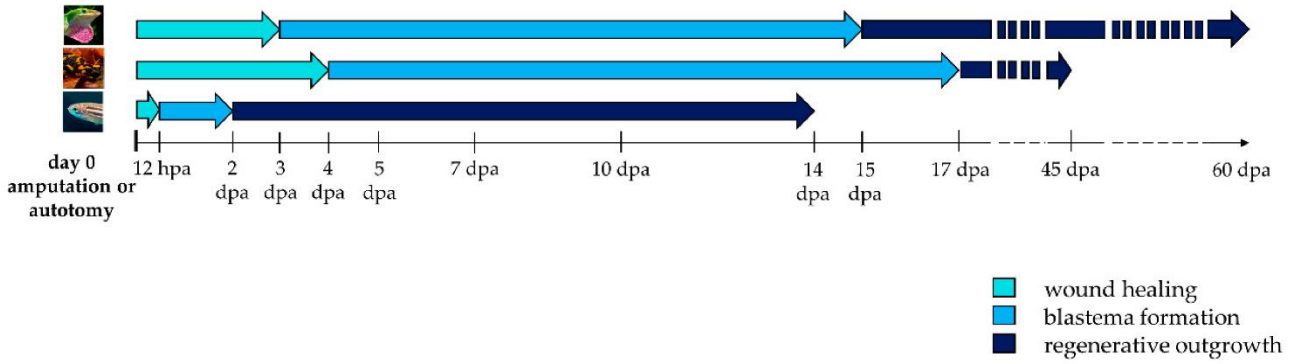

Figure 2. Timeline activation of wound healing, blastema formation and regenerative outgrowth during appendage regeneration in vertebrates. Arrows indicate the duration of each regenerative step in lizard, salamander, and zebrafish. Hpa: hours post-amputation; dpa: days post-amputation.

Initially, after autotomy or amputation, a blood clot forms. Lizard's tail stump has evolved the presence of vascular sphincters located proximal to fracture planes that contract to avoid excessive bleeding and to facilitate hemostasis [61]. Within a few hours, epithelial cells begin to migrate to

cover the wound, forming an epithelial layer called the wound epidermis. The integrity of the wound epidermis is essential to accomplish regeneration in lizard and salamander. Impeding its formation by excision or suture prevents the appendage to regenerate [62,63]. Repetitive amputations seem to trigger a persistent wound healing response, and result in a decline in regenerative fidelity in lizard and salamander [64,65]. In the newt *Notophthalmus viridescens*, repeated amputation of the limb can lead to severe morphological abnormalities [66]. To the contrary, in zebrafish, repeated amputations do not perturb regeneration and instead lead to an increase in the dermal bone thickness [67].

After several days, in salamander and zebrafish, the thick wound epidermis forms a specialized structure, the apical epidermal cap (AEC) that acts as a layer of signaling cells coordinating the regenerative process [61,68]. For this reason, AEC needs to be continuously in contact, and to communicate with, the underneath mesenchymal cells. Interposition of dermis or the formation of basement membrane between the two structures inhibits blastema formation and regeneration [69]. This property suggests that diffusible signaling factors are produced in the AEC and signal to the underlying mesenchyme. In lizards, this thick epithelium has a different morphology, owing a discontinuous basement membrane, and is often referred to as an apical epidermal peg (AEP) [70]. As quickly as the wound epidermis thickens, the tissues below undergo degeneration and histolysis. The dynamic remodeling of extracellular matrix (ECM) plays a crucial role in this process. The secretion of acid hydrolases and proteinases of the matrix metalloproteinases (MMPs) family at the level of the basal layer of the wound epidermis helps degrading ECM components, such as collagens and laminins. This process is likely facilitating cell migration and cell communication by disturbing basement membrane re-assembly [71–73]. MMPs also favor the elimination of cellular residues and debris generated by tissue destruction and by the bactericidal activity of neutrophils and macrophages [69]. In lizard and salamander, the degradation involves primarily bone and muscle [74,75]. In zebrafish, in which the caudal fin is mainly composed of bone, the establishment of a cryoinjury-mediated tissue damage triggers a similar osteolytic process [76]. The degeneration of stump tissues, or “histolysis”, favors the release of progenitor cells that will contribute to the formation of blastema. Comparative anatomy of regenerating appendages in lizard, salamander, and zebrafish is depicted in **Figure 3**.

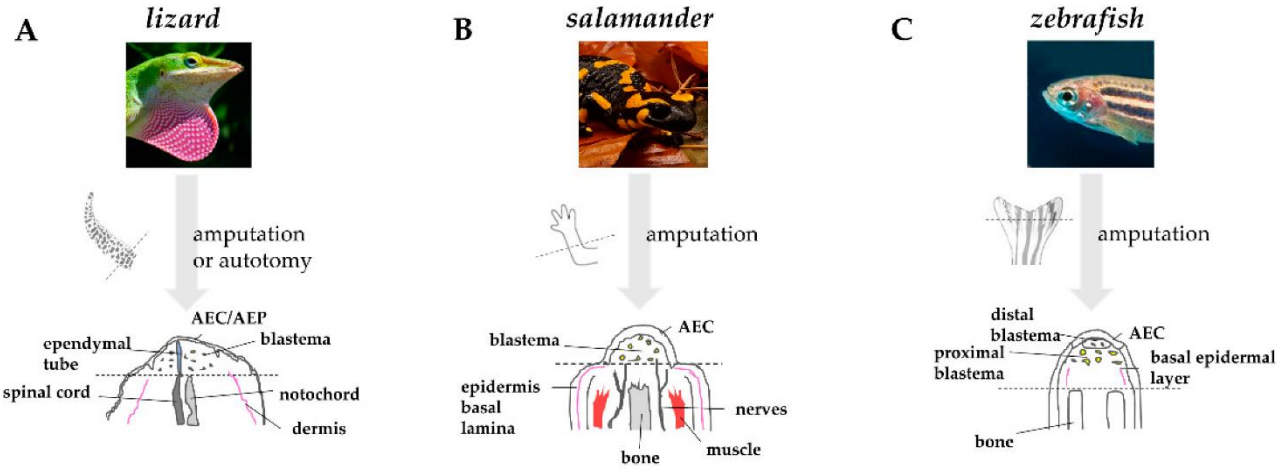

Figure 3. Comparative anatomy of regenerating appendages in lizard, salamander, and zebrafish. (A) Amputation or autotomy of lizard tail induces the formation of a cone-like shaped blastema, covered by a thick wound epidermis that will form the apical epidermal peg(AEP), whose correspondence to the apical epidermal cap (AEC) found in amphibians and fish is still uncertain. During blastema formation, likely in response to AEP signals, the central canal of the original spinal cord, the ependymal tube, elongates and infiltrates the proliferating tail blastema. **(B)** After amputation of salamander limb, the wound epidermis quickly covers the stump. Within days, the wound epithelium becomes innervated, thickens, and becomes a specialized AEC. The AEC induces dedifferentiation in the underlying stump tissue and attracts cells, which accumulate below the AEC to form the blastema. Modified from Payzin-Dogru and Whited, 2018. **(C)** After zebrafish fin amputation, epithelial cells migrate to cover the wound, forming the AEC. Under the AEC, stump tissues dedifferentiate to form the blastema. Within 24 h, blastemal cells segregate into two compartments: the distal blastema, populated by slowly proliferating cells, and the proximal blastema, in which cells rapidly proliferate and differentiate to replace the amputated tissue. Dotted lines indicate the site of amputation/autotomy.

Role and Origin of Blastema: Dedifferentiation versus Stem Cells

Blastema is the key component of the epimorphic process and the primary source of differentiated cells responsible for appendage regeneration. Blastema formation occurs within 10–15 days post-amputation in most lizard species [20,77]. After tail autotomy of the leopard gecko *Eublepharis macularius*, blastema can be identified after 3 days, and continues to expand until 8 days post-autotomy [78]. In adult newts, blastema cells appear within 4-5 days post-amputation [69] and accumulate around 7 days post-amputation in axolotl [79,80]. In zebrafish, blastema can be identified at day 2 post-amputation (**Figure 2**) [68,81].

Despite the role of blastema as the necessary and sufficient structure for the progression of regeneration, its origin is still controversial and debated. Two competing hypotheses have emerged to define the source of activated progenitor cells within the blastema. The first one points to resident stem cells characterized by self-renewal potency and the ability to produce one or more differentiated cell types [82]. The second hypothesis foresees a cell conversion event by which differentiated cells dramatically change their identity. One of the mechanisms associated with this conversion is

dedifferentiation, in which differentiated cells lose their specialized function and revert to a less-differentiated stage with higher potential, akin to the events taking during the generation of induced pluripotent stem cells from dermis [83]. The other possible mechanism is direct transdifferentiation, in which differentiated cells switch lineage and are converted into another cell type within or across germ layers. Transdifferentiation is naturally observed during lens regeneration in newts where removal of the lens induces the formation of a new lens derived from the cells of the iris [84,85]. Direct transdifferentiation occurs without going through a stem/progenitor-like cell [86–88].

In lizard tail regeneration fails when the amputation occurs at its base, in the non-autotomous region. This phenomenon has been hypothesized as caused by the depletion of stem cells after the basal amputation of the tail [77]. Indeed, histological, immunocytochemical, and autoradiographic studies indicate the presence of slowly cycling, putative resident stem/progenitor cells in various tissues of lizards' original tail, including satellite cells of muscles and ganglia, and chondroblasts localized in intervertebral cartilages and vertebrae [89,90]. Following injury, these cells can activate, as demonstrated by the immune detection of telomerase and c-myc, and migrate to contribute to the blastema [91,92]. Transcriptomic and histological works on Anolis carolinensis tail regeneration led to the identification of a population of PAX7+ satellite cells, pointing to a stem-cell mediated process [20,93].

On the other hand, a study on the lizard *Podarcis muralis* suggests that the activation of a dedifferentiation process could be linked to a degree of tissue damage. After 3-4 days post-autotomy, fragmented myofibers showed an infiltration by macrophages indicating phagocytosis and gave origin to small cells with euchromatic nuclei, interpreted as dedifferentiated muscle fibers. Similarly, the spinal cord, fibrocytes of the dermis or inter-muscle connective tissues, adipose and cartilaginous tissues, following damage, gave rise to viable, proliferating cells [94]. A recent lineage tracking study on the mourning gecko (*Lepidodactylus lugubris*) indicates that during tail regeneration, differentiated cartilage cells contribute to muscle and differentiated muscle cells contribute to cartilage in the regenerated tissue, suggesting that dedifferentiation or even transdifferentiation could play a role [95]. The contribution of muscle to cartilage cells was also described during axolotl tail regeneration [96]. These findings are in contrast with what was reported for limb regeneration. Using a GFP transgene to track limb tissues, Kragl et al. showed that limb blastema cells are lineage-restricted and only capable to give origin to cells from the same germ layer. Dermis was able to form cartilage and tendons, derived from the lateral plate mesoderm, but not muscle, that derives from the presomitic mesoderm. In the same way, muscle was able to give origin to only muscle and not cartilage [30]. These contradictory findings could, in part, be explained by the embryonic differences

between tail and limb buds, with the former having a pluripotent nature and being able to give origin to all the three germ layers [97]. Differences are also seen when comparing blastemas of Anolis lizards and leopard gecko *Eublepharis macularius*. In the Anolis lizard, no cell proliferation was detectable leading some authors to question whether this was a real blastema [20,78,93], whereas the leopard gecko blastema was reported to be rich in actively proliferating cells [72,98,99]. A recent study by Lozito and Tuan suggests that Anolis tail regeneration could require cell populations of different origin. This study was aimed to clarify why proximal regenerated lizard tail skeleton undergoes hypertrophy and endochondral ossification, whereas the distal regenerate remains cartilaginous. The study shows that the proximal regenerated lizard tail skeleton is derived from progenitor/stem cells within the vertebrae periosteum in response to BMP and Ihh signaling, whereas more distal regions are derived from multipotent blastema cells and respond to Shh signals [100].

Different contributions to blastema are also found within closely related species. In the newt *Notophthalmus viridescens*, myofiber dedifferentiation is required for blastema formation and generates PAX7− cells that will later give rise to new muscle in the regenerated tissue. In axolotl, after amputation, myofibers give rise to neither proliferative cells in the blastema nor to regenerated muscle. Instead, the primary contributors to blastema are PAX7+ satellite cells [101,102]. However, a combination of the two mechanisms cannot be excluded. A recent single-cell RNA-sequencing study on axolotl limb identified the presence of PAX7+ cells and, likely, tendons progenitor cells together with a population of multipotent fibroblasts able to form joints, cartilage, and bone of the regenerate [103]. Whether fibroblasts derive from rare specialized progenitor populations or from general activation of already differentiated fibroblasts, remains to be determined.

Blastema formation in zebrafish caudal fin occurs mainly, if not exclusively, by dedifferentiation. Studies employing different cell-tracking methods revealed that cells followed lineage restriction. Knopf et al. demonstrated that osteoblasts temporarily dedifferentiate in response to amputation. In the caudal fin, a strong expression of the mature osteoblast marker osteocalcin was detected in the bony rays. Following the amputation and ensuing regeneration, sequential induction of *runx2*, pre-osteoblasts marker at 2 days post-amputation, *osterix/sp7*, marker for intermediate differentiation of osteoblasts at 3 days post-amputation and *osteocalcin* at 6–7 days post-amputation were detected [44]. The same authors, using *Cre*-loxP-based fate-mapping, demonstrated that dedifferentiating osteoblasts enter fin blastema and give rise only to osteoblasts during zebrafish fin regeneration. They implemented a double transgenic fish line carrying tamoxifen-inducible CreERT2 under the osterix promoter (osterix:CreERT2) in conjunction with a floxed DsRedStop cassette under the control of a heat shock promoter expressing GFP after the excision of the DsRed-Stop cassette (hsp70:loxP

DsRed2 loxP nlsEGFP). During regeneration, GFP+ cells were found within the blastema, forming new osteoblasts, without significantly contributing to other lineages [44]. A similar approach was used by another group and led to the same results [104].

Tu and Johnson generated mosaic fish by inserting a XenEF1α:GFP transgene by Tol2 transposition into 1–2 cell embryos [105]. The EF1α promoter, driving GFP expression, was silenced in adult tissues, and its expression was restricted to the blastema during fin regeneration, providing a useful tool to visualize differentiating cells in regenerative tissues [106]. Co-occurrence analysis for GFP labeled clones showed that caudal fin is formed by 9 distinct lineage classes: the unipotent osteoblast, fibroblast, glial, iridophore, epidermis, and lateral line; the bipotent vessel/artery and melanophore/xanthophore. After amputation, the labeled cells always regenerated the same cell type and did not contribute to other cell types [105]. Also, after amputation of caudal fins using fish with labeled cells in the body, but not in the fin, no labeled cells were found in the regenerate, excluding a distant cell contribution during regeneration [105].

This apparent variety of mechanisms (**Table 2**) recapitulates the heterogeneity of tissue repair and regeneration of vertebrates. Thus, a better understanding of blastema origin will have implications in regenerative medicine.

Table 5. Mechanisms of cellular derivation of blastema in vertebrates. The green tick indicates what cellular conversion process has been documented during blastema formation in different species.

		Lizard			**Salamander**	**Zebrafish**
	A. carolinensis	***L. lugubris***	***P. muralis***	***A. mexicanum***	***N. viridescens***	***D. rerio***
Dedifferentiation		✓ [95]	✓ [94]	✓ [30,107]	✓ [102]	✓ [44,104,105]
Transdifferentiation		✓ [95]				
Stem cell recruitment	✓ [20,90,93]		✓ [89]	✓ [101,102]		

Epigenetic Changes in Regeneration

When damage or injury triggers appendage regeneration, a series of cellular and molecular responses are activated, such as inflammation, dedifferentiation, proliferation, and differentiation. Currently, a great effort has been placed in regenerative medicine to reprogram somatic cells toward a stem-like state, and then induce their differentiation to cells with the desired functionality. To this purpose, the understanding of the epigenetic changes regulating these processes is fundamental. Epigenetic regulation of gene expression can be achieved through covalent modification of DNA and associated

histones, chromatin remodeling, and the action of non-coding RNAs [108]. The best characterized is DNA methylation occurring on cytosines belonging to cytosine and guanine repetitive clusters (CpG islands) [109]. Methylation maintenance relies on DNA methyltransferase 1 (DNMT1), while *de novo* methylation requires DNA methyltransferase 3 (DNMT3) and results in a change of expression [109]. DNMT3s are essential during early embryonic development [110] and are important regulators of cell differentiation [111,112]. Recent studies indicate that *de novo* DNA methylation also acts during regeneration to control cell behavior and fate. A nerve-dependent downregulation of the axolotl DNMT3a during limb regeneration was associated with the transition of the wound epidermis into a functional AEC [113]. In an experimental assay, the treatment of axolotl skin wounds with a DNMT inhibitor induced cells to participate in blastema formation and resulted in a regenerative response [113]. After zebrafish caudal fin amputation, the level of cytosine methylation was transiently reduced and associated with an increased expression of demethylation genes [114]. The degree of methylation was gradually recovered during fin regeneration and at 72 h post-amputation the expression of three zebrafish orthologues of mammalian *DNMT3A* and *DNMT3B* (*dnmt3aa, dnmt3ab,* and *dnmt4*) [115,116] was clearly detected in blastema cells [117]. The presence of a dynamic role of DNA methylation has yet to be investigated during lizard tail regeneration. MicroRNAs (miRNAs), short non-coding RNAs, mediate post-transcriptional repression by binding the 3′ untranslated region (UTR) of target mRNAs. Among their multiple roles as epigenetic regulators, they are fundamental to control cell differentiation and fate [118]. Microarray analysis of miRNAs expression during axolotl limb regeneration reported the overexpression of miR-21 in the mid-bud blastema, which presumably maintains blastema cell differentiation through a negative regulation of the developmental gene *Jagged1* [119].

miR-133a, miR-133b, and miR-206, already known as regulators of muscle development and differentiation [120,121], were found to be differentially expressed during Anolis carolinensis tail regeneration, with an increased expression in the proximal portion with respect to tail tip [122].

miR-133 was found to be also highly expressed in uninjured fins and depleted during zebrafish caudal fin regeneration [123]. Interestingly, the depletion was dependent on FGF signaling, indicating a significant role of this pathway in maintaining low miR-133 levels besides its essential role for blastema formation and maintenance. It would be interesting to investigate its epigenetic role also in lizards. Another study on zebrafish caudal fin regeneration indicates that the other master regulator of regeneration, the Wnt/β-catenin pathway, is also regulated by miRNAs. This study showed that miR-203 specifically targets the Wnt signaling transcription factor Lef1 and acts as a negative regulator of regeneration [124].

These data indicate that epigenetic changes, as during development, play fundamental roles during regeneration and are sometimes conserved in different species. The success of regenerative therapies based on induced dedifferentiation will likely depend on the ability to recreate and regulate these specific epigenetic changes.

Patterning and Positional Memory

A classical regeneration restores not only the lost appendage, but also its threedimensional architecture and size. Indeed regeneration, similar to development, involves morphogenetic processes to shape the regenerated tissues. The proximodistal, anteroposterior, and dorsoventral developmental axes are reorganized within the regenerative blastema, guided presumably by diffusible as well as positional clues permitting, among others, size preservation. One of the first and most popular explanations for this phenomenon was proposed by Wolpert. He hypothesized a simple coordinate system that provides cells with a positional value that, together with the cells' genetic heritage, determines a specific response during ontogenetic pattern formation [125]. In the context of a regenerative process, this phenomenon is defined "positional memory" and refers to the information that blastema cells retain about their position along the proximodistal axis.

The properties of blastema during the patterning and outgrowth phase were initially studied using regenerating salamander limbs. Butler and colleagues proposed the rule of distal transformation that refers to the ability of blastema to regenerate along any level of the proximodistal axis and always proceeds in a direction distal to the stump surface. The rule was tested by inverting the proximodistal axis of an Ambystoma regenerating limb by suturing the autopod to the body trunk, and then cutting the circularized limb. This gave rise to two limbs, one of which had reversed polarity, but still regenerated all limb elements distal to the level of the amputation surface (**Figure 4A**) [126].

The stump tissues can also "sense" discontinuities along the proximodistal axis. Experiments in which gap discontinuities were created in regenerating limbs revealed that cells tend to proliferate and eliminate them in a process named intercalation. For instance, when a distal blastema was grafted onto an upper limb stump, the intermediate limb parts arose from the stump tissue, whereas in the converse experiment, grafting of a proximal blastema onto a wrist stump resulted in regeneration directly from the wrist and intercalation did not occur (**Figure 4B**) [127]. Much remains to be learned from a molecular and cellular point of view on how regenerating appendages are precisely replaced. Various observations suggest that positional memory may be related to a proximal-distal gradient of ligands and receptors with higher concentrations inducing more distal fates. For instance, one of the most intriguing findings was the ability of retinoic acid (RA) to reprogram proximo-distal values of

blastema cells. Treatment of regenerating salamander limb with RA resulted in proximalization of the wrist blastema, so that an entire limb could be regenerated. The extent of proximalization was dependent on the exposure time and RA concentration [128]. A differential screening comparing newt RA-treated distal limb blastema with untreated one was used subsequently to identify cell-surface molecules able to act as effectors of positional memory [11]. This method led to the identification of Prod1, a GPI-anchored receptor belonging to the Ly6 family. The likely role of Prod1 is to determine positional memory via a gradient of cell adhesion. Indeed, the gene is highly expressed in newt proximal limb blastema and upregulated in response to RA [11,13]. Furthermore, overexpression of Prod1 in axolotl limb blastema re-specified cells to attain a more proximal position in the regenerated limb [129]. Lizard *Gekko japonicus* CD59 expression, originally interpreted as the ortholog of Prod1 [11], was found to increase following tail amputation and was upregulated by RA [12]. Also, overexpression of CD59 in lizard distal blastema re-specified transfected cells to a more proximal location, similarly to what has been shown during salamander limb regeneration [12]. Although no putative CD59 homolog has been identified in zebrafish, some CD59 related transcripts and proteins expressed in proximal to distal gradients have been found in the regenerating caudal fin. Furthermore, *aldh1a2* involved in RA synthesis and the anterior gradient protein *agr2*, identified as a Prod1 ligand [130], are expressed in proximally enriched gradients [41].

The 3D structure of the Prod1 protein was solved by nuclear magnetic resonance (NMR) spectroscopy in order to perform a comparative study to other members of the three-finger protein (TFP) superfamily, to which Prod1 belongs. The molecular phylogeny, based on both sequence and structural criteria, indicates that Prod1 has no known orthologues in other vertebrate taxa [131]. Patterning and size control during growth and regeneration are also regulated by bioelectric signaling. Several well-studied zebrafish mutants with mutations in K+ channels show altered appendage growth. The *another longfin* (*alf*) phenotype is due to a mutation in Kcnk5b, which directly increases potassium conductance, and causes fin overgrowth [132]. In contrast, the *short fin* (*sof*) mutation occurs in the *connexin43* (*cx43*) gene, which encodes a protein involved in gap junction formation, and results in shorter fins [133]. The correlation between ion current and patterning is largely unknown, and possibly depends on electrical coupling between cells [134,135]. It is interesting to notice that ion current has been implicated in several examples of tissue regeneration, including salamanders and newts. For instance, after amputation, forelimb stumps are traversed by a strong, steady, and polarized Na+ electric current that originates at the injury site [136]. Reducing this current resulted in inhibited or abnormal limb regeneration [137].

Recently, a role for heat shock proteins (HSPs) as regulators of shape during tail regeneration of the newt *Pleurodeles waltl* has been proposed [138]. Considering that HSPs expression has been proven necessary for blastema formation during axolotl limb [139] and zebrafish caudal fin regeneration [140,141], it would be of interest to elucidate if they have morphogenetic functions also during regeneration of other organisms.

Taken together, these findings suggest that mechanisms of patterning and positional memory could be conserved and adapted in the different species. Further studies are needed to clarify the effectors of the latest stages of regeneration and how they are phylogenetically correlated. Most importantly, it will be relevant to determine which of these signals have been further preserved in the evolution and could be potentially reactivated for biomedical purposes.

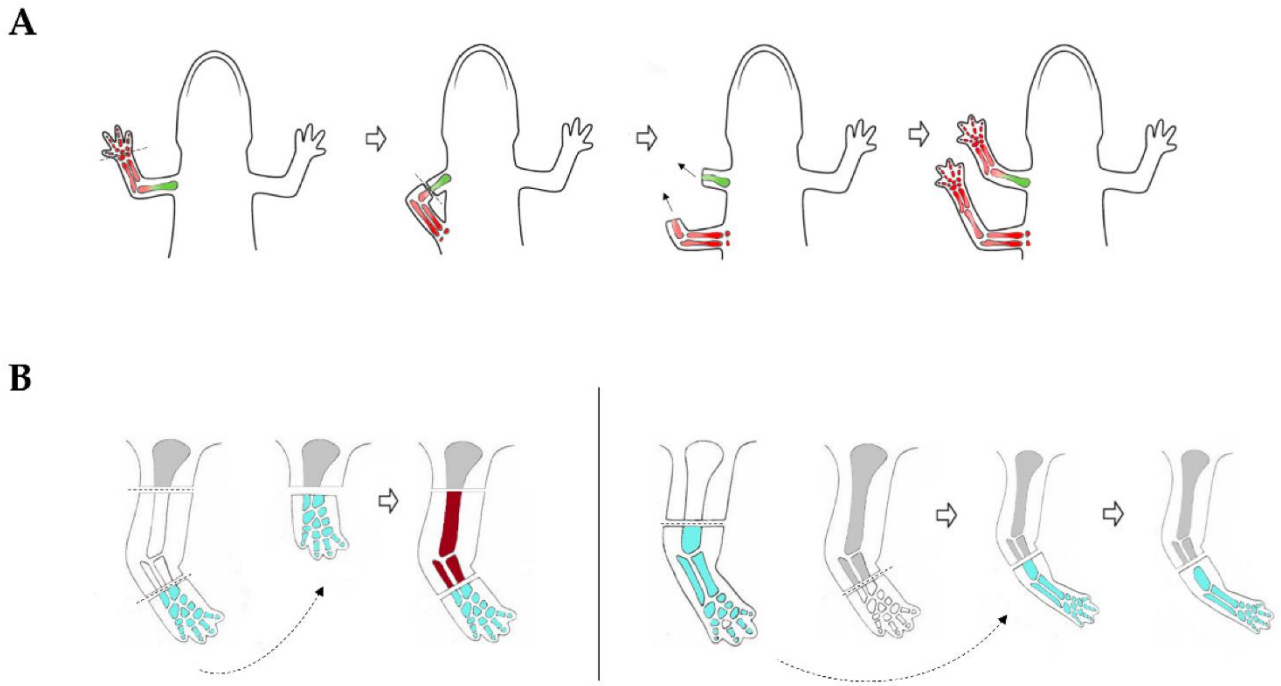

Figure 4. Experiments illustrating the principles of positional memory in salamander limb. (A) Rule of distal transformation. After the creation of a circularized limb, successive amputation induces the creation of two stumps, one with correct polarity and one with reversed polarity. Both stumps regenerate distal elements from the level of amputation, thus duplicating the distal segments already present in the reversed stump. The proximo-distal axis is indicated with a gradient of green (indicating proximal elements) and red (indicating distal elements). **(B)** Intercalation. Intercalary regeneration (dark red) occurs if a hand is grafted to an upper arm (left), but not if an upper arm segment is grafted to a forearm (right). Adapted from Carlson 2007.

Role of Inflammation

The key role of macrophages as key mediators of inflammation during mammalian tissue repair associated with the deposition of fibrotic tissue and scar formation is well known [142]. In the past decades, a large body of data has been collected on the role of macrophages in organizing and

controlling the inflammatory responses during wound healing of species characterized by high regenerative potency. Godwin et al. contributed to one of the major studies on urodele inflammatory response after limb amputation. The authors demonstrated an increased level of myeloid cells in regenerating axolotl tissues within one day after amputation. During the early stages of regeneration, a balanced expression of pro-inflammatory cytokines (TNF-α, IL-1β, IL-16, IL-17, IL-23, IFN-γ) and anti-inflammatory cytokines (IL-4, IL-5, IL-10, IL-13) is required. Indeed, the use of clodronate liposome, a well-established method to selectively deplete macrophages in vivo, led to an unbalanced increase of pro-inflammatory/anti-inflammatory cytokine ratio, reduced MMPs secretion, and resulted in non-functional wound epidermis [143]. The tracking of myeloid cells in transgenic zebrafish lines revealed a similar response, with circulating neutrophils and resident macrophages accumulating in the injury site at 6 h post-amputation and 3 days post-amputation, respectively. Although the creation of a neutropenic environment did not considerably affect the regeneration rate, genetic macrophage ablation resulted in reduced tissue regrowth in this model [53]. A recent study explored the role of macrophages in lizard regenerating tail, revealing an increase in the phagocytic cell population within the blastema starting from 3 days post-amputation. Clodronate liposome treated lizards failed to form blastema and to regrow amputated tail, further confirming the importance of macrophages in regeneration [144]. Another recent work reported the presence of anti-inflammatory M2-like macrophages underneath the wound epidermis and near the ependyma in the regenerating *Podarcis muralis* tail, which similarly to the amphibian limb, support and stimulate regeneration [145]. This is in contrast with lizard scarring limb in which only M1-like macrophages were detected [146]. Taken together, these results indicate that a timely activation of macrophages is required during the early steps of regeneration for a correct blastema formation and the onset of the regenerative process. During this phase, macrophages contribute to the establishment of an inflammatory environment through the secretion of cytokines and MMPs to degrade ECM components and tissue debris facilitating cell migration and communication [17,143,144]. Furthermore, the presence of an early anti-inflammatory response is related to a resolutive and anti-fibrotic activity that may be critical to both resolve inflammation and to carry on regeneration [147] by preventing fibrotic deposition and scarring [142]. The clearance of senescent cells is another suggested role for macrophages during the early regeneration phase. In fact, amputation or injury triggers apoptosis and cellular senescence [148,149]. In salamander for instance, it was demonstrated that senescent cells were transiently induced following amputation and subsequently cleared by macrophages. Since the depletion of macrophages led to senescent cells accumulation [150], perhaps the effective removal of senescent cells by them is a physiological mechanism during the regenerative program. Nevertheless, a role for macrophages during the later steps of regeneration cannot be excluded. Indeed, ablation of

macrophages after blastema formation does not affect regeneration rate, but compromises fin patterning and bone formation in zebrafish [53]. In salamander, the lack of macrophages during the later stages of regeneration associates with a reduction of surface vasculature, implying another possible functional role for macrophages during tissue outgrowth [143].

Immune System and Regeneration

The strong, scar-free regenerative potential in selected vertebrate species has raised the question whether differences in immune systems can affect the outcome of tissue regeneration. One of the indications of a negative effect of the immune system on regeneration was described in anuran amphibians which lose their robust regeneration ability after metamorphosis when the immune response is enhanced [17].

Lizard, salamander, and zebrafish heavily rely on an efficient innate immunity, consisting of diverse components such as antimicrobial peptides, neutrophils, macrophages, and the complement system [151–154]. Their adaptive immunity, however, differs from that of mammals by missing lymphoid organs such as Peyer's patches and lymph nodes [151,155,156].

Lizards, of the three species the closest related to mammals, share similarities with them in terms of generation of antibody diversity, but produce slower and less robust adaptive humoral responses [151]. Their B cells are characterized by phagocytic activity, a feature shared with salamanders and still under debate for zebrafish [155,157,158], and act as a component of innate immunity [151]. The strong innate immune system seen in this group of vertebrates could be sufficient to protect from microbial infections present in the first stages of life, making efficient adaptive immunity non-essential. Salamanders are generally considered "immunodeficient" since they have a weak cellmediated immune response, and their humoral immunity is based only on IgM production and is apparently amnestic [152]. Moreover, they have a restricted MHC class II diversity, likely resulting in a poor T-helper stimulation and a low cytokine synthesis [159] that could in part explain the low inflammatory response seen during limb regeneration. Zebrafish develop their adaptive immunity later, at the end of their embryo phase [160]. Their T-cell responses are negatively affected by low body temperature [161]. RAG1 protein, essential for antibody and T-cell receptor V(D)J recombination, is conserved in zebrafish. However, homozygous *rag1* mutant fish, lacking functional T and B lymphocytes, reach adulthood and are fertile [162,163], suggesting that these cells are likely not necessary for an efficient immune response. An ultrastructural study of the regenerating tail of the lizard *Podarcis muralis* showed that repeated amputations or cauterization trigger an increase in the number of immune cells such as granulocytes, macrophages, and lymphocytes within the blastema

and led to the deposition of fibrinoid material with scarring [64]. The study supports the hypothesis that the evolution of the immune system may be associated to the reduced regeneration ability in lizards, and in amniotes in general. Further studies are needed to clarify how immune cells and mesenchymal cells of the blastema communicate and interact during regeneration.

Nerve-Dependency of Regeneration

The knowledge that the nervous system is involved in the regenerative process was reported as early as 1823, when Todd demonstrated that denervation of the amputated salamander limb inhibited or caused defective regeneration [164]. Nerve-dependency became one of the most intensively studied topics in regeneration only from the mid of the 20th century when Singer performed a series of elegant experiments on denervated salamander limbs (reviews of his work [165,166]). He pointed out that not a specific type of nerve, but all nerve fibers contribute equally to the regenerative process. Also, he observed that regeneration never occurred if the number of nerves did not exceed a certain threshold [167,168]. Based on these findings, the neurotrophic hypothesis was formulated, stating that the nerve produced trophic factors crucial for the survival and proliferation of blastema cells. Regenerating nerves interact with the wound epidermis and sustain apical epidermal cap (AEC) formation and maintenance [169]. Potential trophic factors include substance P, insulin, transferrin, neuregulin-1, FGFs and BMPs [170] but the main candidate trophic factor is the anterior gradient protein (AGP), a ligand for the blastema cell surface receptor Prod1 cited previously, that offers a molecular explanation for nerve-dependence in urodeles. AGP is strongly expressed in Schwann cells of newt limbs in the first phase of regeneration and later shifts to the glandular structures of the wound epidermis [130]. Similarly, in axolotl, which do not possess subepidermal glandular cells, AGP expression was observed in Leydig cells [171], and denervation of limbs abolished AGP production. This suggests that, in both newt and salamanders, nerves induce the production of the protein that is then secreted by epithelial cells to blastema cells with a holocrine mechanism. Nerve-dependency of regeneration is a phenomenon that extends across phylogeny. Destruction of the spinal cord disrupts regeneration in lizard in a mechanism following the concept of a required threshold of nerve fibers [172]. In particular, the ependymal tube seems to be crucial for initiating regeneration [173]. If white and grey matter are damaged alone, but the ependymal population is maintained, regeneration still occurs [174]. Furthermore, transplanted segments of the ependymal tube can initiate blastema formation and produce ectopic tails at grafting sites [174,175], demonstrating that this structure alone is capable of starting regeneration. How exactly the ependymal tube mediates regeneration remains unclear. The supporting role of nerves to wound epidermis and AEC is confirmed in zebrafish regenerating pectoral fin. In this model, thickening of the wound epidermis and AEC formation are

negatively affected by denervation [176]. The demand for regeneration of a threshold number of nerve fibers is extended also to this organism. Indeed, the complete absence of nerve fibers impedes blastema formation and regeneration, whereas a reduced number of nerves allows smaller and deformed fin to regenerate [176]. The AGP homolog *agr2* was found to be expressed in the mucus-secreting cells of the epidermis, although no difference was seen between control and denervated fins. Furthermore, if denervation was applied after blastema formation, fin rays regenerated, but presented a narrowed and crooked structure [176]. This last observation supports the critical role of nerves during the initial stages of regeneration and points to their effect also during regenerative outgrowth and patterning.

An exception to the nerve-dependency phenomenon is the aneurogenic salamander limb created by removing the neural tube from embryos. Aneurogenic limbs have never been innervated but are still able to regenerate [177]. However, aneurogenic limbs become nerve-dependent upon complete innervation from the host [178]. Thus, a fascinating explanation for why aneurogenic limbs regenerate is that critical regeneration factors are initially produced in the developing limb, but after innervation, they are supplied by nerves. After that, a neural–epidermal relationship is created, and the epidermis becomes dependent on neural factors to promote and sustain the regenerative process [170,179]. It will be interesting to investigate the conservation of this phenomenon in other species. Taken together, the findings reported in the different species support the idea that nerves produce trophic factors promoting and regulating blastema proliferation and differentiation and possibly the subsequent patterning. The nerve-dependent regeneration is detected in most regenerating organisms, but mechanisms differ. Investigating the evolution of nerve-dependency in different regenerating vertebrate species would likely help to get further insight into this process.

Molecular Pathways Implicated in Regeneration

Further identification of the signaling networks involved in the regeneration remains one of the key research directions in this field. In the past decades, much knowledge was acquired about the molecular mechanisms that mediate the regenerative processes in various organisms, pointing to the presence of shared signals (**Figure 5**). Indeed, the molecular comparison among different regenerating vertebrates reveals that FGF and Wnt/β-catenin signaling pathways play fundamental roles during blastema formation and proliferation in all of them and can reasonably be considered as universal regulators of regeneration. An interesting study comparing lizard regenerating tail and scarring limb transcriptomes shows that many genes belonging to the Wnt pathway (*wnt2b, wnt5a, wnt5b, wnt6*) are upregulated in the tail blastema, but absent in the scarring limb. Instead, the scarring

limb expressed genes that act like inhibitors of the Wnt pathway (such as dkk2), impeding cell proliferation, stimulating differentiation and tissue repair leading to scarring [21]. Wnt pathway is also required for axolotl limb regeneration. Overexpression of Axin1, an intracellular inhibitor of the Wnt pathway, in the regenerating limb inhibited regeneration and resulted in spike-like regenerated limbs lacking the digits [180].

FGF1 and FGF2 were detected in the regenerating lizard tail, especially in the wound epidermis and in the spinal cord [181] and inhibition of their activity eventually stopped regeneration [182]. Interestingly, FGFs are absent from lizard scarring limb [183] and if administrated after lizard limb amputation stimulate the formation of the AEP and the regeneration of cartilaginous femur, tibia, and fibula, although never of an autopodium (digits), confirming their requirement for a successful regeneration [184]. During salamander limb blastema formation, *fgf8* and *fgf10*, already present in the intact limb, are upregulated [185]. It has been proposed that this pattern of expression correlates with the "readiness" to regenerate [185]. Denervation of the limb prevents *fgf8* and *fgf10* upregulation [185], given their neurotrophic properties [186]. In zebrafish, the wound healing phase begins immediately following the amputation coinciding with the induction of *wnt10a* and *fgf20a* [43,56]. Disruption of either signaling pathways using transgenic fish lines or pharmacological inhibitors resulted in an abnormal wound epidermis and altered blastema formation [43,56,187]. A strong expression of *aldh1a2*, the rate-limiting enzyme in RA synthesis, was also detected early in the stump. RA administration increased the levels of Wnt/β-catenin and FGF ligands *wnt10b* and *fgf20a*, demonstrating that these signals belong to a complex network orchestrating and coordinating blastema formation [188]. After blastema forms, it compartmentalizes in two domains: a low proliferating distal-most blastema, and a large proximal blastema populated by highly proliferating and differentiating cells [81]. RA, Wnt/ β-catenin and FGF pathways remain active in the blastema to sustain proliferation and survival. Noncanonical Wnt signaling mediated by wnt5b, instead, plays an antagonistic role and inhibits regeneration [43]. The induction of cell proliferation is one of the essential and early stages of regeneration. Recently, Myristoylated alanine-rich C-kinase substrate (MARCKS)-like protein (MLP) was identified to be responsible for the induction of an early regenerative response in axolotl tail and limbs [189]. MARCKS, and MARCKS-like proteins, have been previously described as widely distributed, intracellular substrate for protein kinase C (PKC) that coordinate membrane–cytoskeletal signaling events, such as cell adhesion, membrane trafficking, and phagocytosis [190,191]. In vivo injection of Axolotl MLP (AxMLP) into uninjured axolotl tissue induces cell cycle re-entry of multiple cell types, such as epidermis, spinal cord, notochord and myotubes, while its morpholino knock-down prevents cell cycle onset and

regeneration [189]. Interestingly, despite the protein lacking a signal peptide [192], immunohistochemical analysis of AxMLP distribution in epidermal and spinal cord tissues shows that the protein was mostly cytoplasmic in uninjured tissue, and, following injury, was translocated to the membrane and secreted [189]. How AxMLP induces cell proliferation and is extracellular release is still unknown. The induction of MARCK-like protein in the lizard regenerating tail suggests that this protein may be an initiator of regeneration also in this organism [21,70]. Since MLP secretion was reported only in axolotl so far, it would be interesting to assess if this unconventional process is also present in other vertebrates with regenerative ability. The communication between wound epidermis and blastema is fundamental to achieve regeneration. IGF signaling, already known as a regulator of cell growth during development [193], seems to mediate this epidermis-blastema interaction [46]. The ligand *igf2b* is expressed in the zebrafish caudal fin blastema, whereas signal-responsive cells expressing its receptors *igf1ra/b* are located in the wound epidermis. The activation of Igf1r signaling in the wound epidermis promotes and sustains cell survival and wound epidermis specification, but more importantly, it is required also for the normal blastema formation. The inhibition of the signaling affects the expression of both wound epithelial markers *wnt5b* and *lef1* and blastemal markers *msxb* and *fgf20a* [46]. Whereas other members of the TGF-β superfamily are needed in the early phases of the regenerative program, such as activin-βA [99,194], the bone morphogenetic proteins (BMP) pathway is recruited later in the post-blastema phase to promote patterning and morphogenesis. As revealed by investigation on lizard *A. carolinensis*, BMP signaling mediated by BMP-2 and BMP-6 regulates proximal cartilage proliferation and hypertrophy during tail regeneration [100]. Dedifferentiation of muscle cells in the salamander limb blastema in vivo was shown to occur thanks to the activation of BMPs [195]. Another proposed role for BMP signaling during limb regeneration is to trigger cell condensation and apoptosis. In fact, the overexpression of Noggin, a general inhibitor of all BMPs, inhibits both processes [196]. BMPs are expressed in fin osteoblasts during regeneration in zebrafish [197]. A recent work suggests that BMP signaling acts in the later phases of regeneration by activating *dkk* proteins to counter growth induced by the Wnt pathway and promote osteoblasts differentiation [198]. The overexpression of chordin, another BMP signaling inhibitor, in the regenerating caudal fin leads to a reduction in bone matrix deposition due to defects in the maturation and function of bone-secreting cells [197]. *Hsp70* promoter-driven expression of noggin 3 in transgenic fish causes a regression of the outgrowth in regenerating caudal fin exposed at heat shock between 3 and 4 days post-amputation (dpa) [199]. *Sox9a* and *sox9b* genes, known to be involved in condensation and chondrocyte differentiation, are detectable in zebrafish regenerating fin, which has a dermal origin. Their different pattern of expression (mesenchymal cells of the blastema and basal epidermal layer, respectively) and different response to BMP inhibition

(only *sox9a* is downregulated) suggest that they could be regulated by different pathways in the regenerate [197]. Msx homeobox genes, the immediate early BMP response transcription factors [200], are thought to have a role in development and regeneration as well. Despite the lack of expression in *Anolis carolinensis* [20] and *Gekko japonicus* [201], a proximal–distal gradient of Msx1-and -2 generated from the apical blastema was detected in the regenerating tail of the lizard *Podarcis muralis* [202], suggesting a role in blastema maintenance for these proteins in this model. In regenerating urodele limbs, the two Msx genes are differentially expressed: the Msx2 gene is rapidly induced in the wound epidermis and subjacent tissues after amputation, while the Msx1 gene expression is induced only in blastema cells [203]. They possibly have different functional roles, with Msx2 being implicated in wound epidermis-blastema interaction and Msx1 acting to control blastema cells proliferation. The induction of Msx1 expression has been demonstrated to activate salamander myotubes cell cycle entry in vitro [107], suggesting that this molecule may control cellular plasticity during salamander limb regeneration. Finally, Msx genes also have been demonstrated to participate in zebrafish fin regeneration [204]. Zebrafish *msxb/msxc* genes, related to Msx genes of tetrapods [205], are upregulated early in the blastema and were demonstrated to be dependent on Fgfr1 expression [187]. Also, *msxb* shows an interesting pattern of expression during the regenerative outgrowth. In the immature blastema, *msxb* is expressed by slow proliferating blastemal cells. After blastema compartmentalization, *msxb* expression localizes in the distal blastema, suggesting that it acts in this compartment to regulate cell cycle and proliferation [206], similarly to axolotl Msx1 [203]. Confirming this functional role, morpholino knockdown of *msxb* prevented cell proliferation and fin outgrowth [207]. The Hedgehog signaling is possibly the key player of the last phase of regeneration. The morphogen sonic hedgehog (Shh) is expressed in the regions surrounding the ependymal tube in the regenerating lizard tail, where it establishes proximal organization centers and induces chondrogenesis in lizard blastemal cells. Its pattern of expression along the circumference of the tail is probably related to the characteristic lack of dorsal-ventral patterning of the regenerating tail [100]. Developmental studies demonstrated that outgrowth and patterning of salamander limb bud is coordinated by a positive feedback loop between Shh and Fgf [208]. In salamander regenerating limbs, *shh* localizes in the posterior part of the blastema, immediately adjacent to the AEC [209]. A recent study demonstrated that stimulating the Shh signaling pathway in anterior innervated limb tissue was sufficient to sustain limb regeneration and form a normal limb. The posterior cells, instead, are “refractory” and do not respond to *shh* stimulation but proliferate only after overexpression of *fgf8*. Thus, similarly to the developmental process, posteriorly localized shh signal supports anterior expression of *fgf8* in a positive feedback loop that ultimately leads to proliferation and eventually patterning of the limb [210]. In zebrafish regenerating fin, the shh gene is expressed in the cells of

the basal layer of the epidermis, in the area surrounding newly forming fin rays [211]. The bone morphogenetic protein *bmp2* is expressed in both the basal epidermal cells and the adjacent blastema. *Shh* and *bmp2* expression in epidermis is further regulated by cell-cell interactions between basal epidermal cells and blastema [211]. Ectopic expression of *shh* or *bmp2* in the blastema results in bone deposition between fin rays and mispatterning of the regenerated fin [212]. The exposure to cyclopamine, inhibitors of the Shh signaling, reduces proliferation and differentiation of specialized bone-secreting cells within the blastema [212]. *Shh* has also a role in bone patterning and ray branching morphogenesis [213,214].

Taken together, these findings show to what extent the signaling pathways underlying the regenerative processes in different vertebrates are shared. Despite some difference, it seems that there are conserved molecular key players of regeneration that induce similar cellular responses and similar outcomes across phylogeny. Our knowledge is far from complete, but future studies will help unravelling what are the precise functions of these signals and how they differ among different organisms and perhaps will allow for the molecular manipulation of the regeneration process in mammals.

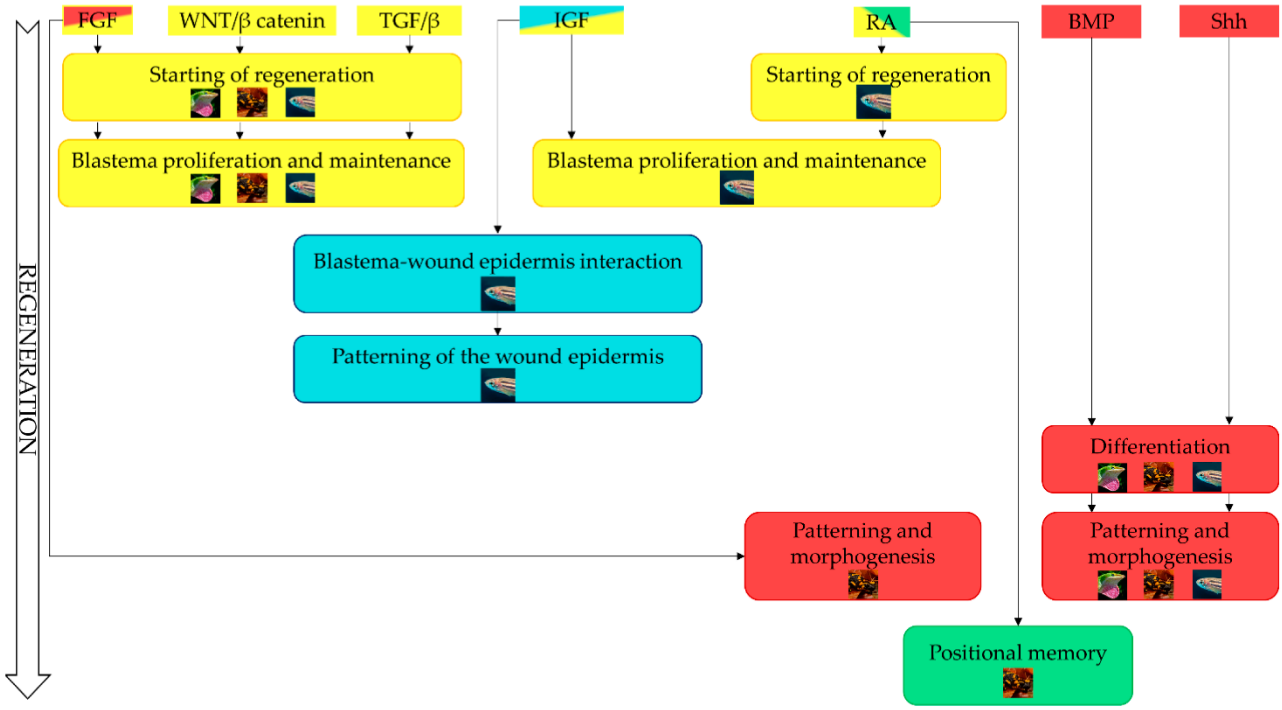

Figure 5. Schematic representation of the molecular signaling regulating the steps of appendage regeneration in vertebrates.

Regeneration and Aging

The aging process is associated with an imbalance between the accumulation of senescent cells and the rate of cell renewal [215]. Interestingly, many invertebrates with high regenerative potential as adults, such as hydra and planaria, show no signs of aging [216–218] supporting a link between regeneration and aging. Various intrinsic and extrinsic factors are associated with the decline of regenerative capacity upon aging: genomic instability, telomere shortening, oxidative damage among the others [219]. The comparative studies of vertebrates with extensive regenerative abilities is a powerful tool to better understand the relationship between regeneration and aging. Unfortunately, only limited work has been done on the topic, but the consensus is that embryos, larvae, and juveniles of diverse species have a stronger regenerative potential compared to older individuals. A study on embryonic and post-natal common lizards (*Lacerta vivipara*) demonstrated that after tail amputation at different stages of embryonic development, regeneration occurs only in late-stage embryos, while early-stage embryos fail to regenerate [220]. The explanation for these unexpected results could be linked to the evolution of tail regeneration in lizards. The process of autotomy as an anti-predation strategy is probably the consequence of natural selection and has no meaning in amniote embryos, which are already protected by their mother's body. Further studies are needed to confirm this hypothesis. Salamanders and zebrafish, however, exhibit extensive and time stable ability to regenerate their appendages. It was demonstrated that salamanders have a strong immune-mediated mechanism that rapidly recognizes and clears senescent cells during limb regeneration [150]. Moreover, both their normal and regenerating tissues show no accumulation of senescent cells with aging [150]. Taken together, these findings may indicate that efficient turnover of senescent cells is a physiological mechanism that can mediate aging and regeneration in these organisms. Thyroxine-induced metamorphosis in age-matched axolotls resulted in reduced regeneration rate and fidelity and increases in the occurrence of morphological alterations in the limb [221], indicating patterning and growth alterations. Also, metamorphosis seems to alter cell dynamics during regeneration and decreases the number of proliferating blastema cells [221]. Metamorphosis is not necessarily related to age; however, these findings imply that developmental stages are important modulators of regeneration rate. Another view of metamorphosis as a destructive and reconstructive process providing molecular and cellular sources that can be re-utilized during adult life to regenerate appendages has been recently suggested [222,223]. Indeed, various genes expressed during metamorphosis are also upregulated during regeneration in amphibians and fish [223]. More detailed research will be relevant to clarify this correlation. The relationship between aging and regeneration rate and ability is poorly understood also in zebrafish. Although age and sex-related differences seem

to affect regeneration of the pectoral fin [224], the results reported for caudal fin regeneration remain controversial. A study showed that fin regeneration was impaired, and telomerase activity was reduced in the regenerating fin of older fish, indicating a correlation between telomerase activity, a marker of aging, and regeneration efficiency [225]. Genotoxic stress caused by ionizing radiation was also shown to enhance the process of aging and impair caudal fin regeneration [226]. Contrary to these results, another study reported a comparable caudal fin regeneration rate between young and old fish and supported the idea that zebrafish keep their regeneration capacity throughout the lifespan [227].

Many factors affect the aging and regenerative processes and unraveling the correlation among them is difficult. More studies are needed in order to clarify what are the regenerative-time windows in vertebrates and the nature of the genetic and epigenetic alterations that occur during lifespan and change regenerative capacity. This type of study would have implication not only in regenerative medicine but could also help to understand what are the factors that affect aging and age-related disorders in humans.

Regeneration Models as a Tool for Biomedical Research

Zebrafish is not only a fascinating example of vertebrate regeneration, but also represents a well-known vertebrate model for disease and has already contributed to several examples of successful phenotype-based drug discovery, providing a tool with many different applications in biomedical research, especially in the field of bone biology. Indeed, zebrafish skeleton conserves the general basis of development, gene expression and cell types that are found in mammals [47]. In this scenario, the remarkably fast regeneration of zebrafish caudal fin provides an excellent tool to easy monitor bone formation over time in healthy and pathological conditions [47]. The evaluation of bone regeneration rate can be performed in combination with drug administration to discover new molecules promoting regenerative and/or osteogenic activity. As an example, after fin amputation bone growth can be followed in juveniles kept in small tanks with limited water volumes and amount of drug, allowing high throughput analysis at low cost [228]. To these purposes, the availability of transgenic lines and bone assays including fluorescent dyes such as calcein and alizarin red, which stain calcified tissue, provides a simple and fast way to visualize the effect of a specific compound on bone [229]. One of the challenges for such approaches is how to control and predict the amount of the administrated drug although direct injection of the drug in fin rays can be used to overcome this limitation [230].

At the time, regeneration in other vertebrate models such as lizard and salamander is not exploited for drug discovery, but the rapid advances in molecular techniques could likely overcome such obstacle.

Conclusions

Mammals, humans included, are incapable of regenerating amputated or lost limbs. Damage or injury can be sometimes life threatening and is reasonable to wonder how we might be able to enhance our own regenerative potential. For this purpose, the understanding of cellular and molecular mechanisms orchestrating regeneration is crucial. In the past years, the field of regenerative biology has seen considerable progress, particularly thanks to the study of organisms with a high regenerative potential. Although morphological mechanisms and cell contributors of regeneration can vary widely even among close species, the comparison of the three vertebrate models here discussed allows to identify an overall common strategy to successfully restore a lost appendage. So, what makes this possible? As it seems, a combination of multiple factors. First, the formation of a thick wound epidermis/AEC that supports the regenerative process without scarring. The formation of a blastema, which provides the source of differentiated cells that will restore the lost tissues is the key process present in vertebrates with regenerative ability. Proper activation of specific molecular pathways has been proven necessary for successful regeneration. The data collected on the three described models unequivocally points to the role of Wnt/β-catenin and FGFs as master regulators of the process. The expression of these key molecules is not only necessary for regeneration to occur but is also able to promote it in organs with limited regenerative potential, such as lizard limb. Blastema growth is also strictly related to the level of immunosurveillance. Lizard tail, salamander limb and zebrafish caudal fin can be considered immuno-privileged organs, in which inflammation triggered by injury equilibrates with the presence of healing, anti-inflammatory macrophages. Each model presents advantages and limitations. Salamanders are considered the master regenerators being the only vertebrate able to regenerate a full limb. Since its discovery in the 18th century [231], the regenerating limb system was used to perform fundamental experiments to delineate the basic properties of regeneration. However, many aspects of the urodelian life cycle are at odds with those of higher vertebrates. The axolotl, the most used salamander for regenerative studies, is neotenic and retains all its juvenile features even when it reaches adulthood. Lizards, on the other hand, follow a similar development as mammals and therefore are more appealing from a developmental point of view. However, as amniotes, their regenerative ability is restricted to the complex structure of the tail, and their lost appendages undergo an imperfect regeneration. Given the simplicity of using powerful genetic tools, zebrafish has quickly emerged as a model of choice to study regeneration. Zebrafish

present several advantages, such as the external fertilization and the transparency of embryos that makes them particularly appealing for forward genetic approaches allowing to investigate regeneration in health and disease. Our knowledge of regenerative mechanisms is strictly related to the tools we can use. Thus, the possibility to apply more advanced genetic tools also on powerful regenerators such as salamander and lizard could represent a key step forward. The recent reports of Iberian ribbed newt (*Pleurodeles waltl*) and axolotl (*Ambystoma mexicanum*) complete genomes, together with the recent generation of a CRISPR/Cas9 Anolis lizard, will hopefully provide new tools to increase the use of these organisms to find the answer to regenerative questions still unsolved. No unique model for regeneration exists, and the comparative study of vertebrates with high regenerative ability is fundamental to achieve significant insights on what are the factors driving regeneration, aiming to translate them into the field of regenerative medicine. Indeed, the field of regenerative biology has made an enormous step forward in the past decade, taking advance of imaging, genomics, and genome editing to identify key cell types and molecules involved in the regeneration of many model organisms. Yet, it can be difficult to foresee when and how findings from these studies will really advance regenerative medicine. The identification of genes modulating the origins and fates of blastemal progenitor cells will likely be the key to achieve appendage regeneration, and it will provide novel targets for gene manipulation in mammals.

Author Contributions: Conceptualization, V.D., P.T. and A.F.; writing—original draft preparation, V.D.; writing—review and editing, V.D., P.T. and A.F.; visualization, V.D.; funding acquisition, A.F. All authors have read and agreed to the published version of the manuscript.

Funding: This project has received funding by Italian Ministry of Education, University and Research (MIUR) [Dipartimenti di Eccellenza (2018–2022)].

Institutional Review Board Statement: Not applicable.

Informed Consent Statement: Not applicable.

Data Availability Statement: Data sharing not applicable.

Conflicts of Interest: The authors declare no conflict of interest. The funders had no role in the writing of the manuscript, or in the content of the review.

Manuscript 2 - References

1. Joven, A.; Elewa, A.; Simon, A. Model systems for regeneration: Salamanders. *Development* **2019**, *146*.
2. Darnet, S.; Dragalzew, A.C.; Amaral, D.B.; Sousa, J.F.; Thompson, A.W.; Cass, A.N.; Lorena, J.; Pires, E.S.; Costa, C.M.; Sousa, M.P.; et al. Deep evolutionary origin of limb and fin regeneration. *Proc. Natl. Acad. Sci. USA* **2019**, *116*, 15106–15115.
3. Gemberling, M.; Bailey, T.J.; Hyde, D.R.; Poss, K.D. The zebrafish as a model for complex tissue regeneration. *Trends Genet.* **2013**, *29*, 611–620.
4. Jafari, P.; Muller, C.; Grognuz, A.; Applegate, L.A.; Raffoul, W.; di Summa, P.G.; Durand, S. First Insights into Human Fingertip Regeneration by Echo-Doppler Imaging and Wound Microenvironment Assessment. *Int. J. Mol. Sci.* **2017**, *18*, 1054.
5. Seifert, A.W.; Muneoka, K. The blastema and epimorphic regeneration in mammals. *Dev. Biol.* **2018**, *433*, 190–199.
6. Matias Santos, D.; Rita, A.M.; Casanellas, I.; Brito Ova, A.; Araújo, I.M.; Power, D.; Tiscornia, G. Ear wound regeneration in the African spiny mouse Acomys cahirinus. *Regeneration* **2016**, *3*, 52–61.
7. Kierdorf, U.; Kierdorf, H.; Szuwart, T. Deer antler regeneration: Cells, concepts, and controversies. *J. Morphol.* **2007**, *268*, 726–738.
8. Jacyniak, K.; McDonald, R.P.; Vickaryous, M.K. Tail regeneration and other phenomena of wound healing and tissue restoration in lizards. *J. Exp. Biol.* **2017**, *220*, 2858–2869.
9. Bely, A.E.; Nyberg, K.G. Evolution of animal regeneration: Re-emergence of a field. *Trends Ecol. Evol.* **2010**, *25*, 161–170.
10. Maginnis, T.L. The costs of autotomy and regeneration in animals: A review and framework for future research. *Behav. Ecol.* **2006**, *17*, 857–872.
11. Da Silva, S.M.; Gates, P.B.; Brockes, J.P. The Newt Ortholog of CD59 Is Implicated in Proximodistal Identity during Amphibian Limb Regeneration. *Dev. Cell* **2002**, *3*, 547–555.
12. Wang, Y.; Wang, R.; Jiang, S.; Zhou, W.; Liu, Y.; Wang, Y.; Gu, Q.; Gu, Y.; Dong, Y.; Liu, M.; et al. Gecko CD59 is implicated in proximodistal identity during tail regeneration. *PLoS ONE* **2011**, *6*, e17878.
13. Kumar, A.; Gates, P.B.; Brockes, J.P. Positional identity of adult stem cells in salamander limb regeneration. *C R Biol.* **2007**, *330*, 485–490.

14. Wagner, G.P.; Misof, B.Y. Evolutionary modification of regenerative capability in vertebrates: A comparative study on teleost pectoral fin regeneration. *J. Exp. Zool.* **1992**, *261*, 62–78.
15. Cuervo, R.; Hernández-Martínez, R.; Chimal-Monroy, J.; Merchant-Larios, H.; Covarrubias, L. Full regeneration of the tribasal Polypterus fin. *Proc. Natl. Acad. Sci. USA* **2012**, *109*, 3838–3843.
16. Noack, K.; Zardoya, R.; Meyer, A. The complete mitochondrial DNA sequence of the bichir (Polypterus ornatipinnis), a basal ray-finned fish: Ancient establishment of the consensus vertebrate gene order. *Genetics* **1996**, *144*, 1165–1180.
17. Mescher, A.L. Macrophages and fibroblasts during inflammation and tissue repair in models of organ regeneration. *Regeneration (Oxf)* **2017**, *4*, 39–53.
18. Slack, J.M. Animal regeneration: Ancestral character or evolutionary novelty? *EMBO Rep.* **2017**, *18*, 1497–1508.
19. Alfoldi, J.; Di Palma, F.; Grabherr, M.; Williams, C.; Kong, L.; Mauceli, E.; Russell, P.; Lowe, C.B.; Glor, R.E.; Jaffe, J.D.; et al. The genome of the green anole lizard and a comparative analysis with birds and mammals. *Nature* **2011**, *477*, 587–591.
20. Hutchins, E.D.; Markov, G.J.; Eckalbar, W.L.; George, R.M.; King, J.M.; Tokuyama, M.A.; Geiger, L.A.; Emmert, N.; Ammar, M.J.; Allen, A.N.; et al. Transcriptomic analysis of tail regeneration in the lizard Anolis carolinensis reveals activation of conserved vertebrate developmental and repair mechanisms. *PLoS ONE* **2014**, *9*, e105004.
21. Vitulo, N.; Dalla Valle, L.; Skobo, T.; Valle, G.; Alibardi, L. Transcriptome analysis of the regenerating tail vs. the scarring limb in lizard reveals pathways leading to successful vs. unsuccessful organ regeneration in amniotes. *Dev. Dyn.* **2017**, *246*, 116–134.
22. Vitulo, N.; Dalla Valle, L.; Skobo, T.; Valle, G.; Alibardi, L. Downregulation of lizard immuno-genes in the regenerating tail and myogenes in the scarring limb suggests that tail regeneration occurs in an immuno-privileged organ. *Protoplasma* **2017**, *254*, 2127–2141.
23. Degan, M.; Dalla Valle, L.; Alibardi, L. Gene expression in regenerating and scarring tails of lizard evidences three main key genes (wnt2b, egfl6, and arhgap28) activated during the regulated process of tail regeneration. *Protoplasma* **2020**.
24. Xu, C.; Hutchins, E.D.; Tokuyama, M.A.; Wilson-Rawls, J.; Kusumi, K. Transcriptional analysis of scar-free wound healing during early stages of tail regeneration in the green anole lizard, Anolis carolinensis. *J. Immunol. Regen. Med.* **2020**, *7*, 100025.

25. Rasys, A.M.; Park, S.; Ball, R.E.; Alcala, A.J.; Lauderdale, J.D.; Menke, D.B. CRISPR-Cas9 Gene Editing in Lizards through Microinjection of Unfertilized Oocytes. *Cell Rep.* **2019**, *28*, 2288–2292.
26. Tazaki, A.; Tanaka, E.M.; Fei, J.F. Salamander spinal cord regeneration: The ultimate positive control in vertebrate spinal cord regeneration. *Dev. Biol.* **2017**, *432*, 63–71.
27. Godwin, J.W.; Debuque, R.; Salimova, E.; Rosenthal, N.A. Heart regeneration in the salamander relies on macrophage-mediated control of fibroblast activation and the extracellular landscape. *NPJ Regen. Med.* **2017**, *2*, 1–11.
28. Kumar, A.; Simon, A. *Salamanders in Regeneration Research: Methods and Protocols*; Springer: Berlin, Germany, 2015; pp. 1–357.
29. Elewa, A.; Wang, H.; Talavera-Lopez, C.; Joven, A.; Brito, G.; Kumar, A.; Hameed, L.S.; Penrad-Mobayed, M.; Yao, Z.; Zamani, N.; et al. Reading and editing the Pleurodeles waltl genome reveals novel features of tetrapod regeneration. *Nat. Commun.* **2017**, *8*, 2286.
30. Kragl, M.; Knapp, D.; Nacu, E.; Khattak, S.; Maden, M.; Epperlein, H.H.; Tanaka, E.M. Cells keep a memory of their tissue origin during axolotl limb regeneration. *Nature* **2009**, *460*, 60–65.
31. Zhu, W.; Pao, G.M.; Satoh, A.; Cummings, G.; Monaghan, J.R.; Harkins, T.T.; Bryant, S.V.; Randal Voss, S.; Gardiner, D.M.; Hunter, T. Activation of germline-specific genes is required for limb regeneration in the Mexican axolotl. *Dev. Biol.* **2012**, *370*, 42–51.
32. Hayashi, T.; Takeuchi, T. Mutagenesis in Newts: Protocol for Iberian Ribbed Newts. *Methods Mol. Biol.* **2016**, *1338*, 119–126.
33. Sun, C.; Shepard, D.B.; Chong, R.A.; Lopez Arriaza, J.; Hall, K.; Castoe, T.A.; Feschotte, C.; Pollock, D.D.; Mueller, R.L. LTR retrotransposons contribute to genomic gigantism in plethodontid salamanders. *Genome Biol. Evol.* **2012**, *4*, 168–183.
34. Nowoshilow, S.; Schloissnig, S.; Fei, J.F.; Dahl, A.; Pang, A.W.C.; Pippel, M.; Winkler, S.; Hastie, A.R.; Young, G.; Roscito, J.G.; et al. The axolotl genome and the evolution of key tissue formation regulators. *Nature* **2018**, *554*, 50–55.
35. Smith, J.J.; Timoshevskaya, N.; Timoshevskiy, V.A.; Keinath, M.C.; Hardy, D.; Voss, S.R. A chromosome-scale assembly of the axolotl genome. *Genome Res.* **2019**, *29*, 317–324.
36. Flowers, G.P.; Timberlake, A.T.; McLean, K.C.; Monaghan, J.R.; Crews, C.M. Highly efficient targeted mutagenesis in axolotl using Cas9 RNA-guided nuclease. *Development* **2014**, *141*, 2165–2171.

37. Dwaraka, V.B.; Smith, J.J.; Woodcock, M.R.; Voss, S.R. Comparative transcriptomics of limb regeneration: Identification of conserved expression changes among three species of Ambystoma. *Genomics* **2019**, *111*, 1216–1225.
38. Gerber, T.; Murawala, P.; Knapp, D.; Masselink, W.; Schuez, M.; Hermann, S.; Gac-Santel, M.; Nowoshilow, S.; Kageyama, J.; Khattak, S.; et al. Single-cell analysis uncovers convergence of cell identities during axolotl limb regeneration. *Science* **2018**, *362*.
39. Howe, K.; Clark, M.D.; Torroja, C.F.; Torrance, J.; Berthelot, C.; Muffato, M.; Collins, J.E.; Humphray, S.; McLaren, K.; Matthews, L.; et al. The zebrafish reference genome sequence and its relationship to the human genome. *Nature* **2013**, *496*, 498–503.
40. Schebesta, M.; Lien, C.L.; Engel, F.B.; Keating, M.T. Transcriptional profiling of caudal fin regeneration in zebrafish. *ScientificWorldJournal* **2006**, *6* (Suppl. 1), 38–54.
41. Rabinowitz, J.S.; Robitaille, A.M.; Wang, Y.; Ray, C.A.; Thummel, R.; Gu, H.; Djukovic, D.; Raftery, D.; Berndt, J.D.; Moon, R.T. Transcriptomic, proteomic, and metabolomic landscape of positional memory in the caudal fin of zebrafish. *Proc. Natl. Acad. Sci. USA* **2017**, *114*, E717–E726.
42. Nauroy, P.; Guiraud, A.; Chlasta, J.; Malbouyres, M.; Gillet, B.; Hughes, S.; Lambert, E.; Ruggiero, F. Gene profile of zebrafish fin regeneration offers clues to kinetics, organization and biomechanics of basement membrane. *Matrix Biol.* **2019**, *75–76*, 82–101.
43. Stoick-Cooper, C.L.; Weidinger, G.; Riehle, K.J.; Hubbert, C.; Major, M.B.; Fausto, N.; Moon, R.T. Distinct Wnt signaling pathways have opposing roles in appendage regeneration. *Development* **2007**, *134*, 479–489.
44. Knopf, F.; Hammond, C.; Chekuru, A.; Kurth, T.; Hans, S.; Weber, C.W.; Mahatma, G.; Fisher, S.; Brand, M.; Schulte-Merker, S.; et al. Bone regenerates via dedifferentiation of osteoblasts in the zebrafish fin. *Dev. Cell* **2011**, *20*, 713–724.
45. Wehner, D.; Cizelsky, W.; Vasudevaro, M.D.; Ozhan, G.; Haase, C.; Kagermeier-Schenk, B.; Roder, A.; Dorsky, R.I.; Moro, E.; Argenton, F.; et al. Wnt/beta-catenin signaling defines organizing centers that orchestrate growth and differentiation of the regenerating zebrafish caudal fin. *Cell Rep.* **2014**, *6*, 467–481.
46. Chablais, F.; Jazwinska, A. IGF signaling between blastema and wound epidermis is required for fin regeneration. *Development* **2010**, *137*, 871–879.
47. Tonelli, F.; Bek, J.W.; Besio, R.; De Clercq, A.; Leoni, L.; Salmon, P.; Coucke, P.J.; Willaert, A.; Forlino, A. Zebrafish: A Resourceful Vertebrate Model to Investigate Skeletal Disorders. *Front. Endocrinol.* **2020**, *11*.

48. Wise, P.A.D.; Vickaryous, M.K.; Russell, A.P. An Embryonic Staging Table for In Ovo Development of Eublepharis macularius, the Leopard Gecko. *Anat. Rec.* **2009**, *292*, 1198–1212.
49. Zhang, Y.; Du, W.; Zhu, L.-J. Differences in body size and female reproductive traits between two sympatric geckos, Gekko japonicus and Gekko hokouensis. *Folia Zool. Praha* **2009**, *58*, 113.
50. Ji, X.; Braña, F. Among Clutch Variation in Reproductive Output and Egg Size in the Wall Lizard (Podarcis muralis) from a Lowland Population of Northern Spain. *J. Herpetol.* **2000**, *34*, 54–60.
51. Kimmel, C.B.; Ballard, W.W.; Kimmel, S.R.; Ullmann, B.; Schilling, T.F. Stages of embryonic development of the zebrafish. *Dev. Dyn.* **1995**, *203*, 253–310.
52. Hayashi, T.; Yokotani, N.; Tane, S.; Matsumoto, A.; Myouga, A.; Okamoto, M.; Takeuchi, T. Molecular genetic system for regenerative studies using newts. *Dev. Growth Differ.* **2013**, *55*, 229–236.
53. Petrie, T.A.; Strand, N.S.; Yang, C.T.; Rabinowitz, J.S.; Moon, R.T. Macrophages modulate adult zebrafish tail fin regeneration. *Development* **2014**, *141*, 2581–2591.
54. Fei, J.-F.; Schuez, M.; Knapp, D.; Taniguchi, Y.; Drechsel, D.N.; Tanaka, E.M. Efficient gene knockin in axolotl and its use to test the role of satellite cells in limb regeneration. *Proc. Natl. Acad. Sci. USA* **2017**, *114*, 12501.
55. Suzuki, M.; Hayashi, T.; Inoue, T.; Agata, K.; Hirayama, M.; Suzuki, M.; Shigenobu, S.; Takeuchi, T.; Yamamoto, T.; Suzuki, K.-i.T. Cas9 ribonucleoprotein complex allows direct and rapid analysis of coding and noncoding regions of target genes in Pleurodeles waltl development and regeneration. *Dev. Biol.* **2018**, *443*, 127–136.
56. Whitehead, G.G.; Makino, S.; Lien, C.L.; Keating, M.T. fgf20 is essential for initiating zebrafish fin regeneration. *Science* **2005**, *310*, 1957–1960.
57. Morgan, T.H. *Regeneration*; Macmillan: New York, NY, USA, 1901.
58. Agata, K.; Saito, Y.; Nakajima, E. Unifying principles of regeneration I: Epimorphosis versus morphallaxis. *Dev. Growth Differ.* **2007**, *49*, 73–78.
59. Carlson, B.M. Chapter 1—An Introduction to Regeneration. In *Principles of Regenerative Biology*; Carlson, B.M., Ed.; Academic Press: Burlington, VT, USA, 2007; pp. 1–29.
60. Fisher, R.E.; Geiger, L.A.; Stroik, L.K.; Hutchins, E.D.; George, R.M.; Denardo, D.F.; Kusumi, K.; Rawls, J.A.; Wilson-Rawls, J. A histological comparison of the original and regenerated tail in the green anole, Anolis carolinensis. *Anat. Rec.* **2012**, *295*, 1609–1619.

61. Londono, R.; Sun, A.X.; Tuan, R.S.; Lozito, T.P. Tissue Repair and Epimorphic Regeneration: An Overview. *Curr. Pathobiol. Rep.* **2018**, *6*, 61–69.
62. Thornton, C.S. The effect of apical cap removal on limb regeneration in Amblystoma larvae. *J. Exp. Zool.* **1957**, *134*, 357–381.
63. Mescher, A.L. Effects on adult newt limb regeneration of partial and complete skin flaps over the amputation surface. *J. Exp. Zool.* **1976**, *195*, 117–128.
64. Alibardi, L. Tail regeneration reduction in lizards after repetitive amputation or cauterization reflects an increase of immune cells in blastemas. *Zool. Res.* **2018**, *39*, 413–423.
65. Bryant, D.M.; Sousounis, K.; Payzin-Dogru, D.; Bryant, S.; Sandoval, A.G.W.; Martinez Fernandez, J.; Mariano, R.; Oshiro, R.; Wong, A.Y.; Leigh, N.D.; et al. Identification of regenerative roadblocks via repeat deployment of limb regeneration in axolotls. *NPJ Regen. Med.* **2017**, *2*, 30.
66. Dearlove, G.E.; Dresden, M.H. Regenerative abnormalities in *Notophthalmus viridescens* induced by repeated amputations. *J. Exp. Zool.* **1976**, *196*, 251–262.
67. Azevedo, A.S.; Grotek, B.; Jacinto, A.; Weidinger, G.; Saúde, L. The Regenerative Capacity of the Zebrafish Caudal Fin Is Not Affected by Repeated Amputations. *PLoS ONE* **2011**, *6*, e22820.
68. Pfefferli, C.; Jazwinska, A. The art of fin regeneration in zebrafish. *Regeneration* **2015**, *2*, 72–83.
69. Stocum, D.L. Mechanisms of urodele limb regeneration. *Regeneration* **2017**, *4*, 159–200.
70. Alibardi, L. Review: Biological and Molecular Differences between Tail Regeneration and Limb Scarring in Lizard: An Inspiring Model Addressing Limb Regeneration in Amniotes. *J. Exp. Zool. B Mol. Dev. Evol.* **2017**, *328*, 493–514.
71. Bai, S.; Thummel, R.; Godwin, A.R.; Nagase, H.; Itoh, Y.; Li, L.; Evans, R.; McDermott, J.; Seiki, M.; Sarras, M.P., Jr. Matrix metalloproteinase expression and function during fin regeneration in zebrafish: Analysis of MT1-MMP, MMP2 and TIMP2. *Matrix Biol.* **2005**, *24*, 247–260.
72. Delorme, S.L.; Lungu, I.M.; Vickaryous, M.K. Scar-free wound healing and regeneration following tail loss in the leopard gecko, Eublepharis macularius. *Anat. Rec.* **2012**, *295*, 1575–1595.
73. Stocum, D.L. Chapter 8—Regeneration of Appendages. In *Regenerative Biology and Medicine*, 2nd ed.; Stocum, D.L., Ed.; Academic Press: San Diego, CA, USA, 2012; pp. 183–226.

74. Thornton, C.S. The histogenesis of the regenerating fore limb of larval Amblystoma after exarticulation of the humerus. *J. Morphol.* **1938**, *62*, 219–241.
75. Campbell, L.J.; Crews, C.M. Molecular and Cellular Basis of Regeneration and Tissue Repair. *Cell. Mol. Life Sci.* **2007**, *65*, 73.
76. Chassot, B.; Pury, D.; Jazwinska, A. Zebrafish fin regeneration after cryoinjury-induced tissue damage. *Biol. Open* **2016**, *5*, 819–828.
77. Alibardi, L. *Morphological and Cellular Aspects of Tail and Limb Regeneration in Lizards. A Model System with Implications for Tissue Regeneration in Mammals*; Springer: Berlin, Germany, 2010; Volume 207, pp. 1–112.
78. Gilbert, E.A.; Delorme, S.L.; Vickaryous, M.K. The regeneration blastema of lizards: An amniote model for the study of appendage replacement. *Regeneration* **2015**, *2*, 45–53.
79. Rao, N.; Jhamb, D.; Milner, D.J.; Li, B.; Song, F.; Wang, M.; Voss, S.R.; Palakal, M.; King, M.W.; Saranjami, B.; et al. Proteomic analysis of blastema formation in regenerating axolotl limbs. *BMC Biol.* **2009**, *7*, 83.
80. McCusker, C.; Bryant, S.V.; Gardiner, D.M. The axolotl limb blastema: Cellular and molecular mechanisms driving blastema formation and limb regeneration in tetrapods. *Regeneration* **2015**, *2*, 54–71.
81. Iovine, M.K. Conserved mechanisms regulate outgrowth in zebrafish fins. *Nat. Chem. Biol.* **2007**, *3*, 613–618.
82. Weissman, I.L.; Anderson, D.J.; Gage, F. Stem and progenitor cells: Origins, phenotypes, lineage commitments, and transdifferentiations. *Annu. Rev. Cell Dev. Biol.* **2001**, *17*, 387–403.
83. Lowry, W.E.; Richter, L.; Yachechko, R.; Pyle, A.D.; Tchieu, J.; Sridharan, R.; Clark, A.T.; Plath, K. Generation of human induced pluripotent stem cells from dermal fibroblasts. *Proc. Natl. Acad. Sci. USA* **2008**, *105*, 2883–2888.
84. Colucci, V. Sulla rigenerazione parziale dell'occhio nei tritoni: Istogenesi e sviluppo. *Mem. Accad. Sci. Ist. Bologna Ser.* **1891**, *5*, 593–629.
85. Wolff, G. Entwicklungsphysiologische Studien. *Arch. Für Mikrosk. Anat.* **1895**, *1*, 380–390.
86. Jopling, C.; Boue, S.; Izpisua Belmonte, J.C. Dedifferentiation, transdifferentiation and reprogramming: Three routes to regeneration. *Nat. Rev. Mol. Cell Biol.* **2011**, *12*, 79–89.
87. Merrell, A.J.; Stanger, B.Z. Adult cell plasticity in vivo: De-differentiation and transdifferentiation are back in style. *Nat. Rev. Mol. Cell Biol.* **2016**, *17*, 413–425.

88. Ahrens, T.D.; Caglayan, S.; Staerk, J.; Cieślar-Pobuda, A. Chapter 4—Transdifferentiation—Changing Cell Identity. In *Stem Cells and Biomaterials for Regenerative Medicine*; Łos, M.J., Hudecki, A., Wiecheć, E., Eds.; Academic Press: Cambridge, MA, USA, 2019; pp. 37–56.
89. Alibardi, L. Immunolocalization indicates that both original and regenerated lizard tail tissues contain populations of long retaining cells, putative stem/progenitor cells. *Microsc. Res. Tech.* **2015**, *78*, 1032–1045.
90. Alibardi, L. Original and regenerating lizard tail cartilage contain putative resident stem/progenitor cells. *Micron* **2015**, *78*, 10–18.
91. Alibardi, L. Immunolocalization of c-myc-positive cells in lizard tail after amputation suggests cell activation and proliferation for tail regeneration. *Acta Zool.* **2017**, *98*, 114–124.
92. Alibardi, L. Immunocalization of telomerase in cells of lizard tail after amputation suggests cell activation for tail regeneration. *Tissue Cell* **2016**, *48*, 63–71.
93. Palade, J.; Djordjevic, D.; Hutchins, E.D.; George, R.M.; Cornelius, J.A.; Rawls, A.; Ho, J.W.K.; Kusumi, K.; Wilson-Rawls, J. Identification of satellite cells from anole lizard skeletal muscle and demonstration of expanded musculoskeletal potential. *Dev. Biol.* **2018**, *433*, 344–356.
94. Alibardi, L. Ultrastructural analysis of early regenerating lizard tail suggests that a process of dedifferentiation is involved in the formation of the regenerative blastema. *J. Morphol.* **2018**, *279*, 1171–1184.
95. Londono, R.; Wenzhong, W.; Wang, B.; Tuan, R.S.; Lozito, T.P. Cartilage and Muscle Cell Fate and Origins during Lizard Tail Regeneration. *Front. Bioeng. Biotechnol.* **2017**, *5*, 70.
96. Echeverri, K.; Clarke, J.D.; Tanaka, E.M. In vivo imaging indicates muscle fiber dedifferentiation is a major contributor to the regenerating tail blastema. *Dev. Biol.* **2001**, *236*, 151–164.
97. Griffith, C.M.; Wiley, M.J.; Sanders, E.J. The vertebrate tail bud: Three germ layers from one tissue. *Anat. Embryol.* **1992**, *185*, 101–113.
98. McLean, K.E.; Vickaryous, M.K. A novel amniote model of epimorphic regeneration: The leopard gecko, *Eublepharis macularius*. *BMC Dev. Biol.* **2011**, *11*, 50.
99. Gilbert, R.W.; Vickaryous, M.K.; Viloria-Petit, A.M. Characterization of TGFbeta signaling during tail regeneration in the leopard Gecko (*Eublepharis macularius*). *Dev. Dyn.* **2013**, *242*, 886–896.
100. Lozito, T.P.; Tuan, R.S. Lizard tail skeletal regeneration combines aspects of fracture healing and blastema-based regeneration. *Development* **2016**, *143*, 2946–2957.

101. Morrison, J.I.; Loof, S.; He, P.; Simon, A. Salamander limb regeneration involves the activation of a multipotent skeletal muscle satellite cell population. *J. Cell Biol.* **2006**, *172*, 433–440.

102. Sandoval-Guzman, T.; Wang, H.; Khattak, S.; Schuez, M.; Roensch, K.; Nacu, E.; Tazaki, A.; Joven, A.; Tanaka, E.M.; Simon, A. Fundamental differences in dedifferentiation and stem cell recruitment during skeletal muscle regeneration in two salamander species. *Cell Stem Cell* **2014**, *14*, 174–187.

103. Leigh, N.D.; Dunlap, G.S.; Johnson, K.; Mariano, R.; Oshiro, R.; Wong, A.Y.; Bryant, D.M.; Miller, B.M.; Ratner, A.; Chen, A.; et al. Transcriptomic landscape of the blastema niche in regenerating adult axolotl limbs at single-cell resolution. *Nat. Commun.* **2018**, *9*, 5153.

104. Sousa, S.; Afonso, N.; Bensimon-Brito, A.; Fonseca, M.; Simoes, M.; Leon, J.; Roehl, H.; Cancela, M.L.; Jacinto, A. Differentiated skeletal cells contribute to blastema formation during zebrafish fin regeneration. *Development* **2011**, *138*, 3897–3905.

105. Tu, S.; Johnson, S.L. Fate restriction in the growing and regenerating zebrafish fin. *Dev. Cell* **2011**, *20*, 725–732.

106. Thummel, R.; Burket, C.T.; Hyde, D.R. Two different transgenes to study gene silencing and re-expression during zebrafish caudal fin and retinal regeneration. *Sci. World J.* **2006**, *6* (Suppl. 1), 65–81.

107. Kumar, A.; Velloso, C.P.; Imokawa, Y.; Brockes, J.P. The regenerative plasticity of isolated urodele myofibers and its dependence on MSX1. *PLoS Biol.* **2004**, *2*, E218.

108. Palacios, D. Chapter 1—Epigenetics and Regeneration: An Overview. In *Epigenetics and Regeneration*; Palacios, D., Ed.; Academic Press: Cambridge, MA, USA, 2019; Volume 11, pp. 1–15.

109. Law, J.A.; Jacobsen, S.E. Establishing, maintaining and modifying DNA methylation patterns in plants and animals. *Nat. Rev. Genet.* **2010**, *11*, 204–220.

110. Okano, M.; Bell, D.W.; Haber, D.A.; Li, E. DNA Methyltransferases Dnmt3a and Dnmt3b Are Essential for De Novo Methylation and Mammalian Development. *Cell* **1999**, *99*, 247–257.

111. Challen, G.A.; Sun, D.; Jeong, M.; Luo, M.; Jelinek, J.; Berg, J.S.; Bock, C.; Vasanthakumar, A.; Gu, H.; Xi, Y.; et al. Dnmt3a is essential for hematopoietic stem cell differentiation. *Nat. Genet.* **2011**, *44*, 23–31.

112. Hu, B.; Gharaee-Kermani, M.; Wu, Z.; Phan, S.H. Epigenetic regulation of myofibroblast differentiation by DNA methylation. *Am. J. Pathol.* **2010**, *177*, 21–28.

113. Aguilar, C.; Gardiner, D.M. DNA Methylation Dynamics Regulate the Formation of a Regenerative Wound Epithelium during Axolotl Limb Regeneration. *PLoS ONE* **2015**, *10*, e0134791.

114. Hirose, K.; Shimoda, N.; Kikuchi, Y. Transient reduction of 5-methylcytosine and 5-hydroxymethylcytosine is associated with active DNA demethylation during regeneration of zebrafish fin. *Epigenetics* **2013**, *8*, 899–906.

115. Xie, S.; Wang, Z.; Okano, M.; Nogami, M.; Li, Y.; He, W.-W.; Okumura, K.; Li, E. Cloning, expression and chromosome locations of the human DNMT3 gene family. *Gene* **1999**, *236*, 87–95.

116. Campos, C.; Valente, L.M.P.; Fernandes, J.M.O. Molecular evolution of zebrafish dnmt3 genes and thermal plasticity of their expression during embryonic development. *Gene* **2012**, *500*, 93–100.

117. Takayama, K.; Shimoda, N.; Takanaga, S.; Hozumi, S.; Kikuchi, Y. Expression patterns of dnmt3aa, dnmt3ab, and dnmt4 during development and fin regeneration in zebrafish. *Gene Expr. Patterns* **2014**, *14*, 105–110.

118. Oliveira-Mateos, C.; Sánchez-Castillo, A.; Guil, S. Chapter 4—Noncoding RNAs as Regulators of Gene Expression in Pluripotency and Differentiation. In *Epigenetics and Regeneration*; Palacios, D., Ed.; Academic Press: Cambridge, MA, USA, 2019; Volume 11, pp. 73–105.

119. Holman, E.C.; Campbell, L.J.; Hines, J.; Crews, C.M. Microarray analysis of microRNA expression during axolotl limb regeneration. *PLoS ONE* **2012**, *7*, e41804.

120. Chen, J.-F.; Mandel, E.M.; Thomson, J.M.; Wu, Q.; Callis, T.E.; Hammond, S.M.; Conlon, F.L.; Wang, D.-Z. The role of microRNA-1 and microRNA-133 in skeletal muscle proliferation and differentiation. *Nat. Genet.* **2006**, *38*, 228–233.

121. Kim, H.K.; Lee, Y.S.; Sivaprasad, U.; Malhotra, A.; Dutta, A. Muscle-specific microRNA miR-206 promotes muscle differentiation. *J. Cell Biol.* **2006**, *174*, 677–687.

122. Hutchins, E.D.; Eckalbar, W.L.; Wolter, J.M.; Mangone, M.; Kusumi, K. Differential expression of conserved and novel microRNAs during tail regeneration in the lizard Anolis carolinensis. *BMC Genom.* **2016**, *17*, 339.

123. Yin, V.P.; Thomson, J.M.; Thummel, R.; Hyde, D.R.; Hammond, S.M.; Poss, K.D. Fgf-dependent depletion of microRNA-133 promotes appendage regeneration in zebrafish. *Genes Dev.* **2008**, *22*, 728–733.

124. Thatcher, E.J.; Paydar, I.; Anderson, K.K.; Patton, J.G. Regulation of zebrafish fin regeneration by microRNAs. *Proc. Natl. Acad. Sci. USA* **2008**, *105*, 18384.

125. Wolpert, L. Positional information and pattern formation. *Curr. Top. Dev. Biol.* **1971**, *6*, 183–224.

126. Butler, E.G. Regeneration of the urodele forelimb after reversal of its proximo-distal axis. *J. Morphol.* **1955**, *96*, 265–281.

127. Pescitelli, M.J., Jr.; Stocum, D.L. The origin of skeletal structures during intercalary regeneration of larval Ambystoma limbs. *Dev. Biol.* **1980**, *79*, 255–275.

128. Maden, M. Vitamin A and pattern formation in the regenerating limb. *Nature* **1982**, *295*, 672–675.

129. Echeverri, K.; Tanaka, E.M. Proximodistal patterning during limb regeneration. *Dev. Biol.* **2005**, *279*, 391–401.

130. Kumar, A.; Godwin, J.W.; Gates, P.B.; Garza-Garcia, A.A.; Brockes, J.P. Molecular basis for the nerve dependence of limb regeneration in an adult vertebrate. *Science* **2007**, *318*, 772–777.

131. Garza-Garcia, A.; Harris, R.; Esposito, D.; Gates, P.B.; Driscoll, P.C. Solution structure and phylogenetics of Prod1, a member of the three-finger protein superfamily implicated in salamander limb regeneration. *PLoS ONE* **2009**, *4*, e7123.

132. Perathoner, S.; Daane, J.M.; Henrion, U.; Seebohm, G.; Higdon, C.W.; Johnson, S.L.; Nusslein-Volhard, C.; Harris, M.P. Bioelectric signaling regulates size in zebrafish fins. *PLoS Genet.* **2014**, *10*, e1004080.

133. Iovine, M.K.; Higgins, E.P.; Hindes, A.; Coblitz, B.; Johnson, S.L. Mutations in connexin43 (GJA1) perturb bone growth in zebrafish fins. *Dev. Biol.* **2005**, *278*, 208–219.

134. Watanabe, M.; Iwashita, M.; Ishii, M.; Kurachi, Y.; Kawakami, A.; Kondo, S.; Okada, N. Spot pattern of leopard Danio is caused by mutation in the zebrafish connexin41.8 gene. *EMBO Rep.* **2006**, *7*, 893–897.

135. Oviedo, N.J.; Morokuma, J.; Walentek, P.; Kema, I.P.; Gu, M.B.; Ahn, J.M.; Hwang, J.S.; Gojobori, T.; Levin, M. Long-range neural and gap junction protein-mediated cues control polarity during planarian regeneration. *Dev. Biol.* **2010**, *339*, 188–199.

136. Borgens, R.B.; McGinnis, M.E.; Vanable, J.W., Jr.; Miles, E.S. Stump currents in regenerating salamanders and newts. *J. Exp. Zool.* **1984**, *231*, 249–256.

137. Jenkins, L.S.; Duerstock, B.S.; Borgens, R.B. Reduction of the current of injury leaving the amputation inhibits limb regeneration in the red spotted newt. *Dev. Biol.* **1996**, *178*, 251–262.

138. Radugina, E.; Grigoryan, E. Heat shock response and shape regulation during newt tail regeneration. *J. Biol.* **2018**, *71*, 171–179.

139. Lévesque, M.; Guimond, J.C.; Pilote, M.; Leclerc, S.; Moldovan, F.; Roy, S. Expression of heat-shock protein 70 during limb development and regeneration in the axolotl. *Dev. Dyn* **2005**, *233*, 1525–1534.

140. Makino, S.; Whitehead, G.G.; Lien, C.-L.; Kim, S.; Jhawar, P.; Kono, A.; Kawata, Y.; Keating, M.T. Heat-shock protein 60 is required for blastema formation and maintenance during regeneration. *Proc. Natl. Acad. Sci. USA* **2005**, *102*, 14599.

141. Pei, W.; Tanaka, K.; Huang, S.C.; Xu, L.; Liu, B.; Sinclair, J.; Idol, J.; Varshney, G.K.; Huang, H.; Lin, S.; et al. Extracellular HSP60 triggers tissue regeneration and wound healing by regulating inflammation and cell proliferation. *NPJ Regen. Med.* **2016**, *1*, 16013.

142. Wynn, T.A.; Vannella, K.M. Macrophages in Tissue Repair, Regeneration, and Fibrosis. *Immunity* **2016**, *44*, 450–462.

143. Godwin, J.W.; Pinto, A.R.; Rosenthal, N.A. Macrophages are required for adult salamander limb regeneration. *Proc. Natl. Acad. Sci. USA* **2013**, *110*, 9415–9420.

144. Londono, R.; Tighe, S.; Milnes, B.; DeMoya, C.; Quijano, L.M.; Hudnall, M.L.; Nguyen, J.; Tran, E.; Badylak, S.; Lozito, T.P. Single Cell Sequencing Analysis of Lizard Phagocytic Cell Populations and Their Role in Tail Regeneration. *J. Immunol. Regen. Med.* **2020**, *8*.

145. Alibardi, L. Autoradiography and inmmunolabeling suggests that lizard blastema contains arginase-positive M2-like macrophages that may support tail regeneration. *Ann. Anat. Anat. Anz.* **2020**, *231*, 151549.

146. Alibardi, L. Immunolocalization of 5BrdU long retaining labeled cells and macrophage infiltration in the scarring limb of lizard after limb amputation. *Tissue Cell* **2016**, *48*, 197–207.

147. Godwin, J.W.; Rosenthal, N. Scar-free wound healing and regeneration in amphibians: Immunological influences on regenerative success. *Differentiation* **2014**, *87*, 66–75.

148. Mescher, A.L.; White, G.W.; Brokaw, J.J. Apoptosis in regenerating and denervated, nonregenerating urodele forelimbs. *Wound Repair Regen.* **2000**, *8*, 110–116.

149. Da Silva-Alvarez, S.; Guerra-Varela, J.; Sobrido-Camean, D.; Quelle, A.; Barreiro-Iglesias, A.; Sanchez, L.; Collado, M. Cell senescence contributes to tissue regeneration in zebrafish. *Aging Cell* **2020**, *19*, e13052.

150. Yun, M.H.; Davaapil, H.; Brockes, J.P. Recurrent turnover of senescent cells during regeneration of a complex structure. *eLife* **2015**, *4*, e05505.

151. Zimmerman, L.M.; Vogel, L.A.; Bowden, R.M. Understanding the vertebrate immune system: Insights from the reptilian perspective. *J. Exp. Biol.* **2010**, *213*, 661–671.

152. Harty, M.; Neff, A.W.; King, M.W.; Mescher, A.L. Regeneration or scarring: An immunologic perspective. *Dev. Dyn.* **2003**, *226*, 268–279.

153. Rauta, P.R.; Nayak, B.; Das, S. Immune system and immune responses in fish and their role in comparative immunity study: A model for higher organisms. *Immunol. Lett.* **2012**, *148*, 23–33.

154. Alibardi, L. Hyaluronic acid in the tail and limb of amphibians and lizards recreates permissive embryonic conditions for regeneration due to its hygroscopic and immunosuppressive properties. *J. Exp. Zool. B Mol. Dev. Evol.* **2017**, *328*, 760–771.

155. Parra, D.; Takizawa, F.; Sunyer, J.O. Evolution of B cell immunity. *Annu. Rev. Anim. Biosci.* **2013**, *1*, 65–97.

156. Renshaw, S.A.; Trede, N.S. A model 450 million years in the making: Zebrafish and vertebrate immunity. *Dis. Model. Mech.* **2012**, *5*, 38–47.

157. Li, J.; Barreda, D.R.; Zhang, Y.A.; Boshra, H.; Gelman, A.E.; Lapatra, S.; Tort, L.; Sunyer, J.O. B lymphocytes from early vertebrates have potent phagocytic and microbicidal abilities. *Nat. Immunol.* **2006**, *7*, 1116–1124.

158. Page, D.M.; Wittamer, V.; Bertrand, J.Y.; Lewis, K.L.; Pratt, D.N.; Delgado, N.; Schale, S.E.; McGue, C.; Jacobsen, B.H.; Doty, A.; et al. An evolutionarily conserved program of B-cell development and activation in zebrafish. *Blood* **2013**, *122*, e1–e11.

159. Tournefier, A.; Laurens, V.; Chapusot, C.; Ducoroy, P.; Padros, M.R.; Salvadori, F.; Sammut, B. Structure of MHC class I and class II cDNAs and possible immunodeficiency linked to class II expression in the Mexican axolotl. *Immunol. Rev.* **1998**, *166*, 259–277.

160. Lam, S.H.; Chua, H.L.; Gong, Z.; Lam, T.J.; Sin, Y.M. Development and maturation of the immune system in zebrafish, Danio rerio: A gene expression profiling, in situ hybridization and immunological study. *Dev. Comp. Immunol.* **2004**, *28*, 9–28.

161. Trede, N.S.; Langenau, D.M.; Traver, D.; Look, A.T.; Zon, L.I. The Use of Zebrafish to Understand Immunity. *Immunity* **2004**, *20*, 367–379.

162. Wienholds, E.; Schulte-Merker, S.; Walderich, B.; Plasterk, R.H. Target-selected inactivation of the zebrafish rag1 gene. *Science* **2002**, *297*, 99–102.

163. Petrie-Hanson, L.; Hohn, C.; Hanson, L. Characterization of rag1 mutant zebrafish leukocytes. *BMC Immunol.* **2009**, *10*, 8.

164. Todd, T. On the process of reproduction of the members of the aquatic salamander. *Quart. J. Sci. Arts Lib.* **1823**, *16*, 84–86.

165. Singer, M. The trophic quality of the neuron: Some theoretical considerations. *Prog. Brain Res.* **1964**, *13*, 228–232.

166. Singer, M. On the Nature of the Neurotrophic Phenomenon in Urodele Limb Regeneration. *Am. Zool.* **1978**, *18*, 829–841.

167. Sidman, R.L.; Singer, M. Stimulation of forelimb regeneration in the newt, Triturus viridescens, by a sensory nerve supply isolated from the central nervous system. *Am. J. Physiol.* **1951**, *165*, 257–260.

168. Singer, M. The influence of the nerve in regeneration of the amphibian extremity. *Q. Rev. Biol.* **1952**, *27*, 169–200.

169. Trampusch, H.A. Nerves as morphogenetic mediators in regeneration. *Prog. Brain Res.* **1964**, *13*, 214–227.

170. Farkas, J.E.; Monaghan, J.R. A brief history of the study of nerve dependent regeneration. *Neurogenesis* **2017**, *4*, e1302216.

171. Kumar, A.; Nevill, G.; Brockes, J.P.; Forge, A. A comparative study of gland cells implicated in the nerve dependence of salamander limb regeneration. *J. Anat.* **2010**, *217*, 16–25.

172. Kamrin, R.P.; Singer, M. The influence of the spinal cord in regeneration of the tail of the lizard, Anolis carolinensis. *J. Exp. Zool.* **1955**, *128*, 611–627.

173. Alibardi, L.; Sala, M.; Miolo, V. Morphology and electron microscopy of experimentally produced tail regenerates in lizard. *Acta Embryol. Morphol. Exp. (1980)* **1988**, *9*, 181–194.

174. Simpson, S.B., Jr. Analysis of Tail Regeneration in the Lizard *Lygosoma Laterale*. I. Initiation of Regeneration and Cartilage Differentiation: The Role of Ependyma. *J. Morphol.* **1964**, *114*, 425–435.

175. Lozito, T.P.; Tuan, R.S. Lizard tail regeneration as an instructive model of enhanced healing capabilities in an adult amniote. *Connect. Tissue Res.* **2017**, *58*, 145–154.

176. Simoes, M.G.; Bensimon-Brito, A.; Fonseca, M.; Farinho, A.; Valerio, F.; Sousa, S.; Afonso, N.; Kumar, A.; Jacinto, A. Denervation impairs regeneration of amputated zebrafish fins. *BMC Dev. Biol.* **2014**, *14*, 49.

177. Yntema, C.L. Regeneration in sparsely innervated and aneurogenic forelimbs of *Amblystoma larvae*. *J. Exp. Zool.* **1959**, *140*, 101–123.

178. Steen, T.P.; Thornton, C.S. Tissue Interaction in Amputated Aneurogenic Limbs of *Ambystoma Larvae*. *J. Exp. Zool.* **1963**, *154*, 207–221.

179. Stocum, D.L. The role of peripheral nerves in urodele limb regeneration. *Eur. J. Neurosci.* **2011**, *34*, 908–916.

180. Kawakami, Y.; Rodriguez Esteban, C.; Raya, M.; Kawakami, H.; Marti, M.; Dubova, I.; Izpisua Belmonte, J.C. Wnt/beta-catenin signaling regulates vertebrate limb regeneration. *Genes Dev.* **2006**, *20*, 3232–3237.

181. Alibardi, L.; Lovicu, F.J. Immunolocalization of FGF1 and FGF2 in the regenerating tail of the lizard *Lampropholis guichenoti*: Implications for FGFs as trophic factors in lizard tail regeneration. *Acta Histochem.* **2010**, *112*, 459–473.

182. Narayanan, A. The Initiation and Progression of Tail Regeneration in Northern House Gecko *Hemidactylus Flaviviridis* at Role of Fibroblast Growth Factor 2 (Fgf2). *Biochip Tiss Chip.* **2015**, *1*, 1–7.

183. Alibardi, L. Observations on FGF immunoreactivity in the regenerating tail blastema, and in the limb and tail scars of lizard suggest that FGFs are required for regeneration. *Belg. J. Zool.* **2012**, *142*, 23–38.

184. Alibardi, L. FGFs treatment on amputated lizard limbs stimulate the regeneration of long bones, opening new avenues for limb regeneration in amniotes: A morphological study. *J. Funct. Morphol. Kinesiol.* **2017**, *2*, 25.

185. Christensen, R.N.; Weinstein, M.; Tassava, R.A. Fibroblast growth factors in regenerating limbs of Ambystoma: Cloning and semi-quantitative RT-PCR expression studies. *J. Exp. Zool.* **2001**, *290*, 529–540.

186. Mullen, L.M.; Bryant, S.V.; Torok, M.A.; Blumberg, B.; Gardiner, D.M. Nerve dependency of regeneration: The role of Distal-less and FGF signaling in amphibian limb regeneration. *Development* **1996**, *122*, 3487–3497.

187. Poss, K.D.; Shen, J.; Nechiporuk, A.; McMahon, G.; Thisse, B.; Thisse, C.; Keating, M.T. Roles for Fgf signaling during zebrafish fin regeneration. *Dev. Biol.* **2000**, *222*, 347–358.

188. Blum, N.; Begemann, G. Retinoic acid signaling controls the formation, proliferation and survival of the blastema during adult zebrafish fin regeneration. *Development* **2012**, *139*, 107–116.

189. Sugiura, T.; Wang, H.; Barsacchi, R.; Simon, A.; Tanaka, E.M. MARCKS-like protein is an initiating molecule in axolotl appendage regeneration. *Nature* **2016**, *531*, 237–240.

190. Aderem, A. The Marcks brothers: A family of protein kinase C substrates. *Cell* **1992**, *71*, 713–716.

191. Sundaram, M.; Cook, H.W.; Byers, D.M. The MARCKS family of phospholipid binding proteins: Regulation of phospholipase D and other cellular components. *Biochem. Cell Biol.* **2004**, *82*, 191–200.

192. El Amri, M.; Fitzgerald, U.; Schlosser, G. MARCKS and MARCKS-like proteins in development and regeneration. *J. Biomed. Sci.* **2018**, *25*, 43.

193. Edgar, B.A. How flies get their size: Genetics meets physiology. *Nat. Rev. Genet.* **2006**, *7*, 907–916.

194. Jazwinska, A.; Badakov, R.; Keating, M.T. Activin-betaA signaling is required for zebrafish fin regeneration. *Curr. Biol.* **2007**, *17*, 1390–1395.

195. Wagner, I.; Wang, H.; Weissert, P.M.; Straube, W.L.; Shevchenko, A.; Gentzel, M.; Brito, G.; Tazaki, A.; Oliveira, C.; Sugiura, T.; et al. Serum Proteases Potentiate BMP-Induced Cell Cycle Re-entry of Dedifferentiating Muscle Cells during Newt Limb Regeneration. *Dev. Cell* **2017**, *40*, 608–617.

196. Guimond, J.C.; Levesque, M.; Michaud, P.L.; Berdugo, J.; Finnson, K.; Philip, A.; Roy, S. BMP-2 functions independently of SHH signaling and triggers cell condensation and apoptosis in regenerating axolotl limbs. *BMC Dev. Biol.* **2010**, *10*, 15.

197. Smith, A.; Avaron, F.; Guay, D.; Padhi, B.K.; Akimenko, M.A. Inhibition of BMP signaling during zebrafish fin regeneration disrupts fin growth and scleroblasts differentiation and function. *Dev. Biol.* **2006**, *299*, 438–454.

198. Stewart, S.; Gomez, A.W.; Armstrong, B.E.; Henner, A.; Stankunas, K. Sequential and Opposing Activities of Wnt and BMP Coordinate Zebrafish Bone Regeneration. *Cell Rep.* **2014**, *6*, 482–498.

199. Thorimbert, V.; Konig, D.; Marro, J.; Ruggiero, F.; Jazwinska, A. Bone morphogenetic protein signaling promotes morphogenesis of blood vessels, wound epidermis, and actinotrichia during fin regeneration in zebrafish. *FASEB J.* **2015**, *29*, 4299–4312.

200. Yokoyama, H. Initiation of limb regeneration: The critical steps for regenerative capacity. *Dev. Growth Differ.* **2008**, *50*, 13–22.

201. Liu, Y.; Zhou, Q.; Wang, Y.; Luo, L.; Yang, J.; Yang, L.; Liu, M.; Li, Y.; Qian, T.; Zheng, Y.; et al. Gekko japonicus genome reveals evolution of adhesive toe pads and tail regeneration. *Nat. Commun.* **2015**, *6*, 10033.

202. Alibardi, L. Msx1-2 immunolocalization in the regenerating tail of a lizard but not in the scarring limb suggests its involvement in the process of regeneration. *Acta Zool.* **2018**, *99*, 143–150.

203. Koshiba, K.; Kuroiwa, A.; Yamamoto, H.; Tamura, K.; Ide, H. Expression of Msx genes in regenerating and developing limbs of axolotl. *J. Exp. Zool.* **1998**, *282*, 703–714.

204. Akimenko, M.A.; Johnson, S.L.; Westerfield, M.; Ekker, M. Differential induction of four msx homeobox genes during fin development and regeneration in zebrafish. *Development* **1995**, *121*, 347–357.

205. Ekker, M.; Akimenko, M.A.; Allende, M.L.; Smith, R.; Drouin, G.; Langille, R.M.; Weinberg, E.S.; Westerfield, M. Relationships among msx gene structure and function in zebrafish and other vertebrates. *Mol. Biol. Evol.* **1997**, *14*, 1008–1022.

206. Nechiporuk, A.; Keating, M.T. A proliferation gradient between proximal and msxb-expressing distal blastema directs zebrafish fin regeneration. *Development* **2002**, *129*, 2607–2617.

207. Thummel, R.; Bai, S.; Sarras, M.P., Jr.; Song, P.; McDermott, J.; Brewer, J.; Perry, M.; Zhang, X.; Hyde, D.R.; Godwin, A.R. Inhibition of zebrafish fin regeneration using in vivo electroporation of morpholinos against fgfr1 and msxb. *Dev. Dyn.* **2006**, *235*, 336–346.

208. Zeller, R.; Lopez-Rios, J.; Zuniga, A. Vertebrate limb bud development: Moving towards integrative analysis of organogenesis. *Nat. Rev. Genet.* **2009**, *10*, 845–858.

209. Torok, M.A.; Gardiner, D.M.; Izpisúa-Belmonte, J.C.; Bryant, S.V. Sonic hedgehog (shh) expression in developing and regenerating axolotl limbs. *J. Exp. Zool.* **1999**, *284*, 197–206.

210. Nacu, E.; Gromberg, E.; Oliveira, C.R.; Drechsel, D.; Tanaka, E.M. FGF8 and SHH substitute for anterior-posterior tissue interactions to induce limb regeneration. *Nature* **2016**, *533*, 407–410.

211. Laforest, L.; Brown, C.W.; Poleo, G.; Geraudie, J.; Tada, M.; Ekker, M.; Akimenko, M.A. Involvement of the sonic hedgehog, patched 1 and bmp2 genes in patterning of the zebrafish dermal fin rays. *Development* **1998**, *125*, 4175–4184.

212. Quint, E.; Smith, A.; Avaron, F.; Laforest, L.; Miles, J.; Gaffield, W.; Akimenko, M.A. Bone patterning is altered in the regenerating zebrafish caudal fin after ectopic expression of sonic hedgehog and bmp2b or exposure to cyclopamine. *Proc. Natl. Acad. Sci. USA* **2002**, *99*, 8713–8718.

213. Zhang, J.; Jeradi, S.; Strahle, U.; Akimenko, M.A. Laser ablation of the sonic hedgehog-a-expressing cells during fin regeneration affects ray branching morphogenesis. *Dev. Biol.* **2012**, *365*, 424–433.

214. Armstrong, B.E.; Henner, A.; Stewart, S.; Stankunas, K. Shh promotes direct interactions between epidermal cells and osteoblast progenitors to shape regenerated zebrafish bone. *Development* **2017**, *144*, 1165–1176.

215. Sharpless, N.E.; DePinho, R.A. Telomeres, stem cells, senescence, and cancer. *J. Clin. Investig.* **2004**, *113*, 160–168.

216. Martínez, D.E. Mortality Patterns Suggest Lack of Senescence in Hydra. *Exp. Gerontol.* **1998**, *33*, 217–225.

217. Schaible, R.; Scheuerlein, A.; Danko, M.J.; Gampe, J.; Martinez, D.E.; Vaupel, J.W. Constant mortality and fertility over age in Hydra. *Proc. Natl. Acad. Sci. USA* **2015**, *112*, 15701–15706.

218. Aboobaker, A.A. Planarian stem cells: A simple paradigm for regeneration. *Trends Cell Biol.* **2011**, *21*, 304–311.

219. Yun, M.H. Changes in Regenerative Capacity through Lifespan. *Int. J. Mol. Sci.* **2015**, *16*, 25392–25432.

220. Moffat, L.A.; Bellairs, A.D. The regenerative capacity of the tail in embryonic and post-natal lizards (Lacerta vivipara Jacquin). *J. Embryol. Exp. Morphol.* **1964**, *12*, 769.

221. Monaghan, J.R.; Stier, A.C.; Michonneau, F.; Smith, M.D.; Pasch, B.; Maden, M.; Seifert, A.W. Experimentally induced metamorphosis in axolotls reduces regenerative rate and fidelity. *Regeneration* **2014**, *1*, 2–14.

222. Alibardi, L. Organ regeneration evolved in fish and amphibians in relation to metamorphosis: Speculations on a post-embryonic developmental process lost in amniotes after the water to land transition. *Ann. Anat.* **2019**, *222*, 114–119.

223. Alibardi, L. Appendage regeneration in anamniotes utilizes genes active during larval-metamorphic stages that have been lost or altered in amniotes: The case for studying lizard tail regeneration. *J. Morphol.* **2020**, *281*, 1358–1381.

224. Nachtrab, G.; Czerwinski, M.; Poss, K.D. Sexually dimorphic fin regeneration in zebrafish controlled by androgen/GSK3 signaling. *Curr. Biol.* **2011**, *21*, 1912–1917.

225. Anchelin, M.; Murcia, L.; Alcaraz-Perez, F.; Garcia-Navarro, E.M.; Cayuela, M.L. Behaviour of telomere and telomerase during aging and regeneration in zebrafish. *PLoS ONE* **2011**, *6*, e16955.

226. Tsai, S.B.; Tucci, V.; Uchiyama, J.; Fabian, N.J.; Lin, M.C.; Bayliss, P.E.; Neuberg, D.S.; Zhdanova, I.V.; Kishi, S. Differential effects of genotoxic stress on both concurrent body growth and gradual senescence in the adult zebrafish. *Aging Cell* **2007**, *6*, 209–224.

227. Itou, J.; Kawakami, H.; Burgoyne, T.; Kawakami, Y. Life-long preservation of the regenerative capacity in the fin and heart in zebrafish. *Biol. Open* **2012**, *1*, 739–746.

228. Mishra, R.; Sehring, I.; Cederlund, M.; Mulaw, M.; Weidinger, G. NF-kappaB Signaling Negatively Regulates Osteoblast Dedifferentiation during Zebrafish Bone Regeneration. *Dev. Cell* **2020**, *52*, 167–182.

229. Brittijn, S.A.; Duivesteijn, S.J.; Belmamoune, M.; Bertens, L.F.; Bitter, W.; de Bruijn, J.D.; Champagne, D.L.; Cuppen, E.; Flik, G.; Vandenbroucke-Grauls, C.M.; et al. Zebrafish development and regeneration: New tools for biomedical research. *Int. J. Dev. Biol.* **2009**, *53*, 835–850.

230. Hyde, D.R.; Godwin, A.R.; Thummel, R. In vivo electroporation of morpholinos into the regenerating adult zebrafish tail fin. *J. Vis. Exp. JoVE* **2012**.

231. Dinsmore, C.E. *A History of Regeneration Research: Milestones in the Evolution of a Science*; Cambridge University Press: Cambridge, UK, 1991.

MANUSCRIPT 3

Zebrafish Tric-b is required for skeletal development and bone cells differentiation

F. Tonelli†, L. Leoni†, **V. Daponte†**, R. Gioia, S. Cotti, I. A. K. Fiedler, D. Larianova, A. Willaert, P. J. Coucke, S. Villani, B. Busse, R. Besio, A. Rossi, P. E. Witten and A. Forlino. *Frontiers in Endocrinology*, 2023. https://doi.org/10.3389/fendo.2023.1002914

Trimeric intracellular cation channels

Trimeric intracellular cation channels (TRICs) are integral membrane proteins responsible for the transport of K^+ ions across the endoplasmic or sarcoplasmic reticulum (ER o SR) membranes acting as counter-ions to allow electroneutral Ca^{2+} exit towards the cytosol. Two TRIC isoforms have been to date identified in mammals: TRIC-A, encoded by *TMEM38A*, and TRIC-B, encoded by *TMEM38B*. TRIC-A, mainly expressed in excitable cells, which works in coordination with ryanodine receptors (RyRs), and the ubiquitous TRIC-B, coupled with inositol 1,4,5-trisphosphate (IP_3Rs) receptors. TRIC-A deficiency impairs RyR-mediated Ca^{2+} release, resulting in unstable Ca^{2+} storage and Ca^{2+} overloading inside the SR. Indeed, *Tric-a*–knockout mice develop hypertension due to increased contractility of vascular smooth muscle cells (VSMCs) (Zhao et al. 2010). Mutations in TRIC-B have been linked to bone and pulmonary diseases (Zhao et al. 2016, Shaheen et al. 2012, Volodarsky et al. 2013).

In the last years, structural studies have been reported on TRIC homologs from bacteria, archaea, and *Caenorhabditis elegans* (Yang et al. 2016, Kasuya et al. 2016). Recently, the crystal structures of two vertebrate TRICs (*Gallus gallus* TRIC-A and *Xenopus laevis* TRIC-B) were solved (Wang et al. 2019), showing similar overall topological organization pattern, trimeric assembly architecture, and surface electrostatic characteristics with prokaryotic TRICs and invertebrate TRICs from *C. elegans* (Wang et al. 2019) (**Figure 1**). Both TRIC-A and TRIC-B are symmetric homotrimers in which each monomer forms a novel fold with seven transmembrane (TM) helices and four amphipathic α-helices lying on the cytoplasmic and luminal surface (Yang et al. 2016). Each protomer is composed of inverted quasi-repeats of triple-helix bundles (THBs) plus an additional TM7. TM1-3 and TM4-6 domains are similar as each adopts a THB fold, while TM7 stands alone filling the crevice between TM4 and TM6 and making contact with the pre-TM helix, TM0 (Yang et al. 2016, Wang et al. 2019). Each monomer has an N-terminal end located in the ER/SR lumen, and a C-terminal end protruding into the cytoplasm. The central pore crosses the ER/SR membrane and is characterized by hydrophobic and positive residues. The KEVXRXXK consensus sequence motif is highly conserved among eukaryotic TRICs. This positively charged motif is required for pore formation and confers voltage sensitivity to the TM4 helix, regulating channel activity.

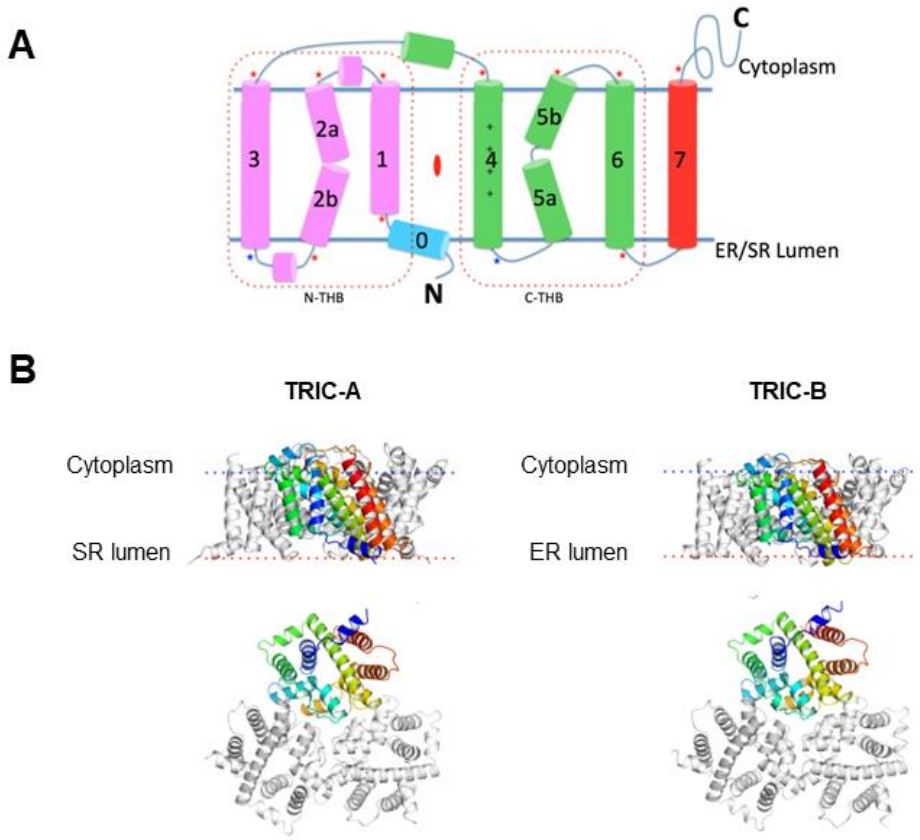

Figure 1. Structure of vertebrates' TRIC channels. (A) Membrane topology diagram. TM1- 3 constitutes N-triple-helix bundles (N-THB), and TM4-6 constitutes C-triple-helix bundles (C-THB), colored in purple and green, respectively. The additional TM0 is in light blue and TM7 is in red. **(B)** Ribbon drawing of TRIC-A (crystal structure from *Gallus gallus)* and TRIC-B (crystal structure from *Xenopus laevis*). Membrane view is shown on the top, intracellular side view on the bottom. Protomers are colored spectrally from dark blue at N-terminus to red at C-terminus (modified from Wang et al. 2019).

OI type XIV

Collagen type I biosynthesis is a calcium-regulated process. In the ER, Ca^{2+} binding to the C-terminal globular domain stabilizes interchain hydrogen and disulfide bonds, necessary for procollagen correct trimerization and folding (Bourhis et al. 2012). Also, the activity of several ER-resident collagen chaperones and enzymes is regulated by luminal [Ca^{2+}] fluctuations (**Figure 2**). For these reasons, ER Ca^{2+} homeostasis is fundamental for collagen type I synthesis and for the correct expression and activities of multiple collagen binding proteins.

TRIC-B channel, balancing calcium release mediated by IP_3R and calcium uptake by the sarco/endoplasmic reticulum Ca^{2+}-ATPases (SERCAs), has a role in maintaining appropriate intracellular Ca^{2+} levels (Yazawa et al. 2007). Few years ago, mutations in *TMEM38B* have been identified as causative of moderately severe OI type XIV (Shaheen et al. 2012, Volodarsky et al. 2013). Fibroblasts and osteoblasts from patients display a decrease of both cytoplasmic [Ca^{2+}] and

IP_3R-mediated Ca^{2+}-flux in Ca^{2+}-free media, indicating an alteration of the ER Ca^{2+} homeostasis (Cabral et al. 2016). The disruption of Ca^{2+} kinetics associates with altered expression and activity of multiple collagen modifying enzymes and chaperones, result in abnormal post-translational modification and folding of collagen type I (Cabral et al. 2016). OI type XIV patients display under-modified collagen type I, likely due to a 20-30% decrease in hydroxylysines content that could be a consequence of dysfunctional LH1 activity (Cabral et al. 2016). This contrasts with the excessive post translational modifications of collagen I typical of classical dominant OI, caused by mutation in the collagen encoding genes, and of the recessive defects in the *CRTAP*, *P3H1* and *PPIB* genes encoding for the proteins involved in the prolyl 3-hydroxylation complex.

Patients' skeletal phenotype is characterized by low bone volume associated with low bone turnover, another feature in contrast with the high bone turnover described in classical OI. Despite bone matrix mineralization being relatively normal, the expression of *ALP*, a pro-mineralization marker, and of *BGLAP* and *OPN*, which inhibit crystal growth (Fujisawa and Tamura 2012, de Bruyn et al. 2013), is increased (Webb et al. 2017). Impaired Ca^{2+} flux in the ER is also associated to an impairment in osteoclast differentiation and activity, as demonstrated by *Tric-b* knockout mice showing reduced expression of *Ctsk* and *Atp6vd02* genes (Zhao et al. 2016).

Tric-b knockout mice, which have impaired IP_3R mediated Ca^{2+} release resulting in ER Ca^{2+} overloading, develop an OI-like phenotype, with impaired bone mineralization associated to matrix insufficiency and collagen retention inside the ER (Zhao et al. 2016). However, they are perinatal lethal due to respiratory failure linked to insufficient production and secretion of surfactant lipids by alveolar epithelial cells (Zhao et al. 2016). In order to better investigate the role of TRIC-B channel in skeletal development and bone cell differentiation, viable animal models are needed. In this sense, zebrafish provides a useful tool to study the effect of *TMEM38B* mutations on the skeleton.

In this work, I contributed to generate and characterize two zebrafish *tmem38b* mutants, one with an out of frame mutation introducing a premature stop codon (*tmem38b*$^{-/-}$) and the other one carrying an in-frame deletion removing the KEV motif (*tmem38b*$^{\Delta 120\text{-}7/\Delta 120\text{-}7}$). We demonstrated undermodification and intracellular retention of collagen type I in both models, in line with what observed in OI type XIV patients. While *tmem38b*$^{\Delta 120\text{-}7/\Delta 120\text{-}7}$ presented skeletal features limited to reduced vertebral length at 21 dpf, t*mem38b*$^{-/-}$ showed a skeletal phenotype at the late larval and juvenile stages of development and impaired osteoblasts and osteoclasts activity as demonstrated by caudal fin regeneration experiments. Taken together, our data confirm the relevance of Tric-b channel during early development and in bone cell differentiation.

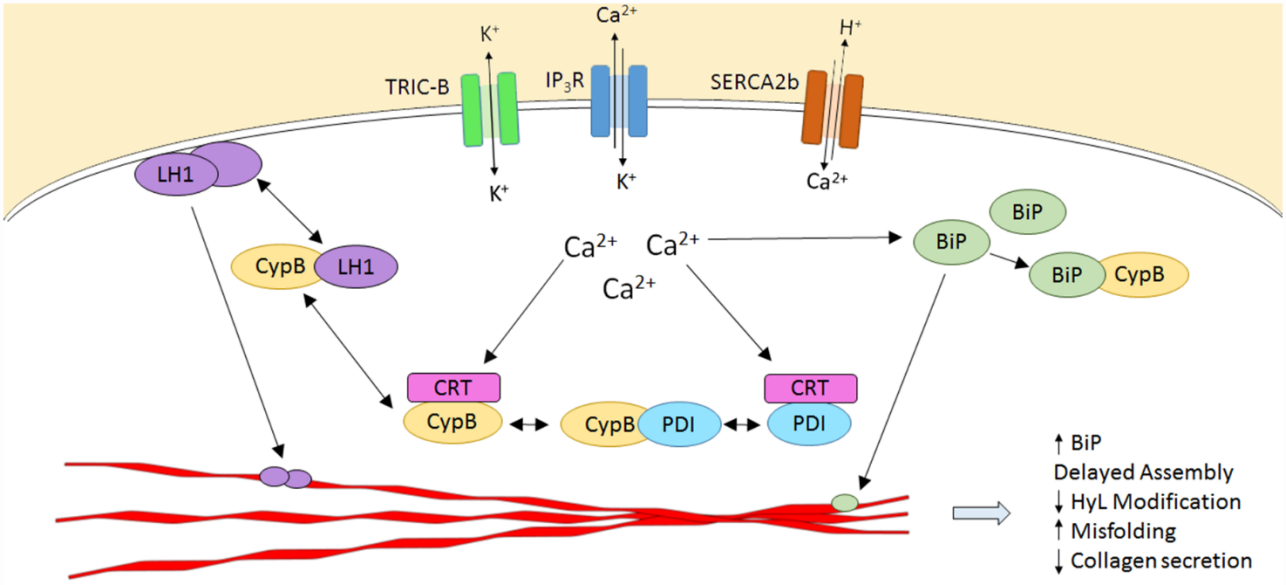

Figure 2. Calcium flux regulates collagen post-translational interactions within the ER. Collagen type I is synthesized in the ER, which represents the major intracellular Ca^{2+} store. In response to extracellular stimuli, Ca^{2+} is released from the ER lumen into the cytoplasm via IP_3Rs and RyRs. Cytoplasmic Ca^{2+} that does not bind signaling proteins involved in gene expression is transported back into the ER via SERCA pumps. The continuous fluctuations in free [Ca^{2+}] to and from the ER are indirectly regulated by TRIC channel activity, which mediates transmembrane K^+ flux to maintain electroneutrality across the ER membrane. In fibroblasts and osteoblasts, ER-resident Ca^{2+}-binding chaperones, including BiP, CyPB, PDI and calreticulin (CRT), directly interact with collagen α chains (red polypeptides) to facilitate or catalyze specific modifications required for their assembly and folding. In the absence of TRIC-mediated K^+ flux, Ca^{2+}-dependent "cycling" of these chaperones between inactive, sequestered forms and active, substrate-interacting forms, is dysregulated. Thus, absence of TRIC-B alters ER luminal [Ca^{2+}], affecting synthesis and secretion of collagen, as well as interactions of collagen-specific chaperones with each other and with their substrate, resulting in abnormal collagen assembly and post-translational modification. BiP, GRP78; CyPB, cyclophilin B; CRT, calreticulin; IP3R, inositol triphosphate receptor; LH1, lysyl hydroxylase 1; PDI, protein disulfide isomerase; SERCA2b, sarcoplasmic-endoplasmic reticulum Ca^{2+}-ATPase isoform 2b; TRIC-B, trimeric intracellular cation channel subtype B (from Cabral et al. 2016).

Personal contribution to Manuscript 3

- Collagen type I SDS-PAGE running and analysis.
- Evaluation of ER cisternae size from TEM images.
- Hsp47b whole mount immunostaining and analysis.
- Alizarin Red staining on caudal fins and mineralization analysis.
- Double Alizarin Red/Calcein staining and bone formation analysis on larvae.
- qPCR.
- TRAP staining.
- Picro Sirius Red staining.
- Manuscript writing and editing.
- Figure making.

References

Bourhis, J. M., N. Mariano, Y. Zhao, K. Harlos, J. Y. Exposito, E. Y. Jones, C. Moali, N. Aghajari & D. J. Hulmes (2012) Structural basis of fibrillar collagen trimerization and related genetic disorders. *Nat Struct Mol Biol,* 19**,** 1031-6.

Cabral, W. A., M. Ishikawa, M. Garten, E. N. Makareeva, B. M. Sargent, M. Weis, A. M. Barnes, E. A. Webb, N. J. Shaw, L. Ala-Kokko, F. L. Lacbawan, W. Högler, S. Leikin, P. S. Blank, J. Zimmerberg, D. R. Eyre, Y. Yamada & J. C. Marini (2016) Absence of the ER Cation Channel TMEM38B/TRIC-B Disrupts Intracellular Calcium Homeostasis and Dysregulates Collagen Synthesis in Recessive Osteogenesis Imperfecta. *PLoS Genet,* 12**,** e1006156.

de Bruyn, J. R., M. Goiko, M. Mozaffari, D. Bator, R. L. Dauphinee, Y. Liao, R. L. Flemming, M. S. Bramble, G. K. Hunter & H. A. Goldberg (2013) Dynamic light scattering study of inhibition of nucleation and growth of hydroxyapatite crystals by osteopontin. *PLoS One,* 8**,** e56764.

Fujisawa, R. & M. Tamura (2012) Acidic bone matrix proteins and their roles in calcification. *Front Biosci (Landmark Ed),* 17**,** 1891-903.

Kasuya, G., M. Hiraizumi, A. D. Maturana, K. Kumazaki, Y. Fujiwara, K. Liu, Y. Nakada-Nakura, S. Iwata, K. Tsukada, T. Komori, S. Uemura, Y. Goto, T. Nakane, M. Takemoto, H. E. Kato, K. Yamashita, M. Wada, K. Ito, R. Ishitani, M. Hattori & O. Nureki (2016) Crystal structures of the TRIC trimeric intracellular cation channel orthologues. *Cell Res,* 26**,** 1288-1301.

Shaheen, R., A. M. Alazami, M. J. Alshammari, E. Faqeih, N. Alhashmi, N. Mousa, A. Alsinani, S. Ansari, F. Alzahrani, M. Al-Owain, Z. S. Alzayed & F. S. Alkuraya (2012) Study of autosomal recessive osteogenesis imperfecta in Arabia reveals a novel locus defined by TMEM38B mutation. *J Med Genet,* 49**,** 630-5.

Volodarsky, M., B. Markus, I. Cohen, O. Staretz-Chacham, H. Flusser, D. Landau, I. Shelef, Y. Langer & O. S. Birk (2013) A deletion mutation in TMEM38B associated with autosomal recessive osteogenesis imperfecta. *Hum Mutat,* 34**,** 582-6.

Wang, X. H., M. Su, F. Gao, W. Xie, Y. Zeng, D. L. Li, X. L. Liu, H. Zhao, L. Qin, F. Li, Q. Liu, O. B. Clarke, S. M. Lam, G. H. Shui, W. A. Hendrickson & Y. H. Chen (2019) Structural basis for activity of TRIC counter-ion channels in calcium release. *Proc Natl Acad Sci U S A,* 116**,** 4238-4243.

Webb, E. A., M. Balasubramanian, N. Fratzl-Zelman, W. A. Cabral, H. Titheradge, A. Alsaedi, V. Saraff, J. Vogt, T. Cole, S. Stewart, N. J. Crabtree, B. M. Sargent, S. Gamsjaeger, E. P. Paschalis, P. Roschger, K. Klaushofer, N. J. Shaw, J. C. Marini & W. Högler (2017) Phenotypic Spectrum in Osteogenesis Imperfecta Due to Mutations in TMEM38B: Unraveling a Complex Cellular Defect. *J Clin Endocrinol Metab,* 102**,** 2019-2028.

Yang, H., M. Hu, J. Guo, X. Ou, T. Cai & Z. Liu (2016) Pore architecture of TRIC channels and insights into their gating mechanism. *Nature,* 538**,** 537-541.

Yazawa, M., C. Ferrante, J. Feng, K. Mio, T. Ogura, M. Zhang, P. H. Lin, Z. Pan, S. Komazaki, K. Kato, M. Nishi, X. Zhao, N. Weisleder, C. Sato, J. Ma & H. Takeshima (2007) TRIC channels are essential for Ca2+ handling in intracellular stores. *Nature,* 448**,** 78-82.

Zhao, C., A. Ichimura, N. Qian, T. Iida, D. Yamazaki, N. Noma, M. Asagiri, K. Yamamoto, S. Komazaki, C. Sato, F. Aoyama, A. Sawaguchi, S. Kakizawa, M. Nishi & H. Takeshima (2016) Mice lacking the intracellular cation channel TRIC-B have compromised collagen production and impaired bone mineralization. *Sci Signal,* 9**,** ra49.

Zhao, X., D. Yamazaki, K. H. Park, S. Komazaki, A. Tjondrokoesoemo, M. Nishi, P. Lin, Y. Hirata, M. Brotto, H. Takeshima & J. Ma (2010) Ca2+ overload and sarcoplasmic reticulum instability in tric-a null skeletal muscle. *J Biol Chem,* 285**,** 37370-6.

Abstract

Introduction: Trimeric intracellular potassium channels TRIC-A and -B are endoplasmic reticulum (ER) integral membrane proteins, involved in the regulation of calcium release mediated by ryanodine (RyRs) and inositol 1,4,5-trisphosphate (IP_3Rs) receptors, respectively. While TRIC-A is mainly expressed in excitable cells, TRIC-B is ubiquitously distributed at moderate level. TRIC-B deficiency causes a dysregulation of calcium flux from the ER, which impacts on multiple collagen specific chaperones and modifying enzymatic activity, leading to a rare form of osteogenesis imperfecta (OI Type XIV). The relevance of TRIC-B on cell homeostasis and the molecular mechanism behind the disease are still unknown.

Results: In this study, we exploited zebrafish to elucidate the role of TRIC-B in skeletal tissue. We demonstrated, for the first time, that *tmem38a* and *tmem38b* genes encoding Tric-a and -b, respectively are expressed at early developmental stages in zebrafish, but only the latter has a maternal expression. Two zebrafish mutants for *tmem38b* were generated by CRISPR/Cas9, one carrying an out of frame mutation introducing a premature stop codon (*tmem38b*$^{-/-}$) and one with an in frame deletion that removes the highly conserved KEV domain (*tmem38b*$^{\Delta 120\text{-}7/\Delta 120\text{-}7}$). In both models collagen type I is under-modified and partially intracellularly retained in the endoplasmic reticulum, as described in individuals affected by OI type XIV. *Tmem38b*$^{-/-}$ showed a mild skeletal phenotype at the late larval and juvenile stages of development whereas *tmem38b*$^{\Delta 120\text{-}7/\Delta 120\text{-}7}$ bone outcome was limited to a reduced vertebral length at 21 dpf. Caudal fin regeneration study pointed towards impaired activity of osteoblasts and osteoclasts associated with mineralization impairment.

Discussion: Our data support the requirement of Tric-b during early development and in bone cell differentiation.

Introduction

The trimeric cation channels, TRICs, are responsible for the transport of K+ ions across the endoplasmic or sarcoplasmic reticulum (ER/SR) membranes where they act as counter-ions to allow electroneutral Ca^{2+} exit from the ER/SR lumen to the cytosol. The mammalian family of TRICs is composed by TRIC-A and TRICB subtypes, encoded by *TMEM38A* and *TMEM38B*, respectively. TRIC-A mediated Ca2+ release throughout coupling with ryanodine receptors (RyRs) is particularly relevant in excitable cells, especially in striated muscle and brain (1), while TRIC-B, synchronizing with inositol trisphosphate receptors (IP_3Rs), ubiquitously mediates Ca2+ release (2). Calcium plays important roles both as cofactor and stabilizing ion for several proteins with enzymatic and/or chaperone functions and as second messenger in various signal transduction pathways, thus its homeostasis affects multiple cell functions, including contraction and relaxation, motility, metabolism, protein synthesis, modification and folding, secretion, cell-cycle progression, apoptosis and gene expression (3, 4). The impairment in RyRs- and IP_3Rs- mediated Ca^{2+} release observed in TRIC-A and TRIC-B knock-out mouse models, respectively, supports the tissue specific role of the channels in modulating calcium signaling. TRIC-A knock-out mice show reduced or irregular muscle contractile responses and develop hypertension (5, 6), while TRIC-B knock-out mice suffer from pulmonary dysfunction and die perinatally due to an insufficient alveoli surfactant production (7). Interestingly, TRIC-B knock-out mice reveal also skeletal abnormalities, such as reduced body size and impaired ossification associated with insufficient collagen matrix production (8). A skeletal phenotype is similarly described in humans with loss of function mutations in *TMEM38B*, which are affected by a recessive form of osteogenesis imperfecta (OI), classified as OI type XIV (OMIM 615066) (9). They are characterized, similarly to the most OI individuals with dominant and other recessive forms (10), by wide phenotypical variability, ranging from asymptomatic to severe, with different degrees of bone deformities, low bone mass, mild to recurrent fractures, growth retardation and short stature (11). The primary fibroblasts and osteoblasts isolated from affected individuals display a reduced level of helical lysyl hydroxylation, suggesting a dysfunctional activity of lysyl hydroxylase 1 (LH1) that is a calcium dependent enzyme. LH1 is necessary for proper lysine hydroxylation in the collagen type I helical domain and formation of stable intermolecular cross-linking (12). Furthermore, hydroxylysines are substrates for collagen specific ER O-linked glycosylation process (13, 14). In OI type XIV individuals this results in the synthesis of undermodified collagen type I (15, 16), which is susceptible to cell retention causing ER stress and increased degradation. Furthermore, abnormally secreted molecules are not properly incorporated in the extracellular matrix fibers (17). Also, osteoblasts from TRIC-B knockout mice present enlarged

ER cisternae due to intracellular collagen retention (8). In vitro long term cultured primary human OI type XIV osteoblasts display reduced expression of early markers of differentiation such as *RUNX2* and *SP7* and increased expression of the later markers *BGLAP* and *OPN*, which inhibit crystal growth (16, 18). Osteoclasts are also impaired, since their number and activity are reduced (16). In immortalized human Foetal Osteoblasts (hFOB) knock-out for *TMEM38B* a decreased proliferation and mineralization have been recently demonstrated (19). In the last decade, zebrafish proved to be a very reliable animal model to reproduce human common and heritable disorders, including skeletal diseases. Its high reproductive rate, larvae transparency and small size together with the ease of manipulation of its genome made zebrafish a high throughput and low-cost model to understand the molecular basis of human diseases as well as to identify new targets and to test innovative pharmacological approaches. The development of high-resolution imaging techniques further strength the use of teleost in bone research (20). Zebrafish can regenerate several organs and tissues including bone and indeed fin ray regeneration represents a powerful tool to investigate bone formation in adult animals. In this study we mapped for the first time the spatial and temporal expression of *tmem38a* and *tmem38b* during zebrafish early developmental stages and their expression in adult tissues. By CRISPR/Cas9 targeting of *tmem38b* in zebrafish we proved the relevance of Tric-b for skeletal development and collagen biosynthesis. Using a caudal fin regeneration assay we demonstrated that lack of *tmem38b* affects both osteoblasts and osteoclasts activity.

Materials and methods

Zebrafish husbandry and ethical statement

Wild-type (WT) AB zebrafish were obtained by the European Zebrafish Research Center (EZRC) (Germany). Zebrafish embryos were kept in petri dishes in zebrafish water (1.2 mM $NaHCO_3$, instant ocean 0.1 g/L, 1.4 mM $CaSO_4$, methylene blue 0.00002% w/v) at 28°C until 6 days post fertilization (dpf), then housed in ZebTEC semiclosed recirculation housing systems (Techniplast) at 28°C, pH 7.5 and conductivity 500 μS on a 14/10 light/dark cycle. Adult zebrafish were fed three times a day alternating dry food and brine shrimps. For the experiments, larvae and adult zebrafish were anesthetized using 0.016% w/v tricaine (3-amino benzoic acidethylester, Sigma Aldrich) in zebrafish water and sacrificed by tricaine overdose (0.03% w/v). All the experiments were performed in agreement with EU Directive 2010/63/EU. The experimental protocol was approved by Italian Ministry of Health (Approval Animal Protocol No.1191/2016-PR). 2.2 In silico analysis Synteny maps of the chromosomic regions surrounding transmembrane protein 38A and transmembrane protein 38B (*TMEM38A/B*) genes in *D. rerio*, *H. sapiens* and *M. musculus* were generated using the human genes as reference by combining PhyloView and AlignView from Genomicus 93.01 (http://www. genomicus.biologie.ens.fr) with Ensembl Comparative Genomics data. Conserved domains between zebrafish, human and mouse proteins were identified using UniProt (https://www.uniprot.org).

In situ hybridization

Whole-mount *in situ* hybridization was carried out according to the standard protocol (21). An 841 bp amplicon was obtained by RT-PCR amplification of WT zebrafish *tmem38b* mRNA (ENSDART00000168983) using primers on exon 1 (5'- TCAATCTGAACGAGCTCGCATTT-3', 20-42 nt) and on exon 10 (5'- AAGAAGCAGAAGCCAGCAAAAAG-3', 839-861 nt) and subcloned in T7 pGEM-T-Easy vector (Promega). Plasmid DNA was linearized by enzymatic digestion with SacII (New England BioLabs) for the antisense RNA probe and with SpeI (Promega) for the sense probe. 48 and 72 hours post fertilization (hpf) embryos (n =10 for each group) were fixed in 4% (w/v) paraformaldehyde (PFA) o/n at 4°C, washed in PBS-T (PBS containing 0.1% Tween-20) and digested with 10 μg/mL proteinase K for a time depending on embryos' developmental stage. Digoxigenin uridine-5′ triphosphate (DIG) labeled RNA sense and antisense probes targeting *tmem38b* gene were used after incubation at 64°C. Finally, images were acquired using a Leica M165 FC microscope connected to a Leica DFC425 C digital camera.

Genotyping

The WT, *tmem38b*$^{-/-}$ and *tmem38b*$^{\Delta 120\text{-}7/\Delta 120\text{-}7}$ genomic DNA was extracted depending on the experiment type, from single embryos, pool of embryos or caudal fin biopsies from adult zebrafish. Tissues were digested by proteinase K (2.5 mg/mL, Sigma Aldrich) in lysis buffer (100 mM Tris HCl, pH 8.5, 5 mM EDTA, 0.2% (w/v) SDS, 200 mM NaCl) overnight (o/n) at 55°C, followed by isopropanol precipitation and resuspension in 20 mM Tris-HCl, 1 mM EDTA, pH 8.0. DNA was PCR amplified using the following primers: forward 5'-TTACTGTCCGCTGGATGTGG-3' (11326-11345 nt) and reverse 5'–CAGAGCGTCGCTGTATTTGC-3' (11448-11467 nt) as described in Supplementary Methods. The different amplicon sizes were discriminated on 12% and 10% v/v electrophoresis acrylamide gel in TBE buffer (0.1 M Tris HCl, 0.1 M H3BO3, 2 mM EDTA, pH 8.2), respectively. 2.5 RNA extraction and qPCR RNA was extracted from RNA pools of 20 embryos at different stages of development (from 2-4 cells to 96 hours post fertilization, hpf) and from caudal fins of adult WT, *tmem38b*$^{-/-}$ and *tmem38b*$^{\Delta 120\text{-}7/\Delta 120\text{-}7}$ (WT n = 3, *tmem38b*$^{-/-}$ n = 3, *tmem38b*$^{\Delta 120\text{-}7/\Delta 120\text{-}7}$ n = 3) or from pools of bones, brains, muscles, swim bladders, hearts (WT n = 3 pools, *tmem38b*$^{-/-}$ n = 3 pools, *tmem38b*$^{\Delta 120\text{-}7/\Delta 120\text{-}7}$ n = 3 pools, each pool included samples from 2 fish) using Qiazol (Qiagen) and DNase digestion (Invitrogen) according to manufacturer's instructions. All experiments were performed in triplicate, except when indicated in the figure legend. RNA quantity was determined by NanoDrop spectrophotometer and RNA quality by agarose gel electrophoresis. Reverse-transcription was performed using the High-Capacity cDNA Transcription kit (Applied Biosystems) according to manufacturer's protocol in a final volume of 20 µL. qPCR was performed in triplicate in a 25 µL final volume using Taqman Universal PCR Master mix (Applied Biosystems) and commercial TaqMan probes for *tmem38b*, *tmem38a*, *rpl13a* and *β actin* (Dr03434781_m1, Dr03075180_m1, Dr03119260_g1 and Dr03432610_m1, Applied Biosystems). The relative expression of each gene was calculated using the DDCt method. qPCR for *acp5a* (ENSDART00000004716.10), *bglap* (ENSDART00000100845.5), *ctsk* (ENSDART00000179680.1), *mpeg* (ENSDART00000077637.5), *opg* (ENSDART00000184909.1), *rankl* (ENSDART00000098355.5), *sp7* (ENSDART00000128793.3) and the housekeeping *dna15ta1* (22) was performed in 25 µL reaction mixtures with 12.5 µL SYBR Green Mastermix (Applied Biosystems). Primer sequences are available upon request. The QuantStudio 3 thermocycler and the QuantStudio Design and analysis software (Applied Biosystems) were used. Samples were run in triplicate.

Collagen analysis

Skin and bone were dissected from adult WT (n=2), *tmem38b*$^{-/-}$ (n=2) and *tmem38b*$^{\Delta 120\text{-}7/\Delta 120\text{-}7}$ (n=2) following sacrifice. The tissues were defatted for 6 h in 0.1 N NaOH at 4°C. Bone was decalcified for 48 h in 0.5 M EDTA pH 7.4 at 4°C. The pepsin-soluble collagen fraction (PSC) was obtained as described in (23). Briefly, tissues were digested with 0.1 mg/mL pepsin in 0.5 M acetic acid at 4°C for 48 h. The PSC was precipitated by 0.9 M NaCl in 0.5 M acetic acid o/n at 4° C and quantified using Sircol Soluble Collagen assay (Biocolor). Equal amount of collagen from each sample (2 µg) was loaded on 6% SDS Urea-PAGE in non-reducing conditions. Gels were stained overnight with 0.08 M picric acid, 0.04% Coomassie Brilliant Blue R250 (Sigma Aldrich), destained in water and acquired with ImageQuant LAS 4000 (GE Healthcare) using the ImageQuant LAS 4000 1.2 software. 2.7 Morphometric analysis Images of anesthetized post hatching stages (7, 14, 21 dpf and 1, 2, 4, 6 mpf) WT (n ≥ 13) and *tmem38b*$^{-/-}$ (n ≥ 8) larvae and adult zebrafish were acquired with a M165FC stereomicroscope (Leica) connected to DFC425C digital camera (Leica). For *tmem38b*$^{\Delta 120\text{-}7/\Delta 120\text{-}7}$, images were taken at 21 dpf and 1 mpf (n ≥ 13). Measurements were performed as described (24) using the LAS v4.13 software (Leica). On lateral images, the Standard Length (SL) was measured as the distance from the snout to the caudal peduncle or, in pre-flexion larvae that do not have a caudal peduncle, to the posterior tip of the notochord. Vertebral length and height were evaluated at 21 dpf (WT n ≥22, *tmem38b*$^{-/-}$ n = 25, *tmem38b*$^{\Delta 120\text{-}7/\Delta 120\text{-}7}$ n = 19) and 1 mpf (WT n ≥18, *tmem38b*$^{-/-}$ n = 18, *tmem38b*$^{\Delta 120\text{-}7/\Delta 120\text{-}7}$ n = 18) in both mutants and also at 2 mpf in *tmem38b*$^{-/-}$ (WT n = 13, *tmem38b*$^{-/-}$ n = 14). For each vertebra, the mean of the length measured dorsally and ventrally, and the mean of the height measured anteriorly and posteriorly to the vertebral centrum were evaluated using the LAS v4.13 software (Leica). At 21 dpf, 10 vertebrae starting from the first ossified centrum were considered, while at 1 and 2 mpf the vertebral dimensions were evaluated by measuring from the second centrum articulated with the ribs. In addition, the level of inflation of the swim bladder was evaluated in larvae by counting the numbers of lobes on lateral images at 21 dpf (WT n ≥27, *tmem38b*$^{-/-}$ n = 26, *tmem38b*$^{\Delta 120\text{-}7/\Delta 120\text{-}7}$ n = 21).

Skeletal staining

Bone was stained with Alizarin Red as previously described (25). Both larval and adult WT (n ≥ 28), *tmem38b*$^{-/-}$ (n ≥ 17) and *tmem38b*$^{\Delta 120\text{-}7/\Delta 120\text{-}7}$ (n = 8) zebrafish were sacrificed and fixed overnight in PFA 4% w/v in PBS (Sigma Aldrich) with 0.9 mM $CaCl_2$ and 0.49 mM $MgCl_2$, pH 7.4 at 4°C. Bleaching to remove the pigmentation was performed with 3% v/v H_2O_2, 0.5% w/v KOH at RT followed by two washes in glycerol 25% v/v, 0.1% w/v KOH. Soft tissues were digested with 1

mg/mL trypsin dissolved in a 30% v/v solution of saturated $B_4Na_2O_7$. After the staining in 0.01% w/v Alizarin Red S (Sigma Aldrich), 25% v/v glycerol, 100 mM Tris– HCl, pH 7.5 overnight at RT, fish were washed in increasing 0.1% series of glycerol/KOH and finally stored at 4°C in 100% glycerol, 0.1% KOH. Images were acquired using a Leica M165 FC microscope connected to a Leica DFC425 C digital camera. The mineralization of the notochord was evaluated describing the level of ossification as beginning, intermediate or complete ossification. The mineralization of Alizarin Red stained caudal fins was evaluated in the amputated samples and 5 days post amputation (dpa) (WT n ≥ 9, *tmem38b*$^{-/-}$ n ≥ 8, *tmem38b*$^{\Delta 120\text{-}7/\Delta 120\text{-}7}$ n ≥ 8) by measuring the real mineralized area (RMA) normalized to the ray width (RAY), according to literature (26). In addition, the length of segments per ray was measured on the amputated caudal fins (WT n = 6, *tmem38b*$^{-/-}$ n = 8, *tmem38b*$^{\Delta 120\text{-}7/\Delta 120\text{-}7}$ n = 3). Measurements were performed using the LAS v4.13 software (Leica).

Picro Sirius Red collagen staining

Amputated caudal fins of adult WT (n=3), *tmem38b*$^{-/-}$ (n=4) and *tmem38b*$^{\Delta 120\text{-}7/\Delta 120\text{-}7}$ (n=3) zebrafish were collected and fixed overnight in PFA 4% w/v in PBS. Caudal fins were stained 1 h in 0.1% w/v Sirius Red (Direct Red 80, Sigma Aldrich) in saturated aqueous solution of picric acid (Sigma Aldrich) (27). After staining, caudal fins were washed in 0.5% v/v acetic acid, and directly dehydrated three times in absolute ethanol. Samples were clarified with xylene and mounted with DPX (Sigma Aldrich). Slides were observed under polarized light with the DM2500 microscope (Leica) and acquired using the ICC50 W digital camera (Leica). Measurements were performed using Leica LAS v4.13 software on 20X images. First, the length of each actinotrichia per ray was measured by tracing a line from the most proximal red signal in the ray to the tip of the caudal fin. Then, all the actinotrichia whose length was measured were counted and the mean of the number of actinotrichia per ray was calculated.

Tartrate-resistant acid phosphatase staining

Tartrate-resistant Acid Phosphatase (TRAP) staining was performed (28). Caudal fins of adult WT (n = 7), *tmem38b*$^{-/-}$ (n = 9) and *tmem38b*$^{\Delta 120\text{-}7/\Delta 120\text{-}7}$ (n = 10) zebrafish were fixed in PFA 4% in PBS o/n at 4°C, washed in PBS containing 0.1% v/v Tween-20 and permeabilized in PBS containing 0.3% v/v Triton X-100 for 30 min. Fins were then equilibrated in TRAP buffer (0.1 M sodium acetate, 0.1 M acetic acid, 50 mM sodium tartrate) and colour reaction was performed in TRAP buffer containing 0.1 mg/ml Naphtol AS-MX phosphate (Sigma Aldrich) and 0.3 mg/ml Fast Red Violet LB (Sigma Aldrich). Fins were then bleached in 10% H_2O_2, 1% KOH o/n at RT to remove pigmentation and then stored in 70% glycerol at 4°C. Images were acquired using a Leica M165 FC microscope connected

to a Leica DFC425 C digital camera. The number of TRAP+ cells in the regenerate was counted using the Cell Counter tool on the ImageJ software according to literature (29).

Transmission electron microscopy analysis

For transmission electron microscopy (TEM) analysis, 1 mpf WT (n= 3), *tmem38b*$^{-/-}$ (n=3) and *tmem38b*$^{\Delta 120\text{-}7/\Delta 120\text{-}7}$ (n=3) were fixed for 24 h at RT in 1.5% v/v PFA (Sigma Aldrich), 1.5% v/v glutaraldehyde (Sigma Aldrich), 0.1 M sodium cacodylate buffer (pH 7.4) and 0.001% w/v CaCl2. The samples were decalcified in 0.1 M EDTA for 14 days at 4°C. Samples were rinsed in 0.1 M sodium cacodylate buffer containing 10% sucrose and post fixed for 2 h using 1% w/v OsO_4 in 0.1 M sodium cacodylate buffer at pH 7.4. Subsequently, zebrafish were infiltrated with low-viscosity epoxyembedding medium. Ultra-thin (70 nm) sections of the region of interest (vertebral endplate growth zone) were cut using a Reichert Ultracut E ultramicrotome (Reichert-Jung) with a diamond knife (Diatome Ltd.) and mounted on formvar-coated single slot copper grids. The sections were stained with uranyl acetate and lead citrate and viewed with a Jeol JEM-1010 (Jeol Ltd) TEM operating at 60 kV. Microphotographs were taken with a Veleta camera (Emsis, Germany) (30). TEM images were used to detect the endoplasmic reticulum cisternae enlargement. The area of ER cisternae in WT, *tmem38b*$^{-/-}$ and *tmem38b*$^{\Delta 120\text{-}7/\Delta 120\text{-}7}$ was measured using LAS v4.13 software (Leica). 2.12 4 phenylbutyrate treatment (4PBA) WT, *tmem38b*$^{-/-}$ and *tmem38b*$^{\Delta 120\text{-}7/\Delta 120\text{-}7}$ embryos were manually dechorionated at 24 hpf. Fish were placed in 6 well plates (20 fish per well) in zebrafish water containing 0.003% 1-phenyl 2- thiourea (PTU) to prevent pigmentation and treated with 0.05 mM 4PBA from 1 dpf to 5 dpf. Half of the volume of water with or without 4PBA was replaced every day (23).

Whole-mount immunostaining

Whole mount immunostaining was performed as previously described (23). Briefly, *tmem38b*$^{-/-}$ (n=116) and WT (n=146) untreated and 4PBA treated *tmem38b*$^{-/-}$ (n=113); *tmem38b*$^{\Delta 120\text{-}7/\Delta 120\text{-}7}$ (n=19) and WT (n=43) untreated and 4PBA treated *tmem38b*$^{\Delta 120\text{-}7/\Delta 120\text{-}7}$ (n=34) were collected at 5 dpf, fixed overnight in 4% w/v PFA in PBS, washed in PBS and stored in methanol at -20° C. After tissue digestion with 0.1% w/v proteinase K in PBS at 25°C for 15 min and 2% w/v hyaluronidase in PBS at 25°C for 20 min samples were blocked in 5% w/v bovine serum albumin (BSA, Sigma Aldrich) in PBS-T for 2 h at RT. Hsp47b affinity purified antibody (1:1000 in 5% BSA/PBS-T), kindly provided by Prof. Raimund Wagener, University of Cologne, Germany, and anti-rabbit secondary antibody (1:200 in 1% BSA/PBS-T, Cell Signaling) were used. DAB substrate (Thermo Scientific) was finally added until appearance of the staining. Fish were incubated in increasing glycerol series and stored

at 4°C in 100% glycerol. Images were acquired using a Leica M165 FC microscope connected to a Leica DFC425 C digital camera. Three operators blinded to the genotype and to the treatment of the fish independently evaluated the intensity of the signal as zero, low (+) or high (++). Following imaging, samples underwent stepwise ethanol dehydration and soft epon embedding according to an established protocol (31). Sagittal 4 mm sections were cut on a Microm HM360 microtome (Marshall Scientific), mounted with DPX and observed with an Axio Imager-Z1 microscope (Carl Zeiss).

Statistical analysis

All quantitative variables were expressed as mean with standard deviation (SD) or standard error of the means (SEM), as indicated in figure legend, while qualitative variables using percentage. To evaluate gene expression across genotype (WT, *tmem38b*$^{-/-}$ and *tmem38b*$^{\Delta 120\text{-}7/\Delta 120\text{-}7}$) for each examined organ, non parametric analysis of variance (Kruskall Wallis) was applied, followed by non-parametric unpaired t test with multiple comparison correction. To separately describe the behaviour of WT with respect to each mutant in bone mineralization, swim bladder inflation and Hsp47 signal, chi-squared or Fisher's exact test, if the assumption for chi squared was not respected, was performed. The Bonferroni's correction for multiple tests was applied to adjust the p-value when the Hsp47 signal for untreated and treated mutants was compared to that of WT. Separately, by each time point a comparison between WT and *tmem38b*$^{-/-}$ standard length and vertebral measurements was evaluated using parametric or the equivalent non parametric unpaired t test, when the assumptions for parametric were violated. The same approach was applied to ray segment length, RMA/RAY width, number of TRAP positive cells and number and length of actinotrichia. A $p<0.05$ was considered significant apart from when multiple correction was used. Statistical analyses were performed using SigmaPlot and STATA15®.

Results

TRICs expression in zebrafish

A single copy of *tmem38a* and *tmem38b* encoding the trimeric intracellular cation channels (TRICs) Tric-a and Tric-b, respectively is present in the *D. rerio* genome. The zebrafish *tmem38a* locus is residing on chromosome 11 and similarly to the human and murine gene positioned on chromosome 19 and 8, respectively, consists of 6 exons. The zebrafish *tmem38b* locus is located on chromosome 21 and includes 10 exons, while the human and murine gene is located in chromosome 9 and 4, respectively and consist of 6 exons. The *in silico* analysis of the human, mouse and zebrafish genomic regions surrounding *tmem38a* and *tmem38b loci* supports their common ancestral origin (Figure 1A and Supplementary Table 1). Zebrafish Tric-a consists of 295 amino acids and shows 70.6% and 68.1% identity with the human (299 aa) and the murine (298 aa) protein, respectively, whereas Tric-b (289 aa) shares only 45% and 48% identity with the human (291 aa) and the murine (292 aa) protein, respectively. Zebrafish Tric-a and Tric-b share 41.7% identity. In all three species, homology data support that TRIC channels are symmetrical trimers of identical protomers crossing the endoplasmic reticulum membrane with 7 α helices and characterized by two inverted repeated regions and a C-terminal helix. Each protomer contains a lipid consensus binding sequence KEVXRXXK that likely confers to the channel the voltage-sensitivity and also includes the predicted pore-forming KEV, important to guarantee the K^+ flux (32). Also, the two glycine rich regions in TM2 and TM5 are conserved as well as Gly74 in TRIC-A and Ala74 in TRIC-B that are recognized as luminal calcium binding site relevant for pore opening (32, 33) (Figure 1B). The expression of *tmem38b* at 48 and 72 hours post fertilization (hpf) in the region of cranio-facial cartilages was showed by whole mount in situ hybridization and supports also in teleosts the role of the channel in skeletal tissue starting from early developmental stage (Figure 1C and Supplementary Figure 1A). Temporal analysis of *tmem38a* and *tmem38b* expression in WT zebrafish at different embryonic developmental stages revealed a relevant increase of *tmem38a* expression from 24 hours post fertilization (hpf), while both a maternal and a zygotic expression were detected for *tmem38b* (Figure 1D). The two genes were expressed both in excitable (muscle, brain, heart) and in non-excitable (swim bladder, bone) adult tissues. As expected, the expression of *tmem38a* was particularly abundant in muscle, heart and brain, and surprisingly in bone as well, whereas the highest *tmem38b* expression was found in the swim bladder (Figures 2A, B).

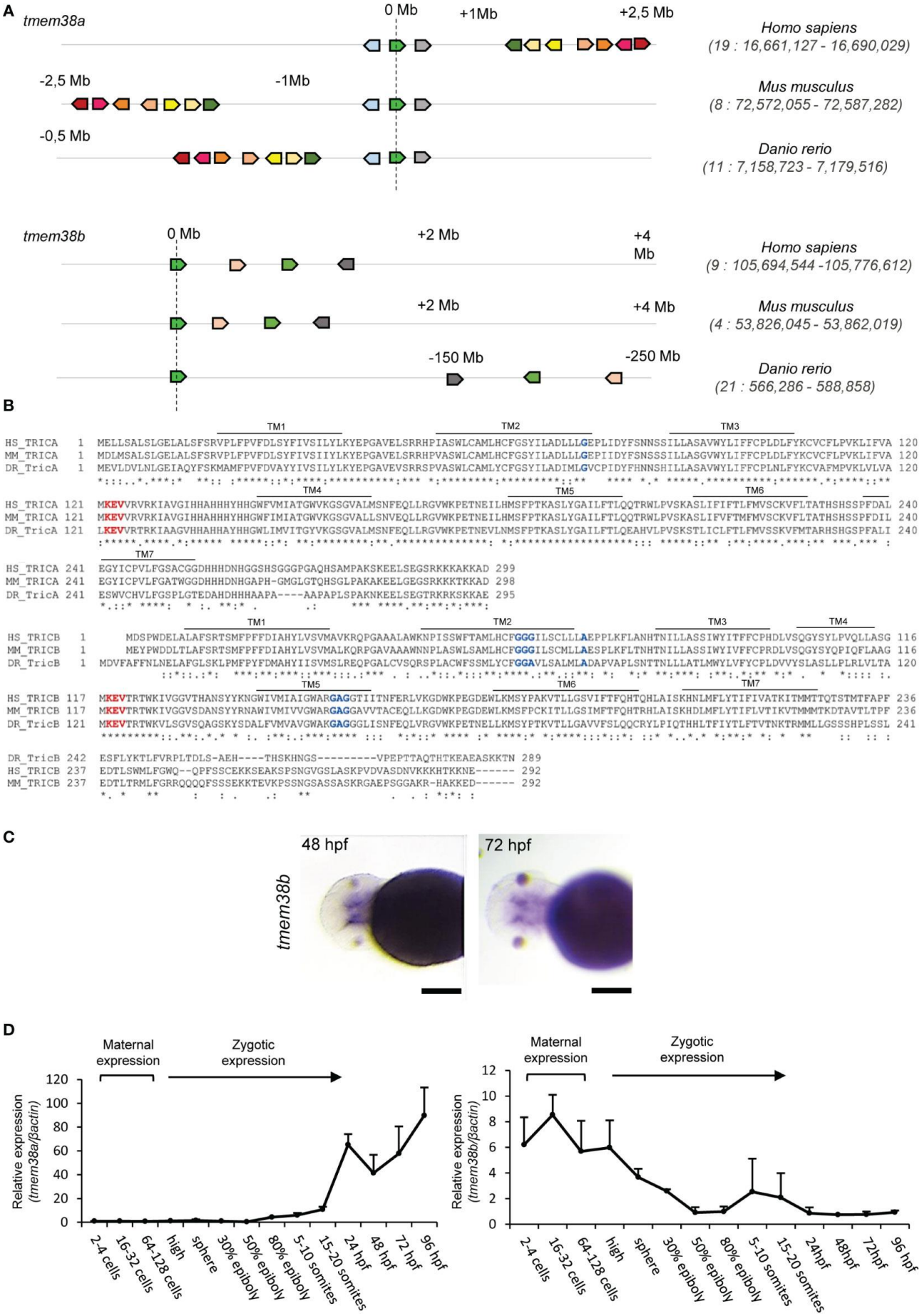
A
tmem38a
0 Mb
+1Mb
+2,5 Mb
Homo sapiens
(19 : 16,661,127 - 16,690,029)
-2,5 Mb
-1Mb
Mus musculus
(8 : 72,572,055 - 72,587,282)
-0,5 Mb
Danio rerio
(11 : 7,158,723 - 7,179,516)
tmem38b
0 Mb
+2 Mb
+4 Mb
Homo sapiens
(9 : 105,694,544 -105,776,612)
+2 Mb
+4 Mb
Mus musculus
(4 : 53,826,045 - 53,862,019)
-150 Mb
-250 Mb
Danio rerio
(21 : 566,286 - 588,858)
B
TM1
TM2
TM3
HS_TRICA 1 MELLSALSLGELALSFSRVPLFPVFDLSYFIVSILYLKYEPGAVELSRRHPIASWLCAMLHCFGSYILADLLLGEPLIDYFSNNSSILLASAVWYLIFFCPLDLFYKCVCFLPVKLIFVA 120
MM_TRICA 1 MDLMSALSLGELALSFSRVPLFPVFDLSYFIVSIIYLKYEPGAVELSRRHPVASWLCAMLHCFGSYILADLLLGEPIIDYFSNSSSILLASGVWYLIFFCPLDLFYKCVCFLPVKLIFVA 120
DR_TricA 1 MEVLDVLNLGEIAQYFSKMAMFPVFDVAYYIVSILYLKYEPGAVEVSRRSPVASWLCAMLYCFGSYILADIMLGVCPIDYFHNNSHILLASAVWYLIFFCPLNLFYKCVAFMPVKLVLVA 120
TM4
TM5
TM6
HS_TRICA 121 MKEVVRVRKIAVGIHHAHHHYHHGWFVMIATGWVKGSGVALMSNFEQLLRGVWKPETNEILHMSFPTKASLYGAILFTLQQTRWLPVSKASLIFIFTLFMVSCKVFLTATHSHSSPFDAL 240
MM_TRICA 121 MKEVVRVRKIAVGIHHAHHHYHHGWFIMIATGWVKGSGVALLSNVEQLLRGVWKPETNEILHMSFPTKASLYGAILFTLQQTRWLPVSKASLIFVFTMFMVSCKVFLTATHSHSSPFDIL 240
DR_TricA 121 LKEVVRTRKIAAGVHHAHHAYHHGWLIMVITGYVKGSGVALMSNFEQLLRGVWKPETNEVLNMSFPTKASLYGAILFTLQEAHVLPVSKSTLICLFTLFMVSSKVFMTARHSHGSPFALI 240
TM7
HS_TRICA 241 EGYICPVLFGSACGGDHHHDNHGGSHSGGGPGAQHSAMPAKSKEELSEGSRKKKAKKAD 299
MM_TRICA 241 EGYICPVLFGATWGGDHHHDNHGAPH-GMGLGTQHSGLPAKAKEELGEGSRKKKTKKAD 298
DR_TricA 241 ESWVCHVLFGSPLGTEDAHDHHHAAPA----AAPAPLSPAKNKEELSEGTRKRKSKKAE 295
TM1
TM2
TM3
TM4
HS_TRICB 1 MDSPWDELALAFSRTSMFPFFDIAHYLVSVMAVKRQPGAAALAWKNPISSWFTAMLHCFGGGILSCLLLAEPPLKFLANHTNILLASSIWYITFFCPHDLVSQGYSYLPVQLLASG 116
MM_TRICB 1 MEYPWDDLTLAFSRTSMFPFFDIAHYLVSVMALKQRPGAVAAAWNNPLASWLSAMLHCFGGGILSCMLLAESPLKFLTNHTNILLASSIWYIVFFCPRDLVSQGYSYQPIQFLAAG 116
DR_TricB 1 MDVFAFFNLNELAFGLSKLPMFPYFDMAHYIISVMSLREQPGALCVSQRSPLACWFSSMLYCFGGAVLSALMLADAPVAPLSNTTNLLLATLMWYLVFYCPLDVVYSLASLLPLRLVLTA 120
TM5
TM6
TM7
HS_TRICB 117 MKEVTRTWKIVGGVTHANSYYKNGWIVMIAIGWARGAGGTIITNFERLVKGDWKPEGDEWLKMSYPAKVTLLGSVIFTFQHTQHLAISKHNLMFLYTIFIVATKITMMTTQTSTMTFAPF 236
MM_TRICB 117 MKEVTRTWKIVGGVSDANSYYRNAWIVMIVVGWARGAGGAVVTACEQLLKGDWKPEGDEWLKMSFPCKITLLGSIMFTFQHTRHLAISKHDLMFLYTIFLVTIKVTMMMTKDTAVTLTPF 236
DR_TricB 121 MKEVTRTWKVLSGVSQAGSKYSDALFVMVAVGWAKGAGGGLISNFEQLVRGVWKPETNELLKMSYPTKVTLLGAVVFSLQQCRYLPIQTHHLTFIYTLFTVTNKTRMMLLGSSSHPLSSL 241
DR_TricB 242 ESFLYKTLFVRPLTDLS-AEH----THSKHNGS---------VPEPTTAQTHTKEAEASKKTN 289
HS_TRICB 237 EDTLSWMLFGWQ--QPFSSCEKKSEAKSPSNGVGSLASKPVDVASDNVKKKHTKKNE------ 292
MM_TRICB 237 EDTLTRMLFGRRQQQQFSSSEKKTEVKPSSNGSASSASKRGAEPSGGAKR-HAKKED------ 292
C
48 hpf
72 hpf
tmem38b
D
Maternal expression
Zygotic expression
Relative expression (tmem38a/βactin)
120
100
80
60
40
20
0
2-4 cells
16-32 cells
64-128 cells
high
sphere
30% epiboly
50% epiboly
80% epiboly
5-10 somites
15-20 somites
24 hpf
48 hpf
72 hpf
96 hpf
Maternal expression
Zygotic expression
Relative expression (tmem38b/βactin)
12
10
8
6
4
2
0
2-4 cells
16-32 cells
64-128 cells
high
sphere
30% epiboly
50% epiboly
80% epiboly
5-10 somites
15-20 somites
24hpf
48hpf
72hpf
96 hpf

Figure 1. Analysis of *tmem38a/b* across species and of their spatio-temporal expression during zebrafish development. **(A)** The sinteny analysis performed on humans (*H. sapiens*), mice (*M. musculus*) and zebrafish (*D. rerio*) supported the existence of a common ancestral chromosomal origin for both *tmem38a* and *tmem38b*. The maps were obtained using the genome browser Genomicus. The human genes were used as roots. The position of the genes (Mb) relative to the investigated locus is based on Ensemble database and shown on top of the chromosome line. The exact chromosomal position of all the conserved genes is reported in the Supplementary Tables S1. The direction of the arrows indicates the gene orientation in respect to the reference gene. **(B)** Trimeric intracellular cation channel A (TRIC-A) and B (TRIC-B) domains are conserved among human, mouse and zebrafish. The 7 transmembrane domains (TM) are indicated. In red is shown the KEV pore channel domain, while in blue are indicated the two glycine reach regions in TM2 and TM5. **(C)** *In situ* hybridization analysis of 48 and 72 hpf WT embryos revealed the presence of *tmem38b* in the region of craniofacial cartilages. **(D)** Relative expression of *tmem38a* and *tmem38b* was evaluated by qPCR demonstrating a maternal expression only for *tmem38b*. The experiment was perfomed in duplicate. Scale bar: 500 µm. Human *TMEM38A* ENSG00000072954, murine *Tmem38a* ENSMUSG00000031791, zebrafish *tmem38a* ENSDARG00000024047; human *TMEM38B* ENSG00000095209, murine *Tmem38b* ENSMUSG00000028420, zebrafish *tmem38b* ENSDARG00000100549. Tric-a: human Q9H6F2, murine Q3PMT8, zebrafish Q6P2T0; Tric-b: human Q9NVV0, murine Q9DAV9, zebrafish Q7ZVP8.

tmem38b mutants generated by CRISPR/Cas9 gene editing

The skeletal phenotype described in osteogenesis imperfecta (OI) type XIV, and caused by *TMEM38B* loss-of-function mutations in mammals, demonstrated a relevant role of TRIC-B in bone homeostasis. Thus, to get further insight on *tmem38b* function in teleosts and to generate a zebrafish model for the human disease, CRISPR/Cas9 was used to target exon 7 (Supplementary Figure 1B, C and Supplementary Materials) which includes the consensus sequence KEVXRXXK important for the formation of the pore channel. Among the generated mutant F1 heterozygous zebrafish (Supplementary Figure 1D), two were selected and crossbred for further experiments. The one carrying a 7 nucleotides deletion (c.524_530delTGAAGGA) predicted to insert a premature stop codon at amino acid 122 of Tric-b was chosen to generate the F2 *tmem38b* knock out model (*tmem38b*$^{-/-}$). The mutant carrying a 24 nucleotides in frame deletion (c.517_540del24nt) predicted to remove the p.Ala120_Thr127 oligopeptide was selected to generate the F2 *tmem38b*$^{\Delta 120\text{-}7/\Delta 120\text{-}7}$ lacking the highly conserved KEV motif (Supplementary Figure 1D). qPCR showed that *tmem38b* expression was significantly reduced in 24 hpf *tmem38b*$^{-/-}$ embryos compared to both WT (WT 1.19± 0.16, *tmem38b*$^{-/-}$ 0.40 ± 0.28, p=0.013) and *tmem38b*$^{\Delta 120\text{-}7/\Delta 120\text{-}7}$ (*tmem38b*$^{-/-}$ 0.40 ± 0.28, *tmem38b*$^{\Delta 120\text{-}7/\Delta 120\text{-}7}$ 2.11 ± 0.87; p= 0.031) while no difference in the expression of *tmem38a* was detected (WT 1.16± 0.14, *tmem38b*$^{-/-}$ 0.88 ± 0.12, *tmem38b*$^{\Delta 120\text{-}7/\Delta 120\text{-}7}$ 1.09 ± 0.17). In addition, the expression of *tmem38b* in various tissues revealed different levels of non-sense mediated mRNA decay (NMD) ranging from 41.2% in bone and muscle to 77.7% in heart for *tmem38b*$^{-/-}$ and from 16.6% in muscle and none in brain for *tmem38b*$^{\Delta 120\text{-}7/\Delta 120\text{-}7}$ (Figure 2A, B). Unfortunately, the lack of specific antibody against Tmem38b did not allow to evaluate the protein expression level.

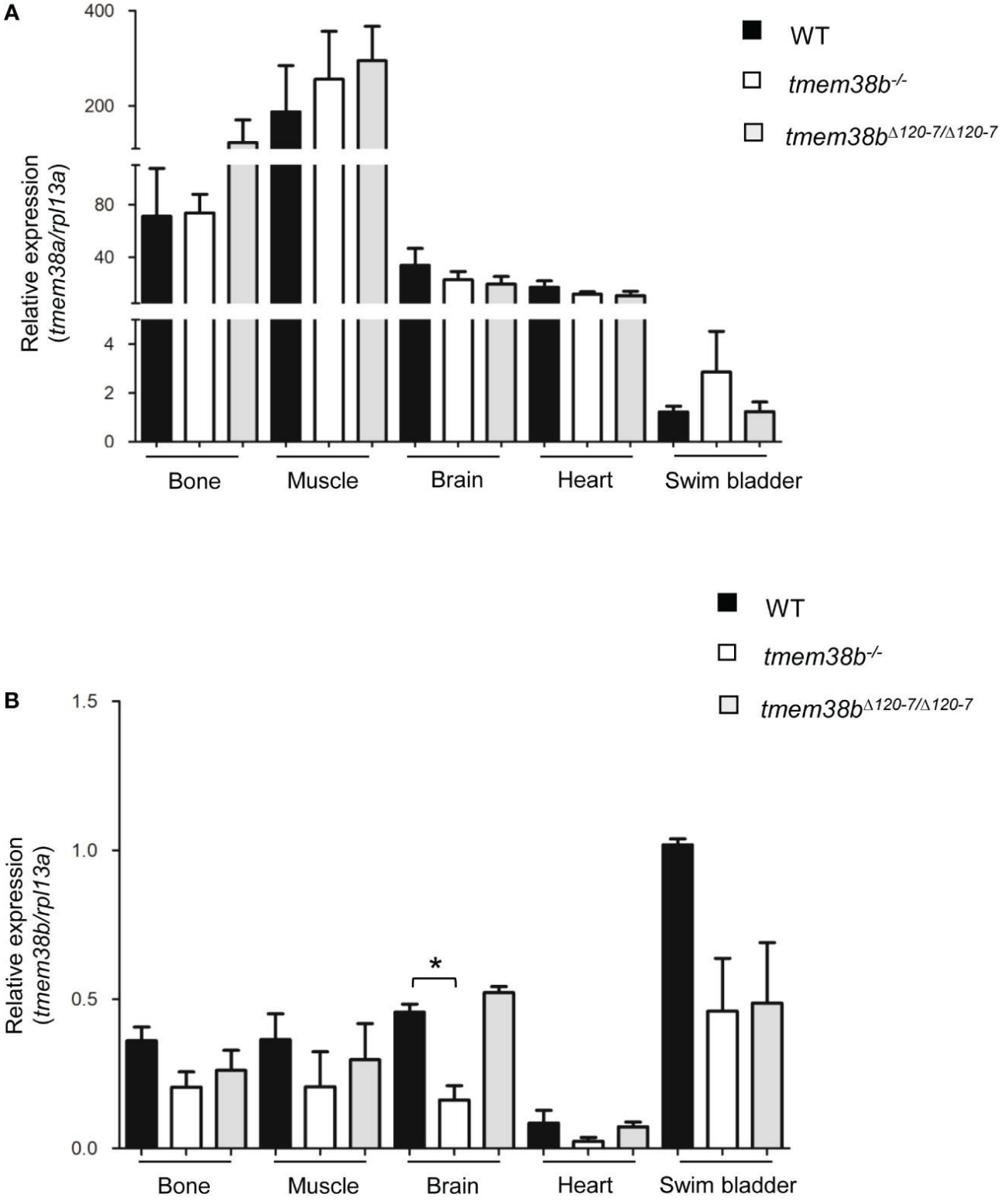

Figure 2. Expression analysis of *tmem38a* and *tmem38b* in excitable (muscle, brain, heart) and non-excitable tissues (bone, swim bladder) from adult WT and *tmem38b* mutants. **(A)** Relative expression of *tmem38a*. No difference in the transcript level was found between WT and *tmem38b* mutants by qPCR. **(B)** Relative expression of *tmem38b*. qPCR analysis revealed a reduced transcript level in almost all *tmem38b*$^{-/-}$ tissues respect to WT. Data are expressed as mean ± SEM. * $p < 0.05$ n = 3 RNA pools per group.

Zebrafish juvenile skeleton is impaired in *tmem38b*$^{-/-}$

Both *tmem38b* mutants were viable, reached adulthood and were fertile. Nevertheless, an increased lethality was observed in *tmem38b*$^{-/-}$ from 7 days post fertilization (dpf) compared to both WT and *tmem38b*$^{+/-}$. Indeed, a significant difference from the expected 1:2:1 Mendelian ratio was observed at 2 and 3 weeks of age (Supplementary Table 2). The growth curve followed from 5 dpf to 6 months post fertilization (mpf) revealed a significant reduction in the standard length (SL) at 21 dpf and 1 mpf in *tmem38b*$^{-/-}$ compared to WT (Figure 3A) and a delay in the inflation of swim bladder lobes was detectable in mutant fish at 21dpf, suggesting a developmental delay rescued at older age (Figure 3B). No difference in SL and in the swim bladder inflation was evident in *tmem38b*$^{\Delta 120\text{-}7/\Delta 120\text{-}7}$ (Supplementary Figures 2A, B). Whole mount Alcian Blue and Alizarin Red staining of 5 and 7 dpf larvae, respectively, did not reveal abnormality in cartilage or skeletal development in *tmem38b*$^{-/-}$ compared to WT (Supplementary Figure 3A-D). A reduced level of mineralization in the tip of notochord sheath was observed in *tmem38b*$^{-/-}$ compared to WT at 14 dpf (Figure 3C). An impaired mineralization of vertebra centra at 21 dpf and 1 mpf, as demonstrated by reduced vertebral length and vertebral height, the latter being smaller also at 2 mpf, was also detected (Figure 3D). Double staining with alizarin red and calcein did not show any difference in bone formation rate between WT and *tmem38b*$^{-/-}$ from 10 dpf to 1mpf (Supplementary Figure 4). The mineralization in mutant fish was partially rescued at 4 mpf, when only vertebral height was still reduced (Supplementary Figure 2C). The vertebral size was unchanged in the *tmem38b*$^{\Delta 120\text{-}7/\Delta 120\text{-}7}$ at the analyzed time points, with the exception of a reduced vertebral length at 21 dpf (Supplementary Figure 2D). MicroCT on both adult (9 mpf) fish models did not reveal any alteration in bone geometrical parameters compared to WT (Supplementary Figure 5 and data not shown). Also, nanoindentation analysis performed on vertebral bone cortex of 2 mpf mutants and control fish showed no differences either in hardness (*tmem38b*$^{-/-}$ 0.598 ± 0.050 GPa; *tmem38b*$^{\Delta 120\text{-}7/\Delta 120\text{-}7}$ 0.628 ± 0.068 GPa; WT 0.642 ± 0.052 GPa) or in elastic modulus (*tmem38b*$^{-/-}$ 13.704 ± 0.665 GPa; *tmem38b*$^{\Delta 120\text{-}7/\Delta 120\text{-}7}$ 13.895 ± 1.029 GPa; WT 14.391 ± 0.795 GPa). Taken together, the skeletal characterization revealed a mild effect of Tric-b absence in zebrafish endoskeleton limited to late larval-juvenile developmental stage when a rapid bone growth is required. The lack of bone phenotype in *tmem38b*$^{\Delta 120\text{-}7/\Delta 120\text{-}7}$ supports a possible residual activity of the in frame mutant Tric-b channel.

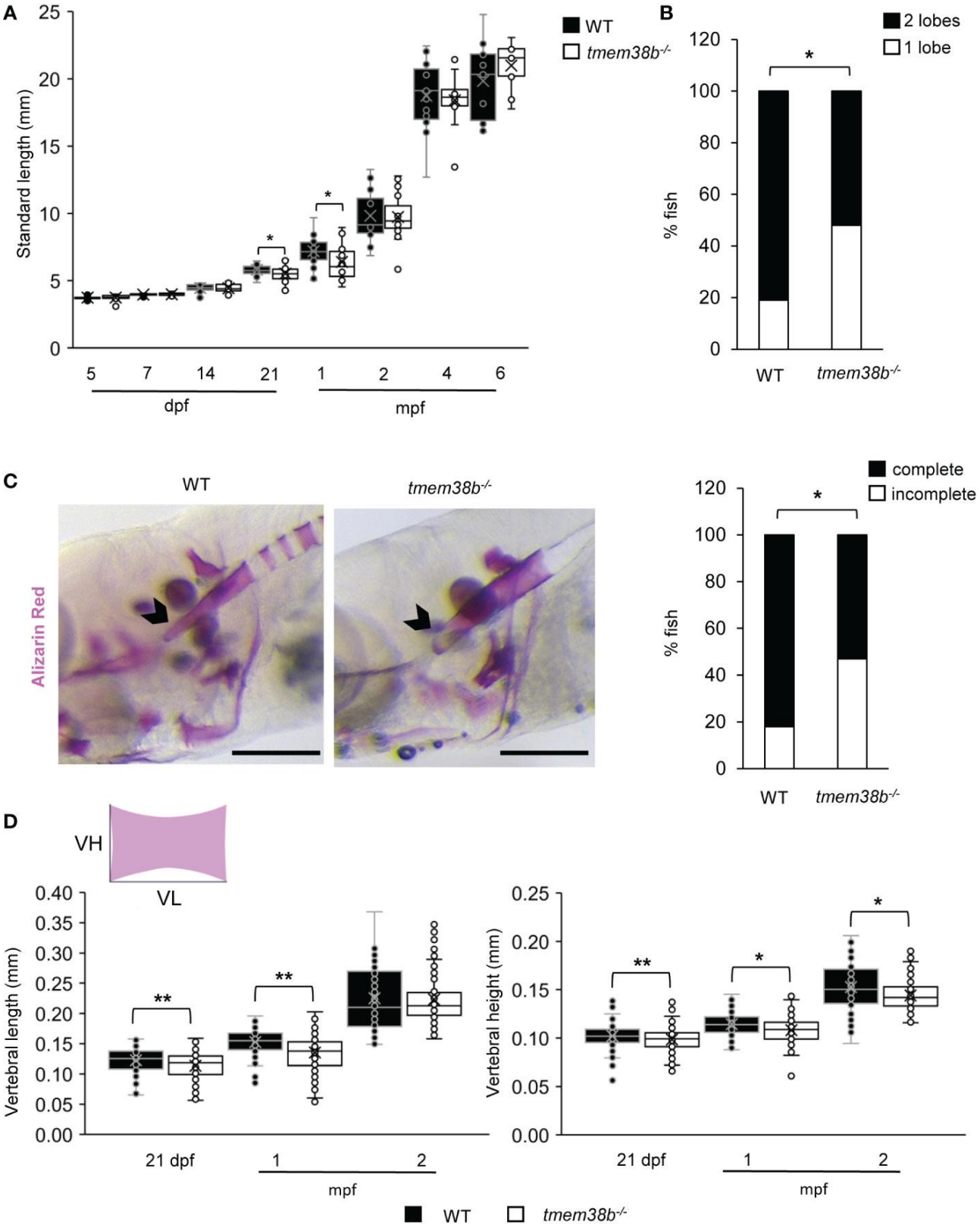

Figure 3. *tmem38b*$^{-/-}$ skeletal phenotype. **(A)** Growth curves representing WT and *tmem38b*$^{-/-}$ standard length measured at 5, 7, 14, 21 dpf, 1, 2, 4 and 6 mpf. At 21 dpf and 1 mpf *tmem38b*$^{-/-}$ were significantly shorter than WT. WT n ≥ 13, *tmem38b*$^{-/-}$ n ≥ 8. **(B)** At 21 dpf a significant delay in the inflation of the swim bladder was observed in *tmem38b*$^{-/-}$ (n = 27) with respect to WT (n = 28). **(C)** Representative lateral view (left panels) of 14 dpf alizarin red stained WT and *tmem38b*$^{-/-}$ fish. The notochord is indicated by the arrowhead. On the right the graph represents the level of the tip of the notochord mineralization, a delayed mineralization was

evident in *tmem38b*$^{-/-}$ (*tmem38b*$^{-/-}$ n = 17) respect to WT (WT n = 28) Scale bar: 500 µm. **(D)** Vertebral length and vertebral height measurement in WT and *tmem38b*$^{-/-}$ zebrafish. Vertebral length (VL) was reduced in *tmem38b*$^{-/-}$ compared to WT at 21 dpf and 1 mpf. Vertebral height (VH) was reduced in *tmem38b*$^{-/-}$ compared to WT at 21 dpf, 1 and 2 mpf. 21 dpf: WT n= 29; *tmem38b*$^{-/-}$ n= 25; 1 mpf: WT n= 24; *tmem38b*$^{-/-}$ n= 18; 2 mpf: WT n= 13; *tmem38b*$^{-/-}$ n= 14. *: $p < 0.05$, ** $p \leq 0.01$.

Collagen type I is retained in the endoplasmic reticulum of *tmem38b* mutants

Collagen type I extracted from WT and both mutants' skin and bone showed a slight faster electrophoretic migration (Figure 4A and Supplementary Figure 6A) supporting the presence of collagen undermodification, as reported in human OI type XIV cells (17). Electron microscopy analysis performed in the vertebral region revealed enlarged ER cisternae size in both fibroblasts and osteoblasts (Figure 4B) of *tmem38b* mutants compared to WT. The expression of Hsp47b, the collagen specific chaperone known to assist procollagen assembly in the ER and its trafficking into the Golgi and whose expression is coupled with collagen synthesis (34), was evaluated by whole mount immunostaining on 5 dpf larvae. Histological sections revealed that Hsp47b signal is intracellular and expressed in the outer epidermal layer (Figure 4C). A stronger and significantly higher Hsp47b signal in mutants compared to WT was detected (Figures 4D–F). Interestingly, the administration of 4 phenyl butyrate (4PBA), a chemical chaperone known to release ER stress in presence of collagen accumulation in dominant (23, 35) and some OI recessive forms (36), reduced Hsp47 signal in both mutants compared to controls supporting its positive role in restoring cell homeostasis also in presence of *tmem38b* mutations (Figures 4D-F).

Caudal fin rays and their regeneration are impaired in *tmem38b*$^{-/-}$

To evaluate the role of Tric-b during bone formation, caudal fin regeneration experiments were carried out. First, zebrafish amputated caudal fins were analyzed following Alizarin Red staining and a significantly increased segment length was detected in *tmem38b*$^{-/-}$ compared to controls (Figures 5A, B). In amputated and regrown samples stained with alizarin red the real mineralization area (RMA) was evaluated for all fin rays and normalized to ray width (RAY) (26). In *tmem38b*$^{-/-}$ a reduced RMA compared to WT was evident in the amputated samples, whereas at 5 days post amputation (dpa) it was significantly increased, suggesting a mineralization boost during early bone formation (Figures 5A, C). qPCR analysis on WT and *tmem38b*$^{-/-}$ pools of caudal fins showed no difference in the expression of the early osteogenic marker *sp7* (*osterix*) at both time points. The increased expression trend of the late marker *osteocalcin* (*bglap*) in the mutant amputated fins compared to WT normalized in 5 dpa regenerates (Figure 5D). No difference in bone mineralization during caudal fin regeneration as well as in the expression of specific markers of bone differentiation was detected in *tmem38b*$^{\Delta 120\text{-}7/\Delta 120\text{-}7}$ compared to WT (Supplementary Figures 6B–D).

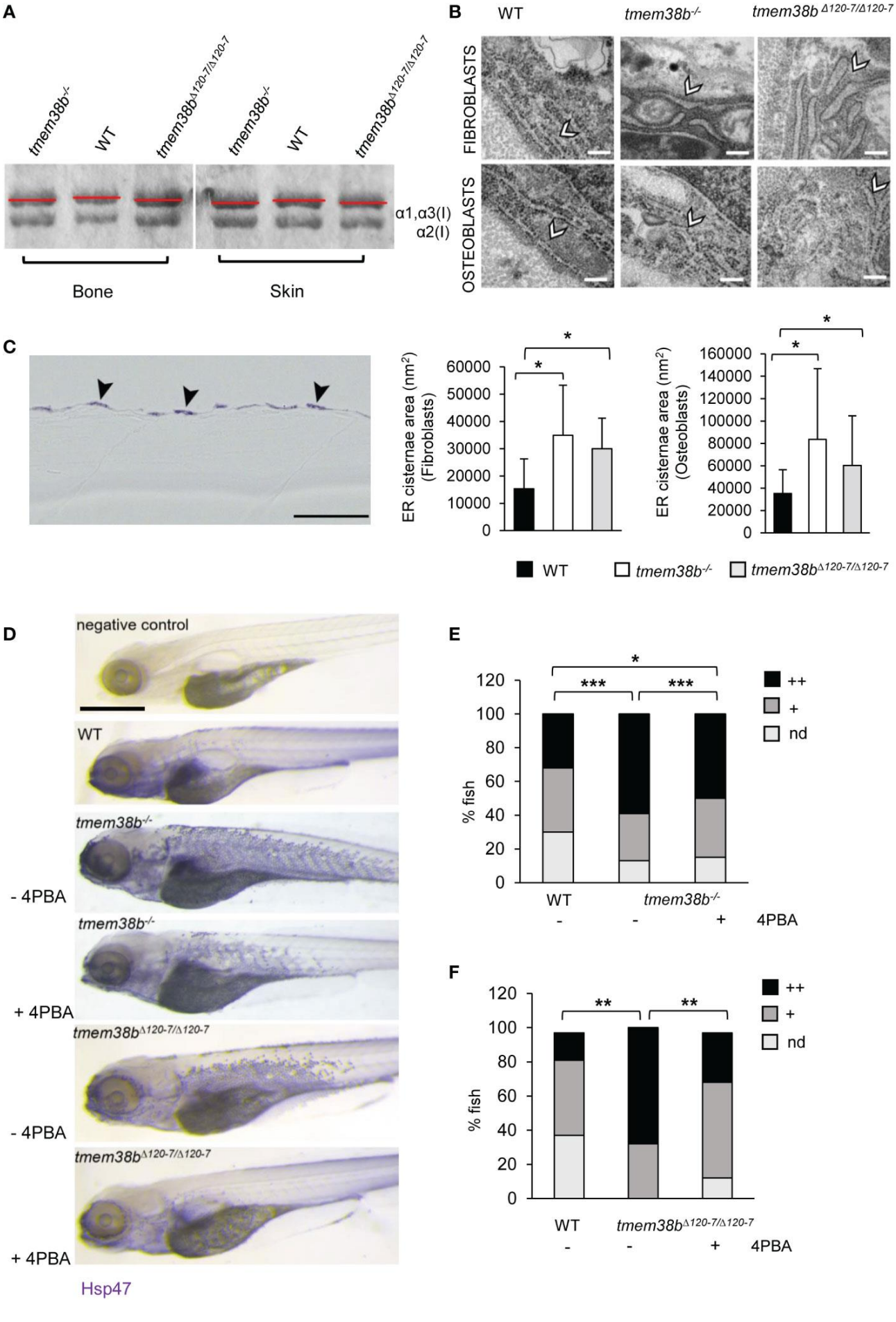
A
tmem38b-/-
WT
tmem38bΔ120-7/Δ120-7
α1,α3(I)
α2(I)
Bone
Skin
B
WT
tmem38b-/-
tmem38bΔ120-7/Δ120-7
FIBROBLASTS
OSTEOBLASTS
C
ER cisternae area (nm2) (Fibroblasts)
ER cisternae area (nm2) (Osteoblasts)
WT
tmem38b-/-
tmem38bΔ120-7/Δ120-7
D
negative control
WT
tmem38b-/-
- 4PBA
tmem38b-/-
+ 4PBA
tmem38bΔ120-7/Δ120-7
- 4PBA
tmem38bΔ120-7/Δ120-7
+ 4PBA
Hsp47
E
% fish
++
+
nd
WT
tmem38b-/-
4PBA
F
% fish
++
+
nd
WT
tmem38bΔ120-7/Δ120-7
4PBA

Figure 4. Collagen type I and ultrastructural analysis. **(A)** Representative Coomassie stained SDS-Urea-PAGE of collagen type I extracted from WT (n = 2) and mutants (*tmem38b*$^{-/-}$ n = 2; *tmem38b*$^{\Delta 120\text{-}7/\Delta 120\text{-}7}$ n = 2) bone and skin. Mutants' collagen α bands presented a slight faster migration compared to WT as highlighted by red lines. **(B)** Transmission electron microscopy images of 1 mpf WT (n = 3), *tmem38b*$^{-/-}$ (n = 3), and *tmem38b*$^{\Delta 120\text{-}7/\Delta 120\text{-}7}$ (n = 3) fibroblasts and osteoblasts at the vertebral endplate. ER cisternae enlargement was evident in mutants (arrowheads). Magnification 80000x. Scale bar: 200 nm. The ER cisternae area quantitation is shown in the graphs (bottom). **(C)** Immunohistochemistry of 5 dpf WT and *tmem38b*$^{-/-}$ with Hsp47b antibody. High magnification details of the skin of WT and *tmem38b*$^{-/-}$ following immunostaining with Hsp47b antibody revealed that Hsp47 signal was located in the fibroblasts of the skin (arrowheads). **(D)** Representative images of 5 dpf fish after whole mount immunohistochemistry with Hsp47b antibody, before and after 4PBA administration. Scale bar: 500 mm. **(E)** Analysis of Hsp47b expression by whole mount immunohistochemistry in WT and in *tmem38b*$^{-/-}$ before and after 4PBA administration. A significant increase of Hsp47 signal was detected in *tmem38b*$^{-/-}$ compared to WT. 4PBA treatment significantly reduced the Hsp47b signal in *tmem38b*$^{-/-}$ compared to untreated mutant fish without reaching WT value (WT n = 146 and *tmem38b*$^{-/-}$ n = 116 untreated and 4PBA treated *tmem38b*$^{-/-}$ n = 113). **(F)** Analysis of Hsp47b expression by whole mount immunohistochemistry in WT and in *tmem38b*$^{\Delta 120\text{-}7/\Delta 120\text{-}7}$ before and after 4PBA administration. A significant increase of Hsp47 signal was present in *tmem38b*$^{\Delta 120\text{-}7/\Delta 120\text{-}7}$ compared to WT. 4PBA treatment significantly reduced the Hsp47b signal in *tmem38b*$^{\Delta 120\text{-}7/\Delta 120\text{-}7}$ compared to untreated mutant fish reaching WT value (WT n = 43 and *tmem38b*$^{\Delta 120\text{-}7/\Delta 120\text{-}7}$ n = 19 untreated and 4PBA treated *tmem38b*$^{\Delta 120\text{-}7/\Delta 120\text{-}7}$ n = 34). Zero (nd), low (+) and high (++) indicate the intensity of the signal. *: $p < 0.05$: ** $p \leq 0.01$, ***: $p \leq 0.001$.

Analysis of bone resorption during caudal fin regeneration in *tmem38b* mutants

Osteoblast and osteoclast activity in bone is tightly coupled and OI mutations frequently lead to an imbalance between bone formation and bone resorption (37). Indeed, in OI type XIV individuals a reduced number of osteoclasts associated to bone resorption was observed (16). To investigate bone resorption in *tmem38b* mutants both histomorphometric and molecular analyses were performed in regenerated caudal fins. Tartrate resistant acid phosphatase (TRAP) staining revealed a significant reduction in the number of TRAP+ cells in the 5 dpa *tmem38b*$^{-/-}$ regenerated caudal fin compared to WT. Interestingly, a strong TRAP staining signal was detected at the amputation plane and in the region corresponding to the new forming rays in *tmem38b*$^{\Delta 120\text{-}7/\Delta 120\text{-}7}$. On the contrary of WT and *tmem38b*$^{-/-}$, no signal was evident in the distal tip of the fin (Figure 6A). Nevertheless, *tmem38b*$^{\Delta 120\text{-}7/\Delta 120\text{-}7}$ and WT had similar number of TRAP+ cells. No difference in the expression of the main osteoclast markers, *acp5a* (encoding for Trap), *ctsk* and in the ratio *rankl/opg* was detected in both mutants compared to WT (Figure 6B). An increased expression of the macrophage marker *mpeg1* was detected in *tmem38b*$^{\Delta 120\text{-}7/\Delta 120\text{-}7}$ respect to WT at 5 dpa, suggesting the presence of high number of osteoclast precursors (Figure 6B).

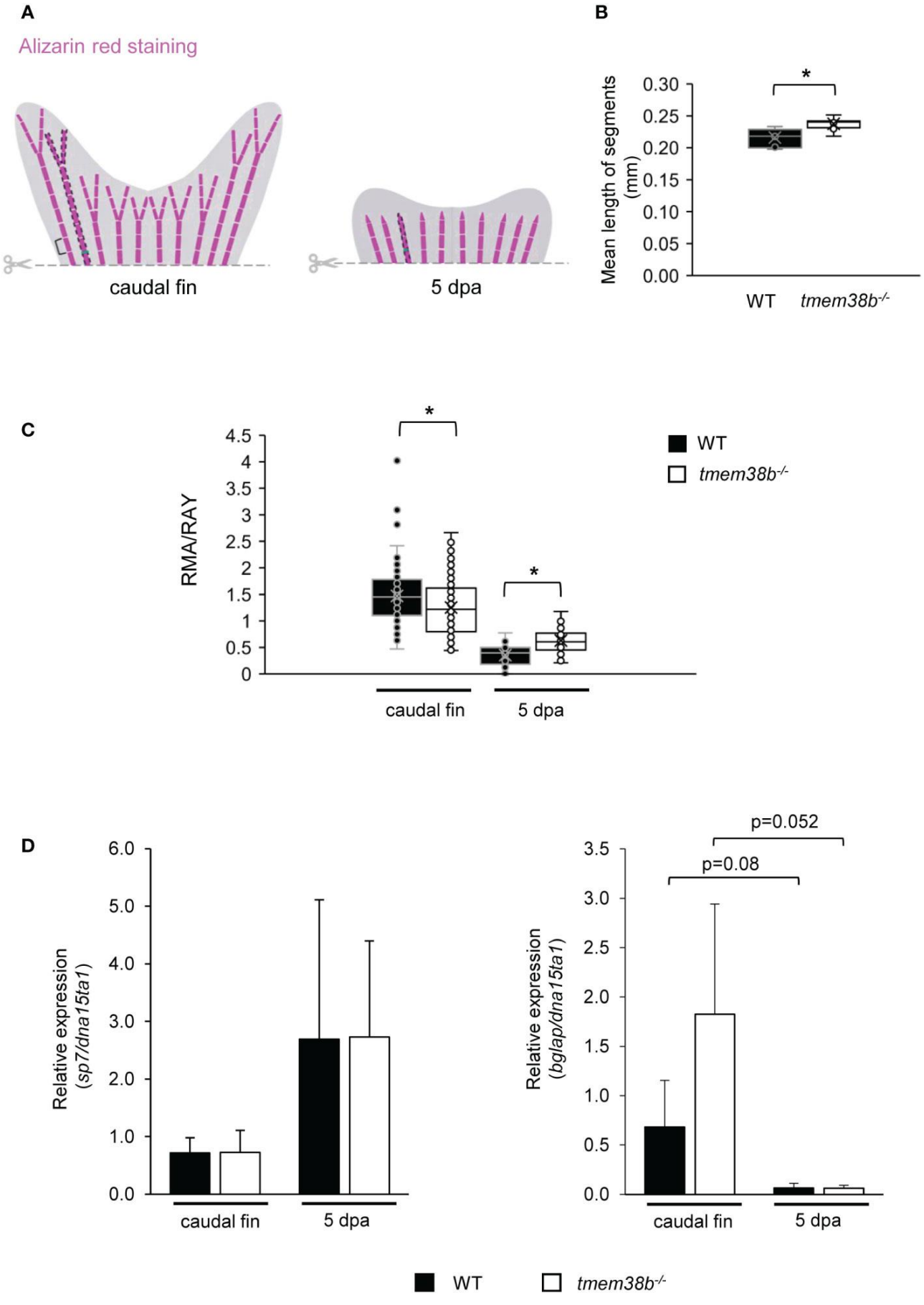
A
Alizarin red staining
caudal fin
5 dpa
B
Mean length of segments (mm)
0.30
0.25
0.20
0.15
0.10
0.05
0.00
*
WT
tmem38b-/-
C
RMA/RAY
4.5
4
3.5
3
2.5
2
1.5
1
0.5
0
*
*
WT
tmem38b-/-
caudal fin
5 dpa
D
Relative expression (sp7/dna15ta1)
6.0
5.0
4.0
3.0
2.0
1.0
0.0
caudal fin
5 dpa
Relative expression (bglap/dna15ta1)
p=0.052
p=0.08
3.5
3.0
2.5
2.0
1.5
1.0
0.5
0.0
caudal fin
5 dpa
WT
tmem38b-/-

Figure 5. Morphometric and bone mineralization analyses during caudal fin regeneration in WT and *tmem38b*$^{-/-}$ mutants. **(A)** Schematic representation of morphometric measurements. Brackets indicate the length of fin ray segment, dashed areas represent the real mineralized areas (RMA) and the green lines indicate the ray widths (RAY). **(B)** The mean length of caudal fin ray segments was evaluated. Segments were significantly longer in *tmem38b*$^{-/-}$ compared to WT. **(C)** The ratio between the real mineralized area (RMA) and the mean ray width (RAY) was measured on alizarin red stained caudal fins to assess mineralization level. *tmem38b*$^{-/-}$ caudal fin was less mineralized respect to the WT. After 5 dpa, the regenerated mineralized area was larger in *tmem38b*$^{-/-}$ respect to the WT (WT $n \geq 9$, *tmem38b*$^{-/-}$ $n \geq 8$) *: $p < 0.05$. **(D)** Relative expression of the early (*sp7*) and late (*bglap*) osteoblastic markers in WT and *tmem38b*$^{-/-}$ caudal fins in amputated and 5 dpa (WT $n = 3$, *tmem38b*$^{-/-}$ $n = 3$) samples. No significant difference was detected in *sp7* and *bglap* expression between WT and *tmem38b*$^{-/-}$ at both time points, even if a trend towards higher value was evident for *bglap* in mutant caudal fins with respect to controls. Data are shown as mean ± SEM.

Actinotrichia formation is impaired in *tmem38b* mutants

Actinotrichia, spear-like structures made of collagen I, collagen II and actinodins 1 and 2 proteins located at the tip of each caudal fin ray, play a morphogenetic role in fin formation, representing a guide for osteoblasts distal migration although synthesized by different cell types, probably basal keratinocytes (27, 38, 39). Upon Picro Sirius Red staining of caudal fins WT and *tmem38b* actinotrichia number and length were evaluated. Polarized light microscopy demonstrated a reduced length of actinotrichia in both mutants compared to WT and limited to *tmem38b*$^{-/-}$ also a significant reduction in their number (Figure 6C).

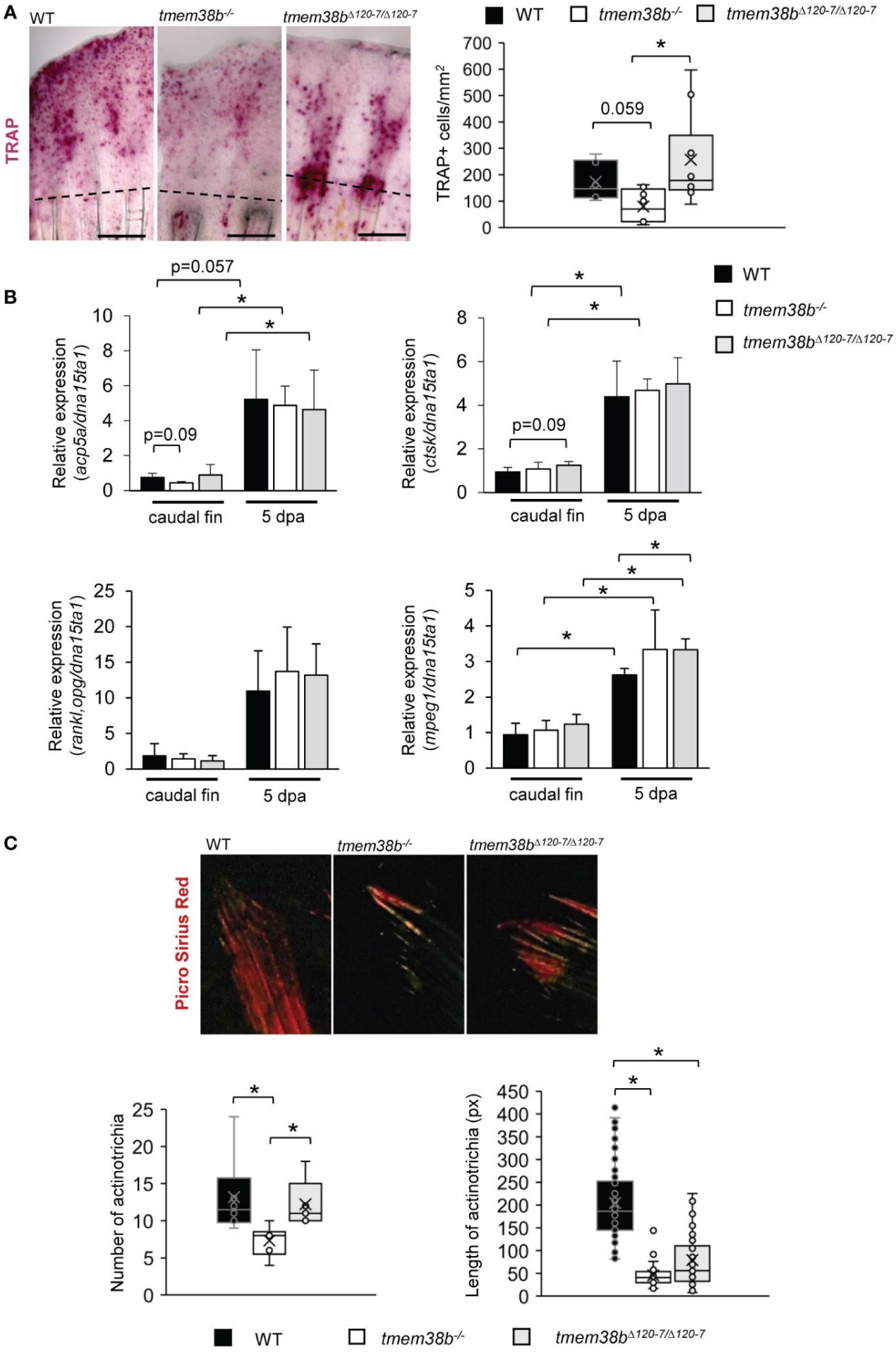
A
WT
tmem38b-/-
tmem38bΔ120-7/Δ120-7
TRAP
TRAP+ cells/mm2
0.059
B
p=0.057
p=0.09
Relative expression (acp5a/dna15ta1)
Relative expression (ctsk/dna15ta1)
Relative expression (rankl,opg/dna15ta1)
Relative expression (mpeg1/dna15ta1)
caudal fin
5 dpa
C
Picro Sirius Red
Number of actinotrichia
Length of actinotrichia (px)

Figure 6. Osteoclast analysis during caudal fin regeneration in *tmem38b* mutants. **(A)** Representative images of TRAP staining of caudal fins of WT and *tmem38b* mutants at 5 dpa (WT n = 7, *tmem38b*$^{-/-}$ n = 9, *tmem38b*$^{\Delta 120\text{-}7/\Delta 120\text{-}7}$ n = 10). In WT, osteoclasts were present in the regenerate. Almost no TRAP activity could be detected in *tmem38b*$^{-/-}$, while in *tmem38b*$^{\Delta 120\text{-}7/\Delta 120\text{-}7}$ it seemed to be mostly localized along the regenerating fin rays. TRAP+ cells were significantly reduced in *tmem38b*$^{-/-}$ respect to the other two groups. **(B)** Relative expression of bone resorption-related markers *acp5a* and *ctsk*, of the macrophage marker *mpeg1* and *rankl/opg* ratio in amputated and 5 dpa caudal fin (WT n = 3, *tmem38b*$^{-/-}$ n = 3, *tmem38b*$^{\Delta 120\text{-}7/\Delta 120\text{-}7}$ n = 3). All markers were increased after amputation. mpeg1 was significantly overexpressed in *tmem38b*$^{\Delta 120\text{-}7/\Delta 120\text{-}7}$ compared to WT at 5 dpa.*: $p < 0.05$. **(C)** Representative images of picro sirius red staining of actinotrichia in caudal fins of WT and *tmem38b* mutants (WT n = 3, *tmem38b*$^{-/-}$ n = 3, *tmem38b*$^{\Delta 120\text{-}7/\Delta 120\text{-}7}$ n = 3). *tmem38b*$^{-/-}$ revealed a reduced number of actinotrichia respect to WT and *tmem38b*$^{\Delta 120\text{-}7/\Delta 120\text{-}7}$, while the length of actinotrichia was reduced in both mutants compared to WT. *: $p < 0.05$.

Discussion

The present study demonstrates, for the first time to the best of our knowledge, the relevance of Tric-b in zebrafish bone during development and bone cells differentiation, providing further insight on the relevance of this channel for the skeleton and supporting a shared role between teleosts and mammals. Both *in silico* and *in vivo* approaches were applied.

Trics are conserved in zebrafish

The retention of trimeric intracellular cation-specific channels TRIC-A and TRIC-B in archaea, bacteria and eukaryotes underlines their relevance in the animal kingdom, and their high level of homology throughout species supports a common phylogenetic origin (40). Indeed, the synteny analysis performed around zebrafish *tmem38a* and *tmem38b loci* demonstrated the presence of conserved synteny blocks shared with *M. musculus* and *H. sapiens*. The identity is higher for TRIC-A than for TRIC-B, nevertheless, in each protomer all the critical amino acids necessary for pore formation and for protomer association into the homotrimeric channels are present (33). In particular, zebrafish Tric sequence contains the glycine rich domains, responsible for the intramembrane kinks interacting with diacylglycerol in the transmembrane helices (TM) 2 and 5 and the voltage sensing domain in TM4, where also the K129 gating residue, corresponding to K125 in *H. sapiens* and *M. musculus*, is conserved. TRICs function in prokaryotes is still unclear, whereas in eukaryotes their localization as integral membrane protein of the sarcoplasmic/endoplasmic reticulum (SR/ER) and their specificity for monovalent cations, in particular potassium, support their function as counter ion channels contributing to maintain the SR/ER membrane electro-neutrality following calcium release. Indeed, *in vitro* and *in vivo* studies in human and murine cells, confirmed an impaired SR/ ER calcium release in their absence (6, 8, 17, 41). Of note, both in invertebrates and in vertebrates, after sperm fertilization Ca^{2+} waves regulate the polarization of cytoplasmic domains in oocytes and drive early embryo patterning and subsequent development (42–46). This early event depends largely on

maternal gene products (47). The calcium responsible for egg activation originates from intracellular storage, mainly the endoplasmic reticulum, through the activity of phospholipase C (PLC) and inositol-tris-phosphate (IP_3) (45, 48), the specific ligand allowing the opening of the inositol 3 phosphate receptor (IP_3R) ER calcium channel. Between the TRIC channel subtypes, TRIC-A and TRIC-B, is the latter, ubiquitously distributed, that is coupled with IP_3R, whereas TRIC-A, most abundantly present in excitable cells, is coupled with ryanodine receptors (RyRs) (2). We first demonstrated that in zebrafish both channels are expressed at early developmental stages, but only *tmem38b* had a maternal expression, supporting its association with IP_3R also in teleosts and its relevance during the first stage of embryo formation. On the contrary, *tmem38a* RNA was detectable only starting from 24 hpf at the appearance of somites, thus confirming the previous study on single-cell gene mapping expression (49), and in adult was present in all excitable and not-excitable analyzed tissue. As in mammals, the highest level of *tmem38a* mRNA in zebrafish is in skeletal muscle, but it is also expressed in bone (1, 50).

Tric-b is necessary in zebrafish for proper bone formation during fast growth developmental stages

In 2014, the identification of *TMEM38B* loss-of-function mutations in individuals affected by the recessive form of osteogenesis imperfecta (OI) type XIV demonstrated an unexpected and relevant role for the ER ion channel TRIC-B in mammalian bone homeostasis (8). Similarly, *Tmem38b* knock out mouse showed bone defects, even if mutant mice are perinatally lethal due to impairment in surfactant production, making difficult to characterize the murine skeletal outcome and its molecular basis (8). Taking into account the high TRIC-B homology in teleosts and mammals and the suitability of zebrafish as a model for dominant and recessive OI forms (23, 25, 51), we targeted zebrafish *tmem38b* by CRISPR/Cas9 both to understand the role of Tric-b in *D. rerio* and to generate the first teleost model for the human disease. Two mutants were created and deeply characterized, the first one carrying a frameshift mutation ($tmem38b^{-/-}$) associated to the insertion of pretermination codon and the second carrying a 24 bp in frame deletion causing the removal of a consensus sequence relevant for channel activity in the voltage-sensing TM4 domain ($tmem38b^{\Delta 120\text{-}7/\Delta 120\text{-}7}$). The highly conserved K122 and R126 amino acids are also lost in this model. On the other hand, the K129 residue with a relevant role in gating Tric channels is kept in $tmem38b^{\Delta 120\text{-}7/\Delta 120\text{-}7}$ leaving open the possibility of a residual activity for the translated protein. The activation of nonsense mediated mRNA decay (NMD) of mutant mRNA, a process generally associated to the insertion of a premature stop codon, was proved in $tmem38b^{-/-}$, and absent in $tmem38b^{\Delta 120\text{-}7/\Delta 120\text{-}7}$. Interestingly, $tmem38b^{-/-}$ NMD was tissue dependent with a mean value of 69% in excitable tissues (muscle, brain, heart) and of 75% in

non-excitable tissues (bone and swimbladder). Tissue specific NMD was previously described in murine models and could indeed be relevant for understanding the genotype-phenotype relationship and the severity in heritable diseases (52, 53). Of note, NMD in bone was below 50% supporting the possibility of a certain level of translation of the truncated protein. Unfortunately, despite the multiple attempts, in none of the models the protein expression could be evaluated due to the lack of specific antibody. No compensatory effect of the *tmem38a* transcript was observed during early stage of development (24 hpf) in mutants compared to WT. Moreover, the increase of *tmem38a* expression (≥ 1.8 fold) detected in bone and muscle of *tmem38b*$^{\Delta 120\text{-}7/\Delta 120\text{-}7}$ during adulthood did not reach significant value. Fish standard length and vertebrae size evaluated at several developmental stages were reduced in *tmem38b*$^{-/-}$only at 21 dpf and 1 mpf. These time points overlap with the larval to juvenile transition that is associated to quick and significant body growth (24), likely demanding Tric-b activity and thus supporting a relevant role of *tmem38b* for early bone development rather than for adult skeletal homeostasis. Indeed, active skeletal growth implies a strong osteoblast activity and thus collagen synthesis and secretion, which indeed have been demonstrated to be altered in TMEM38B knock out human and mice cells (8, 17). Nevertheless, no difference in BFR was detectable between *tmem38b*$^{-/-}$ and WT from 10 dpf to 1mpf. *Tmem38b*$^{-/-}$ body length and vertebral size reach and maintain WT values in adult, in agreement with the reduced fracture frequency and bone properties amelioration after puberty described in OI patients (9, 54, 55). The skeletal phenotype in *tmem38b*$^{\Delta 120\text{-}7/\Delta 120\text{-}7}$, limited to reduced vertebral length at 21 dpf, supported a translation and likely a partial activity of Tric-b in the model and let us to hypothesize that a full active channel is necessary for proper bone formation. *Tmem38b*$^{-/-}$ and *tmem38b*$^{\Delta 120\text{-}7/\Delta 120\text{-}7}$ geometrical and material bone properties revealed by microCT and nanoindentation analysis at vertebral sites were in the normal range, but it should be taken into account that the very small zebrafish size at younger stages did not allow us, due to technical limitations, to evaluate bone properties at 21 dpf and 1 mpf, when differences in length and vertebral size were detectable.

Tric-b is required for proper swim bladder inflation

Fish swim bladder originates from the foregut endoderm, representing an evolutionary similarity with human lungs and, in addition, the presence of collagen type I was described at least in seabass (*Lates calcarifer*) (56). Mutations in *TMEM38B* are associated with pulmonary dysfunction both in OI type XIV individuals and in the Tric-B knock out mouse model, which dies immediately after birth due to respiratory failure (8, 16). Interestingly, *tmem38b*$^{-/-}$ revealed a delay in the inflation of the second lobe of the swim bladder in 21 dpf larvae compared to WT supporting Tric-b requirement for proper organ development, even if its direct role as potassium channel or indirect activity in collagen I

synthesis are still unclear. A delayed swim bladder inflation was already described in the recessive OI type VII and VIII zebrafish models, carrying loss-of-function mutations in *crtap* and *p3h1*, respectively (25) and the complete lack of swim bladder inflation was reported in *col1a1a*$^{-/-}$ (51) proving that a normal amount and/or structure of collagen I in its extracellular matrix is necessary for proper swim bladder inflation. The lack of swim bladder defect in *tmem38b*$^{\Delta 120\text{-}7/\Delta 120\text{-}7}$ further supports in the model the presence of a translated and partial active Tric-b, pointing to its requirement for fish development.

Tric-b plays a role in dermal exoskeletal appendices

Histomorphometric analysis of caudal fin rays in adult mutants revealed a high variability in caudal fin ray segment length with an overall significantly higher mean in *tmem38b*$^{-/-}$ compared to control and *tmem38b*$^{\Delta 120\text{-}7/\Delta 120\text{-}7}$. Fin ray segment length was associated to the conductance activity of Kcnk5b, a plasma membrane potassium channel belonging to the two pore family of channels. Gain-offunction mutations in *kcnk5b* are responsible for the *another longfin* (*alf*) zebrafish phenotype characterized by increased fin ray segment length (57). The hyperpolarization of the membrane consequent to these mutations represents a proof of the relevance of bioelectric signals not only in excitable tissues, but also for development and physiology in the non-excitable ones. Similarly to *tmem38b*$^{-/-}$, the *kcnk5b* mutants are viable and fertile. Interestingly, the activity of Kcnk5b is modulated by calcineurin that acts as channel inhibitor by binding to the cytosolic C-terminal end of the channel (58). Indeed, treatment of WT zebrafish with the calcineurin inhibitor FK506 well reproduces the *alf* phenotype (59). Calcineurin is a calcium dependent protein, whose activity is strongly dependent from intracellular calcium concentration (60). In mammals, the absence of TRIC-B, acting as counter ion for calcium flux from the ER, has been reported to decrease the calcium cytosolic concentration (17), thus the longer *tmem38b*$^{-/-}$ fin ray segments may indeed be the natural consequence of that, supporting a shared role of Tric-b between mammals and teleosts. In alf mutants the longer segments are associated to an overall increase of caudal fin length whereas in *tmem38b*$^{-/-}$ mutant caudal fin size is within normal values (data not shown). Nevertheless, in *tmem38b* mutants a reduced length of actinotrichia is reported, and in *tmem38b*$^{-/-}$ also the number is reduced indicating that either reduction or lack of Tric-b impair their formation. The actinotrichia are spear-like structures containing collagen I located at the tip of each caudal fin ray (27). Fins grow through sequential addition of lepidotrichial segments at their distal tip via migration of mesenchymal cells along the actinotrichia, clusters of collagenous fibers that emerge from the tip of each lepidotrichium (61, 62). Thus, reduced length/number of actinotrichia could indeed negatively affect tail growth counteracting the longer segments.

Tric-b plays a role in osteoblasts differentiation

To address the effect of the absence of *tmem38b* on bone cells differentiation, caudal fin regeneration, a well-organized process that partially recapitulates the events occurring during bone development, was employed. The similar expression of *sp7* both in the amputated samples and 5 dpa regenerates in mutants and controls suggested that the reduced ray mineralization detected in *tmem38b*$^{-/-}$ caudal fin compared to WT was not a consequence of impairments on osteoblast de- and early re-differentiation. The overexpression of *bglap*, previously described in OI type XIV cultured primary osteoblasts as well as in the *TMEM38B* knock out human foetal osteoblasts (hFOB), may be related to the inhibition of hydroxyapatite crystal growth (16, 63) and could indeed explain the reduced alizarin red staining of caudal fin in the amputates samples. Less clear is the increased mineralization during early regeneration phase, suggesting an accumulation of minerals during bone modelling that could be due either to an impaired cellular function or to an increased inter-fibrillar spacing that undergoes remodelling during growth. The effect of *tmem38b* targeting on osteoclasts (OCs) was also addressed using the amputation assay since osteoclasts are involved in zebrafish fin ray healing at the amputation site as well as at newly regenerated rays (28). In *tmem38b*$^{-/-}$ mutant zebrafish Trap+ cells number was reduced compared to WT in presence of normal Rankl/Opg ratio resembling human and murine data (8, 16) and supporting a direct effect of Tric-b on osteoclast activity. Of particular interest, in *tmem38b*$^{\Delta 120\text{-}7/\Delta 120\text{-}7}$ Trap+ cell number was unchanged compared to control, but their distribution was more abundant at the amputation site and along the neo-synthesized ray segment. TRAP is an iron-containing enzyme expressed both in bone resorbing cells and in macrophages, that are one of the source of OCs (64). The increased expression of the macrophage marker *mpeg1* in *tmem38b*$^{\Delta 120\text{-}7/\Delta 120\text{-}7}$ compared to WT suggested that the Trap staining could indeed be due to immature OCs, possibly associated to a low level of anyway active mutant Tric-b (65).

Tric-b is necessary for zebrafish fibroblast and osteoblast homeostasis

Collagen type I extracted from bone and skin of both *tmem38b* zebrafish mutants showed a slightly faster electrophoretic migration resembling the pattern described for collagen type I synthesized by OI type XIV human fibroblasts and osteoblasts, for which a reduced lysine hydroxylation in the triple helical domain was demonstrated (16, 17). Thus, at a cellular level homozygosity for both mutant alleles affects collagen synthesis suggesting a need for a certain threshold of Tric-b conductance to guarantee proper cell homeostasis and that the mutant in frame protein likely conserves only a limited activity, sufficient for bone maintenance, but not enough for cell functionality. In human and murine OI *tmem38b* knock-out cells the collagen was mainly intracellularly retained causing severe matrix

insufficiency. Interestingly, collagen extracellular deposition was also impaired in both zebrafish mutants in which reduced actinotrichia length was evident upon Picro Sirius red staining. A relevant role of lysine hydroxylase 1 in actinotrichia collagen post-translational modification was demonstrated in zebrafish using a knock down morpholino approach. Indeed, *lh1* morphants showed a dorsal curled tail phenotype, no actinotrichia development and defective formation of the fin fold (27). Since calcium regulates several post translational modifiers enzymes, including LH1, the correlation between defects in *TMEM38B* and impaired collagen folding already proposed by Cabral et al. (17) seems to hold up also in teleosts. The mutant collagen retained inside the cells is responsible of enlarged ER cisternae in both zebrafish mutants and OI human and mouse cells. In *tmem38b*$^{-/-}$ and *tmem38b*$^{\Delta 120\text{-}7/\Delta 120\text{-}7}$ the upregulation of Hsp47 confirms impaired collagen secretion. Importantly, using the zebrafish models we demonstrated that the treatment with 4PBA partially rescues Hsp47 overexpression supporting its possible role as OI treatment also for OI type XIV as already demonstrated both *in vitro* and *in vivo* for dominant and some recessive OI forms (23, 35).

Data availability statement

The original contributions presented in the study are included in the article/Supplementary Material. Further inquiries can be directed to the corresponding author.

Ethics statement

The animal study was reviewed and approved by Italian Ministery of Health.

Author contributions

Conceptualization: AF, FT, LL, VD. Methodology: AF, FT, LL, VD, RG, SC, IAKF, DL, SV. Validation: FT, LL, VD, SC, IAKF. Formal analysis: AF, FT, VD, PEW, AW, PC. Resources: AF. Data curation: AF, FT, VD. Writing - original draft: AF, FT, VD, LL. Writing - review and editing: AF, FT, VD, LL, SC, IAKF, AW, PC, BB, RB, SV, AR. Supervision: AF. Project administration: AF. Funding acquisition: AF. All authors contributed to the article and approved the submitted version.

Funding

This research was funded by a Grant of the Italian Ministry of Education, University and Research (MIUR) to the Department of Molecular Medicine of the University of Pavia under the initiative “Dipartimenti di Eccellenza (2018–2022)” and Telethon Exploratory Grant GEP15066 to AF. The funders had no role in study design, data collection and analysis, decision to publish, or preparation of the manuscript.

Acknowledgments

We thank the animal facility “Centro di servizio per la gestione unificata delle attività di stabulazione e di radiobiologia” of the University of Pavia, Pavia, Italy to host the animals; the OPBA of the University of Pavia for supporting in animal protocol drawing up. We thank Dr Nicoletta Gabriella Giannini for initial *tmem38b* mutants characterization.

Conflict of interest

The authors declare that the research was conducted in the absence of any commercial or financial relationships that could be construed as a potential conflict of interest.

Manuscript 3 – References

1. Yazawa M, Ferrante C, Feng J, Mio K, Ogura T, Zhang M, et al. TRIC channels are essential for Ca2+ handling in intracellular stores. Nature (2007) 448(7149):78–82. doi: 10.1038/nature05928

2. Zhou X, Lin P, Yamazaki D, Park KH, Komazaki S, Chen SR, et al. Trimeric intracellular cation channels and sarcoplasmic/endoplasmic reticulum calcium homeostasis. Circ Res (2014) 114(4):706–16. doi: 10.1161/CIRCRESAHA.114.301816

3. Berridge MJ, Bootman MD, Roderick HL. Calcium signalling: dynamics, homeostasis and remodelling. Nat Rev Mol Cell Biol (2003) 4(7):517–29. doi: 10.1038/ nrm1155

4. Marchi S, Patergnani S, Missiroli S, Morciano G, Rimessi A, Wieckowski MR, et al. Mitochondrial and endoplasmic reticulum calcium homeostasis and cell death. Cell Calcium (2018) 69:62–72. doi: 10.1016/j.ceca.2017.05.003

5. Yamazaki D, Tabara Y, Kita S, Hanada H, Komazaki S, Naitou D, et al. TRIC-a channels in vascular smooth muscle contribute to blood pressure maintenance. Cell Metab (2011) 14(2):231–41. doi: 10.1016/j.cmet.2011.05.011

6. Zhao X, Yamazaki D, Park KH, Komazaki S, Tjondrokoesoemo A, Nishi M, et al. Ca2+ overload and sarcoplasmic reticulum instability in tric-a null skeletal muscle. J Biol Chem (2010) 285(48):37370–6. doi: 10.1074/jbc.M110.170084

7. Yamazaki D, Komazaki S, Nakanishi H, Mishima A, Nishi M, Yazawa M, et al. Essential role of the TRIC-b channel in Ca2+ handling of alveolar epithelial cells and in perinatal lung maturation. Development (2009) 136(14):2355–61. doi: 10.1242/ dev.036798

8. Zhao C, Ichimura A, Qian N, Iida T, Yamazaki D, Noma N, et al. Mice lacking the intracellular cation channel TRIC-b have compromised collagen production and impaired bone mineralization. Sci Signal (2016) 9(428):ra49. doi: 10.1126/scisignal.aad9055

9. Shaheen R, Alazami AM, Alshammari MJ, Faqeih E, Alhashmi N, Mousa N, et al. Study of autosomal recessive osteogenesis imperfecta in Arabia reveals a novel locus defined by TMEM38B mutation. J Med Genet (2012) 49(10):630–5. doi: 10.1136/ jmedgenet-2012-101142

10. Garibaldi N, Besio R, Dalgleish R, Villani S, Barnes AM, Marini JC, et al. Dissecting the phenotypic variability of osteogenesis imperfecta. Dis Model Mech (2022) 15(5). doi: 10.1242/dmm.049398

11. Lv F, Xu XJ, Wang JY, Liu Y, Asan, Wang JW, et al. Two novel mutations in TMEM38B result in rare autosomal recessive osteogenesis imperfecta. J Hum Genet (2016) 61(6):539–45. doi: 10.1038/jhg.2016.11

12. Coe H, Michalak M. Calcium binding chaperones of the endoplasmic reticulum. Gen Physiol Biophys (2009) 28:F96–F103.

13. Ishikawa Y, Bächinger HP. A molecular ensemble in the rER for procollagen maturation. Biochim Biophys Acta (2013) 1833(11):2479–91. doi: 10.1016/ j.bbamcr.2013.04.008

14. Perdivara I, Perera L, Sricholpech M, Terajima M, Pleshko N, Yamauchi M, et al. Unusual fragmentation pathways in collagen glycopeptides. J Am Soc Mass Spectrom (2013) 24(7):1072–81. doi: 10.1007/s13361-013-0624-y

15. Marini JC, Forlino A, Bächinger HP, Bishop NJ, Byers PH, Paepe A, et al. Osteogenesis imperfecta. Nat Rev Dis Primers (2017) 3:17052. doi: 10.1038/nrdp.2017.52

16. Webb EA, Balasubramanian M, Fratzl-Zelman N, Cabral WA, Titheradge H, Alsaedi A, et al. Phenotypic spectrum in osteogenesis imperfecta due to mutations in TMEM38B: Unraveling a complex cellular defect. J Clin Endocrinol Metab (2017) 102 (6):2019–28. doi: 10.1210/jc.2016-3766

17. Cabral WA, Ishikawa M, Garten M, Makareeva EN, Sargent BM, Weis M, et al. Absence of the ER cation channel TMEM38B/TRIC-b disrupts intracellular calcium homeostasis and dysregulates collagen synthesis in recessive osteogenesis imperfecta. PloS Genet (2016) 12(7):e1006156. doi: 10.1371/journal.pgen.1006156

18. Fujisawa R, Tamura M. Acidic bone matrix proteins and their roles in calcification. Front Biosci (Landmark Ed) (2012) 17(5):1891–903. doi: 10.2741/4026

19. Leoni L, Tonelli F, Besio R, Gioia R, Moccia F, Rossi A, et al. Knocking out TMEM38B in human foetal osteoblasts hFOB 1.19 by CRISPR/Cas9: A model for recessive OI type XIV. PloS One (2021) 16(9):e0257254. doi: 10.1371/ journal.pone.0257254

20. Tonelli F, Bek JW, Besio R, De Clercq A, Leoni L, Salmon P, et al. Zebrafish: A resourceful vertebrate model to investigate skeletal disorders. Front Endocrinol (Lausanne) (2020) 11:489. doi: 10.3389/fendo.2020.00489

21. Thisse C, Thisse B. High-resolution in situ hybridization to whole-mount zebrafish embryos. Nat Protoc (2008) 3(1):59–69. doi: 10.1038/nprot.2007.514

22. Vanhauwaert S, Van Peer G, Rihani A, Janssens E, Rondou P, Lefever S, et al. Expressed repeat elements improve RT-qPCR normalization across a wide range of zebrafish gene expression studies. PloS One (2014) 9(10):e109091. doi: 10.1371/ journal.pone.0109091

23. Gioia R, Tonelli F, Ceppi I, Biggiogera M, Leikin S, Fisher S, et al. The chaperone activity of 4PBA ameliorates the skeletal phenotype of chihuahua, a zebrafish model for dominant osteogenesis imperfecta. Hum Mol Genet (2017) 26(15):2897–911. doi: 10.1093/hmg/ddx171

24. Parichy DM, Elizondo MR, Mills MG, Gordon TN, Engeszer RE. Normal table of postembryonic zebrafish development: staging by externally visible anatomy of the living fish. Dev Dyn (2009) 238(12):2975–3015. doi: 10.1002/dvdy.22113

25. Tonelli F, Cotti S, Leoni L, Besio R, Gioia R, Marchese L, et al. Crtap and p3h1 knock out zebrafish support defective collagen chaperoning as the cause of their osteogenesis imperfecta phenotype. Matrix Biol (2020) 90:40–60. doi: 10.1016/ j.matbio.2020.03.004

26. Cardeira J, Gavaia PJ, Fernández I, Cengiz IF, Moreira-Silva J, Oliveira JM, et al. Quantitative assessment of the regenerative and mineralogenic performances of the zebrafish caudal fin. Sci Rep (2016) 6:39191. doi: 10.1038/srep39191

27. Durán I, Marı-Beffa M, Santamar´ ıa JA, Becerra J, Santos-Ruiz L. Actinotrichia´ collagens and their role in fin formation. Dev Biol (2011) 354(1):160–72. doi: 10.1016/ j.ydbio.2011.03.014

28. Blum N, Begemann G. Osteoblast de- and redifferentiation are controlled by a dynamic response to retinoic acid during zebrafish fin regeneration. Development (2015) 142(17):2894–903. doi: 10.1242/dev.120204

29. Geurtzen K, Vernet A, Freidin A, Rauner M, Hofbauer LC, Schneider JE, et al. Immune suppressive and bone inhibitory effects of prednisolone in growing and regenerating zebrafish tissues. J Bone Miner Res (2017) 32(12):2476–88. doi: 10.1002/ jbmr.3231

30. Huysseune A, Soenens M, Sire JY, Witten PE. High-resolution histology for craniofacial studies on zebrafish and other teleost models. Methods Mol Biol (2022) 2403:249–62. doi: 10.1007/978-1-0716-1847-9_17

31. Verstraeten B, Sanders E, Huysseune A. Whole mount immunohistochemistry and in situ hybridization of larval and adult zebrafish dental tissues. Methods Mol Biol (2012) 887:179–91. doi: 10.1007/978-1-61779-860-3_16

32. Yang H, Hu M, Guo J, Ou X, Cai T, Liu Z. Pore architecture of TRIC channels and insights into their gating mechanism. Nature (2016) 538(7626):537–41. doi: 10.1038/ nature19767

33. Wang XH, Su M, Gao F, Xie W, Zeng Y, Li DL, et al. Structural basis for activity of TRIC counter-ion channels in calcium release. Proc Natl Acad Sci U S A (2019) 116 (10):4238–43. doi: 10.1073/pnas.1817271116

34. Ito S, Nagata K. Biology of Hsp47 (Serpin H1), a collagen-specific molecular chaperone. Semin Cell Dev Biol (2017) 62:142–51. doi: 10.1016/j.semcdb.2016.11.005

35. Garibaldi N, Contento BM, Babini G, Morini J, Siciliani S, Biggiogera M, et al. Targeting cellular stress in vitro improves osteoblast homeostasis, matrix collagen content and mineralization in two murine models of osteogenesis imperfecta. Matrix Biol (2021) 98:1–20. doi: 10.1016/j.matbio.2021.03.001

36. Besio R, Garibaldi N, Leoni L, Cipolla L, Sabbioneda S, Biggiogera M, et al. Cellular stress due to impairment of collagen prolyl hydroxylation complex is rescued by the chaperone 4-phenylbutyrate. Dis Model Mech (2019) 12(6). doi: 10.1242/dmm.038521

37. Uveges TE, Collin-Osdoby P, Cabral WA, Ledgard F, Goldberg L, Bergwitz C, et al. Cellular mechanism of decreased bone in brtl mouse model of OI: imbalance of decreased osteoblast function and increased osteoclasts and their precursors. J Bone Miner Res (2008) 23(12):1983–94. doi: 10.1359/jbmr.080804

38. König D, Page L, Chassot B, Jaźwińska A. Dynamics of actinotrichia regeneration in the adult zebrafish fin. Dev Biol (2018) 433(2):416–32. doi: 10.1016/j.ydbio.2017.07.024

39. Kuroda J, Iwane AH, Kondo S. Roles of basal keratinocytes in actinotrichia formation. Mech Dev (2018) 153:54–63. doi: 10.1016/j.mod.2018.08.010

40. Silverio AL, Saier MH. Bioinformatic characterization of the trimeric intracellular cation-specific channel protein family. J Membr Biol (2011) 241(2):77–101. doi: 10.1007/ s00232-011-9364-8

41. El-Ajouz S, Venturi E, Witschas K, Beech M, Wilson AD, Lindsay C, et al. Dampened activity of ryanodine receptor channels in mutant skeletal muscle lacking TRIC-a. J Physiol (2017) 595(14):4769–84. doi: 10.1113/JP273550

42. Fuentes R, Tajer B, Kobayashi M, Pelliccia JL, Langdon Y, Abrams EW, et al. The maternal coordinate system: Molecular-genetics of embryonic axis formation and patterning in the zebrafish. Curr Top Dev Biol (2020) 140:341–89. doi: 10.1016/ bs.ctdb.2020.05.002

43. Whitaker M. Calcium at fertilization and in early development. Physiol Rev (2006) 86(1):25–88. doi: 10.1152/physrev.00023.2005

44. Charbonneau M, Moreau M, Picheral B, Vilain JP, Guerrier P. Fertilization of amphibian eggs: a comparison of electrical responses between anurans and urodeles. Dev Biol (1983) 98(2):304–18. doi: 10.1016/0012-1606(83)90361-5

45. Steinhardt RA, Epel D. Activation of sea-urchin eggs by a calcium ionophore. Proc Natl Acad Sci U S A (1974) 71(5):1915–9. doi: 10.1073/pnas.71.5.1915

46. Steinhardt RA, Epel D, Carroll EJ, Yanagimachi R. Is calcium ionophore a universal activator for unfertilised eggs? Nature (1974) 252(5478):41–3. doi: 10.1038/ 252041a0

47. Solnica-Krezel L. Maternal contributions to gastrulation in zebrafish. Curr Top Dev Biol (2020) 140:391–427. doi: 10.1016/bs.ctdb.2020.05.001

48. Crossley I, Swann K, Chambers E, Whitaker M. Activation of sea urchin eggs by inositol phosphates is independent of external calcium. Biochem J (1988) 252(1):257–62. doi: 10.1042/bj2520257

49. Wagner DE, Weinreb C, Collins ZM, Briggs JA, Megason SG, Klein AM. Singlecell mapping of gene expression landscapes and lineage in the zebrafish embryo. Science (2018) 360(6392):981–7. doi: 10.1126/science.aar4362

50. O'Brien F, Eberhardt D, Witschas K, El-Ajouz S, Iida T, Nishi M, et al. Enhanced activity of multiple TRIC-b channels: an endoplasmic reticulum/sarcoplasmic reticulum mechanism to boost counterion currents. J Physiol (2019) 597(10):2691–705. doi: 10.1113/JP277241

51. Gistelinck C, Kwon RY, Malfait F, Symoens S, Harris MP, Henke K, et al. Zebrafish type I collagen mutants faithfully recapitulate human type I collagenopathies. Proc Natl Acad Sci U S A (2018) 115(34):E8037–E46. doi: 10.1073/pnas.1722200115

52. Zetoune AB, Fontanière S, Magnin D, Anczuków O, Buisson M, Zhang CX, et al. Comparison of nonsense-mediated mRNA decay efficiency in various murine tissues. BMC Genet (2008) 9:83. doi: 10.1186/1471-2156-9-83

53. Bateman JF, Freddi S, Nattrass G, Savarirayan R. Tissue-specific RNA surveillance? nonsense-mediated mRNA decay causes collagen X haploinsufficiency in schmid metaphyseal chondrodysplasia cartilage. Hum Mol Genet (2003) 12(3):217–25. doi: 10.1093/hmg/ddg054

54. Ramzan K, Alotaibi M, Huma R, Afzal S. Detection of a recurrent TMEM38B gene deletion associated with recessive osteogenesis imperfecta. Discov (Craiova) (2021) 9(1): e124. doi: 10.15190/d.2021.3

55. Volodarsky M, Markus B, Cohen I, Staretz-Chacham O, Flusser H, Landau D, et al. A deletion mutation in TMEM38B associated with autosomal recessive osteogenesis imperfecta. Hum Mutat (2013) 34(4):582–6. doi: 10.1002/humu.22274

56. Sinthusamran S, Benjakul S, Kishimura H. Comparative study on molecular characteristics of acid soluble collagens from skin and swim bladder of seabass (Lates calcarifer). Food Chem (2013) 138(4):2435–41. doi: 10.1016/j.foodchem.2012.11.136

57. Perathoner S, Daane JM, Henrion U, Seebohm G, Higdon CW, Johnson SL, et al. Bioelectric signaling regulates size in zebrafish fins. PloS Genet (2014) 10(1):e1004080. doi: 10.1371/journal.pgen.1004080

58. Yi C, Spitters TW, Al-Far EAA, Wang S, Xiong T, Cai S, et al. A calcineurinmediated scaling mechanism that controls a k+-leak channel to regulate morphogen and growth factor transcription. Elife (2021) 10. doi: 10.7554/eLife.60691

59. Daane JM, Lanni J, Rothenberg I, Seebohm G, Higdon CW, Johnson SL, et al. Bioelectric-calcineurin signaling module regulates allometric growth and size of the zebrafish fin. Sci Rep (2018) 8(1):10391. doi: 10.1038/s41598-018-28450-6

60. Creamer TP. Calcineurin. Cell Commun Signal (2020) 18(1):137. doi: 10.1186/ s12964-020-00636-4

61. Goss RJ, Stagg MW. The regeneration of fins and fin rays in fundulus heteroclitus. J Exp Zool (1957) 136(3):487–507. doi: 10.1002/jez.1401360306

62. Haas HJ. Studies on mechanisms of joint and bone formation in the skeleton rays of fish fins. Dev Biol (1962) 5:1–34. doi: 10.1016/0012-1606(62)90002-7

63. Romberg RW, Werness PG, Riggs BL, Mann KG. Inhibition of hydroxyapatite crystal growth by bone-specific and other calcium-binding proteins. Biochemistry (1986) 25(5):1176–80. doi: 10.1021/bi00353a035

64. Hayman AR. Tartrate-resistant acid phosphatase (TRAP) and the osteoclast/ immune cell dichotomy. Autoimmunity (2008) 41(3):218–23. doi: 10.1080/ 08916930701694667

65. Paredes LC, Olsen Saraiva Camara N, Braga TT. Understanding the metabolic profile of macrophages during the regenerative process in zebrafish. Front Physiol (2019) 10:617. doi: 10.3389/fphys.2019.00617

Supplementary Material

Supplementary Materials and Methods

Generation of zebrafish *tmem38b* knock out mutants using CRISPR/Cas9

A single guide RNA (gRNA) for the *tmem38b* gene (ENSDARG00000100549, Ensemble 94) was designed using the online freely available software CHOPCHOP (https://chopchop.rc.fas.harvard.edu). The target sequence was selected at the 5' end, in exon 7 (5'-GGTTCTCGTCACTTCCTTCATGG - 3', 11391-11413 nt). The synthesis of target oligonucleotides (Eurofins Genomics), and the preparation of gRNA and Cas9 mRNA were carried out as described in (1). The genomic region surrounding the target sequence was PCR amplified using the following primers: forward 5'-TTACTGTCCGCTGGATGTGG-3' (11326-11345 nt) and reverse 5'–CAGAGCGTCGCTGTATTTGC-3' (11448-11467), with annealing temperature of 56°C, generating a 142 bp amplicon. T7 endonuclease assay was performed to evaluate targeting efficiency as described in (1). The mutations in the heterozygous F1 zebrafish were determined by DNA extraction from tail clip of adult zebrafish followed by Sanger sequencing of the region surrounding the targeting.

To genotype *tmem38b*$^{-/-}$ and *tmem38b*$^{\Delta 120\text{-}7/120\text{-}7}$ mutants, amplicons were checked on 12% and 10% v/v electrophoresis acrylamide gel in TBE buffer (Tris HCl 0.1M, H_3BO_3 0.1M, EDTA 2mM, pH 8.2), respectively. The embryos generated from pairwise breeding were grown to 3 weeks post fertilization (wpf) and the genotyping data were used for Mendelian analysis of surviving homozygous knock out compared to WT and heterozygous zebrafish. Under the null hypothesis of no viability selection, progeny genotypes should conform to an expected Mendelian ratio of 1:2:1. Deviations from expected number of homozygous knock out were tested with goodness- of-fit Chi-square statistical analysis (**Supplementary Table 2**).

Cartilage staining

Cartilages were stained with alcian blue as described in Gioia et al. (2). Briefly, WT and *tmem38b*$^{-/-}$ zebrafish (n = 12 for each genotype) were fixed overnight in 4% (w/v) paraformaldehyde (PFA, Merck KGaA) at 4°C and stained in 0.02% (w/v) Alcian blue (Sigma-Aldrich). Ventral images were acquired using M165 FC stereomicroscope (Leica) connected to DFC425C digital camera (Leica). The presence of cartilage deformities was investigated by measuring the angle of the ceratohyal (CH) cartilage (3). Measurements were performed using LAS v4.5 (Leica).

Bone Formation rate

Bone formation rate was performed on WT and *tmem38b*$^{-/-}$. Briefly, WT (n=9) and *tmem38b* $^{-/-}$ (n= 10) were stained with 0.01% alizarin red s (Sigma-Aldrich) in KOH, pH 7.4, from 6 to 10 dpf for 15 min every day, according to Bensimon-Brito et al 2016 (4). The fish were then stained in 0.2% calcein (Sigma-Aldrich) in 0.9% NaOH at 1 mpf for 10 minutes and then washed over night. Images were acquired using a Leica M165 FC microscope connected to a Leica DFC425 C digital camera. Bone formation rate was measured as the ratio between red operculum area on green operculum area, normalized to the standard length.

uCT

WT (n = 4) and *tmem38b*$^{-/-}$ (n = 4) zebrafish (9 mpf) were analyzed by µCT. Zebrafish were sacrificed, fixed overnight at 4 °C in 4% (w/v) PFA. Zebrafish were kept hydrated in parafilm and placed in a sample holder during µCT acquisitions (Skyscan 1272). For high-resolution scans and quantitative analysis of the 2nd and 3rd precaudal vertebrae, zebrafish were scanned at 40 kV and 230 mA with a voxel size of 3 µm. For all samples, ring artifact and beam hardening correction was kept constant and no smoothing was applied during reconstruction (NRecon, Bruker). After applying a constant global threshold to all samples, the morphological properties: vertebral body length (VBL, µm), bone volume (BV, mm^3), polar moment of inertia (MMIp, surrogate measure for resistance against torsion, mm^4), eccentricity, centrum thickness (C.Th, mm) and bone perimeter (B.Pm, mm) were analyzed according to previously established protocols (5, 6).

Nanoindentation

Elastic modulus *E* and hardness *H* of vertebral bone were determined using nanoindentation (iMicro, Nanomechanics, Inc., Oak Ridge, USA) based on previously established protocols (5). Whole fish samples (WT: n = 4; *tmem38b*$^{-/-}$ and *tmem38b*$^{\Delta 120\text{-}7/120\text{-}7}$ mutants n = 6, 2 mpf) were fixed in 4% formaldehyde, embedded in polymethylmethacrylate, and ground plane parallel until the central sagittal plane was reached. To eliminate surface roughness, blocks were then polished with a 3 mm diamond suspension, followed by a 1 mm diamond suspension and final polishing with a 0.05 mm aluminum-oxide suspension. Finally, samples were ultrasonically cleaned in deionized water to remove surface debris. Using a Berkovich diamond tip and the depth-sensing continuous stiffness mode with a final depth of 1000 nm, indents were placed on the longitudinal plane of the vertebral bone cortex of 4 vertebrae per sample. Applying a Poisson's ratio of 0.3, *E* and *H* were extracted

according to the Oliver-Pharr method (7) using in-house software (inView, Nanomechanics, Inc., Oak Ridge, USA).

Supplementary Results

Generation of *tmem38b* zebrafish models

A specific RNA guide (gRNA) targeting exon 7 of *tmem38b* was microinjected in 1-2 cell stage zebrafish fertilized embryos together with *in vitro* transcribed Cas9 mRNA. F0 mosaic zebrafish were screened for specific targeting at 1 day post fertilization (dpf) by T7 endonuclease I (T7EI) assay and by Sanger sequencing. The mutagenesis rate was 63%. To identify the F0 germ line zebrafish, mosaic fish were further outcrossed to AB WT. F1 progeny was initially screened by T7 endonuclease assay to discriminate the WT from the heterozygous mutant animals and the mutants finally confirmed by Sanger sequencing. The mutant F1 zebrafish carrying the c.524_530delTGAAGGA, predicted to insert a premature stop codon at amino acid 122 of Tric-b was chosen to obtain the F2 *tmem38b* knock out model (*tmem38b*$^{-/-}$). The mutant F1 zebrafish carrying the c.517_540del24nt, predicted to introduce the *in frame* p.Ala120_Thr127 deletion was selected to generate the F2 *tmem38b*$^{\Delta 120\text{-}7/\Delta 120\text{-}7}$. To genotype both *tmem38b*$^{-/-}$ and *tmem38b* $^{\Delta 120\text{-}7/\Delta 120\text{-}7}$ different size of PCR products was evaluated; the expected amplicons were 142 bp for the WT and 135 bp and 118 bp amplicons for *tmem38b*$^{-/-}$ and *tmem38b* $^{\Delta 120\text{-}7/\Delta 120\text{-}7}$, respectively (**Supplementary Figure 1B-D)**.

Supplementary Figures and Tables

Supplementary Figures

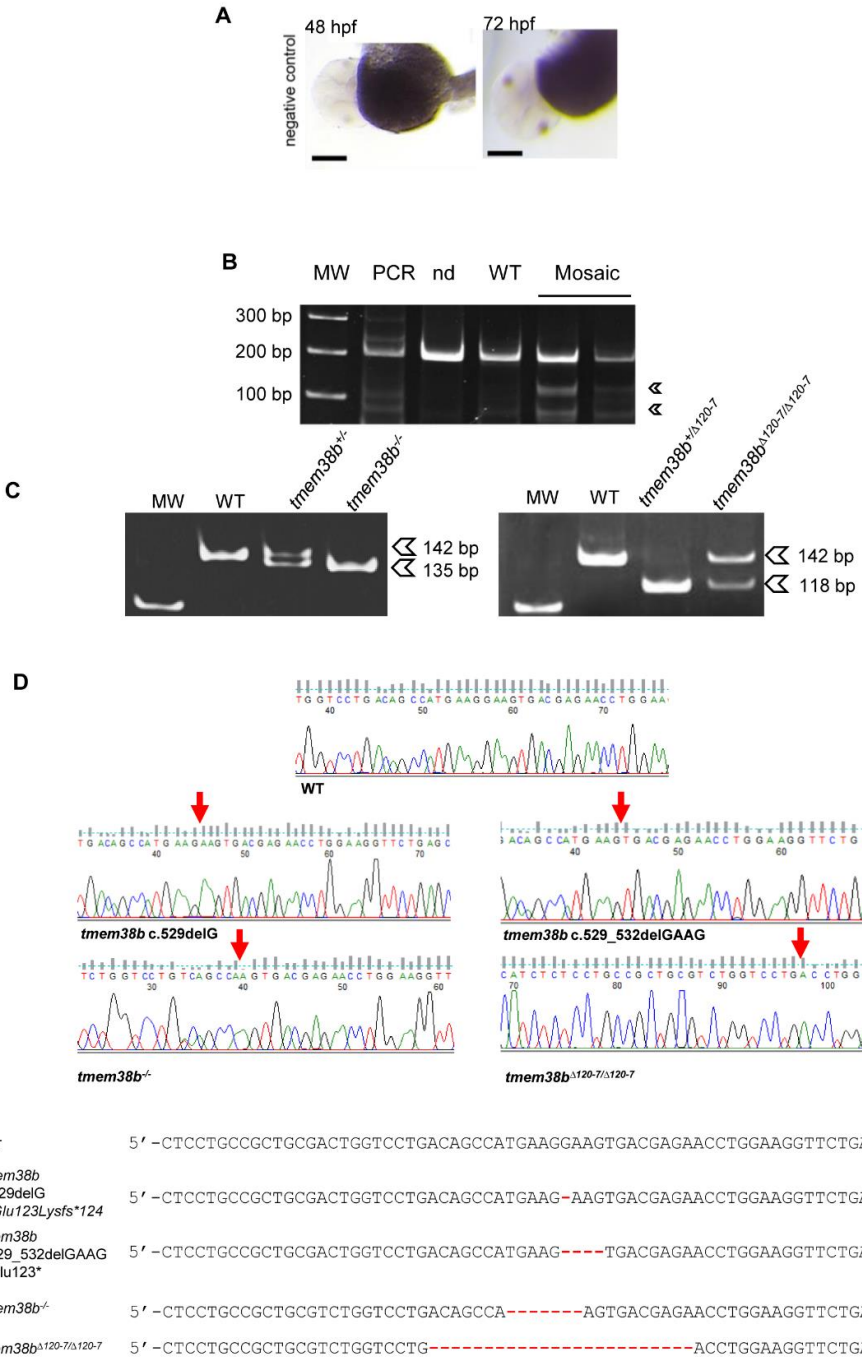

Supplementary Figure 1. (A) *In situ* hybridization performed on 48 and 72 hpf WT embryos using the sense oligonucleotide as negative control. Scale bar: 500 µm. Generation of *tmem38b* zebrafish models using CRISPR/Cas9: **(B)** F0 mosaic fish screening using T7 endonuclease. Amplicons were digested by T7 endonuclease in presence of heterozygosity. MW: molecular weight, nd: not digested. **(C)** PCR analysis to genotype *tmem38b*$^{-/-}$ (left) and *tmem38b*$^{\Delta 120\text{-}7/\Delta 120\text{-}7}$ (right) mutants. Mutations in *tmem38b*$^{-/-}$ and *tmem38b*$^{\Delta 120\text{-}7/\Delta 120\text{-}7}$ could be distinguished by amplicon size. WT: 142 bp, *tmem38b*$^{-/-}$: 135 bp and *tmem38b*$^{\Delta 120\text{-}7/\Delta 120\text{-}7}$: 118 bp. MW: molecular weight. DNA sequences of heterozygous mutations identified in F1 fish population. Red arrows and red dashes indicate nucleotide deletion regions.

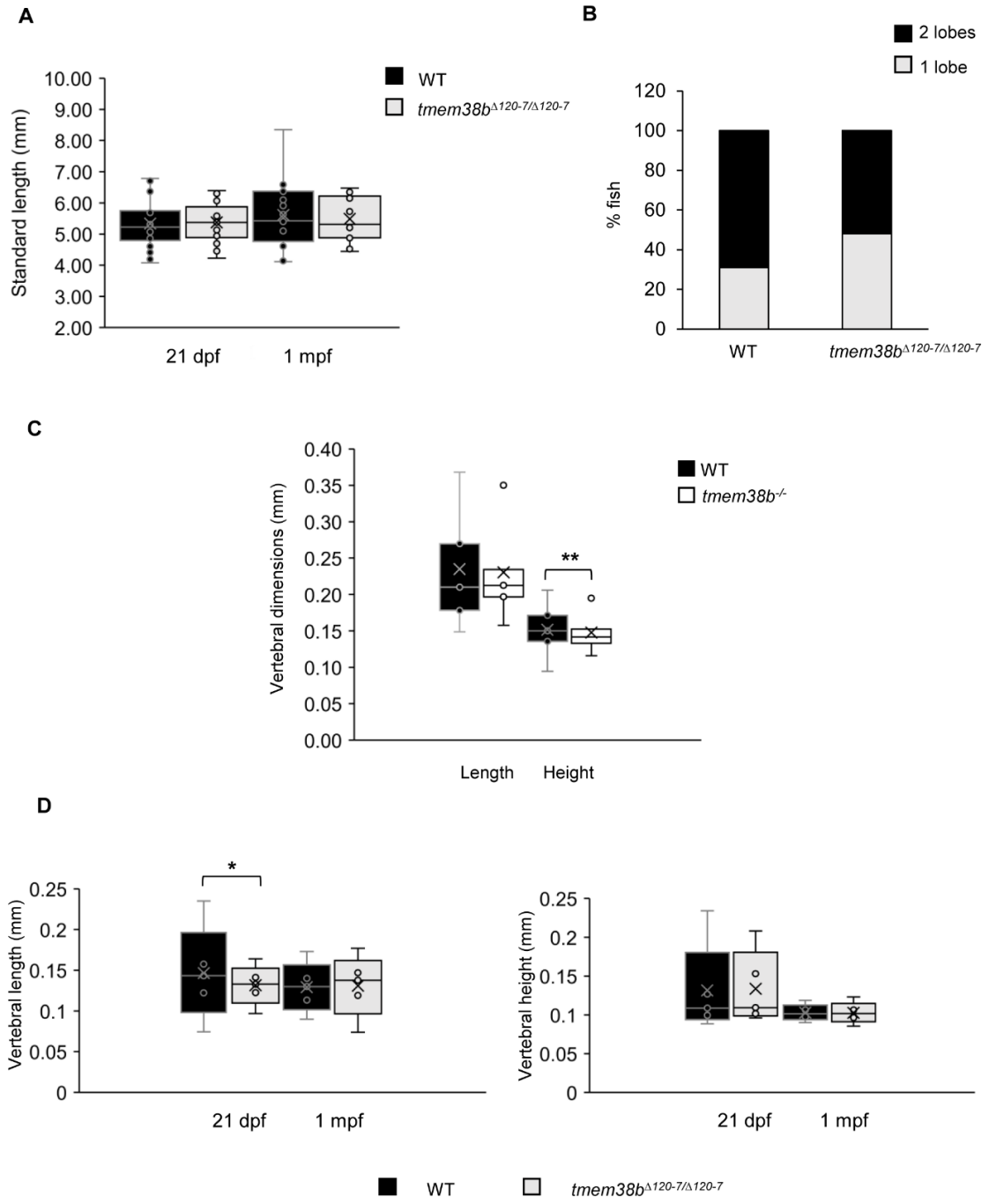

Supplementary Figure 2. Morphometric analysis of WT and *tmem38b*$^{\Delta 120\text{-}7/\Delta 120\text{-}7}$. **(A)** Standard length of WT and *tmem38b*$^{\Delta 120\text{-}7/\Delta 120\text{-}7}$ measured at 21 dpf and 1 mpf. No difference was detected. 21 dpf: WT n=28, *tmem38b*$^{\Delta 120\text{-}7/\Delta 120\text{-}7}$ n=23; 1 mpf: WT n= 21, *tmem38b*$^{\Delta 120\text{-}7/\Delta 120\text{-}7}$ n = 13). **(B)** Swim bladder inflation levels was not impaired in *tmem38b*$^{\Delta 120\text{-}7/\Delta 120}$ respect to WT at 21 dpf (WT n = 26, *tmem38b*$^{\Delta 120\text{-}7/\Delta 120\text{-}7}$ n = 21). **(C)** Vertebral dimensions measured in 4 mpf WT and *tmem38b*$^{-/-}$(WT n = 15, *tmem38b*$^{-/-}$ n = 11). While the vertebral length did not differ between WT and mutants, the vertebral height was reduced in *tmem38b*$^{-/-}$ respect to WT. **: $p < 0.01$. **(D)** Vertebral length was reduced in *tmem38b*$^{\Delta 120\text{-}7/\Delta 120\text{-}7}$ compared to WT at 21 dpf. *tmem38b*$^{\Delta 120\text{-}7/\Delta 120\text{-}7}$ showed no difference in vertebral height compared to WT. 21 dpf: WT n = 24, *tmem38b*$^{\Delta 120\text{-}7/\Delta 120\text{-}7}$ n = 18; 1 mpf: WT n = 24, *tmem38b*$^{\Delta 120\text{-}7/\Delta 120\text{-}7}$ n = 18.

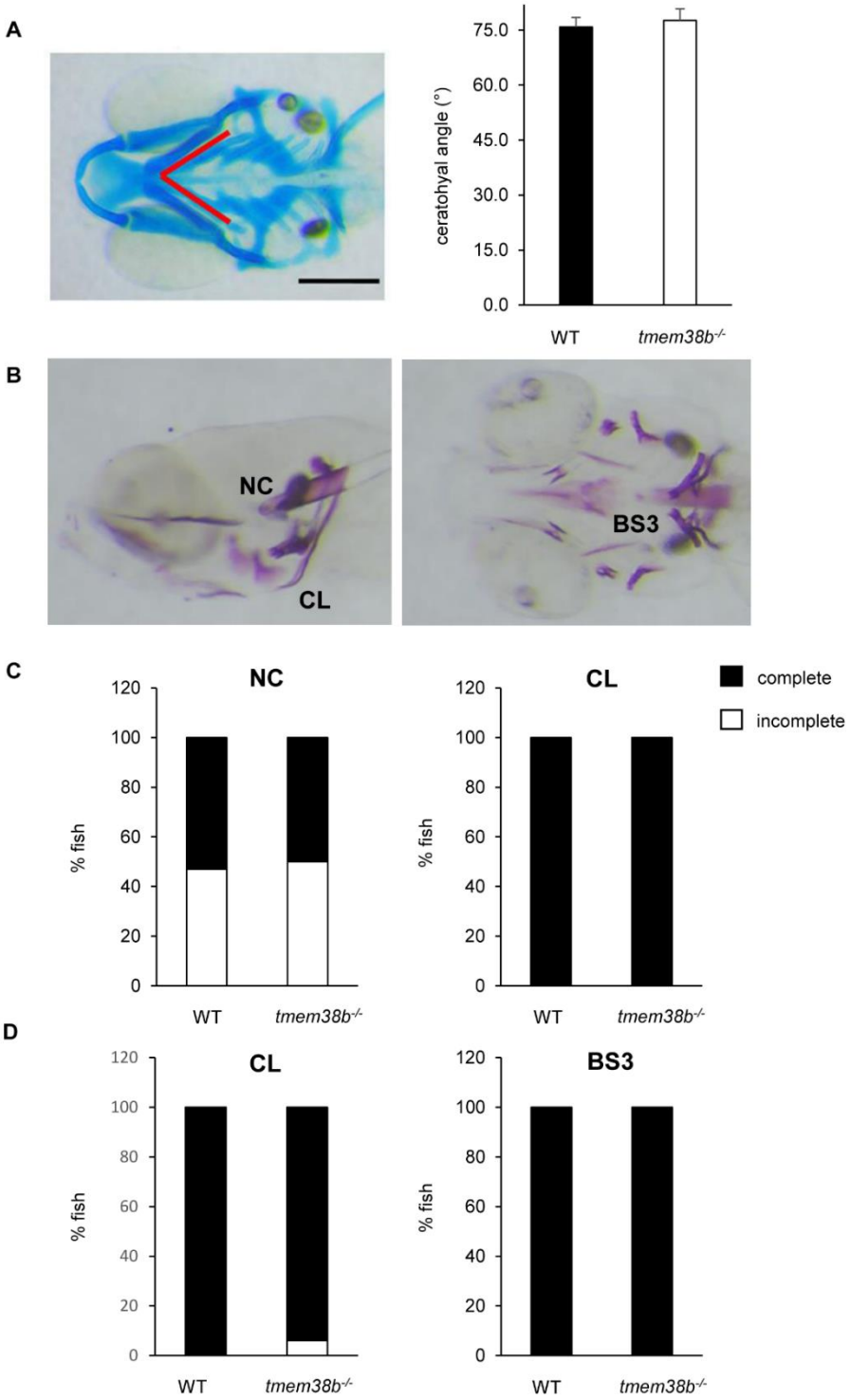

Supplementary Figure 3. *Tmem38b*$^{-/-}$ early skeletal development. **(A)** Representative image of zebrafish cranial cartilage stained with alcian blue (left). At 5dpf no difference in ceratohyal angle (red lines) was observed in *tmem38b*$^{-/-}$ with respect to WT ($n \geq 12$) . **(B)** Representative image of zebrafish cranial bones stained with alizarin red (CL:cleithrum, NC: notochord, BS3: branchiostegal ray 3). **(C)** At 7 dpf no difference in bone mineralization was observed in *tmem38b*$^{-/-}$ with respect to WT ($n \geq 18$). **(D)** At 14 dpf no difference in bone mineralization was observed in *tmem38b*$^{-/-}$ with respect to WT.

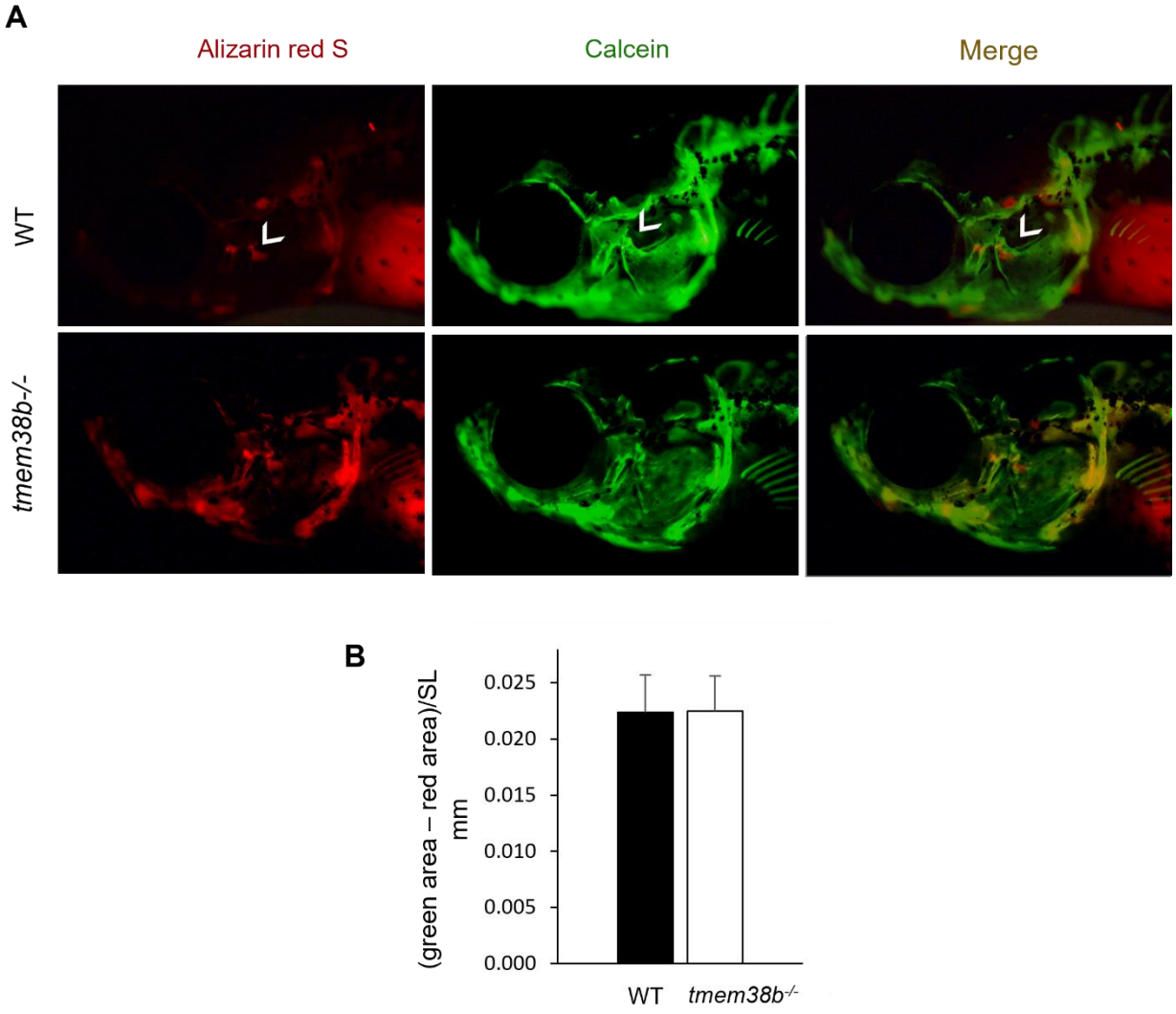

Supplementary Figure 4. Bone formation rate. **(A)** Representative images of WT and *tmem38b*$^{-/-}$ stained with alizarin red S from 6 to 10 dpf and with calcein at 1 mpf and merged image. **(B)** Bone formation rate, measured as the difference between red operculum area on green operculum area and normalized to standard length (SL), did not show difference between WT and *tmem38b*$^{-/-}$. White arrowheads indicate the operculum. Magnification: 5X.

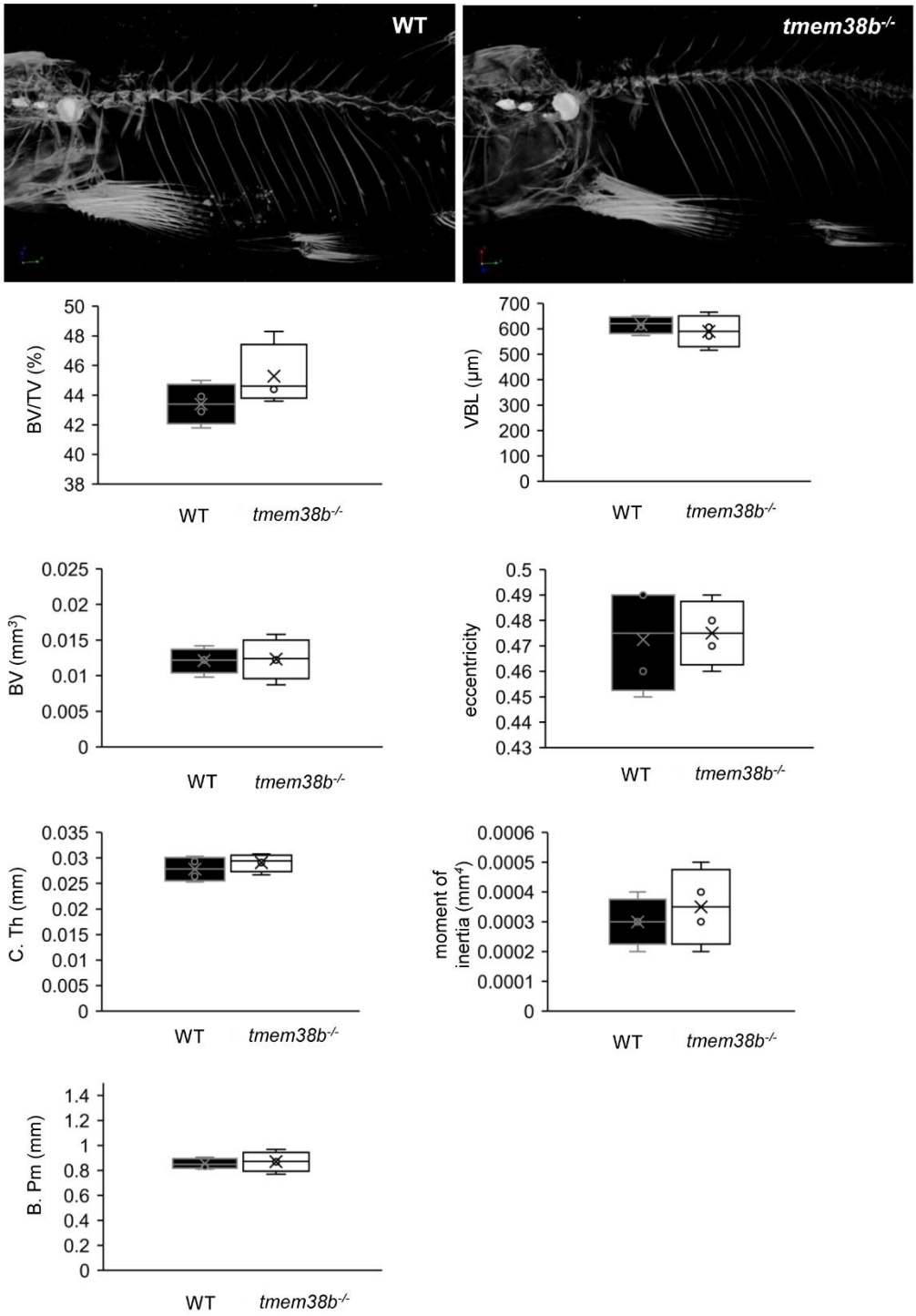

Supplementary Figure 5. µCT scans of adult WT (n = 4), and *tmem38b*$^{-/-}$ (n = 4). Morphometric analysis perfomed on the second and third precaudal vertebrae of each fish showed no difference between WT and *tmem38b*$^{-/-}$ for any of the parameters analyzed. BV/TV: bone volume on tissue volume, VBL: vertebral body length, BV: bone volume, C. Th: centrum thickness, B. Pm: bone perimeter.

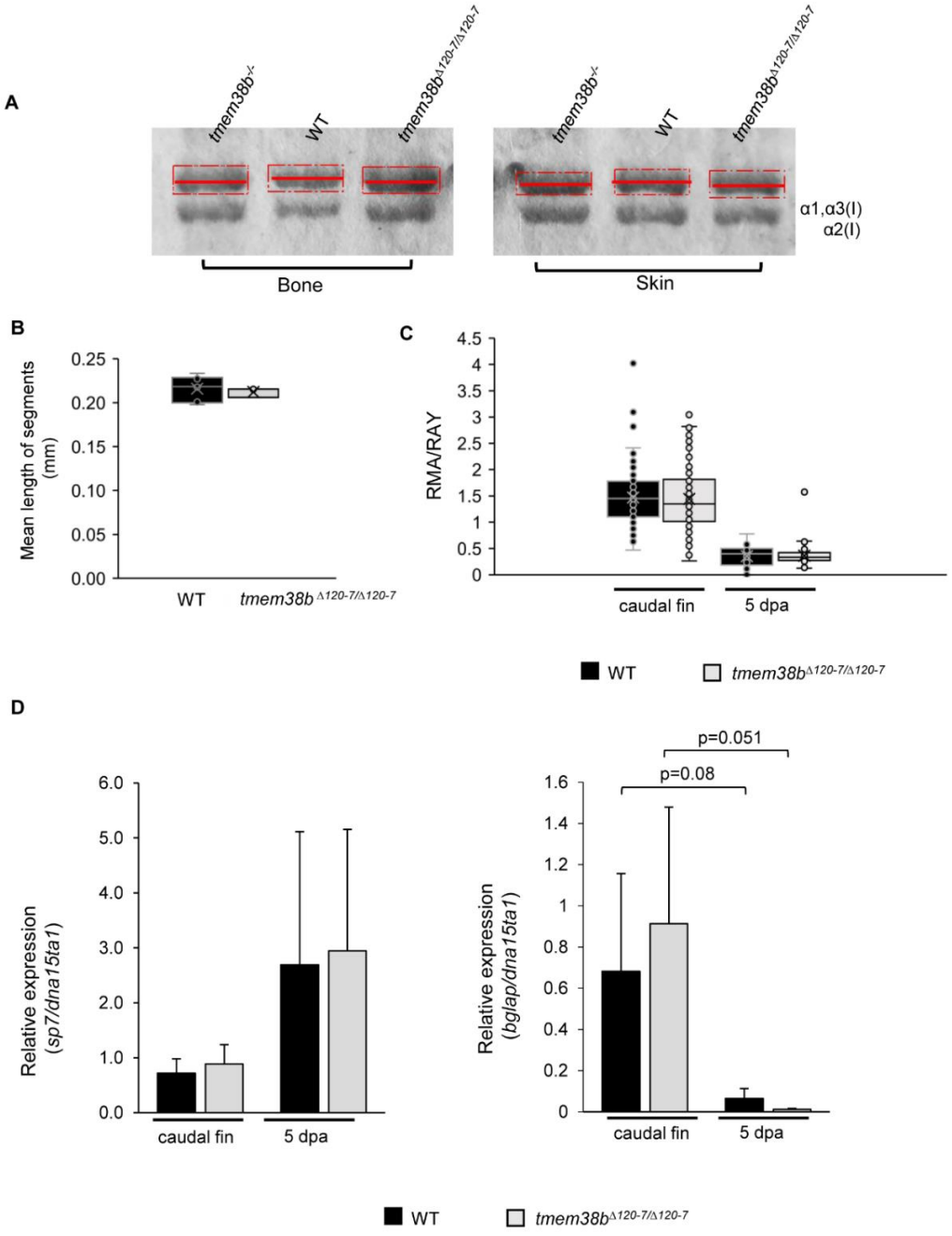

Supplementary Figure 6. (A) Representative Coomassie stained SDS-Urea-PAGE of collagen type I extracted from WT and mutants (*tmem38b*$^{-/-}$; *tmem38b*$^{\Delta 120\text{-}7/\Delta 120\text{-}7}$) bone and skin. Mutants' collagen α bands are boxed in red. A red line crossing the middle of the box is used to underline the different migration. The mutant bands presented a slight faster migration compared to WT. Morphometric and bone mineralization analyses during caudal fin regeneration in WT and *tmem38b*$^{\Delta 120\text{-}7/\Delta 120\text{-}7}$ mutants: **(B)** The number and mean length of caudal fin ray segments were evaluated in the amputated tail. No difference was detected between WT and mutants for both measurements. **(C)** The ratio between the real mineralized area (RMA) and the mean ray width (RAY) was measured on alizarin red stained caudal fins to assess mineralization level. No difference in mineralization was found between WT and mutants in both the amputated and the 5 dpa samples (WT: n ≥ 9, *tmem38b*$^{\Delta 120\text{-}7/\Delta 120\text{-}7}$ n ≥ 8). **(D)** Relative expression of the early (*sp7*) and late (*bglap*) osteoblastic markers in WT and *tmem38b*$^{\Delta 120\text{-}7/\Delta 120\text{-}7}$ caudal fins in the amputated and 5 dpa samples (WT: n = 3, *tmem38b*$^{\Delta 120\text{-}7/\Delta 120\text{-}7}$ n = 3). No difference was detected in *sp7* and *bglap* expression between WT and *tmem38b*$^{\Delta 120\text{-}7/\Delta 120\text{-}7}$ at both time points. Data are expressed as mean ± SD.

Supplementary Tables

Supplementary Table 1. Genes flanking *TMEM38A* and *TMEM38B loci*.

	Homo sapiens			*Mus musculus*			*Danio rerio*		
	Gene name	**Ensembl ID**	**Mb from *TMEM38A***	**Gene name**	**Ensembl ID**	**Mb from *Tmem38a***	**Gene name**	**Ensembl ID**	**Mb from *tmem38a***
	SMIM7	*ENSG00000214046*	-0,029	*Smim7*	*ENSMUSG00000044600*	-0,016	*smim7*	*ENSDARG00000074848*	-0,022
	NWD1	*ENSG00000188039*	0,127	*Nwd1*	*ENSMUSG00000048148*	0,13	*nwd1*	*ENSDARG00000076110*	0,067
	RAB3A	*ENSG00000105649*	1,51	*Rab3a*	*ENSMUSG00000031840*	-1,82	*rab3ab*	*ENSDARG00000043835*	-0,328
	PDE4C	*ENSG00000105650*	1,55	*Pde4c*	*ENSMUSG00000031842*	-1,83	*pde4cb*	*ENSDARG00000002411*	-0,385
	LSM4	*ENSG00000130520*	1,63	*Lsm4*	*ENSMUSG00000031848*	-1,90	*lsm4*	*ENSDARG00000023852*	-0,311
	KHLH26	*ENSG00000167487*	1,98	*Khlh26*	*ENSMUSG00000055707*	-2,11	*khlh26*	*ENSDARG00000053876*	-0,283
	CRTC1	*ENSG00000105662*	2	*Crtc1*	*ENSMUSG00000003575*	-2,14	*crtc1b*	*ENSDARG00000076076*	-0,221
	COMP	*ENSG00000105664*	2,1	*Comp*	*ENSMUSG00000031849*	-2,2	*comp*	*ENSDARG00000098431*	-0,205
	DDX49	*ENSG00000105671*	2,23	*Ddx49*	*ENSMUSG00000057788*	-2,28	*ddx49*	*ENSDARG00000012899*	-0,298

	Homo sapiens			*Mus musculus*			*Danio rerio*		
	Gene name	**Ensembl ID**	**Mb from *TMEM38B***	**Gene name**	**Ensembl ID**	**Mb from *Tmem38b***	**Gene name**	**Ensembl ID**	**Mb from *tmem38b***
	KLF4	*ENSG00000136826*	1,71	*Klf4*	*ENSMUSG00000003032*	1,67	*klf4*	*ENSDARG00000079922*	-0,153
	RAD23B	*ENSG00000119318*	1,55	*Rad23b*	*ENSMUSG00000028426*	1,56	*rad23b*	*ENSDARG00000021550*	-0,178
	ZNF462	*ENSG00000148143*	1,23	*Zfp462*	*ENSMUSG00000060206*	1,22	*znf462*	*ENSDARG00000112909*	-0,217

Supplementary Table 2. Percentage of surviving fish.

Age	WT	*tmem38b*$^{+/-}$	*tmem38b*$^{-/-}$	N	*P* value
5 dpf	27%	49%	24%	49	0.96
7 dpf	39%	45%	16%	49	0.06
14 dpf	32%	47%	21%	132	2.8E-33
21 dpf	32%	47%	22%	133	7.48E-34

N= number of fish, dpf= days post fertilization

References

1. Tonelli F, Cotti S, Leoni L, Besio R, Gioia R, Marchese L, et al. Crtap and p3h1 knock out zebrafish support defective collagen chaperoning as the cause of their osteogenesis imperfecta phenotype. Matrix Biol. 2020;90:40-60.
2. Gioia R, Tonelli F, Ceppi I, Biggiogera M, Leikin S, Fisher S, et al. The chaperone activity of 4PBA ameliorates the skeletal phenotype of Chihuahua, a zebrafish model for dominant osteogenesis imperfecta. Hum Mol Genet. 2017;26(15):2897-911.
3. Costantini A, Alm JJ, Tonelli F, Valta H, Huber C, Tran AN, et al. Novel RPL13 Variants and Variable Clinical Expressivity in a Human Ribosomopathy With Spondyloepimetaphyseal Dysplasia. J Bone Miner Res. 2021;36(2):283-97.
4. Bensimon-Brito A, Cardeira J, Dionísio G, Huysseune A, Cancela ML, Witten PE. Revisiting in vivo staining with alizarin red S--a valuable approach to analyse zebrafish skeletal mineralization during development and regeneration. BMC Dev Biol. 2016;16:2.
5. Fiedler IAK, Schmidt FN, Wölfel EM, Plumeyer C, Milovanovic P, Gioia R, et al. Severely Impaired Bone Material Quality in Chihuahua Zebrafish Resembles Classical Dominant Human Osteogenesis Imperfecta. J Bone Miner Res. 2018;33(8):1489-99.
6. Bouxsein ML, Boyd SK, Christiansen BA, Guldberg RE, Jepsen KJ, Müller R. Guidelines for assessment of bone microstructure in rodents using micro-computed tomography. J Bone Miner Res. 2010;25(7):1468-86.
7. Oliver WC, Pharr GM. An improved technique for determining hardness and elastic modulus using load and displacement sensing indentation experiments. Journal of Materials Research. 1992;7(6):1564-83.

MANUSCRIPT 4

Zebrafish caudal fin regeneration highlights specific effects on bone cell homeostasis in dominant and recessive osteogenesis imperfecta

V. Daponte, *et al*. In preparation.

Abstract

Osteogenesis imperfecta (OI) is a group of rare hereditary skeletal disorders for which definitive cure are still missing. Beyond classical dominant OI forms caused by mutation in collagen I encoding genes, recessive OI due to defect in proteins involved in collage I synthesis and processing and in osteoblast differentiation and activity were and still are continuously discovered. This makes urgent a deep investigation of the molecular basis of each form to develop personalized therapeutic approaches. The dominant OI type III model *Chihuahua* (*Chi/+*), carrying a glycine substitution in collagen α1(I) chain, and the recessive OI type VIII *p3h1*$^{-/-}$ zebrafish, share with patients the delay of collagen type I α chains folding, their overmodification and intracellular retention, leading to impaired cell homeostasis and cell stress. In the last decade, some studies have pointed out to a correlation between altered cell homeostasis and bone cell differentiation. Despite that, few detailed information about bone cell differentiation in OI are currently available. In this study, the bony caudal fin of *Chi/+* and *p3h1*$^{-/-}$ was used to deeply investigate the consequence of collagen intracellular retention on bone cell differentiation in dominant and recessive OI. We demonstrated reduced regenerative ability in both models, associated to impaired osteoblasts differentiation and switch towards adipogenesis only in *Chi/+*. Osteoclast number and activity were reduced in both models during regeneration. The chemical chaperone 4-phenylbutyrate (4-PBA) improved bone formation only in *p3h1*$^{-/-}$ by increasing caudal fin regeneration rate. Taken together, our data strengthen the correlation between cell stress due to collagen retention and altered extracellular matrix and bone cell differentiation specifically in dominant OI, indicating that cellular consequences are likely linked to the type of defect making precision medicine the better approach to treat OI.

Introduction

Osteogenesis imperfecta (OI) is a group of hereditary skeletal disorders sharing reduced bone mineral density, severe bone deformity and frequent fractures. Definitive cure is still not available for OI (Jovanovic, Guterman-Ram and Marini 2022). Classical OI refers to the dominantly inherited types I to IV caused by mutations in *COL1A1* and *COL1A2* genes encoding the α1 and α2 chains of collagen type I, respectively (Sillence, Senn and Danks 1979). In classical OI the most frequent defects are glycine substitutions in the conserved Gly-Xaa-Yaa triple helix motif. The presence of a bulkier amino acid in place of Gly results in the delay of the α chains folding that causes their excessive exposure to post-translational modifying enzymes and the intracellular retention of the overmodified molecules (Marini et al. 2017). More recently, recessive OI has been identified affecting proteins involved in collagen biosynthesis or osteoblasts differentiation and activity (Marini et al. 2017). Among these, OI type VIII is caused by mutation in the enzyme prolyl 3-hydroxylase 1 (P3H1) that belongs to an endoplasmic reticulum (ER) resident complex in which it associates in a 1:1:1 ratio with the chaperone cartilage-associated protein (CRTAP) and the *cis-trans* isomerase cyclophilin B (CyPB). The complex works as a molecular chaperone by favoring triple helix folding and is responsible for the 3-hydroxylation of a specific Pro986 residue in Xaa position in the α1(I) chains (Ishikawa and Bächinger 2013). 3-hydroxylated Pro986 side chains extend externally from the triple helix axis and favor extracellular molecular assembly of the collagen molecules (Hudson and Eyre 2013). Thus, recessive OI type VIII shares with OI classical forms the delay of α(I) chains folding, their overmodification and the intracellular retention of misfolded collagen, leading to impaired cell homeostasis and cell stress (Besio et al. 2019, Tonelli et al. 2020b).

In the last decade it was shown that altered cell homeostasis affects bone cells differentiation. Indeed, an impairment in osteoblast differentiation was described in three OI murine models. The *Brtl* mouse, characterized by a G349C substitution in α1(I) chain, showed reduced early and late osteoblastogenic markers expression and increased adipogenesis *in vitro* (Gioia et al. 2012). In the *Amish* mouse, carrying a G610C substitution in α2(I) chain, reduced transcription of mature osteoblast markers such as *Bglap* was observed *in vitro* and *in vivo* (Mirigian et al. 2016). Finally, an accumulation of immature osteoblasts and increased osteoclastogenesis was reported in the *Oim* mice, carrying a homozygous nucleotide deletion leading to a frameshift mutation in the C-terminal propeptide of *COL1A2* (Li et al. 2010). However, detailed information about bone cell differentiation from OI patients and murine osteoblasts are still scarce in the literature.

Zebrafish (*Danio rerio*) is a proven valid model for the investigation of skeletal diseases, sharing 71% of homology with human genes and conserving both mammalian bone cell and ossification types (Howe et al. 2013, Tonelli et al. 2020a). Several zebrafish mutants for OI have been generated either by forward and reverse genetic approaches, strongly contributing to better dissect the pathology (Henke et al. 2017, Gistelinck et al. 2018, Kague et al. 2016, Tonelli et al. 2020b). Among these, we previously deeply characterized as a model for dominant severe OI type III, the *Chihuahua* (*Chi/+*), obtained by ENU mutagenesis and carrying a p.G736D substitution in α1(I) chain (Fisher, Jagadeeswaran and Halpern 2003, Gioia et al. 2017). More recently, we generated by CRISPR/Cas9 gene editing and characterized the knock-out *p3h1*$^{-/-}$ zebrafish, lacking P3H1 and resembling human OI type VIII phenotype (Tonelli et al. 2020b).

The advantages in using zebrafish as animal models to investigate skeletal diseases are multiple. First, zebrafish can fully regenerate several organs and tissues, including the bony caudal fin (Gemberling et al. 2013). Fin rays, also called lepidotrichia, belong to the dermal skeleton and are directly formed from osteoblasts without a cartilage template. Each ray is constituted by a repetition of ~20 segments, interconnected by collagenous ligaments called joints. After amputation of the caudal fin, a regenerative program starts. The first phase is a rapid wound healing followed by the blastema formation, with mature osteoblasts dedifferentiating, becoming proliferative, and migrating distally to form a region of undifferentiated cells (blastema). In the last phase, named the regenerative outgrowth, bone cells re-differentiate, and sequentially expression of *runx2* (pre-osteoblast marker), *sp7/osterix* (committed osteoblast marker) and finally *bglap/osteocalcin* (mature osteoblast marker) takes place (Knopf et al. 2011, Sousa et al. 2011). Zebrafish caudal fin is easily accessible for manipulation, and after amputation it rapidly regenerates within 2 weeks.

Furthermore, being almost fully transparent for quite same time during growth (Pfefferli and Jaźwińska 2015), after crossing with transgenic fish lines labelling osteoblasts at different developmental stage, zebrafish provide a unique tool to study bone cell differentiation *in vivo*.

Lastly, thanks to the ability to absorb drugs and compounds from the water through the gills, zebrafish provide a convenient tool for drug screening studies. In particular, the study of caudal fin regeneration after drug administration is nowadays a standardized assay to assess the effect of compounds on bone (Cardeira et al. 2016).

Here, caudal fin regeneration allowed to investigate *in vivo* the bone formation in the zebrafish *Chihuahua* (*Chi/+*) and *p3h1*$^{-/-}$, models for dominant and recessive OI, respectively and characterized by altered collagen structure. Reduced regenerative ability was evident in both models, but it was associated to impaired osteoblasts differentiation and osteoblastogenesis/adipogenesis switch only in

Chi/+. On the contrary, reduced osteoclast number and activity were found in both models during regeneration. Interestingly, the chemical chaperone 4-phenylbutyrate (4-PBA) improved bone formation only in *p3h1*$^{-/-}$ by favoring caudal fin growth without affecting bone cell markers expression. Overall, our findings strengthened the link between cell stress due to collagen retention and altered extracellular matrix and bone cell differentiation impairment in dominant OI, pointing to a possible different mechanism in recessive OI form without collagen mutations and raising the question of mutation specific cellular consequences that will make necessary precision medicine approaches to effectively treat OI patients.

Materials and Methods

Zebrafish husbandry and ethical statement

AB wild-type zebrafish used for this study were obtained from the European Zebrafish Research Center (EZRC). The mutant *Chi/+* carrying a G2207A mutation in *col1a1a*, causing a p.G736D (G574D) substitution in the α1 chain of type I collagen, was originally provided by Prof S. Fisher (Boston University, USA). The mutant *p3h1*$^{-/-}$, carrying a c.645delCinsGGAGAA deletion resulting in a stop codon, was previously generated in our laboratory (Tonelli et al. 2020b). Other lines used in this study were *Tg(Ola.bglap:EGFP)*^{hu4008} (referred as *bglap:GFP*) and *Tg(OlSp7:nlsGFP)*^{zf132} (referred as *sp7:GFP*). A detailed list of all fish lines is provided in **Supplementary Table 1**. Zebrafish embryos were kept in petri dishes until 6 days post fertilization (dpf) in zebrafish water (1.2 mM $NaHCO_3$, 0.1 g/L instant ocean, 1.4 mM $CaSO_4$, 0.00002 % w/v methylene blue) at 28 °C and then housed in ZebTEC semi-closed recirculation housing systems (Techniplast) at 28 °C, pH 7.5 and conductivity 500 μS on a 14/10 light/dark cycle. Adult zebrafish were fed three times a day alternating dry food and brine shrimps. For the experiments, larvae and adult zebrafish were anesthetized using 0.016 % w/v tricaine (3-amino benzoic acidethylester, Sigma-Aldrich) in zebrafish water and/or sacrificed by tricaine overdose (0.03 % w/v). All the experiments were performed in agreement with EU Directive 2010/63/EU. The experimental protocol was approved by Italian Ministry of Health (Approval Animal Protocol No.1191/2016-PR and 260/2020-PR).

Genotyping

Genomic DNA was extracted from caudal fin clip of adult fish. Tissue was digested by proteinase K (2.5 mg/mL, Sigma-Aldrich) in lysis buffer (100 mM Tris HCl, pH 8.5, 5 mM EDTA, 0.2 % w/v SDS, 200 mM NaCl) o/n at 55 °C, followed by precipitation with isopropanol and resuspended in Tris-EDTA Buffer (20 mM Tris-HCl, 1 mM EDTA, pH 8.0. DNA) o/n at 55 °C.

PCR amplification of *p3h1* (NC_007122.6) region of interest was carried out using specific primers (FW: 5'-CTACACTAACATGTACATGTATGC-3' (4748-4771 nt), RV: 5'-ACAGTGTGTATATTCTGCATCCC-3' (5181-5203 nt)) using 60 °C annealing temperature. The amplicon was digested with Eco0109I (New England BioLabs) and run an 8 % v/v acrylamide gel in TBE buffer (0.1 M Tris HCl, 0.1 M H_3BO_3, 2 mM EDTA, pH 8.2). Two bands of 319 bp and 125 bp were expected in WT fish, while in *p3h1*$^{-/-}$ a single 444 bp band indicated the lack of the restriction size due to the inserted mutation.

Chi/+ genotyping was carried out taking advantage of the fin fold bending present only in mutants starting from 5 dpf (Gioia et al. 2017).

RNA extraction and qPCR

RNA was extracted from pools of six caudal fins from 8 mpf (adult) WT, *Chi/+* and *p3h1*$^{-/-}$ using QIAzol Lysis Reagent (Qiagen) according to manufacturer's instructions. Contaminant DNA was eliminated using DNA-free kit DNase Treatment & Removal (Invitrogen). RNA quantity was determined by NanoDrop spectrophotometer, and its quality was evaluated by 1 % w/v agarose gel electrophoresis in TBE buffer. Reverse-transcription was performed using the High-Capacity cDNA Transcription kit (Applied Biosystems) according to manufacturer's protocol in a final volume of 20 µL. Real time PCR (qPCR) was used to evaluate gene expression of *runx2a*, *runx2b*, *sox9a*, *sox9b*, *acp5a*, *sp7*, *bglap*, *rankl*, *opg, col1a1a, col12a1a, col12a1b, col14a1a* and *col14a1b* in WT and mutant fish. *dna15ta1*was used as housekeeping (Vanhauwaert et al. 2014). Primer sequences and annealing temperatures are reported in **Supplementary Table 2**. qPCR was performed with SYBR Green Master mix (Applied Biosystems) in triplicate in a 25 µL final volume. The qPCR cycle was the following: 2 minutes of denaturation at 95 °C, 44 cycles of 5 seconds at 95 °C, 30 seconds at the annealing temperature followed by 1 second at 72 °C. A dissociation curve was performed starting with 5 seconds at 95 °C, followed by 1 minute at 58 or 60 °C and finally gradual heating to 95 °C at a ramp-rate of 0.11 °C/s to check the specificity of the amplification. The relative expression was calculated using ΔΔCt method. The QuantStudio 3 thermocycler and the QuantStudio Design & Analysis software (Applied Biosystems) were used.

Bone formation evaluation

The caudal fins of 3 and 8 mpf WT, *Chi/+* and *p3h1*$^{-/-}$ zebrafish were amputated and fin regeneration was evaluated after 7 and 14 days post amputation (dpa). Each fish after amputation was placed in 200 mL of fish water in a bench top tank kept at 26°C and half of the volume was replaced every day. After 7 and 14 dpa fish were stained for 10 min with a 0.2 % w/v solution of calcein (Sigma-Aldrich) and washed until the water was clear to remove unbound dye. Images of 7 and 14 dpa caudal fins were acquired using a Leica M165 FC microscope connected to a Leica DFC425 C digital camera. The regeneration in WT, *Chi/+* and *p3h1*$^{-/-}$ fish was estimated using two parameters, the Regenerated area (REG), representing all the regenerated area, including rays and surrounding connective tissue, and the Estimated mineralized area (EMA) representing the regenerated mineralized rays and inter-ray spaces. The percentage was determined by measuring the ratios REG/total caudal fin area and EMA/total mineralized caudal fin area (Cardeira et al. 2016) (**Supplementary Figure 1**).

Caudal fin morphometry

For histomorphometric analysis caudal fins regeneration assay was performed on WT, *Chi/+* and *p3h1*$^{-/-}$ zebrafish. Calcein vital staining at day 0, 7 dpa and 14 dpa was performed as described before. Number of fin rays and caudal fin size were evaluated at day 0. At each time point the number and length of segments per ray, the number of bifurcations per ray, the distance from the end of the body to the first bifurcation (indicated as distance to bifurcation in the text) were evaluated. Images were acquired both in bright-field and in fluorescence using a Leica M165 FC microscope connected to a Leica DFC425 C digital camera. Measurements were performed using the LAS v4.13 software (Leica). The most lateral, smaller rays were not considered for the analysis.

Tartrate-resistant Acid Phosphatase (TRAP) staining

Tartrate-resistant Acid Phosphatase (TRAP) staining was performed following a published protocol (Blum and Begemann 2015). Caudal fins of adult WT, *Chi/+* and *p3h1*$^{-/-}$ zebrafish were fixed in 4 % PFA in PBS o/n at 4 °C, washed in PBT (0.1 % v/v PBS + Tween-20) and permeabilized in PBTx (0.3 % v/v PBS + Triton X-100). Fins were then equilibrated in TRAP Buffer (0.1 M sodium acetate, 0.1 M acetic acid, 50 mM sodium tartrate) and colour reaction was performed in TRAP Buffer containing 0.1 mg/ml Naphtol AS-MX phosphate (Sigma-Aldrich) and 0.3 mg/ml Fast Red Violet LB (Sigma-Aldrich). Fins were finally bleached in 10 % H_2O_2 + 1 %KOH o/n at RT to remove pigmentation and then stored in 70 % glycerol at 4 °C until acquisition. Images were acquired using a Leica M165 FC microscope connected to a Leica DFC425 C digital camera. The number of TRAP+ cells in the amputated and regenerate was counted using the Cell Counter tool of Fiji (ImageJ) software. In the stump, where TRAP signal was more intense, the TRAP area was measured on individual rays and normalized to ray width.

4-phenylbutyrate (4-PBA) treatment

Caudal fins of 3 and 8 mpf WT, *Chi/+* and *p3h1*$^{-/-}$ zebrafish were amputated and allowed to regrow in presence or absence (placebo, indicated as control) of the chemical chaperone 4-PBA. In detailed 5 groups of fish were analyzed: WT, *Chi/+* and *p3h1*$^{-/-}$ controls, *Chi/+* and *p3h1*$^{-/-}$ 4-PBA treated. After amputation each fish was kept in 200 mL of fish water and half of the volume was replaced every day as already described (Gioia et al. 2017). In treated fish tanks, 0.05 mM 4-PBA was added daily and its effect evaluated at 3, 5, 7 or 14 dpa depending on the experiment.

Whole-mount immunofluorescence on caudal fins

Amputated caudal fins from WT, *Chi/+* and *p3h1*$^{-/-}$ were fixed in 4 % PFA in PBS o/n at 4 °C and decalcified in 0.5 M EDTA pH 7.4 at 4 °C for four days. Samples were permeabilized in 1 % v/v Triton X-100 for 1 hour at RT, rinsed three times in wash solution (0.8 % v/v Triton X-100 in PBS) for 5 minutes at RT and incubated in saturation solution (0.8 % v/v Triton X-100, 1 % v/v DMSO, 5 % BSA in PBS) for 4 hours at RT. Samples were then incubated in saturation solution containing primary antibodies o/n at 4 °C under gentle agitation (**Supplementary Table 3**). As for primary antibodies, samples were incubated in saturation solution containing the secondary antibodies o/n at 4 °C under gentle agitation, quickly rinsed in wash solution at RT and finally incubated with 0.5 µg/ml 4',6-diamidino-2-phenylindole (DAPI, Sigma-Aldrich) for 10 minutes. Dako (Agilent) was used for mounting. Images of the 2-3 lateral fin rays (excluding the most-lateral fin ray) were acquired by confocal microscope TCS SP8 (Leica). GFP intensity was measured in each segment and normalized to segment area using Fiji (ImageJ).

Immunofluorescence on sections

Amputated caudal fins from WT, *Chi/+* and *p3h1*$^{-/-}$ were fixed in 4 % PFA in PBS o/n at 4 °C. Samples were embedded in 1.5 % w/v agarose/5 % w/v sucrose in PBS and agarose blocks were kept in 30 % sucrose in PBS o/n at 4 °C. Agarose blocks were then immersed in optimum cutting temperature compound (OCT, Histoline) and snap frozen in dry ice. Frozen blocks were stored at -80 °C until cryosectioning. Thick sections (16 µm) were obtained using a Leica CM1850 UV cryostat at -22 °C.

Cryosections were incubated 30 minutes in saturation buffer (1 % BSA in PBS) at RT. Primary antibodies were diluted in saturation buffer and applied on sections for 1 hour at RT (**Supplementary Table 3**). Sections were then rinsed four times, 5 minutes each, in PBS at RT. Secondary antibodies were diluted in saturation buffer and applied on sections for 1 hour at RT. Sections were rinsed and then incubated in PBS containing Hoechst or DAPI 1:4000 for 5 minutes at RT. Finally, sections were rinsed in PBS and then in ddH_2O, mounted with Dako (Agilent), and stored in the dark at 4 °C until imaging.

Oil Red O staining

Oil Red O staining was performed on cryosections. For the staining, sections were let air dry for at least 30 minutes and then fixed in 10 % neutral buffered formalin (Sigma-Aldrich). Slides were quickly dipped in 60 % isopropanol and stained in 0.18 % Oil Red O solution. After washing with 60 % isopropanol and water, samples were counterstained with Mayer's Hematoxylin (Sigma-Aldrich)

and mounted with Mowiol. Images were acquired using a Leica DM6B wide-field microscope equipped with a DFC7000T camera.

For quantification, an area of ~3000 μm^2, traced starting 50 µm far from the distal point of the caudal fin, was measured on 63X images. The number of lipid drops was then counted inside the area using the Cell counter tool on Fiji (Image J) software.

Transmission electron microscopy (TEM)

Following anesthesia, caudal fin biopsies were obtained from adult WT and *Chi/+* fish and rapidly transferred in Karnowsky fixative (0.1 M sodium cacodylate, pH 7.8, 1.5 % v/v glutaraldehyde, 4 % w/v paraformaldehyde) overnight at 4 °C. Samples were then decalcified in 14 % w/v EDTA pH 7.1 at 4 °C, for 24 h for *Chi/+* and 48 h for WT. The samples were then post-fixed in 2 % w/v OsO_4 in H_2O for 2 hours at RT, rinsed in distilled water and dehydrated in ethanol. The specimens were infiltrated with LR White acrylic resin overnight at 4 °C and polymerized in gelatin capsules at 60 °C for 24 h. Thick sections (60–70 nm) were cut on a Reichert OM-U3 ultramicrotome with a diamond blade and collected on 300-mesh nickel grids. The grids were finally stained with saturated aqueous uranyl acetate followed by lead citrate and observed with a Zeiss EM900 electron microscope, operated at 80 kV with an objective aperture of 30 mm.

Swimming behavior analysis

Swimming behavior of 10 mpf *Chi/+* and WT zebrafish (n = 8 for each genotype) was analyzed in a custom-made dark observation chamber (Noldus) equipped with the Basler GenICam capturing 25 frames/second for top-view image acquisition. Data was analyzed using the EthoVision XT 17 software (Noldus). Zebrafish were placed individually in a tank (16 cm (L) x 10 cm (W) x 8 cm (H)) and were allowed to acclimatize for 10 minutes prior to a 10-minute analysis period. The complete experiment was performed in the dark. For each zebrafish, nose-point, center-point and tail-base detection was performed in the EthoVision software. Movement was expressed as total distance travelled (in cm) during the 10 min analysis period. To obtain information about the difference in tail movement, the ratio of the total distance moved by the tail-base over the center-point was calculated and is coined the tail/center movement ratio. The swimming pattern was analyzed in the Ethovision software using the Track Visualization module displaying the movement of the center-point in red and the tail-base in purple. Representative profiles where the animals were moving a straight path were selected for publication to illustrate the tail movement. Absolute head direction meandering was calculated automatically by dividing the turn angle by the distance moved in the EthoVision software and is a measure to compare turning in animals that move at different speeds.

Statistical analysis

All values are expressed as mean ± standard deviation (SD) except when indicated. Statistical analysis of data was performed with GraphPad Prism 9.3.1. Student's *t* test was used for unpaired data applying Welsh's correction when samples had significantly different SDs. Multiple comparisons were conducted using ordinary one-way ANOVA with Dunnett's post hoc test or two-way ANOVA with Tukey's post hoc test. Normality was tested through the Shapiro-Wilk's test. A $P < 0.05$ was considered significant.

Results

Caudal fin regeneration ability is reduced in dominant and recessive OI zebrafish models

Caudal fin regeneration, a well-known and standardized system to evaluate bone formation in zebrafish, was assessed in WT and *Chi/+* and *p3h1*$^{-/-}$ OI fish by means of vital calcein staining. The regenerated caudal fin area and fin rays at 7 and 14 day post amputation (dpa) were analysed. To evaluate a possible impact of aging on regenerative ability, a question that is still debated in the field (Tsai et al. 2007, Anchelin et al. 2011, Itou et al. 2012), the study was performed in fish at 3 month post fertilization (mpf), representing juvenile to adult transition, and at 8 mpf, corresponding to the adulthood. The regeneration ability was significantly compromised at both ages in mutants respect to WT. The percentage of the Regenerated area (REG) and of the Estimated Mineralized Area (EMA) were significantly reduced in *Chi/+* and *p3h1*$^{-/-}$ compared to WT both at 7 and 14 dpa (**Figure 1**). No effect of aging was detectable in the regeneration capacity of WT and mutants. The reduced regenerative ability observed *in vivo* in *Chi/+* and *p3h1*$^{-/-}$ compared to WT demonstrated an impaired bone formation in both OI models.

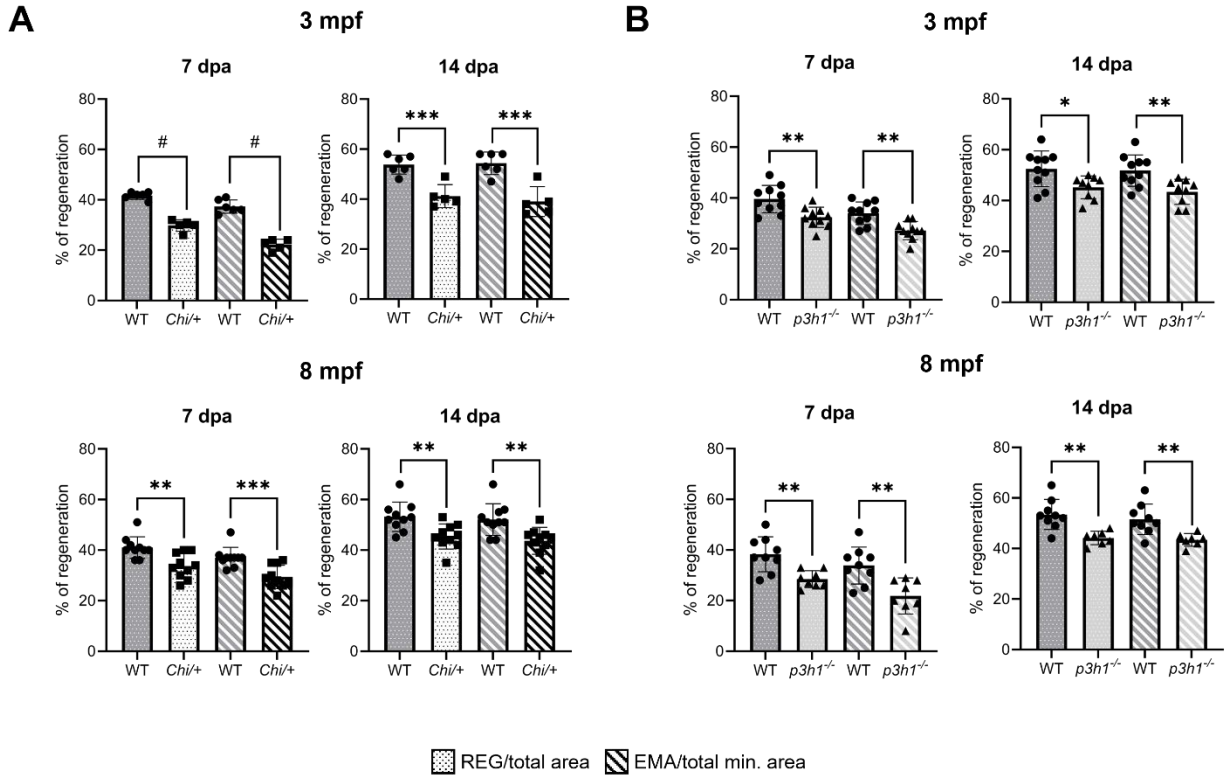

Figure 1. Caudal fin regeneration is reduced in *Chi/+* and *p3h1*$^{-/-}$ compared to WT. (A) Caudal fin regeneration of WT and *Chi/+* siblings. *Chi/+* fish at 3 and 8 mpf exhibited a significantly reduced caudal fin regeneration compared to WT both at 7 and 14 dpa. (3 mpf: n = 6 for each genotype; 8 mpf: n = 10 for each genotype). **(B)** Caudal fin regeneration of WT and *p3h1*$^{-/-}$ siblings. *p3h1*$^{-/-}$ mutants at 3 and 8 mpf showed a significantly reduced caudal fin regeneration compared to WT (n = 9 for each genotype and age) both at 7 and

14 dpa. dpa: days post amputation; mpf: months post fertilization; REG: Regenerated area; EMA: Estimated mineralized area. * P < 0.05, ** P < 0.01, *** P < 0.001, # P < 0.0001.

Caudal fin morphology is impaired in dominant and recessive OI

To deeply investigate caudal fin morphology in adult and during regeneration, detailed morphometric analysis was carried out in WT, *Chi/+* and *p3h1*$^{-/-}$ at 7 and 14 dpa and compared to the original caudal fin (indicated from now on as sample at day 0). Representative images are shown in **Supplementary Figure 2**.

A significantly reduced number of fin rays in the caudal fin was detectable only in *p3h1*$^{-/-}$ respect to WT, suggesting a possible developmental defect in these fish (**Figure 2A**).

The caudal fin size was significantly reduced only in *Chi/+* respect to WT (**Figure 2B**). While the number of segments did not differ between WT and *Chi/+* (**Figure 2C**), the mean length of segments was reduced at all time points, coherently with the smaller caudal fin that characterizes these mutants (**Figure 2D**). On the contrary, an increased number of segments was evident in *p3h1*$^{-/-}$ respect to WT at day 0 (**Figure 2C**), but their length was reduced similarly to *Chi/+* (**Figure 2D**). At 14 dpa, *p3h1*$^{-/-}$ segment length showed normal value, while their number was significantly reduced respect to WT, compatibly with *p3h1*$^{-/-}$ reduced regenerative ability (**Figure 2D**).

Fin rays of *Chi/+* had significantly reduced number of bifurcations respect to WT at day 0 and 14 dpa. Interestingly, *p3h1*$^{-/-}$ showed significantly increased number of bifurcations respect to WT at day 0 and 7 dpa. No difference was observed at 14 dpa, when WT fish reached the same number of bifurcations as *p3h1*$^{-/-}$. No differences in the distance from the first bifurcation to the caudal fin base were detected in both *Chi/+* and *p3h1*$^{-/-}$ respect to WT (**Figure 2E**).

Taken together, these data clearly indicate a morphology defect in *Chi/+* and *p3h1*$^{-/-}$ fish. The former are characterized by shorter fin rays that never bifurcate, while the latter have less fin rays with increased number of bifurcations.

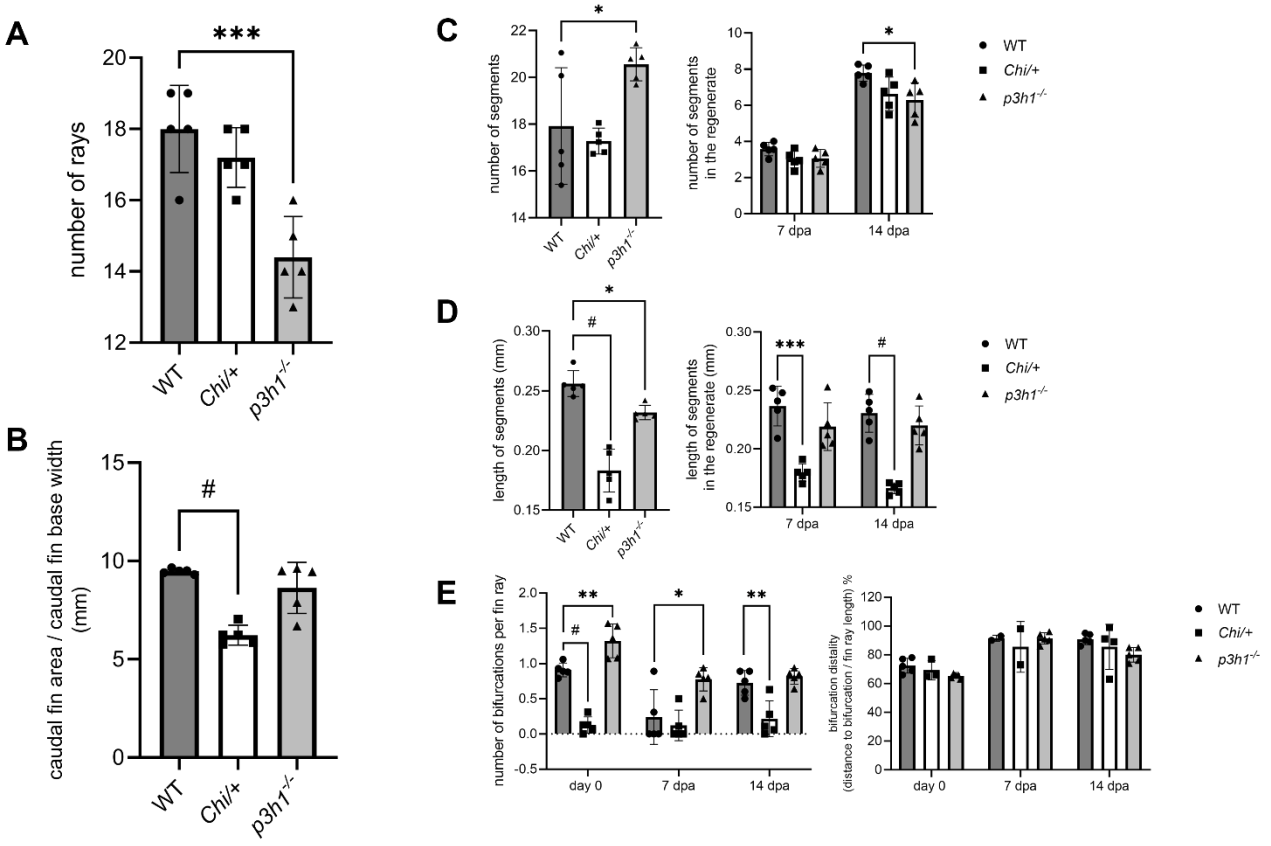

Figure 2. Morphometric analysis of WT, *Chi/+* and *p3h1*$^{-/-}$ caudal fin before and during regeneration. (A) A general reduction in the number of rays was detected in *p3h1*$^{-/-}$ compared to WT. **(B)** Caudal fin area, normalized to the fin base width, was significantly reduced in *Chi/+* respect to WT. **(C)** At day 0 the number of segments, increased in *p3h1*$^{-/-}$ respect to WT, was reduced in the 14 dpa regenerate, compatibly with overall reduced bone formation. **(D)** The mean length of segments was reduced in *p3h1*$^{-/-}$ respect to WT at day 0 and in *Chi/+* respect to WT before and during regeneration. **(E)** *P3h1*$^{-/-}$ fish presented an increased number of bifurcations at day 0 and 7 dpa, while *Chi/+* rays had significantly less bifurcations at day 0 and at 14 dpa respect to WT. No differences were found in the distance to bifurcation between all fish (n = 5 for each genotype). dpa: days post amputation. * $P < 0.05$, ** $P < 0.01$, *** $P < 0.001$, # $P < 0.0001$.

Early osteoblast differentiation is not affected during caudal fin regeneration in OI

The key osteoblastogenic differentiation pathways are conserved during zebrafish caudal fin regeneration (Valenti et al. 2020). To explore in depth the molecular basis of impaired caudal fin regeneration in the two OI zebrafish models, early differentiation was evaluated through qPCR analysis on RNA extracted from caudal fins pools from WT, *Chi/+* and *p3h1*$^{-/-}$. The time points selected for the analysis were day 0 (basal state), 3 dpa (when early differentiation markers are strongly expressed in the caudal fin (van der Meulen et al. 2005, Smith et al. 2006)), and 5 dpa (when late markers start to be expressed (Knopf et al. 2011)). The expression of the master osteoblastogenic marker *runx2*, duplicated in zebrafish as the two orthologues *runx2a* and *runx2b*, and *sox9*, involved in mesenchymal condensation and also duplicated in the two isoforms *sox9a* and *sox9b* were evaluated as the two main markers of early osteoblastogenesis.

In both WT and mutant fish the level of *runx2a* and *sox9a* and *sox9b* markers increased at 3 dpa, during the early regenerative process, and showed a decreasing trend at 5 dpa, with the exception of *sox9b* that stayed upregulated (**Figure 3**). On the contrary, the expression levels of *runx2b* did not show any variation among time points and genotypes analyzed.

Taken together, these data supported normal early osteoblastogenic differentiation in OI *Chi/+* and *p3h1*$^{-/-}$ fish.

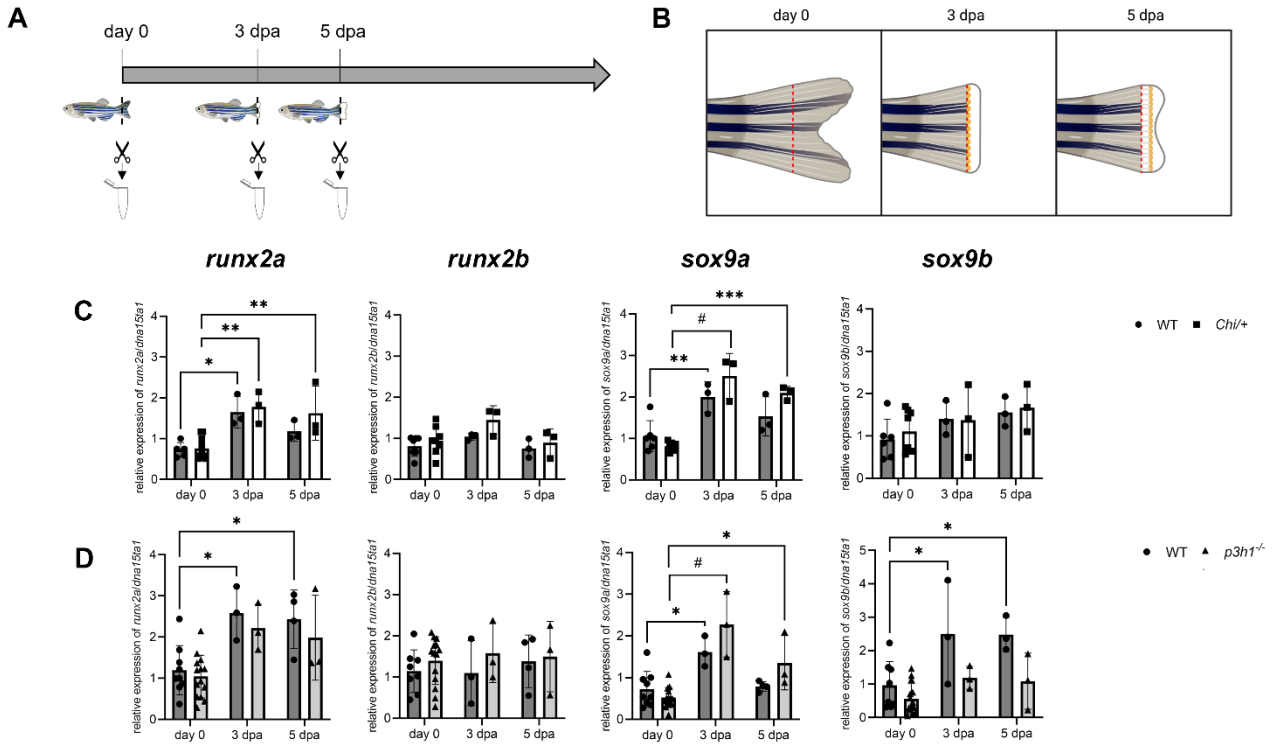

Figure 3. Sample collection and gene expression analysis of the early differentiation markers *runx2a*, *runx2b*, *sox9a* and *sox9b* in WT and mutants. (A) RNA was collected from pools of six caudal fins at day 0, 3 and 5 dpa as shown in the scheme. **(B)** Detailed schematic view of caudal fin samples. Day 0 refers to the portion of the caudal fin collected after the first amputation at basal state; 3 dpa and 5 dpa regenerates were collected above the amputation plane. Created with BioRender.com. **(C)** qPCR analysis in WT and *Chi/+* fish. *Runx2a* and *sox9a* showed a significant increase after amputation, with no difference among genotypes. **(D)** qPCR analysis in WT and *p3h1*$^{-/-}$ revealed the same trend observed in the previous group. n ≥ 3 pools of caudal fins for each genotype. dpa: days post amputation. * P < 0.05, ** P < 0.01, *** P < 0.001, # P < 0.0001.

Osteoblast differentiation is impaired in *Chi/+*, but not in *p3h1*$^{-/-}$

Osteoblast differentiation upon cell commitment was first investigated by qPCR gene expression analysis of the early-intermediate marker *sp7/osterix* and the late marker *bglap/osteocalcin.* An *in vivo* analysis of the expression of the same markers was then undertaken by confocal microscopy on the mutants crossed with the transgenic fish lines *sp7*:GFP and *bglap*:GFP. GFP intensity and distribution within the segments and in the regenerated rays were evaluated. The study was performed

at day 0, 3 and 5 dpa except for *bglap*, that was not investigated at 3 dpa due to its low expression at this time point.

In both *Chi/+* and WT fish *Sp7* mRNA level started to increase at 3 dpa compared to day 0 as expected (Knopf et al. 2011), but no difference was detectable between mutant and WT at any of the analyzed time points (day 0: p = 0.15, 3 dpa: p = 0.18, 5 dpa: p = 0.38) (**Figure 5A**). Interestingly, in *Chi/+; sp7*:GFP a significant increased GFP intensity was evident in the ray segments at 0 and 3 dpa respect to WT (**Figure 5B**). At the latter time point an accumulation of *sp7*:GFP+ positive cells at the tip of the regenerating fin rays in mutants was detected (**Figure 5C**). No significant differences were found at 5 dpa, even if *sp7*:GFP intensity at the tip of the regenerating rays was still higher in mutants respect to WT (**Figure 5B-C**).
The expression of *bglap* was significantly reduced in *Chi/+* respect to WT at day 0 (**Figure 4A**). This result was confirmed by confocal microscopy. Indeed, *Chi/+; bglap*:GFP showed decreased GFP intensity in the ray segments at day 0 respect to WT (**Figure 4B**). At this time point, the analysis of GFP distribution inside fin ray segments showed an homogeneous distribution of GFP signal along the segment in WT, while *Chi/+* presented an accumulation of *bglap*:GFP+ cells in the center of the segment (**Figure 4C**). qPCR did not reveal difference between WT and mutant in *bglap* expression at 5 dpa (**Figure 4A**), but *bglap*:GFP intensity was significantly increased in *Chi/+* respect to WT, interestingly an intensity peak of GFP signal was detected at the level of the amputation plane (**Figure 4B-C**).

Taken together, these data indicate an increased number of immature osteoblasts and a reduction of mature osteoblasts both in the amputated and regenerated caudal fin rays in *Chi/+* compared to WT, supporting a delay in osteoblast differentiation.

No change in *sp7* and *bglap* expression was detected in *p3h1*$^{-/-}$ at any time points. Coherently with these results, *p3h1*$^{-/-}$*; sp7*:GFP and *p3h1*$^{-/-}$; *bglap*:GFP presented a similar GFP intensity and distribution compared to WT siblings, indicating normal osteoblast differentiation in this model (**Figures 6 and 7**).

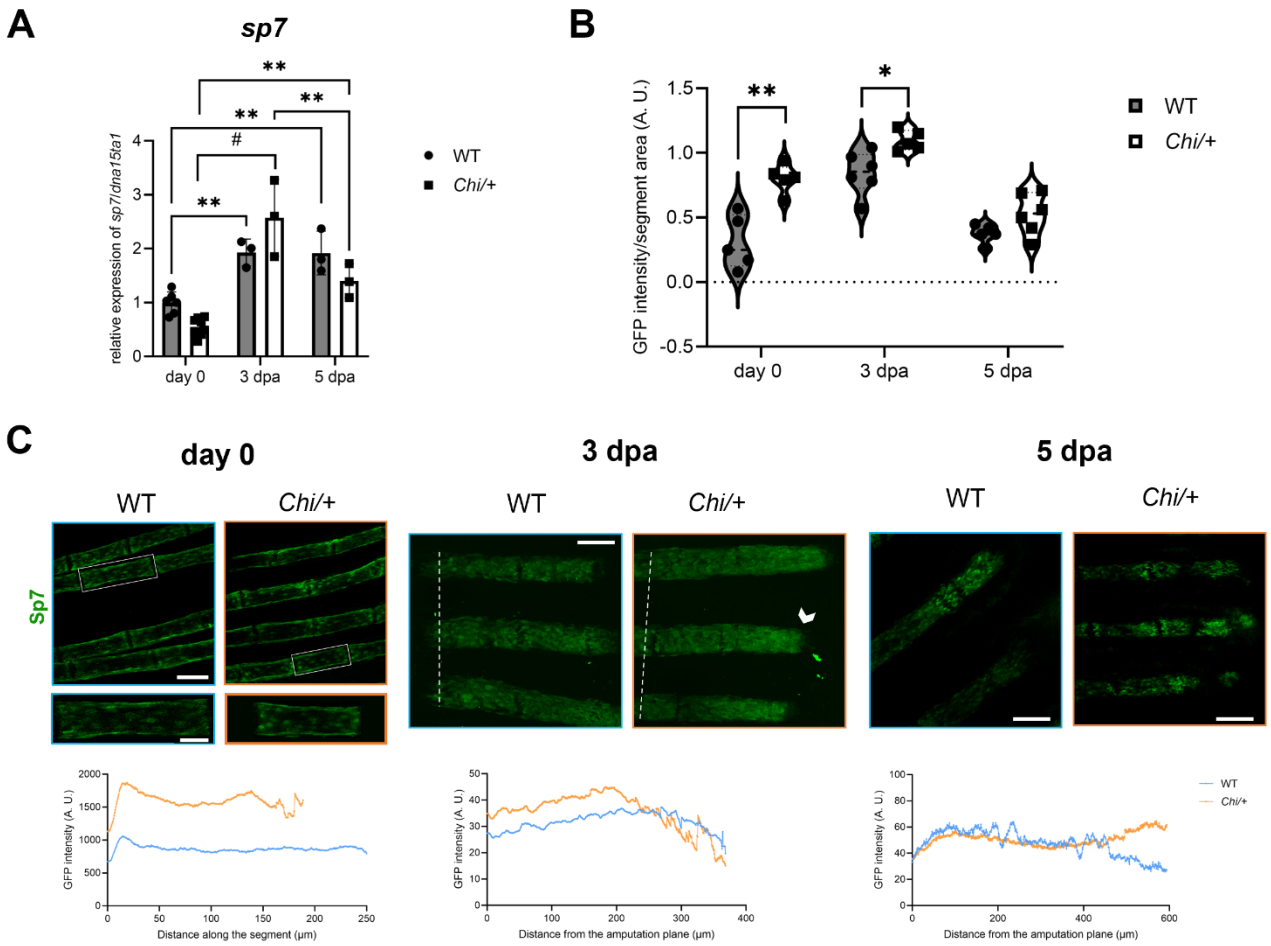

Figure 4. *Sp7* expression analysis in *Chi/+* and WT caudal fins. (A) qPCR analysis showed increased expression of *sp7* at 3 dpa and decreased level at 5 dpa in both WT and mutant. No differences in *sp7* expression between genotypes (n ≥ 3 pools of six caudal fins for each genotype) were detected. dpa: days post amputation. **(B)** *Sp7*:GFP intensity was increased at 3 and 5 dpa in *Chi/+* respect to WT (n ≥ 5 fish for each genotype). **(C)** Analyses of GFP distribution along the segment at day 0, and from the amputation plane (dotted line) at 3 and 5 dpa. No significant differences were found between WT and *Chi/+*, but an accumulation of *sp7*:GFP+ cells could be observed at the tip of the fin rays at 3 dpa (arrowhead). Scale bar: 100 µm. * $P < 0.05$, ** $P < 0.01$, # $P < 0.0001$.

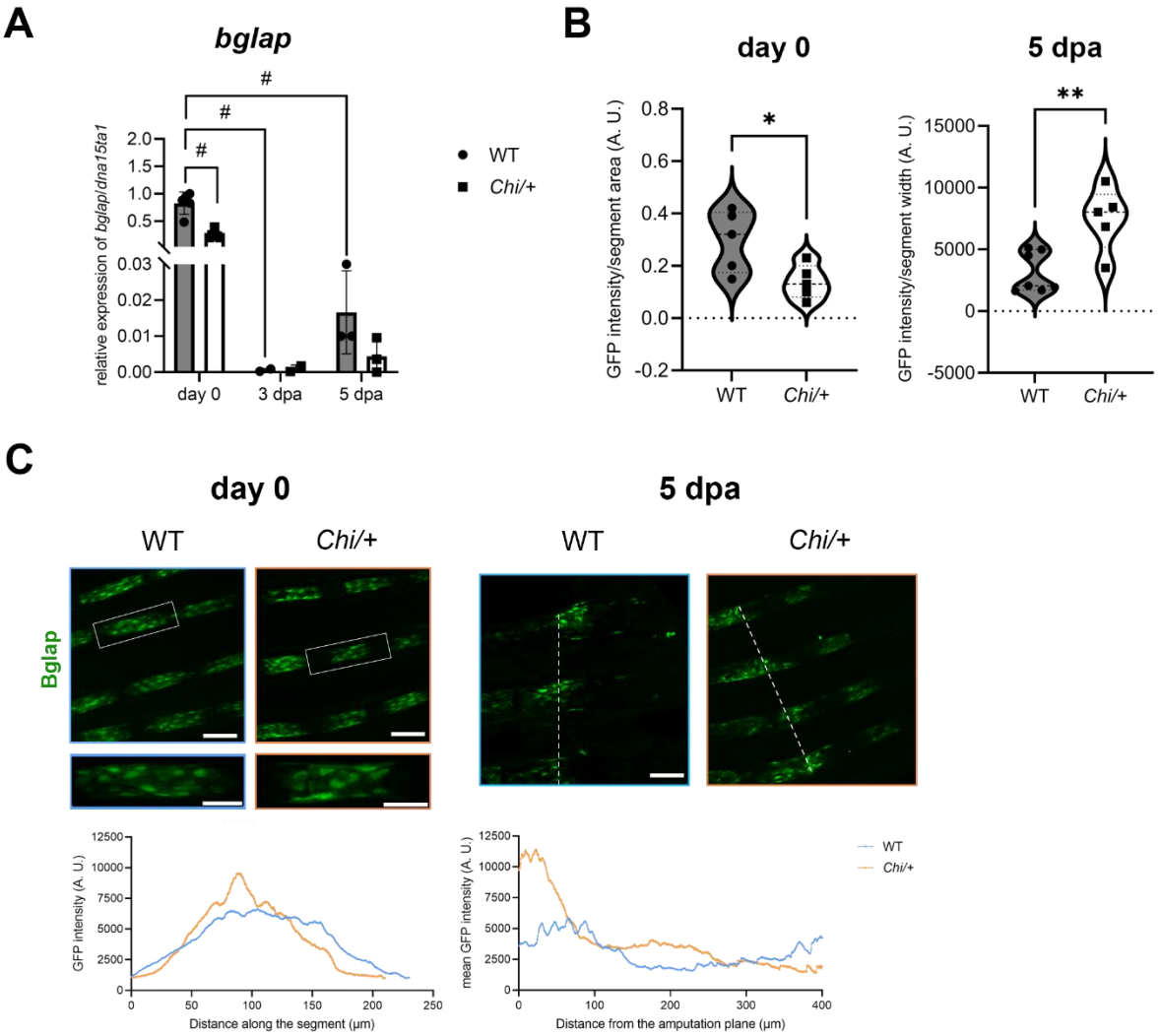

Figure 5. *Bglap* expression analysis in *Chi/+* caudal fins. (A) qPCR analysis revealed a reduction in *bglap* expression in *Chi/+* respect to WT at day 0 ($n \geq 3$ pools of six caudal fins for each genotype). dpa: days post amputation. **(B)** *bglap*:GFP intensity was decreased at day 0 and increased at 5 dpa in *Chi/+* respect to WT ($n \geq 5$ fish for each genotype). **(C)** Analyses of GFP distribution along the segment at day 0, and from the amputation plane at 5 dpa (dotted line). At day 0, *bglap*:GFP+ cells accumulated in the middle of the segment in *Chi/+*. At 5 dpa, a peak of *bglap*:GFP+ cells in *Chi/+* respect to WT, was detected at the level of the amputation plane. Scale bar: 100 µm. * $P < 0.05$, ** $P < 0.01$, # $P < 0.0001$.

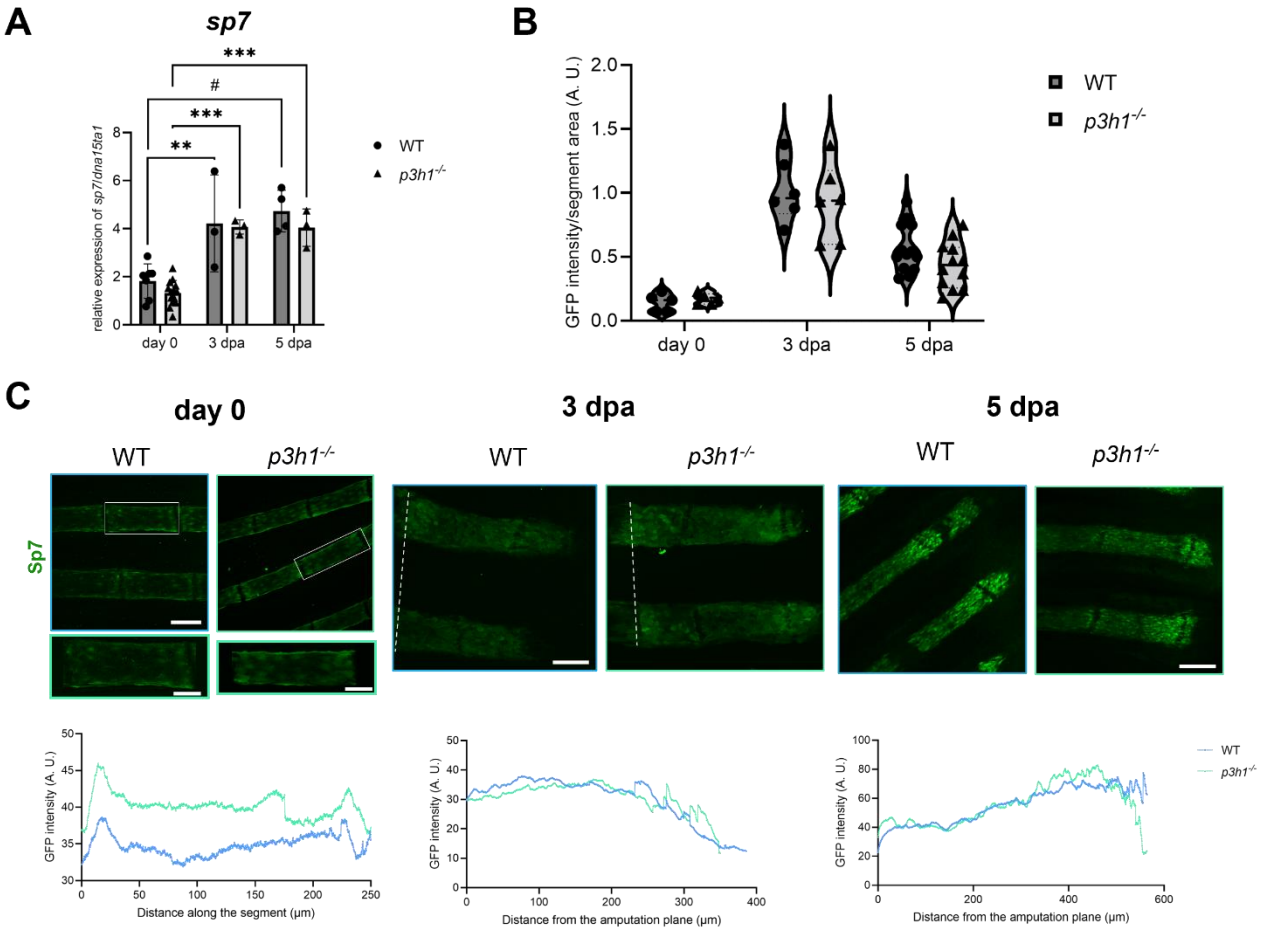

Figure 6. *Sp7* expression analysis in *p3h1*$^{-/-}$ caudal fins. (A) qPCR analysis did not show differences in *sp7* expression between genotypes (n ≥ 3 pools of six caudal fins for each genotype). dpa: days post amputation. **(B)** No differences in s*p7*:GFP intensity were found between WT and *p3h1*$^{-/-}$ (n ≥ 5 fish for each genotype). **(C)** Analyses of GFP distribution along the segment at day 0, and from the amputation plane at 3 and 5 dpa (dotted line). *Sp7*:GFP signal was distributed in a similar way in WT and *p3h1*$^{-/-}$ fin rays. Scale bar: 100 µm. ** P < 0.01, *** P < 0.001, # P < 0.0001.

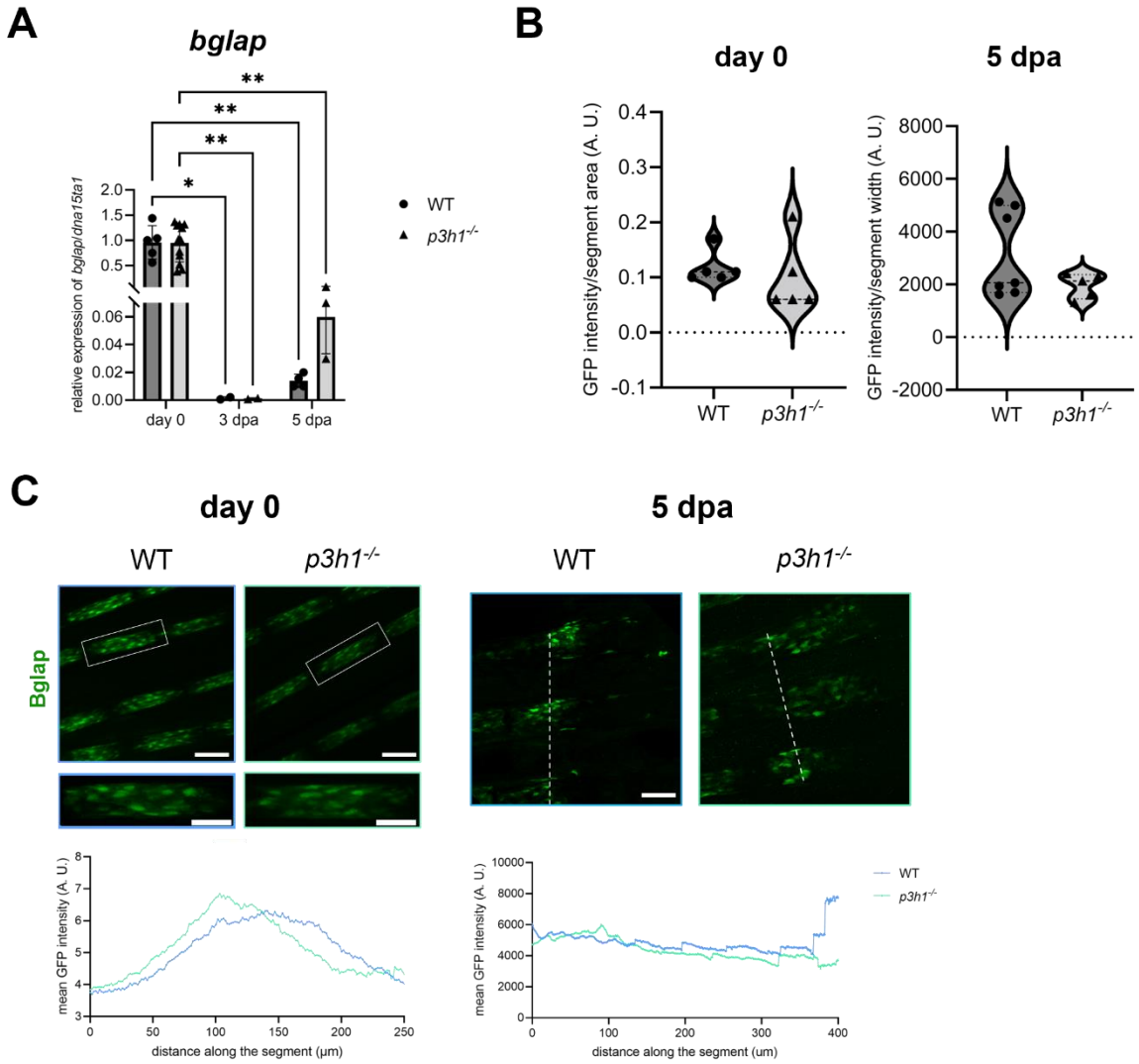

Figure 7. *Bglap* expression analysis in *p3h1*$^{-/-}$ caudal fins. (A) qPCR analysis showed normal expression of *bglap* transcript in *p3h1*$^{-/-}$ at all time points analyzed (n ≥ 3 pools of six caudal fins for each genotype). dpa: days post amputation. **(B)** *bglap*:GFP intensity in *p3h1*$^{-/-}$ appeared normal before and during regeneration (n ≥ 5 fish for each genotype). **(C)** Analyses of GFP distribution along the segment at day 0, and from the amputation plane at 5 dpa (dotted line). No differences were detected between WT and *p3h1*$^{-/-}$ fish. Scale bar: 100 µm. * $P < 0.05$, ** $P < 0.01$.

Chi/+ caudal fin shows an increased number of adipocytes

Impaired osteoblasts differentiation in dominant OI was previously associated to increased adipogenesis (Gioia et al. 2012), thus adipocytes were evaluated in *Chi/+* caudal fins at day 0, the time point in which delayed osteoblast differentiation was stronger as well as in *p3h1*$^{-/-}$, in which no compromised osteoblast differentiation was proved. Oil Red O (ORO) staining on longitudinal caudal fin sections was undertaken focusing on the most-distal part of the fin, where less adipocytes should be present in normal conditions (Imrie and Sadler 2010). While the number of ORO-stained lipid drops was low and did not differ between WT and *p3h1*$^{-/-}$, they were significantly increased in *Chi/+*, proving a switch toward adipogenesis during precursor cells differentiation (**Figure 8**).

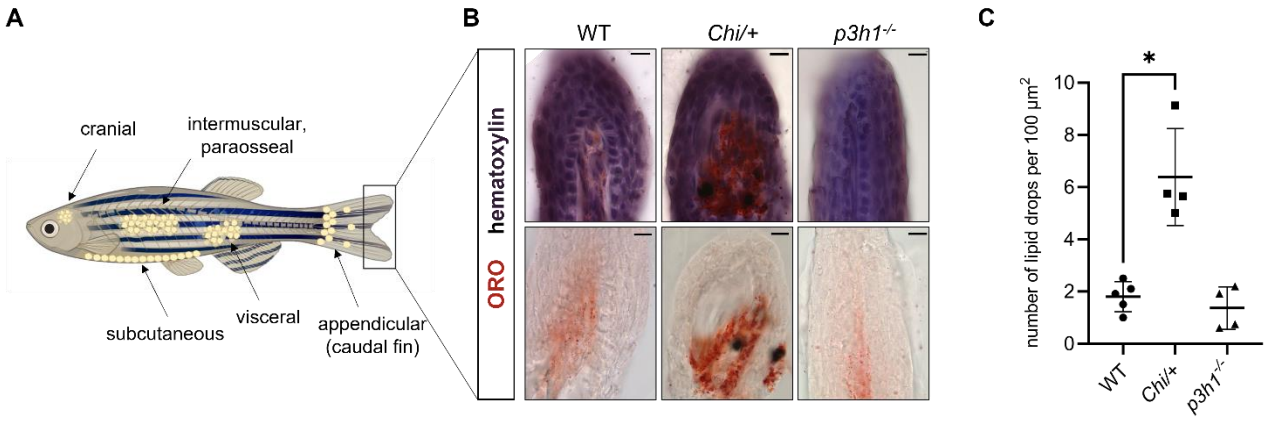

Figure 8. Adipocytic differentiation in the distal extremity of the caudal fin. (A) Representative image of adipocyte localization in zebrafish. Adipocytes can be found in the cranium, in the viscera, and in the subcutaneous, intermuscular and paraosseal tissues. Appendicular adipocytes have also been described in the caudal fin base; vice versa, in the distal extremity of the caudal fin, few or no adipocytes should be present. Created with BioRender.com. **(B)** Oil Red O (ORO) and hematoxylin counterstaining of WT (n = 5), *Chi/+* (n = 4) and *p3h1*$^{-/-}$ (n = 4) longitudinal caudal fin sections. Double staining on the top, ORO staining on the bottom. Scale bar: 10 µm. **(C)** Quantification of the number of ORO-stained lipid drops in the distal caudal fin revealed an increased adipogenesis in *Chi/+* fish. * $p < 0.05$.

Osteoclast activity is reduced in mutants' caudal fin regenerates

Bone homeostasis requires together with the activity of osteoblasts, responsible for bone formation, also the presence of osteoclasts, driving bone resorption. To investigate bone resorption in *Chi/+* and *p3h1*$^{-/-}$ mutants, we investigated both the expression at the transcript level and the enzymatic activity of Tartrate-Resistant Acid Phosphatase (TRAP), a well-known osteoclast marker.

The expression of *acp5a*, encoding TRAP, was investigated at 0 and 5 dpa by qPCR. a*cp5a* level significantly increased in WT, *Chi/+* and *p3h1*$^{-/-}$ after amputation. No differences were detected between genotypes at day 0. Interestingly, a significantly decreased expression of the gene was detected in *Chi/+* at 5 dpa respect to WT (**Figure 9A**). On the contrary, the *acp5a* expression in *p3h1*$^{-/-}$ at 5 dpa was similar to the WT value (**Figure 10A**).

TRAP staining was performed on caudal fins collected at day 0 (indicated as pre-amputation) and at 5 dpa. The number of TRAP+ cells was significantly increased in the caudal fin of *Chi/+* respect to WT and significantly reduced at 5 dpa (**Figure 9B**). On the contrary, *p3h1*$^{-/-}$ showed no differences in the number of TRAP+ cells at day 0, but significantly reduced TRAP+ cells respect to WT were present at 5 dpa (**Figure 10B**). The intensity of TRAP signal, measured at the level of the amputation plane, was normal in *Chi/+* (**Figure 9B**), but significantly reduced in *p3h1*$^{-/-}$ respect to WT (**Figure 10B**).

The *rankl* expression was increased in WT and in both mutants at 5dpa compared to the amputated caudal fin, whereas no difference was detectable in *opg* level. The *rankl/opg* ratio was similar in WT

and both mutants at day 0 and 5 dpa (**Figures 9C-10C**). However, interestingly *rankl/opg* ratio was significantly increased at 5 dpa respect to day 0 in WT and *p3h1*$^{-/-}$, but not in *Chi/+* fish.

These data supported a higher presence and activity of osteoclasts only in the *Chi/+* caudal fin and pointed to a reduced number and activity of osteoclasts during regeneration in both models.

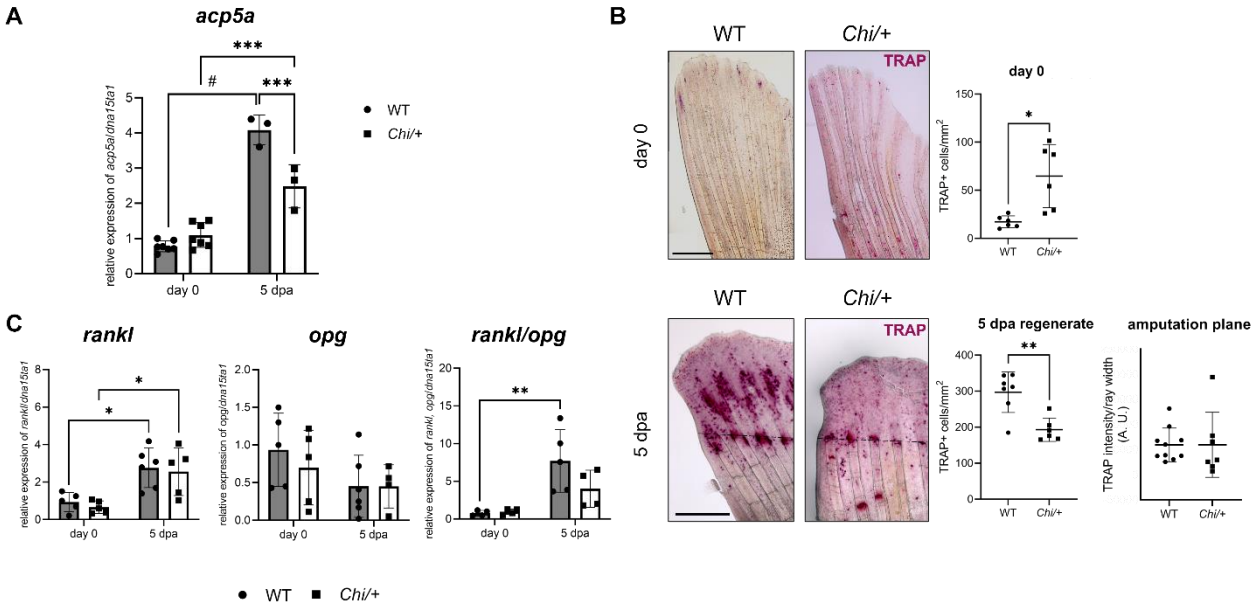

Figure 9. Osteoclast expression and activity in *Chi/+*. (A) qPCR analysis of *acp5a* expression at day 0 and 5 dpa revealed a reduced transcript expression in *Chi/+* at 5 dpa (n ≥ 3 pools of six caudal fins for each genotype). **(B)** TRAP staining of WT and *Chi/+* caudal fin samples collected at day 0 and at 5 dpa (the amputation site is indicated by the black dotted line). Osteoclast activity was increased at day 0 and reduced at 5 dpa in mutants respect to WT (n ≥ 6 caudal fins for each genotype, as indicated by the dots). Scale bar: 500 µm. **(C)** qPCR analysis of *rankl*, *opg* and *rankl/opg* ratio. No significant differences were detected between genotypes (n ≥ 4 pools of six caudal fins for each genotype). dpa: days post amputation. * P < 0.05, ** P < 0.01, *** P < 0.001, # P < 0.0001.

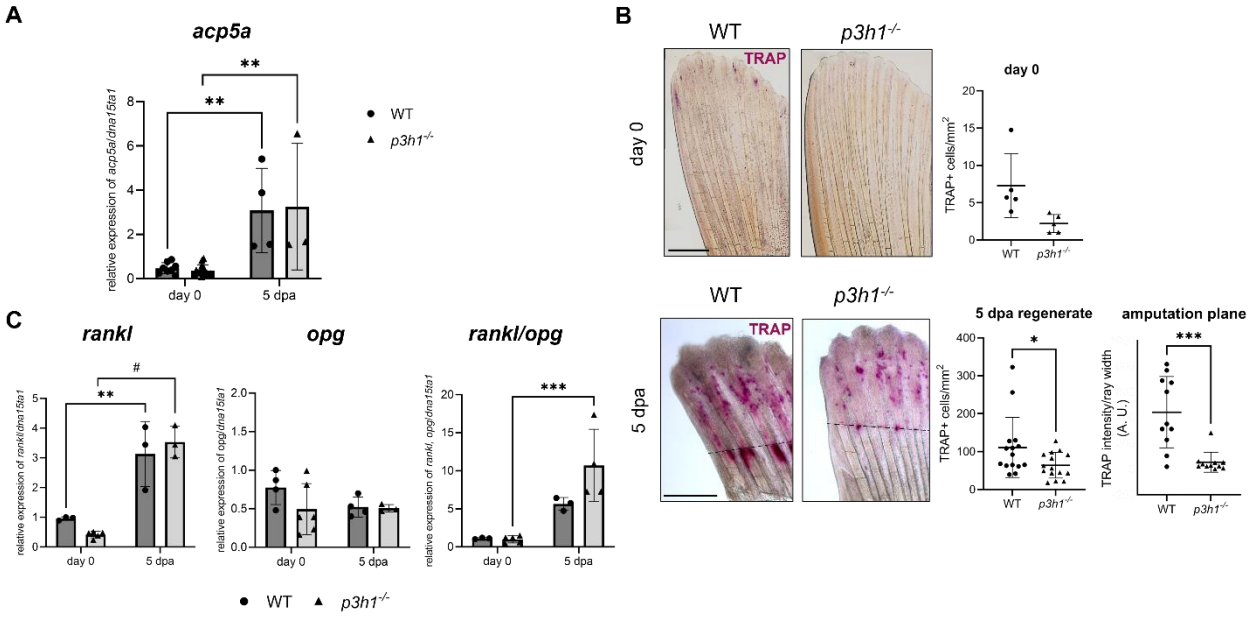

Figure 10. Osteoclast expression and activity in *p3h1*$^{-/-}$. (A) qPCR analysis of *acp5a* expression at day 0 and 5 dpa showed no differences between genotypes (n ≥ 3 pools of six caudal fins for each genotype). **(B)** TRAP staining of WT and *p3h1*$^{-/-}$ caudal fin samples collected at day 0 and at 5 dpa (the amputation site is indicated by the black dot line). While osteoclast activity of *p3h1*$^{-/-}$ fish was normal at day 0, it significantly decreased at 5 dpa respect to WT in both regenerate and amputation plane (n ≥ 5 caudal fins for each genotype, as indicated by the dots). Scale bar: 500 µm. **(C)** qPCR analysis of *rankl*, *opg* and *rankl/opg* ratio. No significant differences were detected between genotypes (n ≥ 3 pools of six caudal fins for each genotype). dpa: days post amputation. * P < 0.05, ** P < 0.01, *** P < 0.001, # P < 0.0001.

Defective caudal fin morphometry and bone cells defects impair *Chi/+* swimming behavior

The caudal fin is a major source of propulsion in fish locomotion and the abnormal fin shape reported for *Chi/+* zebrafish suggested to further investigate the impact of morphometrical and bone cell defects on movement in this model. The swimming behavior of WT and *Chi/+* was evaluated using an observation chamber equipped with a camera. Spontaneous swimming behavior demonstrated a significant decrease in the total distance travelled by *Chi/+* zebrafish compared to their WT siblings during a 10-minute analysis period (**Figure 11A**). To assess the difference in caudal fin movement, the ratio of the distance moved by the tail-base over the distance moved by the center-point of the zebrafish was calculated and showed a significantly increased ratio in *Chi/+* compared to WT zebrafish, indicating increased movement of the caudal fin in *Chi/+* zebrafish (**Figure 11B**). The path of the center-point and tail-base, plotted in **Figure 11C**, highlights a smooth S-shaped curvature of the tail-base in WT zebrafish, whereas a more erratic (spastic), less symmetrical movement (compared to the center-point) of the caudal fin is observed in *Chi/+*. Indeed, in contrast to WT zebrafish which often swam a straight path, *Chi/+* zebrafish had difficulties to swim straight and their paths were often more curved compared to WT. This was confirmed by quantifying the head direction

meandering, which was significantly higher in *Chi*/+ zebrafish compared to WT siblings (**Figure 11D**).

Taken all together the data indicated an impaired swimming ability of *Chi*/+ compared to WT at least in part due to altered caudal fin shape and morphometry.

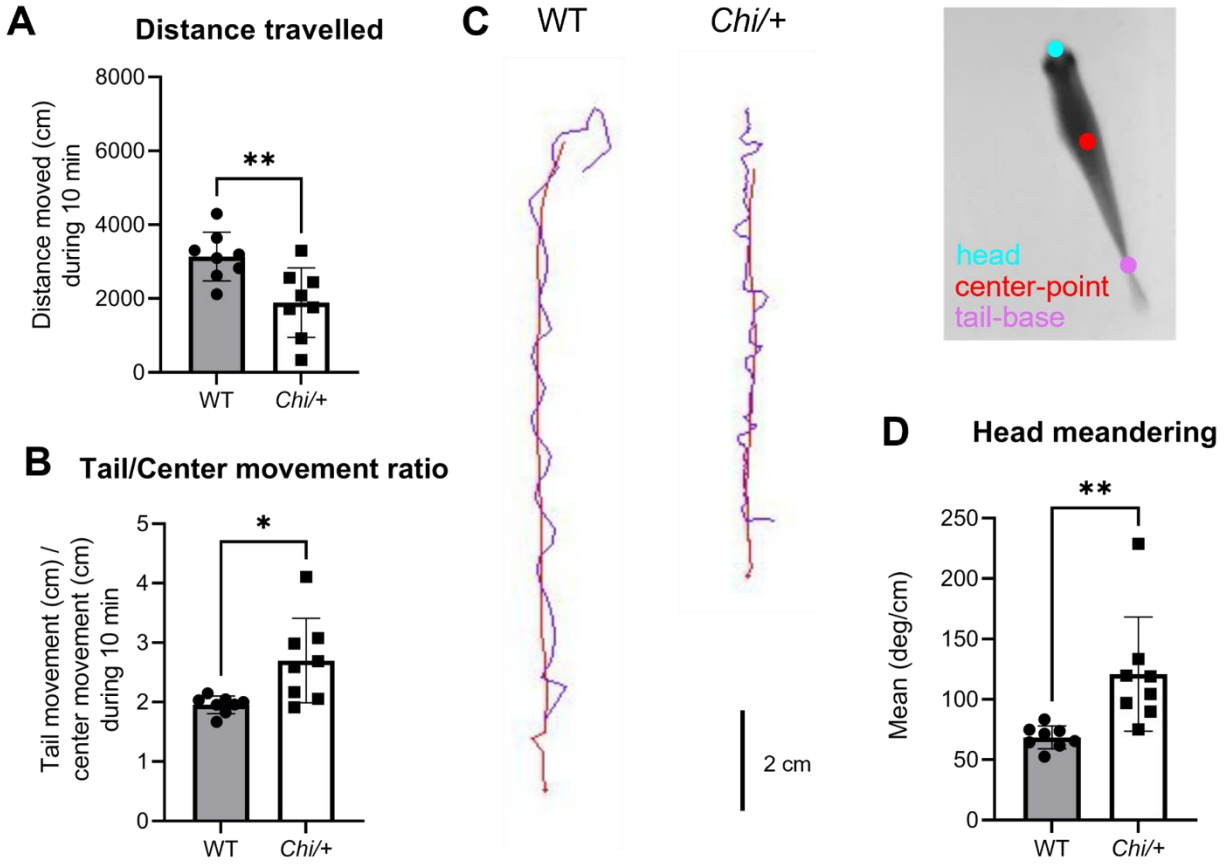

Figure 11. Spontaneous swimming behavior of WT and *Chi*/+ fish. (A) The distance moved was significantly lower in *Chi*/+ zebrafish, compared to their WT siblings. **(B)** The ratio of the distance moved by the tail-base over the distance moved by the center-point of the zebrafish measured during 10 minutes in the dark showed an increased ratio in *Chi*/+ zebrafish, indicating increased movement of the caudal fin. **(C)** The swimming pattern of WT zebrafish shows an S-shaped movement of the caudal fin (track = 2s). In contrast, *Chi*/+ zebrafish showed a more erratic movement of the caudal fin with a higher beat frequency (purple) and decreased distance travelled (track = 7s). The red line depicts movement of the centerpoint, the purple line depicts movement of the tail-base as indicated on the inserted image. **(D)** Absolute head direction meandering was increased in *Chi*/+ zebrafish. Data are represented as mean ± SEM. n = 10 for each genotype. * $P < 0.05$, ** $P < 0.01$.

Chi/+ caudal fin joint matrix is disorganized

Caudal fin movement and flexibility are allowed by several joints located in the caudal fin rays. To assess whether *Chi*/+ impairment swimming behavior was linked to defects in caudal fin joints organization, electron microscopy analysis was performed. TEM images of WT fish showed well organized collagen fibers with a parallel orientation linking consecutive ray segments. The typical

collagen banding was clearly visible. On the contrary. *Chi/+* joints were characterized by a complete disorganization of collagen fibrils, with irregular intersecting directions and lacking the typical collagen banding (**Figure 12A**). Collagen type I structure and organization in the caudal fin were then also investigated by immunofluorescence. Collagen type I fibrils were distributed parallel to the fin rays and around and inside the caudal fin joints. No difference in collagen general orientation was found between WT and mutants. Nevertheless, in *Chi/+* some collagen fibril aggregates could be detected as well as an accumulation of fibrils near the fin rays, further demonstrating an impairment in collagen deposition (**Figure 12B**).

To deeply address dysregulation of collagen type I fibrillogenesis, two Fibril-Associated Collagens with Interrupted Triple Helices (FACITs) collagen XII and collagen XIV, known to interact with collagen I fibrils (Ansorge et al. 2009, Izu et al. 2021), were investigated by immunofluorescence. Surprisingly, collagen XIV was found to be specifically expressed inside the caudal fin joints, an observation never reported before in the literature. Collagen XII was widely distributed in the caudal fin, with its pattern being strongly similar to the one of collagen I. No abnormalities in collagen XII fibrils were detected in *Chi/+*. Interestingly, collagen XIV fluorescence intensity was significantly higher in mutant and being strongly expressed at the joint allowed to appreciate a wider inter-joint space in *Chi/+* respect to WT, further supporting the matrix disorganization observed by TEM (**Figure 12B-C**). Of note, joint deformities in *Chi/+* were detected also in the regenerating caudal fin at 5 dpa. Nevertheless, a deeper investigation of collagen XIV distribution in 5 dpa progressive transversal caudal fin sections from WT and *Chi/+* revealed no anomalies in collagen XIV distribution along the fin rays (**Supplementary Figure 3**).

qPCR analysis of *col1a1*, *col12a1a*, *col12a1b*, *col14a1a* and *col14a1b* did not show differences in transcripts expression among the two genotypes. Interestingly, *col12a1b* expression was detectable in 5 dpa samples only in mutants but not in WT (**Figure 12D**).

Immunofluorescence and qPCR experiments were also carried out for *p3h1*$^{-/-}$ fish to evaluate collagens organization. Collagen type I showed normal orientation in these fish, but fibrils appeared wavy and strongly disorganized, with some collagen I signal trapped inside the fin rays. No alterations were detected for collagen XII and XIV (**Supplementary Figure 4**).

These data indicated a collagen type I disorganization in both *p3h1*$^{-/-}$ and *Chi/+* mutants, although the segment joints were altered only in the latter.

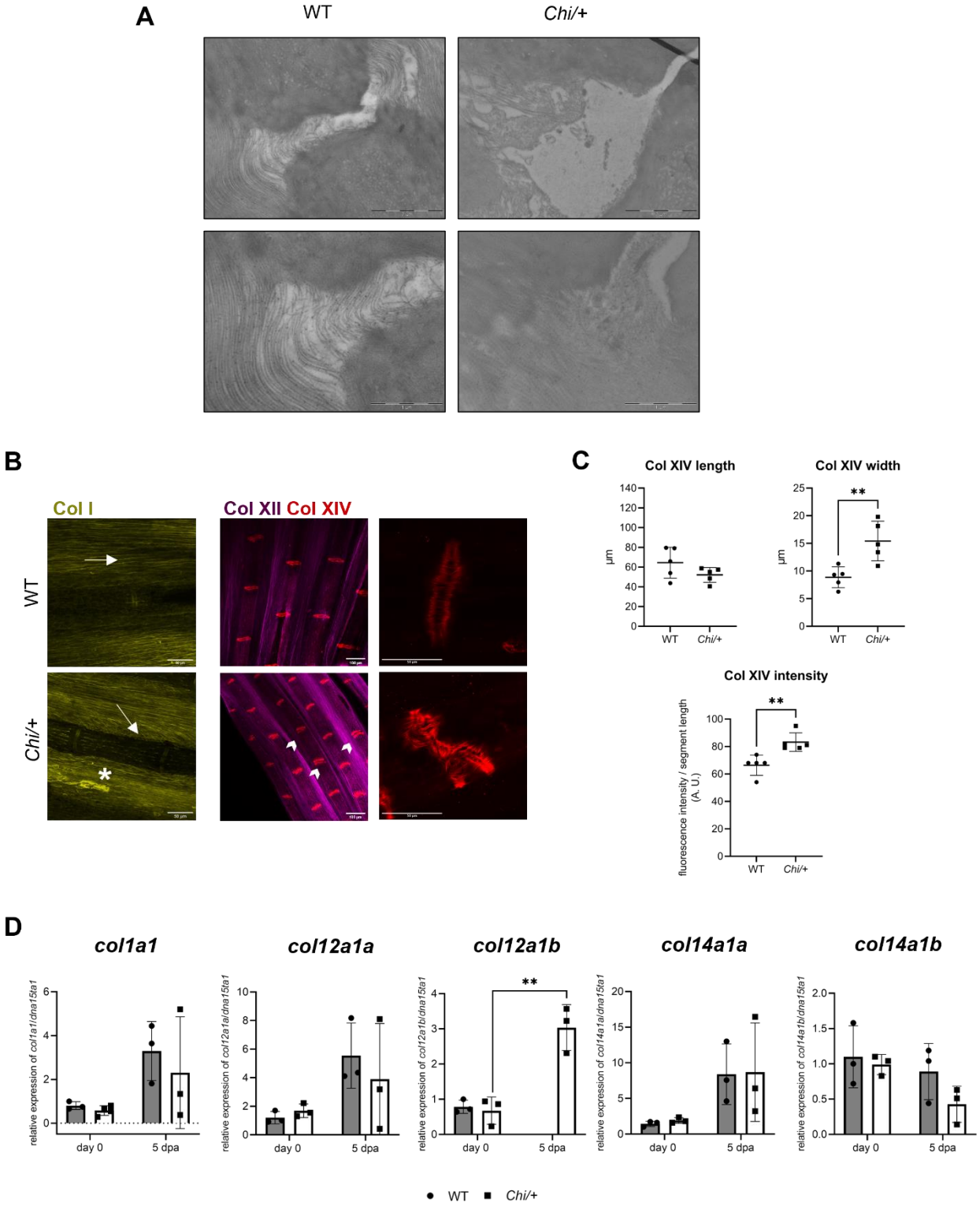

Figure 12. Collagen disorganization in the caudal fin of *Chi*/+ fish. (A) TEM images of WT (n = 1) and *Chi*/+ (n = 3) collagen fibrils at the caudal fin joints. In the WT several parallel, well organized collagen fibrils connect the inter-joint surfaces. In the mutant, the joint structure appeared disrupted, with fibrils having different orientations and being scattered in the extracellular space. Scale bar top: 2 µm. Scale bar bottom: 1 µm. **(B)** Representative immunofluorescence of collagen I, XII and XIV in WT and *Chi*/+ caudal fin. Collagen I fibrils were thick and parallel to the fin ray in WT (arrow). In *Chi*/+ they accumulated in proximity to the fin ray (arrow), in some cases forming aggregates (asterisk). Collagen XII was distributed widely in the caudal fin, similarly to collagen I. Collagen XIV specifically localized in the fin ray joints. In *Chi*/+, joints showed

altered structure and increased inter-joint space, as indicated by the arrowheads. **(C)** Collagen XIV analysis revealed increased joint width and fluorescence intensity in *Chi/+* respect to WT (n = 5 for each genotype). ** $p < 0.01$. **(D)** qPCR analysis of collagens did not show differences between the two genotypes (n = 3 pools of six caudal fins for each genotype). dpa: days post amputation.

The improved bone regeneration following 4-PBA treatment is not affecting bone cell markers expression

Both *Chi/+* and *p3h1*$^{-/-}$ OI models are characterized by overglycosylated collagen I, which is retained in the ER (Gioia et al. 2017, Tonelli et al. 2020b). The consequent cellular stress therefore represents a possible target for OI therapy.

We previously demonstrated the positive effect of 4-phenylbutyrate (4-PBA) as a chemical chaperone able to improve bone mineralization in *Chi/+* larvae (Gioia et al. 2017). Here, we tested 4-PBA effect on adult *Chi/+* and *p3h1*$^{-/-}$ during caudal fin regeneration to investigate its potential treatment effect on bone formation and gene expression of bone cell-related genes.

The effect of 4-PBA administration on bone regeneration was evaluated on 3 and 8 mpf WT, *Chi/+* and *p3h1*$^{-/-}$ at 7 and 14 dpa by measuring REG and EMA parameters as described above.

4-PBA administration did not show any effect on the regeneration capacity of *Chi/+* fish at any ages and time point analyzed (**Figure 13)**. In 3 mpf at 14 dpa 4-PBA rescued *p3h1*$^{-/-}$ REG that reached WT value, whereas *p3h1*$^{-/-}$ EMA remained significantly less than untreated WT.

Interestingly, 4-PBA treatment on 8 mpf rescued in *p3h1*$^{-/-}$ the delay in bone formation respect to controls at both 7 and 14 dpa. REG and EMA of *p3h1*$^{-/-}$ treated fish reached WT value at 14 dpa. (**Figure 13**).

The effect of 4-PBA treatment on the expression of the early (*runx2a*, *runx2b*, *sox9a*, *sox9b*, *sp7*) and late (*bglap)* osteoblasts markers and on the *acp5a* osteoclast marker was also evaluated on 3 and 5 dpa *Chi/+* and *p3h1*$^{-/-}$ caudal fins. No difference was detected for all these genes for all genotypes and times analyzed (**Figures 14-15**).

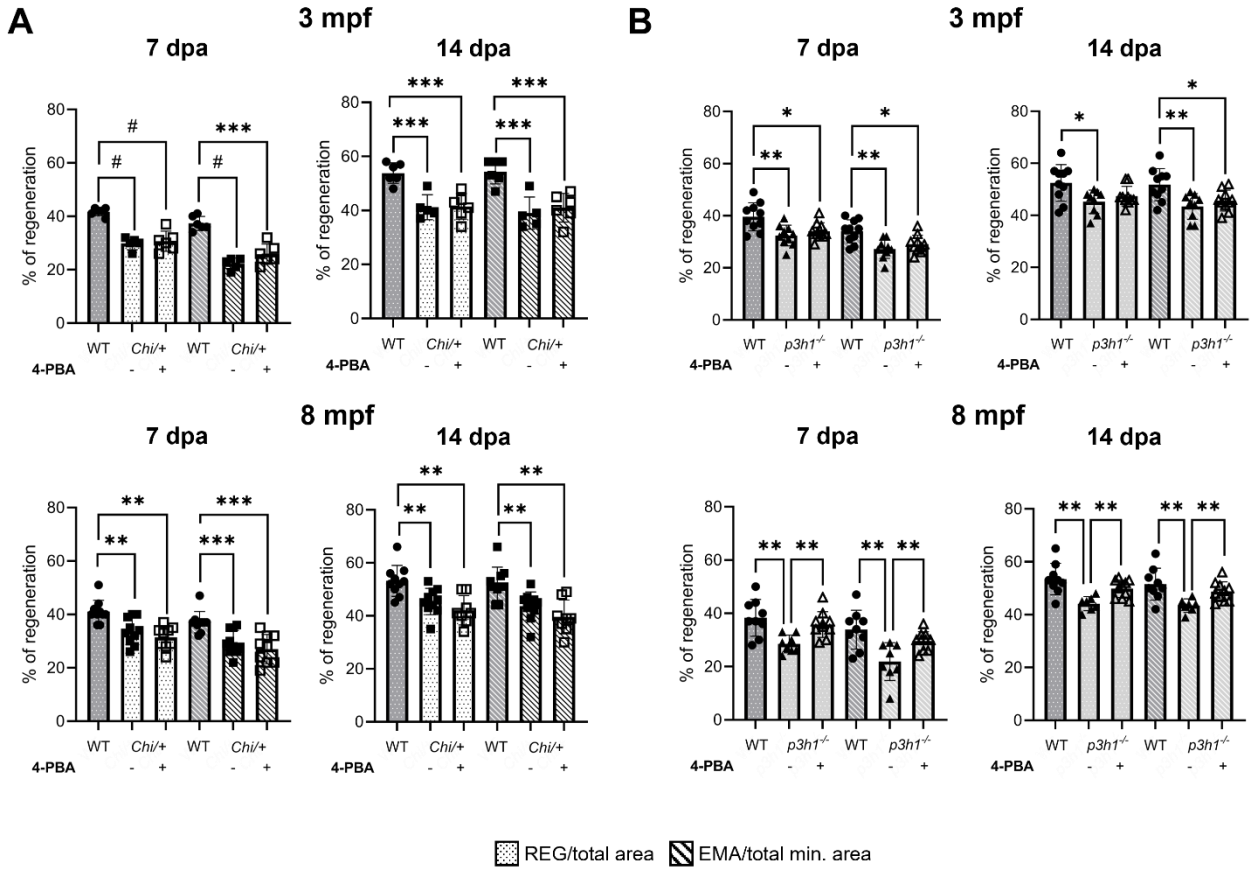

Figure 13. 4-PBA administration significantly improves caudal fin regeneration only in *p3h1*$^{-/-}$. (A) Caudal fin regeneration of WT and *Chi*/+ siblings. *Chi*/+ fish at 3 and 8 mpf exhibited a significantly reduced caudal fin regeneration compared to WT both at 7 and 14 dpa. 4-PBA treatment did not improve either REG or EMA between controls and treated fish at all age and time points analyzed (3 mpf: WT n = 6, *Chi*/+ controls n = 5, treated *Chi*/+ n = 6; 8 mpf: WT n = 10, *Chi*/+ controls n = 10, treated *Chi*/+ n = 8). **(B)** Caudal fin regeneration of WT and *p3h1*$^{-/-}$ siblings. *p3h1*$^{-/-}$ mutants at 3 and 8 mpf showed a significantly reduced caudal fin regeneration compared to WT. 4-PBA administration significantly increased REG and EMA parameters in 8 mpf treated respect to controls, reaching WT value (3 mpf: WT n = 10, *p3h1*$^{-/-}$ controls n ≥ 9, treated *p3h1*$^{-/-}$ n = 10; 8 mpf: WT n = 9, *p3h1*$^{-/-}$ controls n ≥ 7, treated *p3h1*$^{-/-}$ n = 10). dpa: days post amputation; mpf: months post fertilization; REG: Regenerated area; EMA: Estimated mineralized area. * $P < 0.05$, ** $P < 0.01$, *** $P < 0.001$, # $P < 0.0001$.

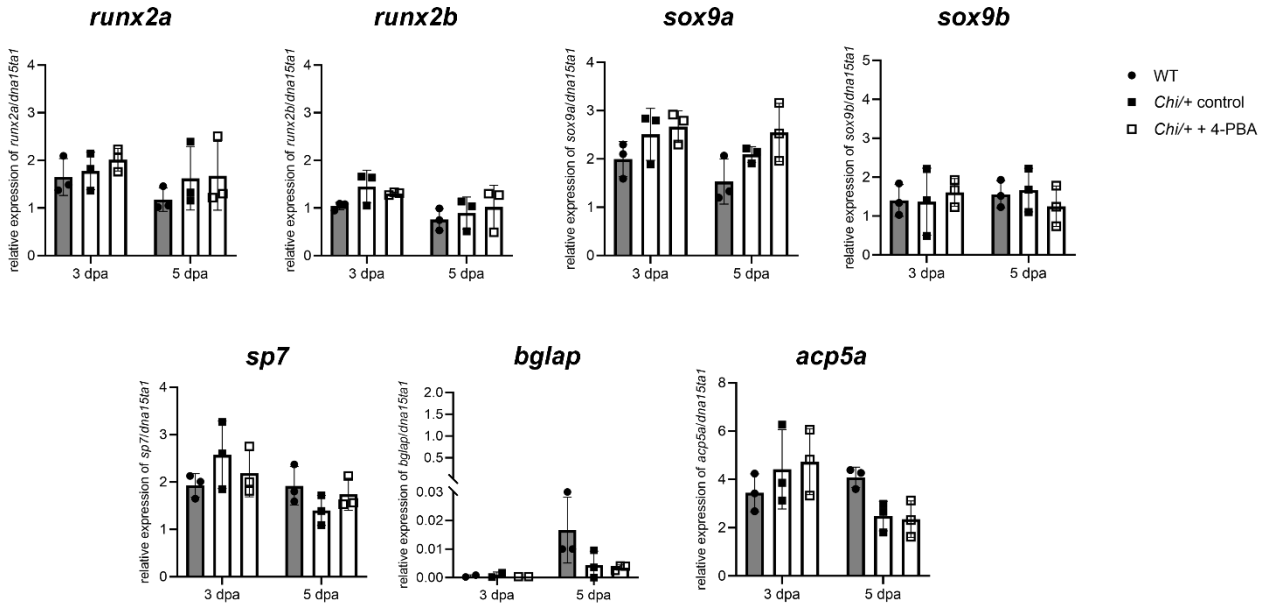

Figure 14. 4-PBA administration does not affect the expression of bone-related markers in *Chi/+*. qPCR analysis of early and late osteoblast and osteoclast markers did not show changes after 4-PBA administration at 3 and 5 dpa. n = 3 pools of six caudal fins for each genotype. dpa: days post amputation.

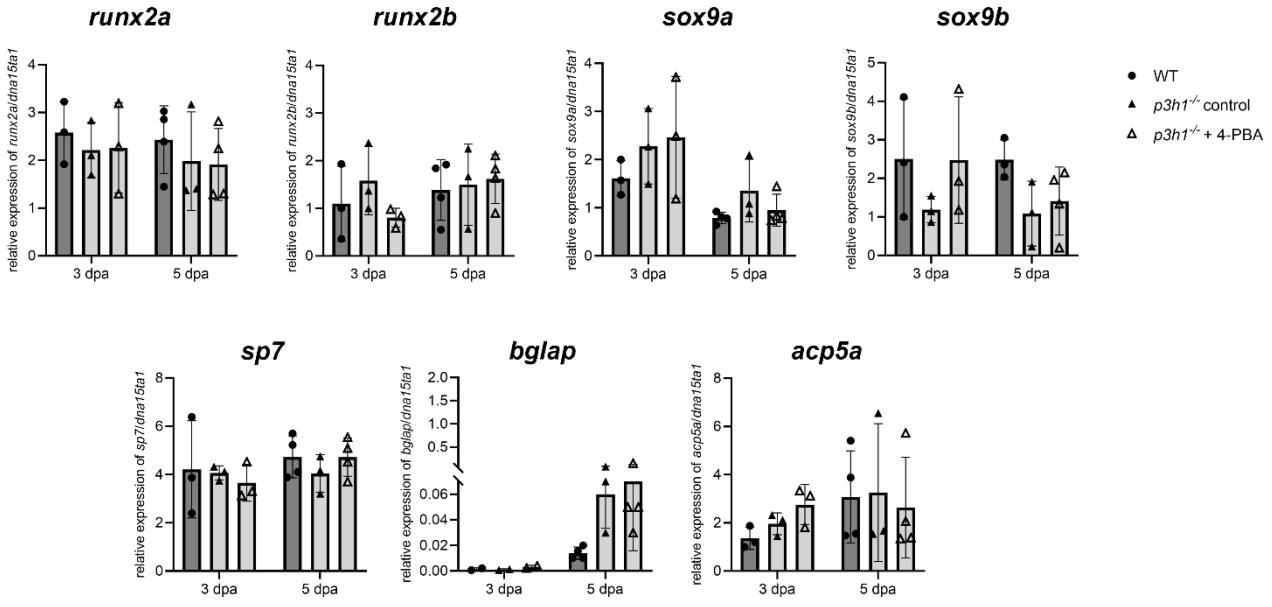

Figure 15. 4-PBA administration does not affect the expression of bone-related markers in *p3h1*$^{-/-}$. qPCR analysis of early and late osteoblast and osteoclast markers did not show changes after 4-PBA administration at 3 and 5 dpa. n ≥ 3 pools of six caudal fins for each genotype. dpa: days post amputation.

Discussion

This study shows for the first time the application of zebrafish caudal fin regeneration analysis to deeply investigate bone cell differentiation and activity in two different zebrafish models of OI. Here we demonstrate how altered cellular homeostasis as a consequence of misfolded and partially intracellular retained structural proteins, is a cause of impaired bone formation in OI. Despite causing a similar skeletal phenotype, mutations occurring directly on collagen type I have different outcome on a cellular and molecular level respect to recessive mutations affecting protein involved in collagen type I post translational modification.

Dominant and recessive OI mutations negatively affect caudal fin regeneration in zebrafish

A typical phenotype shared by patients affected by different OI forms is the delay in bone formation, as represented by their short stature (Forlino and Marini 2016). Indeed, the medium height is strongly reduced in OI type III (Jain et al. 2019) as well as in OI type VIII patients (Fratzl-Zelman et al. 2016a) and murine models (Vranka et al. 2010).
An easy and quick method to investigate bone formation over time is the regeneration ability of the zebrafish caudal fin after amputation, since it is mainly composed by bony rays and soft tissue (Poss, Keating and Nechiporuk 2003). The caudal fin regeneration ability of dominant *Chi/+* and recessive *p3h1*$^{-/-}$ OI models was evaluated after 7 and 14 days post amputation (dpa) in both young and adult fish and an impairment in bone formation was detected at both ages with respect to WT, confirming the delay in bone formation also in the zebrafish models of OI.

Caudal fin morphometry is differentially affected depending on the type of OI mutation

The detailed investigation of caudal fin morphometry demonstrated several impairments in fin ray morphology in *Chi/+* and *p3h1*$^{-/-}$. Normally, the bony caudal fin is constituted by 16-18 fin rays which are segmented and eventually bifurcate (Pfefferli and Jaźwińska 2015). Our results highlighted a reduced number of fin rays in the caudal fin of *p3h1*$^{-/-}$ fish compared to both WT and *Chi/+* (14.40 ± 1.14, $p < 0.01$). It is tempting to speculate that the defect in the number of the rays specific of this model could be a consequence of a defect in the cartilaginous plates supporting the fin rays, strengthening the already known role of P3h1 protein on cartilage structures. Indeed, fin rays derive from endochondral hypurals located at the end of the fish body. During zebrafish larval development, epiphyseal growth zones localized at the distal end of each hypural provide support for unidirectional formation of the mineralized fin rays (Desvignes, Carey and Postlethwait 2018). Two cartilaginous plates constituted by hyaline-cell cartilage containing elastin fibers, cover the distal ends of hypurals

to support the rays (Witten, Huysseune and Hall 2010, Bensimon-Brito et al. 2012). Interestingly, the *crtap* and the *p3h1* knock out murine models show growth plate disorganization and cartilage abnormalities as a consequence of lack of 3-hydroxylation of collagen type II (Morello et al. 2006, Vranka et al. 2010). Furthermore, we previously demonstrated a thickening of the notochord sheath, with disorganized collagen type II interspersed in the matrix in the *p3h1*$^{-/-}$ fish (Tonelli et al. 2020b). We observed an increase in the number of segments with reduced length in the day 0 caudal fin of *p3h1*$^{-/-}$. At the same time-point, *p3h1*$^{-/-}$ showed an increased number of bifurcations per ray. Since it is known that the most distal segments are generally shorter than the proximal ones (Haas 1962), and indeed we observed shorter segments in the regions above the bifurcations in *p3h1*$^{-/-}$ (data not shown), we can hypothesize that the increased number of bifurcations in this mutant creates more regions of distality resulting in overall increased number of shorter segments respect to WT.
The reduced length of segments at day 0 and throughout regeneration in *Chi/+* is probably related to the collagen defect in this model. It was previously demonstrated how collagen mutations impact collagen-rich structures such as the fin rays. For instance, the zebrafish *prp* mutation in Collagen IX results in wavy and fused fin rays due to altered osteoblast localization (Huang et al. 2009), a phenotype shared with *Chi/+*. *Chi/+* regenerating caudal fin fails to synthesize the actinotrichia, structures composed of Collagen I and II and localized at the distal extremity of the fin rays (Durán et al. 2011). A morphogenetic role for actinotrichia in driving correct fin ray morphogenesis has been already proposed (Santamaría and Becerra 1991). Our current results strengthen this interpretation, by linking the collagen and the actinotrichia defects to impaired fin ray segmentation.

In the 14 dpa regenerate of *p3h1*$^{-/-}$ we detected a reduced number of segments. During development and regeneration, fin rays grow by sequential addition of segments to their distal end (Haas 1962). We speculate that the reduced bone formation in this model results in the addition of less segments respect to WT. In *Chi/+* reduced bone formation did not result in reduced number of segments probably due to the fact that they are already shorter.

Dominant OI mutation has a severe impact on osteoblast differentiation during caudal fin regeneration

An impairment in osteoblast differentiation was reported both in OI patients as well as in murine models. Paediatric OI type III and IV are characterized by increased number of osteoblasts producing a smaller amount of matrix, indicative of altered differentiation or functionality of these cells (Rauch et al. 2000). In the *Oim* mouse, model for OI type III, a block of osteogenic differentiation before the terminal stage of mature osteoblasts was observed by the significantly lower expression of *bglap* in

mutants compared to WT (Li et al. 2010). The reduced *bglap* expression was also described for the *Amish* mouse, carrying a G610C substitution in α2(I) chain (Mirigian et al. 2016). The *Brtl* mouse, characterized by a G349C substitution in α1(I) chain, showed reduced expression of early and late osteoblastogenic markers *in vitro* (Gioia et al. 2012).

Up to date, most of the data on osteoblasts differentiation in OI refer to *in vitro* experiments, here the use of zebrafish allowed to add to *in vitro* also *in vivo* data. Indeed, during regeneration, caudal fin bone cells undergo a precise sequence of differentiation steps, with *sox9* inducing mesenchymal condensation, *runx2*+ osteoblast progenitors starting to accumulate until 3 dpa, then followed by *sp7*+ committed osteoblasts and finally by *bglap*+ fully differentiated osteoblasts (Knopf et al. 2011). This sequence of events, being also present in mammals, allows to evaluate bone cell differentiation in healthy and pathological conditions using caudal fin regeneration in zebrafish models. In both *Chi/*+ and *p3h1*$^{-/-}$ respect to WT, no differences were detected in *runx2* and *sox9* transcript expression before and during regeneration, indicating that the early differentiation steps before osteoblast commitment are not affected in OI.

In basal conditions, while no difference in *sp7* expression was found, a reduced *bglap* expression was detected in *Chi/*+ compared to WT, similarly to what described for dominant OI patients and murine models (Li et al. 2010, Gioia et al. 2012, Mirigian et al. 2016). During regeneration, the fluorescence intensity of *sp7*+ cells was increased in *Chi/*+ respect to WT at 3 dpa, and this value was still higher at 5 dpa ($p = 0.08$), a time-point in which osteoblasts should have started to become mostly mature. Also, the intensity of *bglap*+ cells was increased in *Chi/*+ respect to WT at 5 dpa, but the distribution analysis showed how most of these cells were "stuck" at the level of the amputation site. These results clearly indicate a delay in osteoblast maturation and migration to the site of future fin rays, where bone formation is required.

No differences were observed neither at the transcript nor at the protein level in osteoblast differentiation and distribution in *p3h1*$^{-/-}$fish, indicating a different impact of dominant and recessive OI mutations on bone molecular and cellular components.

Delayed osteoblastogenesis results in adipocytic switch in zebrafish

Mesenchymal stem cells (MSCs) are a heterogeneous group of cells that can give rise to osteoblast, adipogenic and chondrogenic lineages. Multiple evidence highlighted how delayed osteoblast differentiation in dominant OI patients was linked to increased plasticity towards the adipocytic lineage. Indeed, the expression of adipocytic markers such as peroxisome proliferator activated receptor gamma (PPARγ), the primary regulator of adipogenesis, was found to be increased during

MSCs differentiation in OI (Kaneto et al. 2017). Furthermore, Oil Red O staining on MSCs from the *Brtl* mouse, a dominant OI model characterized by impaired osteoblastogenesis, showed increased adipogenic colony-forming units, more adipocytes per colony and increased number and size of lipid drops per cell (Gioia et al. 2012).

The transparent zebrafish caudal fin provides a unique opportunity to investigate adipogenesis *in vivo* in OI. The main adipogenic pathways are conserved in zebrafish, and so the cellular origin, with caudal fin (appendicular) adipocytes having a mesodermal origin (Imrie and Sadler 2010). Perivascular-derived MSCs from the zebrafish caudal fin show both osteogenic and adipogenic potential (Lund et al. 2014); however, the presence of adipocytes has been described only at the caudal fin base, with few or no adipocytes in the most-distal extremity of the fin (Imrie and Sadler 2010). Here we demonstrate that the zebrafish *Chi/+*, characterized by delayed osteoblast differentiation and reduced levels of the marker *bglap*, shows a significant increased number of lipid drops at the tip of the caudal fin. Vice versa, the recessive OI model *p3h1*$^{-/-}$, which shows normal bone cell differentiation, does not show abnormal adipocyte production. These results, that for the first time evidence the presence of an adipocytic switch in a zebrafish OI model, strengthen the correlation between impaired osteoblastogenesis and increased adipogenesis *in vivo*, supporting this feature as a characteristic of dominant OI.

Osteoclasts fail to differentiate in the regenerating caudal fin of zebrafish OI models

Bone resorption is a fundamental process during bone growth and fracture healing. The high bone turnover due to excessive bone resorption is one of the key features of OI pathology (Marini et al. 2017).

Bone histomorphometry from patients with classical OI shows a high level of remodeling associated to increased number of osteoclasts (Rauch et al. 2000). The *Brtl* mouse displays increased osteoclast surface, and increased number of TRAP+ cells in the long bones throughout life associated to high bone turnover (Uveges et al. 2008). An increased resorption activity was also reported in OI type VIII patients, who showed increased levels tartrate-resistant acid phosphatase (TRACP-5b) in the serum, even with normal number of osteoclasts and bone formation markers comparable to controls (Fratzl-Zelman et al. 2016a). *P3h1* null mice do not have high bone turnover and both osteoblast and osteoclast surfaces appear normal (Fratzl-Zelman et al. 2016b). Also, the low bone mass observed in the OI type VII murine model *Crtap*$^{-/-}$, which is phenotypically and biochemically similar to the *P3h1* null mice, is not linked to an osteoclast increase since osteoclast number and function were normal *in vivo* and *ex vivo* (Morello et al. 2006).

Zebrafish and mammal bones are subjected to bone resorption thanks to the presence of osteoclasts and the same osteoclastogenic markers are conserved between teleosts and mammals (Witten and Huysseune 2009). Osteoclasts are involved in caudal fin regeneration, indeed after 5-6 dpa they can be seen accumulating at the level of the amputation plane as well as along the regenerating fin rays (Blum and Begemann 2015).

Osteoblasts and osteoclasts activity in bone is tightly coupled and mutations causative of OI are frequently associated to an imbalance between bone formation and bone resorption. In particular, the accumulation of immature osteoblasts leads to a change in the bone cellular microenvironment, enhancing osteoclasts differentiation and activity (Uveges et al. 2008). At day 0 in the dominant OI model *Chi/+*, the increase in *sp7+* immature osteoblasts failing to express *bglap* is associated to an increased number of TRAP+ cells respect to WT, suggesting that impaired osteoblasts maturation may induce an increase in bone turnover similar to what observed in patients and murine models (Rauch et al. 2000, Uveges et al. 2008). Nevertheless, it must be considered that the fragile *Chi/+* caudal fins are more prone to fractures, which could partially explain the increase in bone resorption. The level of TRAP+ cells was normal in *p3h1*$^{-/-}$ caudal fin at day 0.

During regeneration, interestingly the number of TRAP+ cells was found to be significantly less expressed at 5 dpa both in *Chi/+* and *p3h1*$^{-/-}$ respect to WT. This result, confirmed also by qPCR analysis in the case of *Chi/+*, was surprising, since to our knowledge this is the first time in which decreased osteoclast activity is described during bone formation in OI. Nevertheless, we should be careful in interpreting these data since bone formation of the dermal caudal fin does not fully recapitulate the formation of the endoskeleton, and the role of osteoclasts in caudal fin regeneration has been still poorly explored.

Of interest, a reduced TRAP signal at the amputation plane was evident in *p3h1*$^{-/-}$ compared to WT fish. We recently described an increased TRAP staining signal at the level of the amputation plane, linked to an increased expression of the macrophage precursor marker *mpeg1* in the regenerating caudal fin of the zebrafish mutant for OI type XIV *tmem38b*$^{\Delta 120\text{-}7/\Delta 120\text{-}7}$, indicating the recruitment of precursors that failed to differentiate (Tonelli, Leoni, Daponte et al. 2023). In our case, the low signal at the amputation plane may indicate a compromised recruitment and migration to the remodeling site.

It tempting to speculate that the lack of 3-hydroxylation of extracellular matrix components resulting in altered extracellular matrix composition may impair the release or diffusion of specific inflammatory cytokines, but further studies are needed to clarify this event.

Differentiation and activity of osteoclasts are regulated through the expression of Rankl and Opg by osteoblasts. Increased Rankl/Opg ratio in *Oim* osteoblasts underlined enhanced osteoclastogenesis (Li et al. 2010) as also reported in children affected by classical OI (Brunetti et al. 2016). However, in the *Brtl* mouse model, Rankl/Opg ratio was reported to be normal (Uveges et al. 2008). We did not detect any variation in the levels of Rankl and Opg alone nor in the Rankl/Opg ratio in our OI fish, indicating that the impaired osteoclastogenesis found in the two models is not directly linked to Rankl stimulation.

Recently, it was demonstrated that caudal fin ray bifurcation depends on a fine-tuned balance between bone formation and bone resorption, in which TRAP+ osteoclasts play a role in defining branchpoint position (Cardeira-da-Silva et al. 2022). Our morphometry results indicate that *p3h1*$^{-/-}$ ray bifurcate early in time respect to WT. Indeed, most of the bifurcations were already present at 7 dpa in *p3h1*$^{-/-}$, whereas WT reached the same number later at 14 dpa. This data, together with the TRAP staining results, may indicate that osteoclast precursors fail to arrive at the remodeling site by 5 dpa, arriving late at 7 dpa thus leading to a "boost" in osteoclasts recruitment resulting in premature fin ray branching.

Impaired caudal fin morphology results in defective swimming ability and matrix alterations in dominant OI

The observation of a weird *Chi/+* movement in the fish tanks, together with the impairment in caudal fin morphology, lead us to deeper investigate the swimming behavior in these fish. Of note, it must be considered that *Chi/+* fish are shorter that their WT siblings as part of their phenotype.

The analysis revealed that *Chi/+* fish tend to swim for shorter paths and with erratic movements respect to WT, confirming a correlation between defective caudal fin morphology and movement.

Since we reasoned that this correlation could be in part due to an altered extracellular matrix, we investigated collagen I and the closely related collagens XII and XIV, involved in collagen I fibrillogenesis as members of the FACITs group (Ricard-Blum 2011). Collagens XII and XIV interact with fibrillar collagen I both directly via their collagenous domains and indirectly by establishing complexes with decorin and cartilage oligomeric matrix protein (COMP) (Font et al. 1993, Koch et al. 1995, Agarwal et al. 2012, Chiquet et al. 2014).

Collagen type I was found to be deposited in a disorganized manner along all the caudal fin in both *Chi/+* and *p3h1*$^{-/-}$, in some cases with the formation of aggregates typical of misfolded proteins, an expected result as a consequence of OI phenotype.

For the first time, we describe specific localization of collagen type XIV in the joints of the zebrafish caudal fin. This could be coherent with the fact that collagen XIV mainly localizes in dense connective tissues, such as tendons (Castagnola et al. 1992). Collagen XIV is transiently expressed during early stages of development, as demonstrated in mouse tendons but also in zebrafish epithelium (Ansorge et al. 2009, Bader et al. 2013). It was also reported that collagen XIV is expressed in a short time frame by highly proliferative epithelial cells during caudal fin regeneration (Nauroy et al. 2019). We found collagen XII to be widely and ordinately distributed along the caudal fin and inside the fin ray segments and joints. Collagen XII is more widely and constantly expressed during development, maturation and aging in most connective tissues (Kato et al. 2000, Bader et al. 2009, Izu et al. 2021). Collagen XII may replace collagen XIV during development or regeneration, as others already suggested (Ansorge et al. 2009), explaining its spreader localization inside the caudal fin.

We found an impaired joint structure in *Chi/+*, with disorganized collagen I fibrils associated to an increase in collagen XIV amount which overall resulted in an increased inter-joint space before and during regeneration. No abnormalities were on the contrary detected in *p3h1*$^{-/-}$ fish.

The unexpected lack of *col12a1b* expression in WT regenerates could be explained by its late transcript expression (Bader et al. 2013). However, its expression only in mutants could not be investigated by immunofluorescence due to both its wider localization, preventing an accurate quantification, and to unclear specificity of our antibody (Bader et al. 2013).

Further studies will be required to clarify the role of the two FACITs in the caudal fin, their timely activation and their specific localization.

4-PBA treatment demonstrates a beneficial effect on caudal fin regeneration only in recessive OI

OI mutations are frequently associated to a delay in collagen type I chains folding and to extensive exposure to post-translational modifications such as hydroxylation and glycosylation.

Collagen type I overmodification was demonstrated in *Chi/+* and *p3h1*$^{-/-}$ by slower migration of α(I) bands. *P3h1*$^{-/-}$ fish also show increased level of lysine and proline residues hydroxylation in collagen type I extracted from bone and skin. Both models are characterized by enlarged ER cisternae size and consequent cell stress (Gioia et al. 2017, Tonelli et al. 2020b).

Nowadays no cure is available for OI and new treatments to ameliorate quality of life of patients are urgently needed. Drug repositioning allows to test already FDA approved drugs on different diseases.

Among these, 4-phenylbutyrate (4-PBA), an ammonia scavenger for the treatment of urea cycle disorders, has recently become more and more of interest in the OI field due to its chemical chaperone activity. Indeed, it was recently demonstrated that *in vitro* 4-PBA ameliorates OI cell homeostasis by reducing unfolded protein response, activating autophagy and reducing apoptosis both in dominant and recessive forms of the disease, both in primary fibroblasts and osteoblasts (Besio et al. 2018, Besio et al. 2019, Garibaldi et al. 2021). Furthermore, 4-PBA showed positive effect on the zebrafish *Chi/+*, both at embryonic and adult stage by improving mineralization and collagen secretion (Gioia et al. 2017).

In this study we demonstrated that treating *p3h1*$^{-/-}$ with 4-PBA significantly increases bone growth during caudal fin regeneration both at 7 and 14 dpa as demonstrated by the rescue of REG and EMA parameters, with a significant effect only on 8 mpf adult fish. Interestingly, despite no effect of aging on caudal fin regeneration ability was observed in the current study, we previously showed that *p3h1*$^{-/-}$ zebrafish phenotype generally worsens with age, with increased number of fractures in the ribs and vertebral compressions in adult fish (Tonelli et al. 2020b). This may support the accentuated effect of 4-PBA in older fish which have a more compromised phenotype and thus can benefit more from the drug administration.

On the contrary and unexpectedly, no effect on bone formation was detected on 4-PBA treated *Chi/+* at both 3 and 8 mpf. In a previous study on adult *Chi/+*, we observed a positive effect of the drug in stimulating collagen secretion in the matrix during caudal fin regrowth (Gioia et al. 2017). Our present results suggest that the increase in extracellular matrix mutant collagen *in vivo* may not be enough to ameliorate bone formation. Nevertheless, also *p3h1*$^{-/-}$ collagen type I has an altered structure, thus the question on why in the two models the effect of 4-PBA is different is quite intriguing. Although we do not have a final answer, we reasoned on two hypotheses. First, in *Chi/+* the mutant collagen consist of a mix of molecules with one or two mutant chains and this heterogeneity has been associated to dishomogeneous mineral matrix distribution (Panaroni et al. 2009). Interestingly *Brtl*$^{-/-}$ mice, homozygous for α1(I)-G349C substitution and thus containing only mutant collagen have a milder or near normal phenotype compared to the moderate outcome of *Brtl*$^{+/-}$ heterozygous animals, supporting the importance of matrix composition (Reich, Cabral and Marini 2012). Indeed, the composition of ECM differs between heterozygous and homozygous mice, in the latter all α1 chains are mutant while heterozygous mice have matrix heterogeneity, with homodimers in 25% of collagen, one mutant chain in 50% of collagen, and no mutant chains in 25% of collagen.

In *p3h1*$^{-/-}$ zebrafish, all collagen I molecules are equally overmodified, producing a homogeneous ECM.

A second hypothesis to explain the detectable positive 4-PBA effect on caudal fin regeneration only in *p3h1*$^{-/-}$ and not in *Chi*/+ is the reduced amount in the latter of mature osteoblasts, which are the target cells of 4-PBA during bone regrowth. It is possible that the amount of secreted collagen upon chaperone administration is not enough in *Chi*/+ to improve bone formation.

We cannot anyway exclude a mutation specific effect of 4-PBA *in vivo* as already suggested from *in vitro* studies on OI patients' fibroblasts (Besio et al. 2018).

4-PBA administration indeed improves the bone phenotype *in vivo* in the dominant OI murine models *Aga2* $^{+/-}$, characterized by mutation in collagen type I C-propeptide resulting in a structural defect (Duran et al. 2022), and *Amish* (Scheiber et al. 2022), but its effect on the *Brtl* mouse which has the same kind of mutation as *Chi*/+ is still uncertain. It would be interesting to validate 4-PBA goodness also in murine models with recessive mutations of the disease.

Finally, 4-PBA effect may be dependent on the type of ossification. In fact, despite improved mineralization was proved in several cranial bones in *Chi*/+ larvae, no effect was detected in the cleithrum, which has a dermal origin as the caudal fin (Gioia et al. 2017).

No effects of 4PBA were detected on gene expression analysis on osteoblastogenic and osteoclastogenic markers in both *Chi*/+ and *p3h1*$^{-/-}$, suggesting that the positive effect of 4-PBA on cellular homeostasis is not due to its known histone deacetylase inhibitor activity (Shi et al. 2020) and does not affect the expression of genes involved in cell differentiation. These findings further support the role of 4-PBA as molecular chaperone in ameliorating OI bone phenotype (Garibaldi et al. 2021, Gioia et al. 2017).

Conclusions

In this study we investigated bone morphology, bone cellular and molecular patterning, and matrix assembly in two zebrafish models of OI using the caudal fin as a tool. For the first time we provide a direct experimental comparison between two models of the disease with different molecular defects: *Chi*/+, characterized by a collagen defect resulting in dominant OI, and *p3h1*$^{-/-}$, affected by an enzymatic defect leading to recessive OI.

We demonstrated that caudal fin regeneration is similarly impaired in both dominant and recessive OI. Nevertheless, only the primary defect in collagen type I has a negative effect on osteoblasts

differentiation that results in a switch towards the adipocytic lineage, already reported *in vitro* for dominant OI, but never before *in vivo*.

An osteoclast impairment during caudal fin regeneration that recapitulates bone formation in zebrafish is reported for the first time in both dominant and recessive OI zebrafish models independently from the Rankl/Opg axis.

The administration of the chemical chaperone 4-PBA rescues caudal fin regeneration in *p3h1*$^{-/-}$, demonstrating for the first time its beneficial effect on recessive OI *in vivo*.

Supplementary Materials and Methods

Supplementary Table 1. List of fish lines used in the study.

Fish line name	Generation	ZFIN Genomic Feature	ZFIN ID	Reference
WT (AB)	crossing	/	ZDB-GENO-960809-7	https://www.ezrc.kit.edu/
Chi/+	ENU	dc124	ZDB-FISH-150901-25831	(Fisher et al. 2003)
p3h1$^{-/-}$	CRISPR/Cas9	upv2	ZDB-FISH-220209-4	(Tonelli et al. 2020b)
WT; *sp7*:GFP	transgenic insertion	zf132Tg	ZDB-FISH-150901-29406	(Spoorendonk et al. 2008)
Chi/+; *sp7*:GFP	crossing	/	/	/
p3h1$^{-/-}$; *sp7*:GFP	crossing	/	/	/
WT; *bglap*:GFP	transgenic insertion	hu4008Tg	ZDB-FISH-150901-7671	(Vanoevelen et al. 2011)
Chi/+; *bglap*:GFP	crossing	/	/	/
p3h1-/-; *bglap*:GFP	crossing	/	/	/

Supplementary Table 2. List of primers used for qPCR. The reference is indicated for primers taken from the literature.

Gene	Ensembl ID	Annealing temp.	Amplicon size	Sequence ('5→'3)	Ref
runx2a	ENSDARG00000040261	58 °C	144 bp	FW: TTGTTGGCAGAAGTGGAAGAGG RV: CCAGTTTCTGTCTGTGTCTTCG	
runx2b	ENSDARG00000059233	58 °C	139 bp	FW: ATACGACCAGACATACCCATCG RV: GTCTGTCGAACCTGGAAGACG	
sox9a	ENSDARG00000003293	60 °C	148 bp	FW: GTCCAGCATGGGAGAAGTGC RV: TCCGGTGTTTTCCTGAAGAGG	
sox9b	ENSDARG00000043923	60 °C	141 bp	FW: CAAAACACTCGGCAAACTCTGG RV: TTCACTGATTTCCTCCGTCTGG	
acp5a	ENSDARG00000019763	58 °C	117 bp	FW: GCCAAAACTGCTTCTCAGATGG RV: GACGTCTTCAAAGGTTTCCTGG	
sp7	ENSDARG00000019516	58 °C	132 bp	FW: TCCTCTCCCGCTTTTGGATT RV: TCCCGAATTTGTTGCAGGTC	(He et al. 2018)
bglap	ENSDARG00000058414	58 °C	102 bp	FW: CCTGATGACTGTGTGTCTGAG RV: CGCTTCACAAACACACCTTC	(Blum and Begemann 2015)
rankl	ENSDARG00000068141	58 °C	81 bp	FW: CTCACCTTCCAATCAAGACGCCC RV: CTTTCATGCCATCCCAGGCTATCT	
opg	ENSDARG00000098377	58 °C	169 bp	FW: GGGTCATTTCTCAGACGCCA RV: CGGGTCGAATACAGCAGTCC	
col1a1a	ENSDARG00000012405	60 °C	109 bp	FW: CTGCAAGAACAGCATTGCAT RV: TAGGCAGACGGGATGTTTTC	(Malbouyres et al. 2022)
col12a1a	ENSDARG00000078322	60 °C	218 bp	FW: AGGGCTCGTCTGTGTCTGAT RV: GTTTTGCAGGATGACCGAGT	(Malbouyres et al. 2022)
col12a1b	ENSDARG00000019601	60 °C	197 bp	FW: CTCCTCAGGACAAGGAGCAC RV: GCACCAGCTTTTCTCCAGAC	(Malbouyres et al. 2022)
col14a1a	ENSDARG00000005762	60 °C	196 bp	FW: TGCTCATTTCTGAGGTGACG RV: GCGAACACTGCAATCTCGTA	(Malbouyres et al. 2022)
col14a1b	ENSDARG00000076623	60 °C	189 bp	FW: GACCACGCTTCCTCTGACTC RV: AGGTTACGCAGCTCCACTGT	(Malbouyres et al. 2022)
dna15ta1	expressed repeat element (not in the database)	58 °C 60 °C	/	FW: TACTGTGCTCAAATTGCTTCA RV: AATGAGTACTGTGAACTTAATCCAT	(Vanhauwaert et al. 2014)

Supplementary Table 3. List of antibodies used for immunofluorescence experiments.

Antibody name	Reference	Type	Host species	Concentration
GFP	Invitrogen, 3E6	Primary, monoclonal	mouse	1:500
Collagen I	Abcam, ab23730	Primary, polyclonal	rabbit	1:100
Collagen I	Novotec, 20171T	Primary, polyclonal	rabbit	1:40
Collagen XII, affinity-purified	kindly provided by F. Ruggiero	Primary, polyclonal	rabbit	1:250
Collagen XIV, affinity-purified	kindly provided by F. Ruggiero	Primary, polyclonal	guinea pig	1:250
Anti-mouse IgG	Thermo Fisher Scientific, A-11030	Secondary, conjugated Alexa Fluor™ 546	goat	1:500
Anti-rabbit IgG	Thermo Fisher Scientific, 35562	Secondary, conjugated DyLight™ 633	goat	1:500
Anti-guinea pig IgG	Thermo Fisher Scientific, A-11076	Secondary, conjugated Alexa Fluor™ 594	goat	1:500

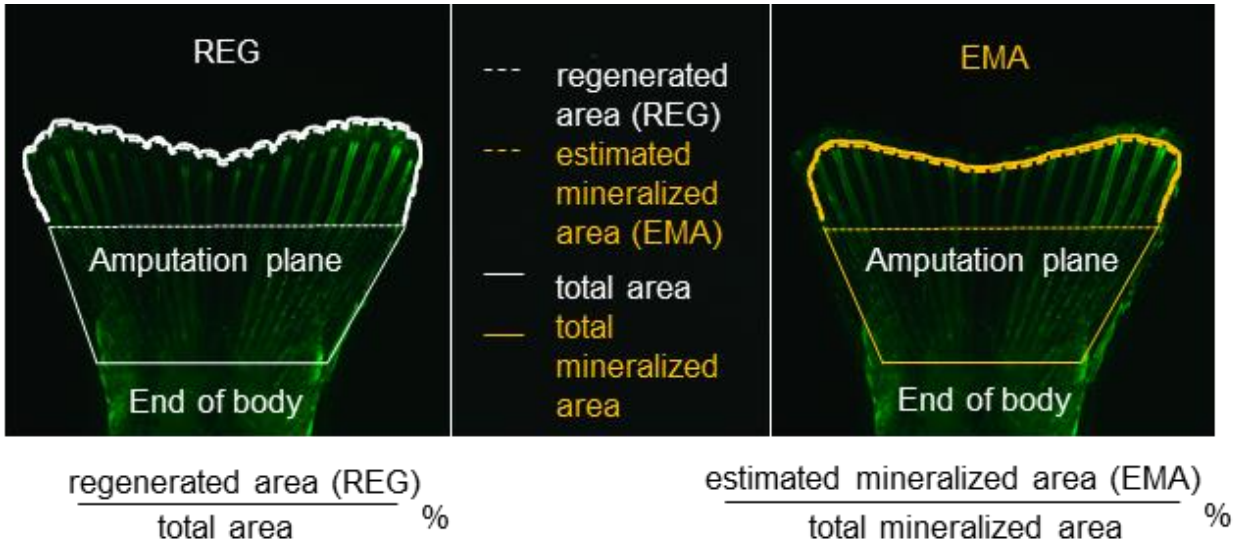

Supplementary Figure 1. Schematic representation of the two measurements performed to evaluate regenerated caudal fin area. On the left: percentage of Regenerated area (REG) is the ratio between the regenerated area, measured above the amputation plane including fin rays and mesenchymal tissue around (white dotted line), and the total area of the caudal fin (white line). On the right: percentage of Estimated mineralized area (EMA) is the ratio between the estimated mineralized area, measured above the amputation plane including only fin rays and inter-ray space (orange dotted line), and the total mineralized area of the caudal fin (orange line).

Supplementary Results

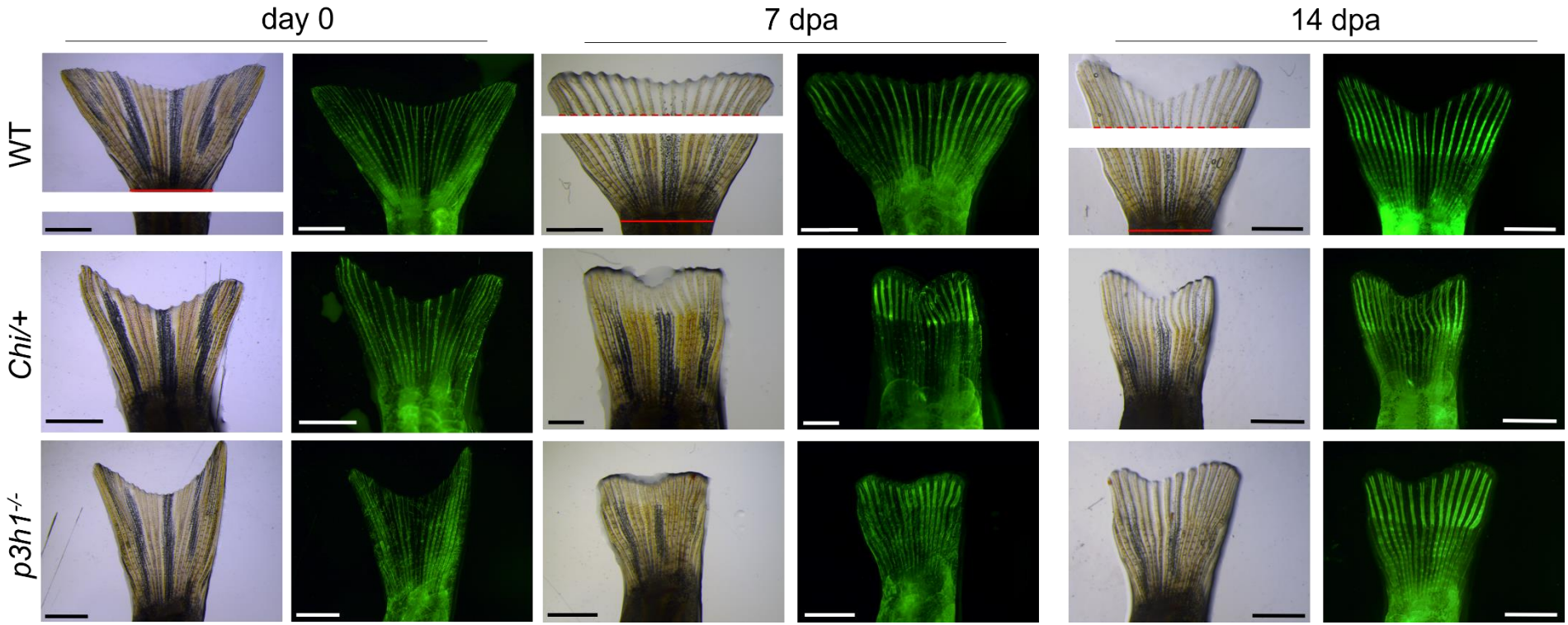

Supplementary Figure 2. Representative images of brightfield and calcein stained caudal fin of WT, *Chi/+* and *p3h1*$^{-/-}$ at day 0, 7 and 14 dpa used for morphometric measurements. Scale bar: 2 mm. The measurements at day 0 and the distance to bifurcation were taken starting from the caudal fin base, represented by the red continuous line. The measurements in the 7 and 14 days post amputation (dpa) regenerates were taken above the amputation plane, indicated by the red dashed line.

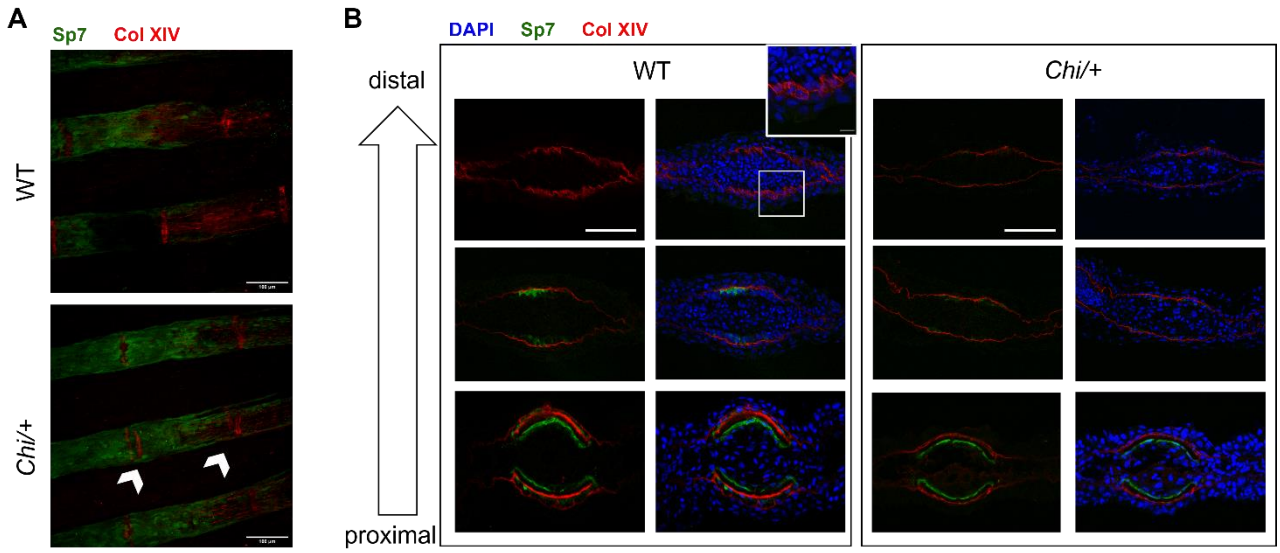

Supplementary Figure 3. Collagen XIV localization in the fin rays of WT and Chi/+ regenerating caudal fin at 5 dpa. (A) Representative image of collagen XIV immunofluorescence in WT and *Chi/+ sp7*:GFP caudal fins. Inter-joint space is increased in *Chi/+* in the regenerating ray, as shown by the arrowheads. Scale bar: 100 µm. **(B)** Immunofluorescence on consecutive transversal sections of regenerating caudal fins of WT and *Chi/+ sp7*:GFP reveals collagen XIV deposition externally to the hemi-rays, even when the osteoblasts are not present. No difference was found between genotypes. Scale bar: 50 µm; detail: 10 µm.

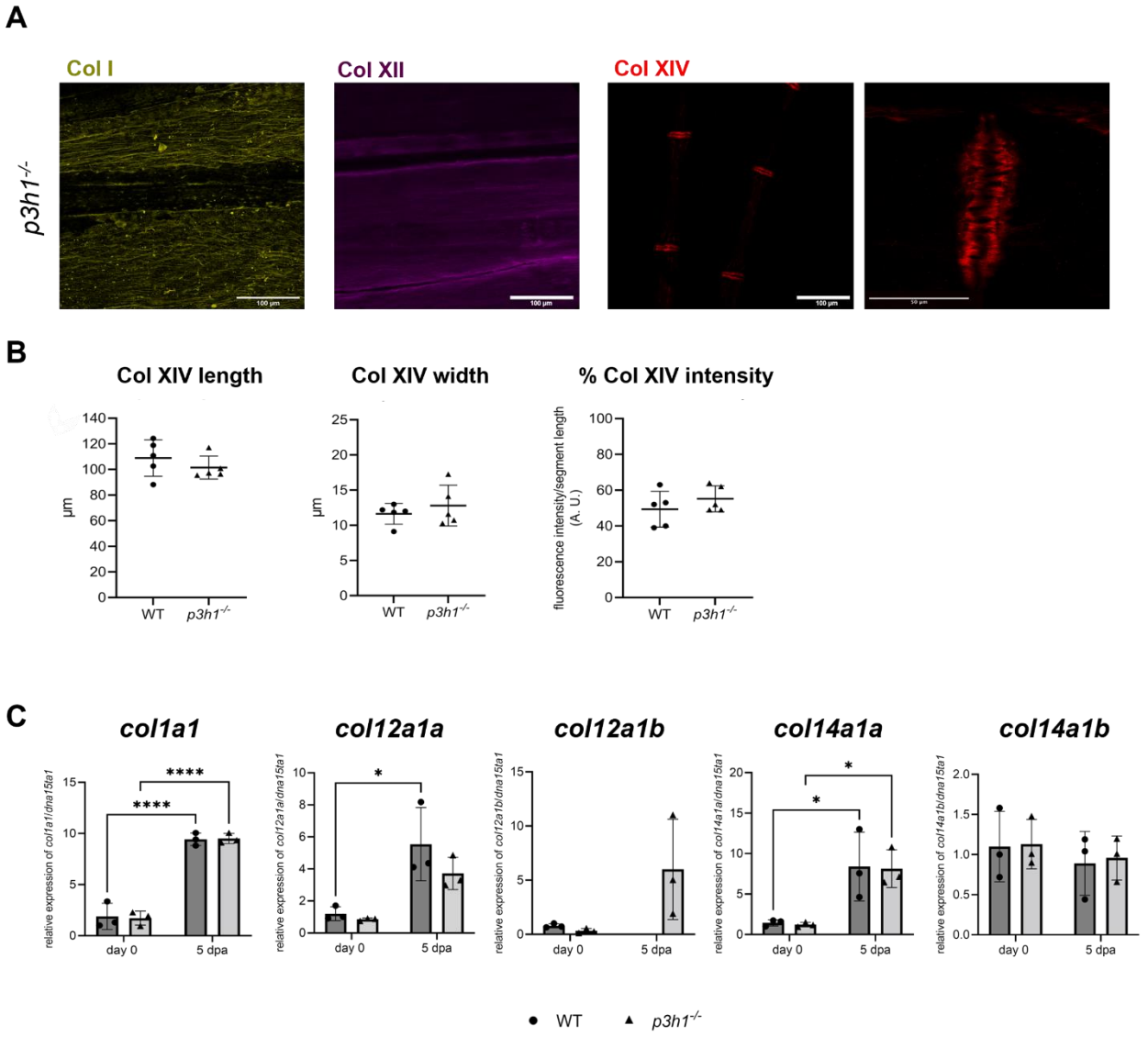

Supplementary Figure 4. Collagen analysis in the caudal fin of *p3h1*$^{-/-}$ fish. (A) Representative immunofluorescence of collagen I, XII and XIV in WT and *p3h1*$^{-/-}$caudal fin. Collagen I fibrils appear wavy and disorganized. Collagen XII and XIV present normal distribution. **(B)** Collagen XIV analysis does not show differences in *p3h1*$^{-/-}$ respect to WT (n = 5 for each genotype). **(C)** qPCR analysis of collagens does not show differences between the two genotypes (n = 3 pools of six caudal fins for each genotype). dpa: days post amputation. * $P < 0.05$, # $P < 0.0001$.

Manuscript 4 - References

Agarwal, P., D. Zwolanek, D. R. Keene, J. N. Schulz, K. Blumbach, D. Heinegård, F. Zaucke, M. Paulsson, T. Krieg, M. Koch & B. Eckes (2012) Collagen XII and XIV, new partners of cartilage oligomeric matrix protein in the skin extracellular matrix suprastructure. *J Biol Chem,* 287**,** 22549-59.

Anchelin, M., L. Murcia, F. Alcaraz-Pérez, E. M. García-Navarro & M. L. Cayuela (2011) Behaviour of telomere and telomerase during aging and regeneration in zebrafish. *PLoS One,* 6**,** e16955.

Ansorge, H. L., X. Meng, G. Zhang, G. Veit, M. Sun, J. F. Klement, D. P. Beason, L. J. Soslowsky, M. Koch & D. E. Birk (2009) Type XIV Collagen Regulates Fibrillogenesis: PREMATURE COLLAGEN FIBRIL GROWTH AND TISSUE DYSFUNCTION IN NULL MICE. *J Biol Chem,* 284**,** 8427-38.

Bader, H. L., D. R. Keene, B. Charvet, G. Veit, W. Driever, M. Koch & F. Ruggiero (2009) Zebrafish collagen XII is present in embryonic connective tissue sheaths (fascia) and basement membranes. *Matrix Biol,* 28**,** 32-43.

Bader, H. L., E. Lambert, A. Guiraud, M. Malbouyres, W. Driever, M. Koch & F. Ruggiero (2013) Zebrafish collagen XIV is transiently expressed in epithelia and is required for proper function of certain basement membranes. *J Biol Chem,* 288**,** 6777-87.

Bensimon-Brito, A., M. L. Cancela, A. Huysseune & P. E. Witten (2012) Vestiges, rudiments and fusion events: the zebrafish caudal fin endoskeleton in an evo-devo perspective. *Evol Dev,* 14**,** 116-27.

Besio, R., N. Garibaldi, L. Leoni, L. Cipolla, S. Sabbioneda, M. Biggiogera, M. Mottes, M. Aglan, G. A. Otaify, S. A. Temtamy, A. Rossi & A. Forlino (2019) Cellular stress due to impairment of collagen prolyl hydroxylation complex is rescued by the chaperone 4-phenylbutyrate. *Dis Model Mech,* 12.

Besio, R., G. Iula, N. Garibaldi, L. Cipolla, S. Sabbioneda, M. Biggiogera, J. C. Marini, A. Rossi & A. Forlino (2018) 4-PBA ameliorates cellular homeostasis in fibroblasts from osteogenesis imperfecta patients by enhancing autophagy and stimulating protein secretion. *Biochim Biophys Acta Mol Basis Dis,* 1864**,** 1642-1652.

Blum, N. & G. Begemann (2015) Osteoblast de- and redifferentiation are controlled by a dynamic response to retinoic acid during zebrafish fin regeneration. *Development,* 142**,** 2894-903.

Brunetti, G., F. Papadia, A. Tummolo, R. Fischetto, F. Nicastro, L. Piacente, A. Ventura, G. Mori, A. Oranger, I. Gigante, S. Colucci, M. Ciccarelli, M. Grano, L. Cavallo, M. Delvecchio & M. F. Faienza (2016) Impaired bone remodeling in children with osteogenesis imperfecta treated

and untreated with bisphosphonates: the role of DKK1, RANKL, and TNF-α. *Osteoporos Int,* 27**,** 2355-2365.

Cardeira, J., P. J. Gavaia, I. Fernández, I. F. Cengiz, J. Moreira-Silva, J. M. Oliveira, R. L. Reis, M. L. Cancela & V. Laizé (2016) Quantitative assessment of the regenerative and mineralogenic performances of the zebrafish caudal fin. *Sci Rep,* 6**,** 39191.

Cardeira-da-Silva, J., A. Bensimon-Brito, M. Tarasco, A. S. Brandão, J. T. Rosa, J. Borbinha, P. J. Almeida, A. Jacinto, M. L. Cancela, P. J. Gavaia, D. Y. R. Stainier & V. Laizé (2022) Fin ray branching is defined by $TRAP^{+}$ osteolytic tubules in zebrafish. *Proc Natl Acad Sci U S A,* 119**,** e2209231119.

Castagnola, P., S. Tavella, D. R. Gerecke, B. Dublet, M. K. Gordon, J. Seyer, R. Cancedda, M. van der Rest & B. R. Olsen (1992) Tissue-specific expression of type XIV collagen--a member of the FACIT class of collagens. *Eur J Cell Biol,* 59**,** 340-7.

Chiquet, M., D. E. Birk, C. G. Bönnemann & M. Koch (2014) Collagen XII: Protecting bone and muscle integrity by organizing collagen fibrils. *Int J Biochem Cell Biol,* 53**,** 51-4.

Desvignes, T., A. Carey & J. H. Postlethwait (2018) Evolution of caudal fin ray development and caudal fin hypural diastema complex in spotted gar, teleosts, and other neopterygian fishes. *Dev Dyn,* 247**,** 832-853.

Duran, I., J. Zieba, F. Csukasi, J. H. Martin, D. Wachtell, M. Barad, B. Dawson, B. Fafilek, C. M. Jacobsen, C. G. Ambrose, D. H. Cohn, P. Krejci, B. H. Lee & D. Krakow (2022) 4-PBA Treatment Improves Bone Phenotypes in the Aga2 Mouse Model of Osteogenesis Imperfecta. *J Bone Miner Res,* 37**,** 675-686.

Durán, I., M. Marí-Beffa, J. A. Santamaría, J. Becerra & L. Santos-Ruiz (2011) Actinotrichia collagens and their role in fin formation. *Dev Biol,* 354**,** 160-72.

Fisher, S., P. Jagadeeswaran & M. E. Halpern (2003) Radiographic analysis of zebrafish skeletal defects. *Developmental Biology,* 264**,** 64-76.

Font, B., E. Aubert-Foucher, D. Goldschmidt, D. Eichenberger & M. van der Rest (1993) Binding of collagen XIV with the dermatan sulfate side chain of decorin. *J Biol Chem,* 268**,** 25015-8.

Forlino, A. & J. C. Marini (2016) Osteogenesis imperfecta. *Lancet,* 387**,** 1657-71.

Fratzl-Zelman, N., A. M. Barnes, M. Weis, E. Carter, T. E. Hefferan, G. Perino, W. Chang, P. A. Smith, P. Roschger, K. Klaushofer, F. H. Glorieux, D. R. Eyre, C. Raggio, F. Rauch & J. C. Marini (2016a) Non-Lethal Type VIII Osteogenesis Imperfecta Has Elevated Bone Matrix Mineralization. *J Clin Endocrinol Metab,* 101**,** 3516-25.

Fratzl-Zelman, N., H. P. Bächinger, J. A. Vranka, P. Roschger, K. Klaushofer & F. Rauch (2016b) Bone matrix hypermineralization in prolyl-3 hydroxylase 1 deficient mice. *Bone,* 85**,** 15-22.

Garibaldi, N., B. M. Contento, G. Babini, J. Morini, S. Siciliani, M. Biggiogera, M. Raspanti, J. C. Marini, A. Rossi, A. Forlino & R. Besio (2021) Targeting cellular stress in vitro improves osteoblast homeostasis, matrix collagen content and mineralization in two murine models of osteogenesis imperfecta. *Matrix Biol,* 98**,** 1-20.

Gemberling, M., T. J. Bailey, D. R. Hyde & K. D. Poss (2013) The zebrafish as a model for complex tissue regeneration. *Trends Genet,* 29**,** 611-20.

Gioia, R., C. Panaroni, R. Besio, G. Palladini, G. Merlini, V. Giansanti, I. A. Scovassi, S. Villani, I. Villa, A. Villa, P. Vezzoni, R. Tenni, A. Rossi, J. C. Marini & A. Forlino (2012) Impaired osteoblastogenesis in a murine model of dominant osteogenesis imperfecta: a new target for osteogenesis imperfecta pharmacological therapy. *Stem Cells,* 30**,** 1465-76.

Gioia, R., F. Tonelli, I. Ceppi, M. Biggiogera, S. Leikin, S. Fisher, E. Tenedini, T. A. Yorgan, T. Schinke, K. Tian, J. M. Schwartz, F. Forte, R. Wagener, S. Villani, A. Rossi & A. Forlino (2017) The chaperone activity of 4PBA ameliorates the skeletal phenotype of Chihuahua, a zebrafish model for dominant osteogenesis imperfecta. *Hum Mol Genet,* 26**,** 2897-2911.

Gistelinck, C., R. Y. Kwon, F. Malfait, S. Symoens, M. P. Harris, K. Henke, M. B. Hawkins, S. Fisher, P. Sips, B. Guillemyn, J. W. Bek, P. Vermassen, H. De Saffel, P. E. Witten, M. Weis, A. De Paepe, D. R. Eyre, A. Willaert & P. J. Coucke (2018) Zebrafish type I collagen mutants faithfully recapitulate human type I collagenopathies. *Proc Natl Acad Sci U S A,* 115**,** E8037-E8046.

Haas, H. J. (1962) Studies on mechanisms of joint and bone formation in the skeleton rays of fish fins. *Dev Biol,* 5**,** 1-34.

He, H., C. Wang, Q. Tang, F. Yang & Y. Xu (2018) Possible mechanisms of prednisolone-induced osteoporosis in zebrafish larva. *Biomed Pharmacother,* 101**,** 981-987.

Henke, K., J. M. Daane, M. B. Hawkins, C. M. Dooley, E. M. Busch-Nentwich, D. L. Stemple & M. P. Harris (2017) Genetic Screen for Postembryonic Development in the Zebrafish (*Danio rerio*): Dominant Mutations Affecting Adult Form. *Genetics,* 207**,** 609-623.

Howe, K., M. D. Clark, C. F. Torroja, J. Torrance, C. Berthelot, M. Muffato, J. E. Collins, S. Humphray, K. McLaren, L. Matthews, S. McLaren, I. Sealy, M. Caccamo, C. Churcher, C. Scott, J. C. Barrett, R. Koch, G. J. Rauch, S. White, W. Chow, B. Kilian, L. T. Quintais, J. A. Guerra-Assunção, Y. Zhou, Y. Gu, J. Yen, J. H. Vogel, T. Eyre, S. Redmond, R. Banerjee, J. Chi, B. Fu, E. Langley, S. F. Maguire, G. K. Laird, D. Lloyd, E. Kenyon, S. Donaldson, H. Sehra, J. Almeida-King, J. Loveland, S. Trevanion, M. Jones, M. Quail, D. Willey, A. Hunt, J. Burton, S. Sims, K. McLay, B. Plumb, J. Davis, C. Clee, K. Oliver, R. Clark, C. Riddle, D. Elliot, G. Threadgold, G. Harden, D. Ware, S. Begum, B. Mortimore, G. Kerry, P. Heath, B.

Phillimore, A. Tracey, N. Corby, M. Dunn, C. Johnson, J. Wood, S. Clark, S. Pelan, G. Griffiths, M. Smith, R. Glithero, P. Howden, N. Barker, C. Lloyd, C. Stevens, J. Harley, K. Holt, G. Panagiotidis, J. Lovell, H. Beasley, C. Henderson, D. Gordon, K. Auger, D. Wright, J. Collins, C. Raisen, L. Dyer, K. Leung, L. Robertson, K. Ambridge, D. Leongamornlert, S. McGuire, R. Gilderthorp, C. Griffiths, D. Manthravadi, S. Nichol, G. Barker, et al. (2013) The zebrafish reference genome sequence and its relationship to the human genome. *Nature,* 496**,** 498-503.

Huang, C. C., T. C. Wang, B. H. Lin, Y. W. Wang, S. L. Johnson & J. Yu (2009) Collagen IX is required for the integrity of collagen II fibrils and the regulation of vascular plexus formation in zebrafish caudal fins. *Dev Biol,* 332**,** 360-70.

Hudson, D. M. & D. R. Eyre (2013) Collagen prolyl 3-hydroxylation: a major role for a minor post-translational modification? *Connect Tissue Res,* 54**,** 245-51.

Imrie, D. & K. C. Sadler (2010) White adipose tissue development in zebrafish is regulated by both developmental time and fish size. *Dev Dyn,* 239**,** 3013-23.

Ishikawa, Y. & H. P. Bächinger (2013) A molecular ensemble in the rER for procollagen maturation. *Biochim Biophys Acta,* 1833**,** 2479-91.

Itou, J., H. Kawakami, T. Burgoyne & Y. Kawakami (2012) Life-long preservation of the regenerative capacity in the fin and heart in zebrafish. *Biol Open,* 1**,** 739-46.

Izu, Y., S. M. Adams, B. K. Connizzo, D. P. Beason, L. J. Soslowsky, M. Koch & D. E. Birk (2021) Collagen XII mediated cellular and extracellular mechanisms regulate establishment of tendon structure and function. *Matrix Biol,* 95**,** 52-67.

Jain, M., A. Tam, J. R. Shapiro, R. D. Steiner, P. A. Smith, M. B. Bober, T. Hart, D. Cuthbertson, J. Krischer, M. Mullins, S. Bellur, P. H. Byers, M. Pepin, M. Durigova, F. H. Glorieux, F. Rauch, B. Lee, V. R. Sutton, S. C. S. Nagamani & M. m. o. t. B. B. D. C. (2019) Growth characteristics in individuals with osteogenesis imperfecta in North America: results from a multicenter study. *Genet Med,* 21**,** 275-283.

Jovanovic, M., G. Guterman-Ram & J. C. Marini (2022) Osteogenesis Imperfecta: Mechanisms and Signaling Pathways Connecting Classical and Rare OI Types. *Endocr Rev,* 43**,** 61-90.

Kague, E., P. Roy, G. Asselin, G. Hu, J. Simonet, A. Stanley, C. Albertson & S. Fisher (2016) Osterix/Sp7 limits cranial bone initiation sites and is required for formation of sutures. *Dev Biol,* 413**,** 160-72.

Kaneto, C. M., P. S. Pereira Lima, K. L. Prata, J. L. Dos Santos, J. M. de Pina Neto, R. A. Panepucci, H. Noushmehr, D. T. Covas, F. J. A. de Paula & W. A. Silva (2017) Gene expression profiling

of bone marrow mesenchymal stem cells from Osteogenesis Imperfecta patients during osteoblast differentiation. *Eur J Med Genet,* 60**,** 326-334.

Kato, T., K. Nakayasu, A. Kanai, T. Nishiyama, Y. Imamura & T. Hayashi (2000) Distribution and isoform characterization of type XII collagen in bovine cornea. *Ophthalmic Res,* 32**,** 215-21.

Knopf, F., C. Hammond, A. Chekuru, T. Kurth, S. Hans, C. W. Weber, G. Mahatma, S. Fisher, M. Brand, S. Schulte-Merker & G. Weidinger (2011) Bone regenerates via dedifferentiation of osteoblasts in the zebrafish fin. *Dev Cell,* 20**,** 713-24.

Koch, M., B. Bohrmann, M. Matthison, C. Hagios, B. Trueb & M. Chiquet (1995) Large and small splice variants of collagen XII: differential expression and ligand binding. *J Cell Biol,* 130**,** 1005-14.

Li, H., X. Jiang, J. Delaney, T. Franceschetti, I. Bilic-Curcic, J. Kalinovsky, J. A. Lorenzo, D. Grcevic, D. W. Rowe & I. Kalajzic (2010) Immature osteoblast lineage cells increase osteoclastogenesis in osteogenesis imperfecta murine. *Am J Pathol,* 176**,** 2405-13.

Lund, T. C., X. Patrinostro, A. C. Kramer, P. Stadem, L. A. Higgins, T. W. Markowski, M. S. Wroblewski, D. S. Lidke, J. Tolar & B. R. Blazar (2014) sdf1 Expression reveals a source of perivascular-derived mesenchymal stem cells in zebrafish. *Stem Cells,* 32**,** 2767-79.

Malbouyres, M., A. Guiraud, C. Lefrançois, M. Salamito, P. Nauroy, L. Bernard, F. Sohm, B. Allard & F. Ruggiero (2022) Lack of the myotendinous junction marker col22a1 results in posture and locomotion disabilities in zebrafish. *Matrix Biol,* 109**,** 1-18.

Marini, J. C., A. Forlino, H. P. Bächinger, N. J. Bishop, P. H. Byers, A. Paepe, F. Fassier, N. Fratzl-Zelman, K. M. Kozloff, D. Krakow, K. Montpetit & O. Semler (2017) Osteogenesis imperfecta. *Nat Rev Dis Primers,* 3**,** 17052.

Mirigian, L. S., E. Makareeva, E. L. Mertz, S. Omari, A. M. Roberts-Pilgrim, A. K. Oestreich, C. L. Phillips & S. Leikin (2016) Osteoblast Malfunction Caused by Cell Stress Response to Procollagen Misfolding in α2(I)-G610C Mouse Model of Osteogenesis Imperfecta. *J Bone Miner Res,* 31**,** 1608-1616.

Morello, R., T. K. Bertin, Y. Chen, J. Hicks, L. Tonachini, M. Monticone, P. Castagnola, F. Rauch, F. H. Glorieux, J. Vranka, H. P. Bächinger, J. M. Pace, U. Schwarze, P. H. Byers, M. Weis, R. J. Fernandes, D. R. Eyre, Z. Yao, B. F. Boyce & B. Lee (2006) CRTAP is required for prolyl 3- hydroxylation and mutations cause recessive osteogenesis imperfecta. *Cell,* 127**,** 291-304.

Nauroy, P., A. Guiraud, J. Chlasta, M. Malbouyres, B. Gillet, S. Hughes, E. Lambert & F. Ruggiero (2019) Gene profile of zebrafish fin regeneration offers clues to kinetics, organization and biomechanics of basement membrane. *Matrix Biol,* 75-76**,** 82-101.

Panaroni, C., R. Gioia, A. Lupi, R. Besio, S. A. Goldstein, J. Kreider, S. Leikin, J. C. Vera, E. L. Mertz, E. Perilli, F. Baruffaldi, I. Villa, A. Farina, M. Casasco, G. Cetta, A. Rossi, A. Frattini, J. C. Marini, P. Vezzoni & A. Forlino (2009) In utero transplantation of adult bone marrow decreases perinatal lethality and rescues the bone phenotype in the knockin murine model for classical, dominant osteogenesis imperfecta. *Blood,* 114**,** 459-68.

Pfefferli, C. & A. Jaźwińska (2015) The art of fin regeneration in zebrafish. *Regeneration (Oxf),* 2**,** 72-83.

Poss, K. D., M. T. Keating & A. Nechiporuk (2003) Tales of regeneration in zebrafish. *Dev Dyn,* 226**,** 202-10.

Rauch, F., R. Travers, A. M. Parfitt & F. H. Glorieux (2000) Static and dynamic bone histomorphometry in children with osteogenesis imperfecta. *Bone,* 26**,** 581-9.

Reich, A., W. Cabral & J. Marini (2012). Homogeneous mutant collagen in osteogenesis imperfecta model mice leads to improved bone phenotype through multiple pathways [Abstract P38]. *Program of the American Society for Bone and Mineral Research Topical Meeting on Bone and Skeletal Muscle Interactions*, Kansas City, MO, 2012.

Ricard-Blum, S. (2011) The collagen family. *Cold Spring Harb Perspect Biol,* 3**,** a004978.

Santamaría, J. A. & J. Becerra (1991) Tail fin regeneration in teleosts: cell-extracellular matrix interaction in blastemal differentiation. *J Anat,* 176**,** 9-21.

Scheiber, A. L., K. J. Wilkinson, A. Suzuki, M. Enomoto-Iwamoto, T. Kaito, K. S. Cheah, M. Iwamoto, S. Leikin & S. Otsuru (2022) 4PBA reduces growth deficiency in osteogenesis imperfecta by enhancing transition of hypertrophic chondrocytes to osteoblasts. *JCI Insight,* 7.

Shi, X., L. Gong, Y. Liu, K. Hou, Y. Fan, C. Li, T. Wen, X. Qu & X. Che (2020) 4-phenylbutyric acid promotes migration of gastric cancer cells by histone deacetylase inhibition-mediated IL-8 upregulation. *Epigenetics,* 15**,** 632-645.

Sillence, D. O., A. Senn & D. M. Danks (1979) Genetic heterogeneity in osteogenesis imperfecta. *J Med Genet,* 16**,** 101-16.

Smith, A., F. Avaron, D. Guay, B. K. Padhi & M. A. Akimenko (2006) Inhibition of BMP signaling during zebrafish fin regeneration disrupts fin growth and scleroblasts differentiation and function. *Dev Biol,* 299**,** 438-54.

Sousa, S., N. Afonso, A. Bensimon-Brito, M. Fonseca, M. Simões, J. Leon, H. Roehl, M. L. Cancela & A. Jacinto (2011) Differentiated skeletal cells contribute to blastema formation during zebrafish fin regeneration. *Development,* 138**,** 3897-905.

Spoorendonk, K. M., J. Peterson-Maduro, J. Renn, T. Trowe, S. Kranenbarg, C. Winkler & S. Schulte-Merker (2008) Retinoic acid and Cyp26b1 are critical regulators of osteogenesis in the axial skeleton. *Development,* 135**,** 3765-74.

Tonelli, F., J. W. Bek, R. Besio, A. De Clercq, L. Leoni, P. Salmon, P. J. Coucke, A. Willaert & A. Forlino (2020a) Zebrafish: A Resourceful Vertebrate Model to Investigate Skeletal Disorders. *Front Endocrinol (Lausanne),* 11**,** 489.

Tonelli, F., S. Cotti, L. Leoni, R. Besio, R. Gioia, L. Marchese, S. Giorgetti, S. Villani, C. Gistelinck, R. Wagener, B. Kobbe, I. A. K. Fiedler, D. Larionova, B. Busse, D. Eyre, A. Rossi, P. E. Witten & A. Forlino (2020b) Crtap and p3h1 knock out zebrafish support defective collagen chaperoning as the cause of their osteogenesis imperfecta phenotype. *Matrix Biol,* 90**,** 40-60.

Tonelli, F., L. Leoni, V. Daponte, R. Gioia, S. Cotti, I. A. K. Fiedler, D. Larianova, A. Willaert, P. J. Coucke, S. Villani, B. Busse, R. Besio, A. Rossi, P. E. Witten & Antonella Forlino (2023). Zebrafish Tric-b is required for skeletal development and bone cells differentiation. *Front Endocrinol (Lausanne)*, accepted for publication.

Tsai, S. B., V. Tucci, J. Uchiyama, N. J. Fabian, M. C. Lin, P. E. Bayliss, D. S. Neuberg, I. V. Zhdanova & S. Kishi (2007) Differential effects of genotoxic stress on both concurrent body growth and gradual senescence in the adult zebrafish. *Aging Cell,* 6**,** 209-24.

Uveges, T. E., P. Collin-Osdoby, W. A. Cabral, F. Ledgard, L. Goldberg, C. Bergwitz, A. Forlino, P. Osdoby, G. A. Gronowicz & J. C. Marini (2008) Cellular mechanism of decreased bone in Brtl mouse model of OI: imbalance of decreased osteoblast function and increased osteoclasts and their precursors. *J Bone Miner Res,* 23**,** 1983-94.

Valenti, M. T., G. Marchetto, M. Mottes & L. Dalle Carbonare (2020) Zebrafish: A Suitable Tool for the Study of Cell Signaling in Bone. *Cells,* 9.

van der Meulen, T., S. Kranenbarg, H. Schipper, J. Samallo, J. L. van Leeuwen & H. Franssen (2005) Identification and characterisation of two runx2 homologues in zebrafish with different expression patterns. *Biochim Biophys Acta,* 1729**,** 105-17.

Vanhauwaert, S., G. Van Peer, A. Rihani, E. Janssens, P. Rondou, S. Lefever, A. De Paepe, P. J. Coucke, F. Speleman, J. Vandesompele & A. Willaert (2014) Expressed repeat elements improve RT-qPCR normalization across a wide range of zebrafish gene expression studies. *PLoS One,* 9**,** e109091.

Vanoevelen, J., A. Janssens, L. F. Huitema, C. L. Hammond, J. R. Metz, G. Flik, T. Voets & S. Schulte-Merker (2011) Trpv5/6 is vital for epithelial calcium uptake and bone formation. *FASEB J,* 25**,** 3197-207.

Vranka, J. A., E. Pokidysheva, L. Hayashi, K. Zientek, K. Mizuno, Y. Ishikawa, K. Maddox, S. Tufa, D. R. Keene, R. Klein & H. P. Bächinger (2010) Prolyl 3-hydroxylase 1 null mice display abnormalities in fibrillar collagen-rich tissues such as tendons, skin, and bones. *J Biol Chem,* 285**,** 17253-62.

Witten, P. E. & A. Huysseune (2009) A comparative view on mechanisms and functions of skeletal remodelling in teleost fish, with special emphasis on osteoclasts and their function. *Biol Rev Camb Philos Soc,* 84**,** 315-46.

Witten, P. E., A. Huysseune & B. K. Hall (2010) A practical approach for the identification of the many cartilaginous tissues in teleost fish. *Journal of Applied Ichthyology,* 26**,** 257-262.

General discussion and perspectives

During my PhD I successfully employed zebrafish as a model for skeletal diseases at both embryo and adult developmental stages and I took advantage of the caudal fin regeneration as a tool for deep investigation of bone cellular homeostasis. I also expanded my knowledge on the regenerative mechanisms by writing a detailed review about appendage regeneration in vertebrates (**Figure 1**).

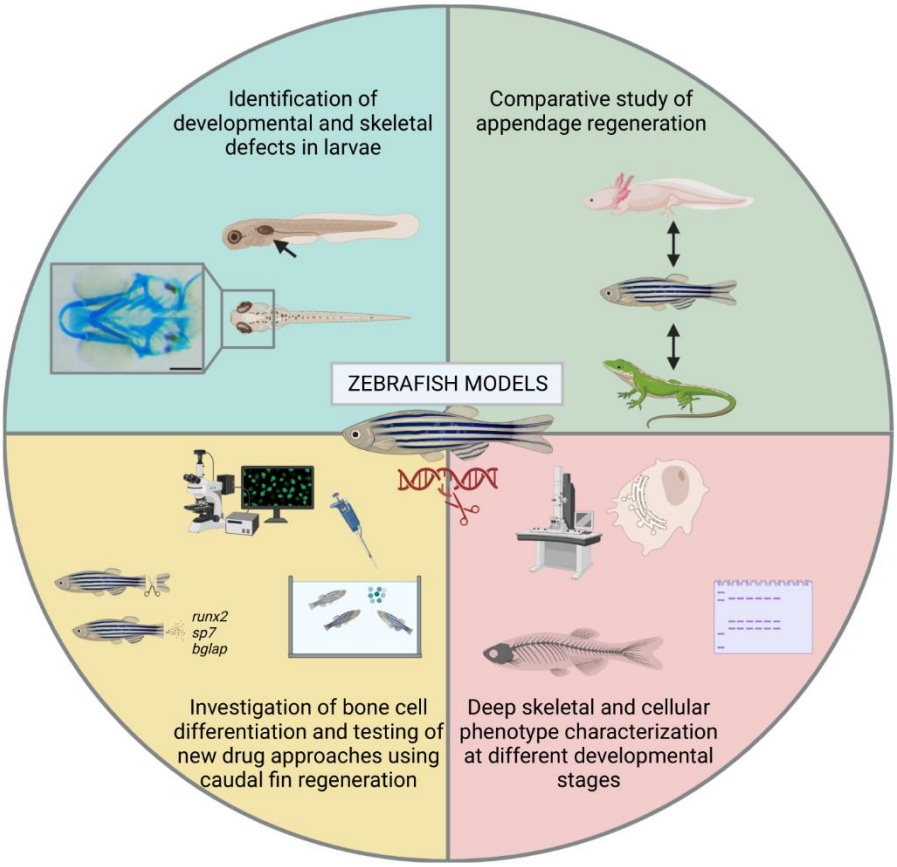

Figure 1. Schematic representation of the variety of approaches that were applied to study zebrafish models in my PhD research. The Alcian Blue staining representative image is from Manuscript 1. Created with BioRender.com.

Manuscript 1

During the first year of my PhD, I contributed to the establishment of a zebrafish model to elucidate the role of the ribosomal protein eL13 on the onset of spondyloepimetaphyseal dysplasia (SEMD), a heterogeneous group of skeletal dysplasias caused by mutations in gene encoding proteins with different functions**.** SEMDs are pathologies affecting development of bone and cartilage, and hallmarks of patients are severe short stature and skeletal abnormalities in the spine, epiphyses, and metaphyses.

In this study, patients from four unrelated families affected by SEMD with a severe growth disorder and uniform radiological features were identified as carriers of *RPL13* mutation. By CRISPR/Cas9

editing, we successfully generated the *rpl13* mutant harboring a seven-nucleotide deletion causing a frameshift predicted to alter the amino acid sequence of the protein. Despite our mutants expressed *rpl13* at both transcript and protein levels, it is very likely that the introduced mutation impairs structure and function of eL13 by disrupting the binding of the C-terminal α-helix to the rRNA. A general developmental delay was detected in 5 and 7 dpf *rpl13* larvae which had delayed swim bladder inflation. Juvenile *rpl13* mutants aged 1 mpf also displayed reduced standard length (SL) and body disproportion respect to WT fish, features shared with SEMD-*RPL13* patients.

Collectively, our *rpl13* mutant partially recapitulated the phenotype of patients with *RPL13* mutations providing a proof-of-principle for the relevant role of eL13 in skeletogenesis and a valuable tool for further studies at later stages.

Manuscript 2

During the 2020 pandemic I worked at this review in which I provide an updated and extensive overview of several aspects of appendage regeneration in lizard, salamander, and zebrafish, in order to identify the shared mechanisms required for a successful regeneration. The three vertebrates share two key processes at a morphological and cellular level: the formation of a thick wound epidermis that supports the regenerative process without scarring, and the formation of a blastema, which provides the source of differentiated cells that will restore the lost tissues. Evidence collected on the three models points towards Wnt/β-catenin and FGFs as master regulators of the regenerative process, being not only necessary for regeneration to occur but also being able to promote it in organs with limited regenerative potential, such as lizard limb. A delicate equilibrium in the level of immunosurveillance is also required. Lizard tail, salamander limb and zebrafish caudal fin can be considered immuno-privileged organs, in which inflammation triggered by injury equilibrates with the presence of healing, anti-inflammatory macrophages. Despite all the similarities, each model is unique and has different advantages and limitations. For this reason, the comparative study of vertebrates with high regenerative ability is fundamental to achieve significant insights on what are the factors driving regeneration. This review represented to me the opportunity to gain knowledge necessary for the success of my PhD.

Manuscript 3

A consistent part of my PhD was dedicated to this work. In this study, we demonstrated the relevance of the potassium channel TRIC-B, encoded by *TMEM38B* and involved in OI type XIV pathogenesis, in zebrafish bone, supporting its shared role in skeletal development between teleosts and mammals. By CRISPR/Cas9 editing we created and deeply characterized the first two zebrafish mutants for

tmem38b. One (*tmem38b*$^{-/-}$) carried a frameshift mutation associated to the insertion of pre-termination codon and in the second (*tmem38b*$^{\Delta 120\text{-}7/\Delta 120\text{-}7}$) a 24 bp *in frame* deletion caused the removal of a consensus sequence relevant for channel activity in the voltage-sensing TM4 domain.

Nonsense mediated mRNA decay (NMD) was activated in *tmem38b*$^{-/-}$ and absent in *tmem38b*$^{\Delta 120\text{-}7/\Delta 120\text{-}7}$. Protein expression could not be investigated due to lack of specific antibody.

Tmem38b$^{-/-}$ showed reduced size at 21 days post fertilization (dpf) and 1 month post fertilization (mpf). The two time points overlap with the larval to juvenile transition, associated to quick and significant body growth, indicating a relevant role of Tric-b for early bone development rather than for early or adult skeletal homeostasis. Consistent with these observations, *tmem38b*$^{-/-}$ larvae revealed reduced notochord mineralization and a delay in swim bladder inflation compared to WT, further supporting the requirement of Tric-b for development.

The skeletal phenotype of *tmem38b*$^{\Delta 120\text{-}7/\Delta 120\text{-}7}$ was limited to reduced vertebral length at 21 dpf, supporting a partial activity of the channel in this model and leading to the hypothesis that a full active channel is necessary for proper bone formation.

While no differences in the osteoblast markers *sp7* and *bglap* were found, caudal fin regeneration studies allowed to identify an increased mineralization during the early regeneration phase, suggesting an accumulation of minerals during bone modelling that could be due either to an impaired cellular function or to an increased inter-fibrillar spacing that undergoes remodeling during growth. In *tmem38b*$^{-/-}$ we detected a reduced number of TRAP+ cells compared to WT in presence of normal Rankl/Opg ratio resembling human and murine data and supporting a direct effect of Tric-b on osteoclast activity. Of particular interest, *tmem38b*$^{\Delta 120\text{-}7/\Delta 120\text{-}7}$ displayed altered localization of TRAP+ cells and increased expression of the macrophage marker *mpeg1*, suggesting the presence of immature precursors associated to a low level of anyway active mutant Tric-b.

Collagen type I extracted from bone and skin of *tmem38b* mutants was undermodified, as already described for patients. Interestingly, actinotrichia, structures rich in collagen I and II located at the distal extremity of the caudal fin rays, were impaired in both *tmem38b* mutants, supporting the already proposed correlation between defects in *TMEM38B* and impaired collagen deposition. We demonstrated mutant collagen retention inside fibroblasts and osteoblasts responsible of enlarged endoplasmic reticulum (ER) cisternae, together with Hsp47 upregulation in both zebrafish mutants, similarly to OI human and mouse cells. We demonstrated that the treatment with 4-PBA partially rescued Hsp47 overexpression supporting its possible role as OI treatment also for OI type XIV as already demonstrated both *in vitro* and *in vivo* for dominant and some recessive OI forms.

Manuscript 4

My main PhD project involved the use of two different OI zebrafish models, the dominant OI type III *Chihuahua* (*Chi*/+) and the recessive OI type VIII *p3h1*$^{-/-}$, to investigate bone homeostasis during caudal fin regeneration.

We found a reduced caudal fin regeneration ability in both *Chi*/+ and *p3h1*$^{-/-}$, compatibly with their OI phenotype as one of the common features shared by patients and murine models is delayed bone formation. Investigation of caudal fin morphometry before and during regeneration demonstrated a reduced number of caudal fin rays and increased number of bifurcations in *p3h1*$^{-/-}$, while *Chi*/+ showed reduced length of segments at basal state and throughout regeneration, likely due to the collagen defect disturbing the patterning of the segments by osteoblasts.

No differences in *runx2* and *sox9* expression were found in both models, indicating that the early differentiation steps before osteoblast commitment were not affected in OI. No differences were observed for osteoblast markers neither at the transcript nor at the protein level in *p3h1*$^{-/-}$ fish. Nevertheless, osteoblast differentiation was impaired in *Chi*/+, as indicated by the reduced *bglap* expression at basal state and the increase in *sp7*+ cells failing to being replaced by *bglap*+ mature osteoblasts during regeneration. These findings were in accordance with what already reported for dominant OI patients as well as murine models. The defect in osteoblast differentiation resulted in a switch towards increased adipogenesis with increased number of lipid drops in *Chi*/+ caudal fin, strengthening the correlation between impaired osteoblastogenesis and increased adipogenesis *in vivo*, already reported *in vitro* in dominant OI patients and murine models. We found that the reduced amount of mature osteoblasts in *Chi*/+ was also matched by an increased number of TRAP+ osteoclasts at basal state. This result was expected since osteoblasts and osteoclasts activity in bone is tightly coupled, and mutations causative of OI are frequently associated to an imbalance between bone formation and bone resorption. On the contrary, the observation of a reduced number of TRAP+ cells in the regenerating caudal fins of *Chi*/+ and *p3h1*$^{-/-}$ was surprising, since to our knowledge this is the first time in which decreased osteoclast activity is described during bone formation in OI. We did not detect any variation in the levels of *Rankl* and *Opg* nor in the *Rankl/Opg* ratio in our OI fish, indicating that the impaired osteoclastogenesis found in the two models was not directly linked to *Rankl* stimulation.

The impaired caudal fin morphology resulted in defective swimming ability in *Chi*/+ fish, that tended to swim for shorter paths and with erratic movements respect to WT. This defect was also related to altered extracellular matrix in the caudal fin, with collagen type I deposited in a disorganized manner

along all the caudal fin in both *Chi/+* and *p3h1*$^{-/-}$, in some cases with the formation of aggregates typical of misfolded proteins. We also found an impaired joint structure in *Chi/+*, with disorganized collagen I fibrils associated to an increase in collagen XIV amount which overall resulted in an increased inter-joint space before and during regeneration. No abnormalities were on the contrary detected in *p3h1*$^{-/-}$ fish.

In order to ameliorate cell homeostasis in both OI models, we tested the already FDA approved 4-phenylbutyrate (4-PBA) on caudal fin regeneration. 4-PBA administration rescued caudal fin regeneration rate in adult *p3h1*$^{-/-}$, proving for the first time its beneficial effect on recessive OI *in vivo* as chemical chaperone.

Perspectives

In my PhD research, a variety of approaches were applied on different zebrafish models to dissect the molecular mechanisms behind rare skeletal diseases *in vivo*.

We successfully generated and validated the *rpl13* mutant as a model for SEMD-RPL13 at larval and juvenile developmental stages. This model is useful for the study of the pathology and will be available for the outcome characterization also at later stages and during adulthood. For instance, growth rate analysis could be performed to identify if the reduced growth, a hallmark of SEMD, is conserved in the fish model, providing a tool to better define its molecular basis. Deeper skeletal investigation could help clarify the role of eL13 in the mineralized tissue. Finally, *in situ* hybridization and expression studies performed at different stages and in different tissues would be useful to address how the lack of a universally required ribosomal protein such as eL13 can result in such a specific SEMD phenotype.

The two *tmem38b* mutants, generated in our laboratory, were deeply characterized from both a skeletal and a cellular point of view. Our findings showed a conserved role of Tric-b channel in zebrafish and several characteristics of our mutants recapitulated the outcome described in OI type XIV patients and murine models. Due to these similarities, *tmem38b* mutants provide a valuable instrument to test new pharmacological approaches. We already demonstrated a positive effect of 4-PBA in reducing Hsp47 overexpression in both *tmem38b*$^{-/-}$ and *tmem38b*$^{\Delta 120\text{-}7/\Delta 120\text{-}7}$, confirming that cellular stress represents a valid target for new drugs. ER-stress markers but also skeletal mineralization could be evaluated after drug administration, even taking advantage of the regenerating caudal fin. The availability of the two mutants with different genetic mutations is very appealing, because it would allow to precisely attribute the role of each mutation in modulating drug

efficacy, allowing to elaborate personalized therapies. In this context, it would be indispensable to clarify the protein defect of both *tmem38b* mutants as soon as specific antibodies will be available.

My main PhD project results clearly proved the zebrafish caudal fin system, during regeneration but also at basal state, as a valid tool for the study of bone cellular homeostasis in pathological conditions. One powerful characteristic is that being mostly transparent, after crossing with transgenic lines it allows to visualize bone cells under confocal microscopy *in vivo*. This is very difficult in murine models, in which intravital imaging is still a challenging technique. Finally, high-throughput screening of drugs with positive effect on bone can be performed by simply keeping the fish in small tanks with limited water volumes and amount of drug while caudal fin regenerates. These approaches, that are increasingly being validated and standardized, have the potential to be extended to other skeletal models to gain further insights on pathological mechanisms at the cellular level.